DOTTORATO DI RICERCA IN
SCIENZE DELLA TERRA

CICLO XXVI

COORDINATORE Prof. Lorenzo Rook

Integration of Remote-Sensing techniques and geomorphological analysis for the characterization and mapping of ground instability at regional scale.

Settore Scientifico Disciplinare GEO/04

Dottorando
Dott. Luca Tanteri

Tutore
Prof. Filippo Catani

Coordinatore
Prof. Lorenzo Rook

Anni 2011/2013

Table of Contents

Aknowledgements

Firenze

December 31, 2013

Luca Tanteri — *"Integration of Remote-Sensing techniques and geomorphological analysis for the characterization and mapping of ground instability at regional scale"*

i

Abstract

Remote-sensing techniques represent a powerful tool to measure and map ground displacement as they offer a synoptic view that can be repeated at different time intervals and that is available at various scales.

The exploding number of new space and airborne platforms (from micro-satellites to unmanned aerial vehicles, UAV) enables an unprecedented observation frequency and especially the advance of interferometric synthetic aperture *radar* (SAR) techniques leads to a change in our view of landslide inventories, moving from a static maps to dynamic digital inventories and constantly updated collections of hazard and risk related information.

Within this PhD programme, applicability and potential of the more recent *remote-sensing* techniques integrated with geomorphological expert knowledge, as a tool for the detection and mapping of subsidence and slope gravitative processes have been explored and tested.

In particular, images acquired by the high-resolution *radar* satellite TerraSAR-X have been exploited and processed with interferometric techniques such as Persistent Scatterers Interferometry (PSI) in order to perform a rapid detection of ground movements in Barcelona and some neighbouring areas.

Furthermore long series of ERS and ENVISAT PSI data have been used for the improvement of the new landslide inventory map for the entire Tuscany region, enhancing the quality of the database, adding new informations to several phenomena, such as activity, temporal evolution of displacements, velocity along with a more detailed delimitation.

Moreover a new database of areas affected by subsidence in Tuscany have been obtained automatically, by combining geometrically the measurements of the ENVISAT PSs in the two orbital configurations.

Along with the exploitation of *radar* interferometric data, the potential of different approaches based on airborne multi-sensor data surveys have been explored in a test site in Valmarecchia (Italy). In such test site multi-spectral, hyper-spectral and LiDAR data acquired in two different surveys have been integrated to detect slope phenomena with rapid kinematic, not monitorable with the proposed interferometric techniques.

Furthermore, a detailed land-cover map of the area have been developed using a *data-fusion* approach on the available data.

Riassunto

Le tecniche di telerilevamento rappresentano uno strumento efficace e ad oggi molto diffuso per effettuare misurazioni su fenomeni deformativi superficiali, in quanto offrono la possibilità di disporre di dati a copertura di intervalli temporali variabili ed eseguire analisi a partire da scale locali fino a scale sinottiche.

L'attuale disponibilità di sensori satellitari ed aviotrasportati rende possibile disporre di una frequenza di osservazione senza precedenti. In particolar modo i sensori satellitari *radar* ad apertura sintetica (SAR), che hanno rivoluzionato le tecniche di realizzazione di mappe inventario di fenomeni di dissesto su vasta scala, fornendo un flusso costante di informazioni al servizio della gestione e valutazione del rischio idrogeologico.

Nell'ambito della presente tesi sono state testate l'applicabilità ed il potenziale delle tecniche di telerilevamento più all'avanguardia integrate con specifiche considerazioni geomorfologiche, nell'individuazione, caratterizzazione e mappatura di fenomeni di dissesto idrogeologico come frane e subsidenza.

In particolare, immagini *radar* acquisite dal satellite TerraSAR-X sono state processate con tecniche interferometriche come l'approccio PSI (*Persistent Scatterers Interferometry*), al fine di individuare e mappare dissesti superficiali nell'area urbana di Barcellona e nelle aree limitrofe. Inoltre, lunghe serie di dati relativi ai satelliti ERS ed ENVISAT sono stati utilizzati al fine di completare l'aggiornamento della mappa inventario dei fenomeni franosi in Toscana, attribuendo ai fenomeni censiti informazioni come stato di attività, evoluzione temporale degli spostamenti, velocità ed estensione areale.

Parallelamente è stata elaborata in modo semi-automatico una mappa inventario delle aree soggette a subsidenza della regione, combinando geometricamente i valori misurati dal satellite ENVISAT nelle due configurazioni orbitali.

Nell'area test Valmarecchia sono state testate le potenzialità di approcci basati sull'integrazione di dati acquisiti mediante piattaforme *multi-sensore* aviotrasportate, al servizio dell'individuazione e mappatura di fenomeni di versante a cinematica rapida (non monitorabili con tecniche PS) e nella realizzazione di mappe dettagliate degli elementi presenti sul territorio.

1.Introduction

Hydrogeological instability events (i.e., landslides and subsidence) represent the major geological hazards, occurring worldwide more frequently than any other natural disasters, including earthquakes, floods and volcanic eruptions (IGOS, 2004). Landslides (and secondarily subsidence phenomena) not only pose great threats to human lives, causing fatalities and injured people, but also produce billions of Euros of direct and indirect socio-economic losses, in terms of property and infrastructure damage and environmental degradation.

Remote-sensing techniques represent a powerful tool to measure and map ground displacement as they offer a synoptic view that can be repeated at different time intervals and that is available at various scales.

Earth Observation and *remote-sensing* have a major role to play for studying geohazard-related events at different stages, such as detection, mapping, monitoring, hazard zonation, modeling and prediction.

Generally, the exploding number of new space and airborne platforms (from micro-satellites to unmanned aerial vehicles, UAV) enables and unprecedented observation frequency and especially the advance of interferometric synthetic aperture *radar* (SAR) techniques [Farina *et al*., 2006; Roering *et al*., 2009] leads to a change in our view of landslide inventories, moving from a static maps to dynamic digital inventories and constantly updated collections of hazard and risk related information.

The rapid dissemination of *remote-sensing* products during the last two decades have been facilitated by their synergies with the Geographical Information Systems (GIS) (Rengers *et al*., 1992), that enabled a wide range of users to manage geospatial datasets, essential task when dealing with environmental issues.

Furthermore, increased computational capacity of modern computers and the implementation of sophisticated codes, algorithms and software led to semi-automatic recognition and mapping of instability phenomena using aerial and satellite images (Mondini *et al*., 2011), valuable issue in emergency situations.

The term "landslide", as simply denoted by Cruden (1991), refers to "the movement of a mass of rock, debris or earth down a slope". Landslide, as a major type of geological hazard, represents one of the natural hazards most frequently occurred worldwide.

According to Nadim et al. (2006), there is an ongoing increase of globally-reported landslide occurrences could be summarized as a consequence of uncontrolled human activities such as overexploited natural resources, intensive deforestation, plus poor land-use planning and undisciplined growing urbanization. This is in accordance to the report of United Nations (UN/ISDR, 2004), which emphasizes the important role of decent land-use planning and management in conducting natural hazard assessment and risk mapping.

Historically, *remote-sensing* techniques have been substantially developed and successfully applied for landslide investigations (Metternicht et al., 2005), exploiting the contributions of stereoscopic aerial-photos, Synthetic Aperture *Radar* Interferometry (InSAR), laser scanning and multi-spectral sensors. In particular, advanced InSAR approaches, generating *radar* benchmarks using a multi-interferogram analysis of SAR images enable detection and mapping of mass movement.

While a strong perception of landslide hazard is already common and have leaded to the development of several works with a huge bibliography (Varnes & IAEG, 1984; Guzzetti et al., 1999; Brenning, 2005; Malet & Maquaire, 2009), subsidence phenomena are generally relegated to a marginal role. This could be due to their minor impact on the media, for their less social damage and their displacement rates, generally very slow and less "catastrophic", excluding rapid sinking phenomena in urban areas as described in Buchignani et al., 2004; D'Amato Avanzi et al., 2004.

Indeed, emerging issues related to the exacerbation of consequences of land subsidence can be related to long periods of drought, decrease of rainfall, overexploitation of natural resources and land use practices.

Satellite InSAR data, thanks to its wide spatial coverage and its millimeter accuracy, is ideally suited to measure the spatial extent and magnitude of surface deformations (subsidences) associated with aquifer-system compaction (Galloway & Burbey, 2011).

In order to keep an adequate safety level, especially in those situations where relevant property and infrastructure are exposed, a thorough understanding of the distribution of hydrogeological instability phenomena, along with their state of activity, is mandatory.

In this thesis, in order to detect and map slow moving processes, such as landslides and subsidences, an approach based on *radar* interferometric data processed with the PSI (*Persistent Scatterers Interferometry*) is proposed.

The capability of PSI techniques in developing ground movements inventories relies on the possibility of assigning a spatial meaning to the point-wise ground displacement measurements provided by the PS technique, through the interpretation aerial-photos and optical satellite imagery, topographic maps and ancillary data. Due to the *remote-sensing* character of the above approach, which allows the acquisition of data over wide areas, and the extremely high precision of the *radar* measurements (Colesanti *et al.*, 2003), this method can be applied at different scales.

In order to detect and map slope processes with rapid kinematic such as flow-type landslides and fluvial dynamics, an approach based on the exploitation of digital aerial multi-spectral images and high resolution Digital Elevation Model is proposed and tested in this thesis.

Historically, investigators have attempted to use remotely sensed images to identify and map landslides using pixel based and object oriented approaches (i.e., Lin *et al.*, 2002; Hervás *et al.*, 2003; Cheng *et al.*, 2004; Rosin & Hervás, 2005; Metternicht *et al.*, 2005; Barlow *et al.*, 2006; Lee & Lee, 2006; Weirich & Blesius, 2007; Martha *et al.*, 2010; Tsai *et al.*, 2010). Most commonly, change detection techniques applied to high-resolution (HR) and very-high-resolution (VHR) optical images are used to identify landslide areas (e.g., Nichol & Wong, 2005; Lee & Lee, 2006; Weirich & Blesius, 2007; Tsai *et al.*, 2010). This requires that pre-event and post-event images are available for the affected area. Investigators have also attempted to exploit HR and VHR monoscopic optical images to detect individual landslides or groups of landslides visually.

The technique works where the visual evidence of the slope failures on the image (i.e., the landslide "signature") is sufficiently clear (Marcelino *et al.*, 2009; Fiorucci *et al.*, 2011), and where geomorphologists experienced in the identification of landslides on aerial and satellite imagery are available.

Finally, since risk assessment must necessarily take into account the type and spatial disposition of elements at risk, *remote-sensing* techniques offer a wide range of possibilities and challenges for the future, starting from automated mapping of the elements of territory.

From this viewpoint, land cover is indeed a crucial variable, and the significance of providing accurate fine-scale land cover maps is emphasized by the evidence of marked impacts of land

cover changes on local surface dynamics (Claessens *et al.*, 2009). *Remote-sensing* data classification represents an essential tool for environmental monitoring and sustainable land use management (Melesse *et al.*, 2007), especially in heterogeneous landscapes characterized by many interconnected natural- and human-induced processes (Forzieri & Catani, 2011). Various cases indicate that changing land cover and land use influence the frequency and magnitude of mass wasting processes (Glade & Crozier, 2005; Meusburger & Alewell, 2008). Considering the current prognoses of the global effects of climate change and urbanization past and present imagery is one of the few sources to reliable quantify land use and land cover changes.

In sum, recently-developed *remote-sensing* techniques have demonstrated a great potential in the framework of risk management, offering valuable tools looking at better characterize geo-hazards and risks.

- ***Aim of the thesis***

This thesis contains the main results of some projects carried out at the Earth Sciences Department of the University of Firenze (DST-UNIFI, Centre of Competence of the Italian Civil Protection for geo-hazards) and at the Institute of Geomatics (Institut de Geomàtica) in Castelldefels (Spain).

The work is aimed to explore the potential of more recent *remote-sensing* techniques commonly applied in hydrogeological risk analysis, such as *radar* interferometric techniques and exploitation of high-resolution multi-temporal data, acquired using airborne LiDAR and multi-spectral/ hyperspectral sensors.

Such techniques have been exploited in three test sites in order to explore their effectiveness in detection and mapping of areas affected by ground movements (landslides and subsidence/uplift) along with the implementation of advanced classification procedures for a detailed mapping of the elements of territory.

The techniques have been exploited in relation with the kinematic of the processes that have to be analyzed, indeed, techniques such as *radar* interferometry have been used in presence of slow kinematic movements (slow moving landslides and land subsidence) whereas a multi-temporal approach based on *change-detection* on multi-spectral and LiDAR data have been proved to be more suitable for phenomena with rapid kinematic (Figure 1).
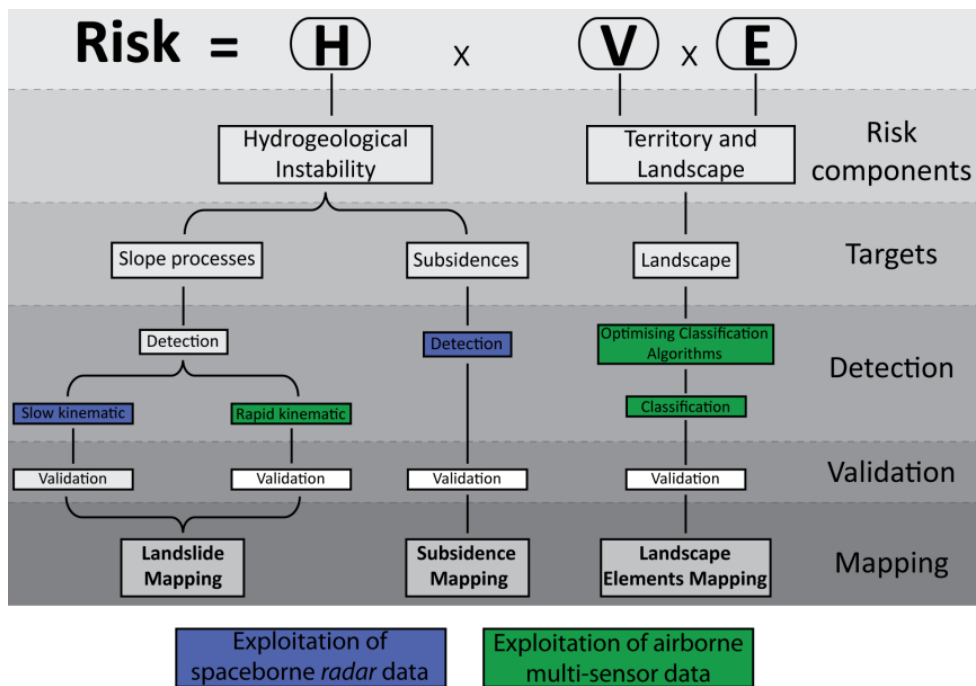
Figure 1. Flow diagram showing the structure of the thesis. The blue and green colors show respectively the cases on which satellite *radar* and airborne multi-sensor data have been used.

To achieve this objective high-resolution TerraSAR-x data, acquired by the *Institut de Geomàtica* in Castelldefels, and processed using a PSI technique developed and owned by the same Institute and described in Crosetto *et al.,* (2011) and Biescas *et al., (*2007), have been exploited for a rapid detection of landslides and subsidence phenomena both in the urban area of Barcelona and in its surroundings, creating a preliminary database presented to the municipal authority of Barcelona.

Furthermore a new database of landslides in Tuscany have been created starting from a previous version, performing an integration of ground displacement measurements provided ERS (1992-2000) and ENVISAT (2002-2010) PSI data with geomorphological expert knowledge. Furthermore a new subsidence inventory for the whole region have been obtained combining EVISAT data acquired in the two orbits.

Such products have been developed in the project DIANA (Interferometric Data for Environmental Analysis: landslides and subsidence) a partnership between the Department of Earth Sciences of Firenze and the Tuscany regional authority.

An approach based on multi-spectral, hyperspectral and LiDAR data synergies have been used in this research in order to detect slope processes with rapid kinematic, not detectable with the PSI technique.

Hence approach based on a *change-detection* technique have been used, comparing airborne sensor data acquired during two different surveys, carried out respectively in 2009 and 2010, over the area of Valmarecchia (province of Rimini).

Furthermore, the data acquired in the survey of 2010 have been used for the automatic development of a land cover map of the area, classifying the landscape by combining the spectral signature of the elements on the ground with height informations derived by high-resolution DEMs. The result of this process is a detailed map of the elements present on the territory (i.e. houses, industries, roads, vegetation and water).

The analyses carried out in Valmarecchia have been performed in the project "Monitoring of the disturbances on gas pipeline network using *change-detection* and *target-detection* techniques and automated procedures for the analysis of remotely-sensed data", a project commissioned to DST-UNIFI by SNAM Rete Gas.

In detail, besides the *Introduction* the thesis is structured as follows:

- *Chapter 2* contains a detailed review of the state of art of the techniques used in the thesis. In the three paragraphs the potential of *radar* interferometric techniques, the hyper-spectral and multi-spectral analysis and the use of high-resolution DEMs obtained using LiDAR sensors are respectively described considering the available literature.

- *Chapter 3* describes the proposed methods, the available data and the procedures used in the thesis for the three study areas: Barcelona, Tuscany and Valmarecchia.

- *Chapter 4* contains the main results and discussion of the proposed approaches. In particular the chapter describes the results of the rapid detection of ground movements in Barcelona using TerraSAR-X data, the two new regional databases of landslides and subsidence in Tuscany obtained using ERS and ENVISAT data, the automated mapping of landslides and elements of territory in Valmarecchia using airborne multi-sensor data.

- *Chapter 5* summarizes the main finding of this thesis in the assessment of the effectivenes of the proposed techniques in order to obtain the main parameters needed for risk evaluation.

- *Chapter 6* contains the main references of this work, listed in alphabetical order.

- *Chapter 7* contains appendices with some tables and results not directly included in the text.

- *Chapter 8* includes the annexes, that is some already published parts of the PhD thesis. In particular the results of the automated landside detection in Valmarecchia and the mapping of natural and urban environments using airborne multi sensor ADS40–MIVIS–LiDAR synergies.

- Annex 1: Lagomarsino, D., Battistini A., Tanteri, L. (2013) *"High resolution multispectral and LiDAR data integration for landslide detection purposes"* Rendiconti Online della Società Geologica Italiana, Vol.24, pp. 187-189

- Annex 2: Forzieri, G., Tanteri, L., Moser, G., Catani, F. (2013) *"Mapping natural and urban environments using airborne multi-sensor ADS40-MIVIS-LiDAR synergies"* International Journal of Applied Earth Observation and Geoinformation, Vol. 23, pp 313-323.

2. Remote-sensing for ground movement analysis: state of art

Remote-sensing, which is simply defined as the approach of obtaining information without physical contact (Lillesand & Kiefer, 1987), is capable to survey distant areas where field works are difficult to be carried out. *Remote-sensing* contributes a valuable tool for landslide studies at different stages, such as detection and mapping, monitoring, hazard zonation and prediction (Canuti *et al.*, 2004; Mantovani *et al.*, 1996; Metternicht *et al.*, 2005).

Generally, the exploding number of new space and airborne platforms (from micro-satellites to unmanned aerial vehicles, UAV) enables and unprecedented observation frequency and especially the advance of interferometric synthetic aperture *radar* (SAR) techniques (Farina *et al.*, 2006; Roering *et al.*, 2009) leads to a change in our view of landslide inventories, moving from a static maps to dynamic digital inventories and constantly updated collections of hazard and risk related information

In this chapter, the previous published contributions of *remote-sensing* to those landslide studies are to be reviewed, arranged by the following useful *remote-sensing* techniques: satellite SAR interferometry (InSAR), *remote-sensing* within optical electromagnetic spectrum, and airborne laser scanning (LiDAR).

2.1. Use of satellite *radar* interferometric data

SAR interferometry (InSAR) is nowadays an important branch of *remote-sensing*, it represents the technique that uses the phase content of *radar* signals for extracting information on deformations of the Earth's surface (Gens & Genderen, 1996). Satellite InSAR is a typical example of repeat-pass interferometry which combines two or more SAR images of a same portion of terrain from slightly displaced passes of the SAR sensor at different times (Massonnet & Feigl, 1998).

It plays an important role in landslide mapping and monitoring applications, owing to its capability of detecting ground movements with millimeter precision (Corsini *et al.*, 2006;

P.Canuti *et al.,* 2007; Rott and Nagle, 2006; Squarzoni *et al.,* 2003). The traditional InSAR processing approach for ground movement detection is mainly focused on the differential InSAR (DInSAR) technique (Massonnet and Feigl, 1998; Rosen *et al.,* 2000). It uses two corresponding interferograms for differential measurements by comparing the possible range variations of two phases with the capability of detecting terrain motions with sub-centimetric accuracy. Several works have indicated the usefulness of DInSAR in landslide studies and for the updating and development of landside and subsidence inventories (Catani *et al.,* 2005; Colesanti *et al.* 2003, Farina *et al.* 2006; Strozzi *et al.,* 2005; Ye *et al.,* 2004; Zhao *et al.,* 2009; Vilardo *et al.,* 2009; Tomas *et al.,* 2010).

Several *radar* satellites are now active and widely used for interferometric applications (Figure 2). They basically differ by three parameters:

- Radiometric resolution (band)
- Revisiting time
- Period of activity

Sensors work at specific bands of the microwave domain, corresponding to different wavelengths (λ). The most commonly used bands in spaceborne *radar* applications are C-band (5-6 GHz, ~5,6 cm wavelength) and X-band (8-12 GHz, ~3,1 cm wavelength) and L-band (1-2 GHz ~23 cm wavelength). Image resolution of SAR images depends on the sensor used and its acquisition mode.
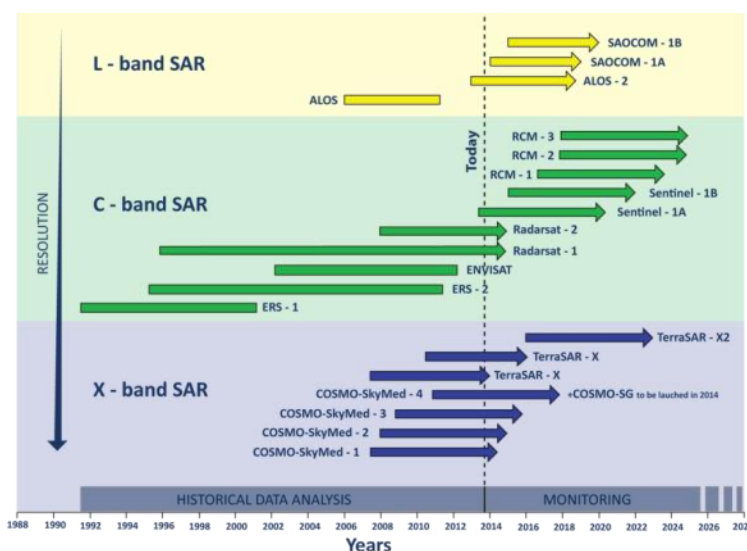
Figure 2. Currently active *radar* satellites.

The time taken for a satellite to re-pass over the same area is called the *revisiting time*.

Typical repeat cycle for the main exploited satellites are 46 days for ALOS PALSAR (Japan Aerospace Exploration Agency, JAXA), 44 days for JERS-1 (National Space Development Agency, NASDA), 35 days for ERS-1/2 and ENVISAT (European Space Agency, ESA), 24 days for *RADAR*SAT (Canadian Space Agency, CSA), 11 days for TerraSAR-X (German Space Agency, DLR) and 8 days for COSMO-SkyMed (Italian Space Agency, ASI).

2.1.   Use of LiDAR data

LiDAR technology provides high-resolution point clouds of the topography and, when repeated datasets are available, has several applications in terms of deformation and displacement monitoring (Abellán *et al.*, 2009; Jaboyedoff *et al.*, 2009c; Oppikofer *et al.*, 2008; Teza *et al.*, 2007; Travelletti *et al.*, 2008). It is mainly used to create accurate and precise Digital Elevation Models (which are 2.5D representations of the topography) or virtual 3D scenes of point clouds. The density mainly depends on the position of the sensor and of the platform (decimetric to centimetric resolution for ALS and centimetric to millimetric resolution for TLS).

For a multi-temporal analysis of LiDAR DEMs and/or LiDAR point clouds, the critical issue is the alignment of the point cloud whose accuracy will determine the range of deformation and displacement that can be monitored.

Point clouds alignment consists in a registration by a visual identification of homologous points and an optimization of the alignment either by the Iterative Closest Points (ICP) algorithm (Besl & McKay, 1992) or by the Roto-Translation technique (Teza *et al.*, 2007). The choice of the alignment procedure depends on the quality of the point clouds and the requested accuracy. Another critical issue is the accurate filtering of the vegetation in order to represent the real ground morphology (and thus the texture in the DEMs) at the surface.

In order to compute differences (elevation changes, displacement, and deformation), several procedures can be applied on the aligned point clouds. Most of the procedures are based on the compilation of either 1) vectors between two points (or areas) or 2) distances between two data sets (point to surface comparison) either in a user-defined direction or as shortest distance between the two surfaces. This difference calculation allows for the computation of volume differences, as is discussed by different authors (Bitelli *et al.*, 2004; Chen *et al.*, 2006; Dewitte *et al.*, 2008; Mueller and Loew, 2009).

In contrast to the relatively high number of studies that used visual interpretation of DEMs and multi-temporal DEMs for extracting landslides from detailed topographic data such as LiDAR only few studies have attempted to develop computer-aided methods. Since the visual identification of landslides features on *remote-sensing* images is based on the recognition of landslide characteristics and alterations of the drainage system, the semi-automated methods

try to translate this expert knowledge in an objective landslide classification method analyzing the morphological features of the available digital DEMs (Figure 3).
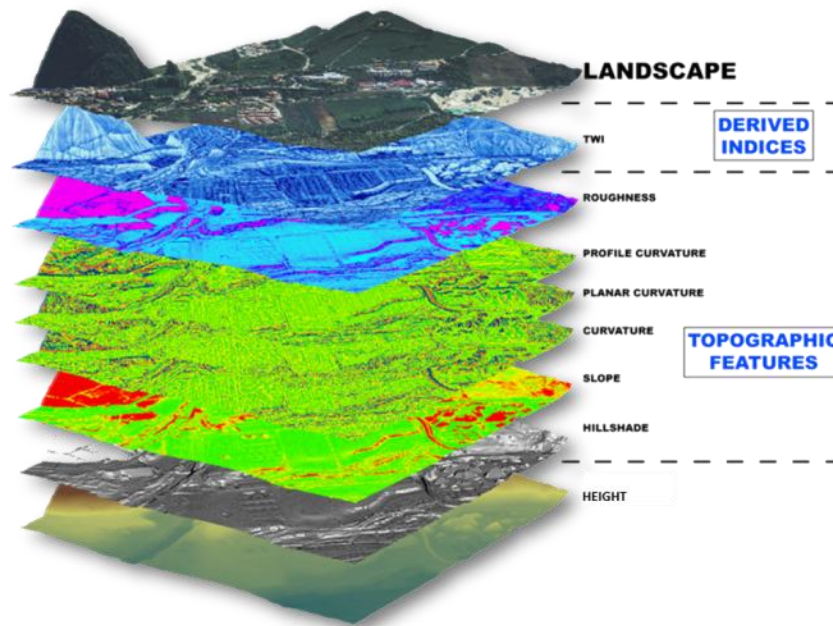
Figure 3. Different thematic maps extracted by an high resolution LiDAR DTM, acquired near Pietracuta Valmarecchia (Rimini)

Previous attempts of automatic landslide identification have been carried out in a pixel-based analysis. McKean and Roering (2004) have applied various surface roughness filters using LiDAR-derived DEMs to map deep-seated landslide sites, based on the notion that landslide surfaces are rougher due to the appearance of cracks, benches and scars. Roering et al., (2005) used slope and curvature maps to distinguish old landslides with subdued morphology from steep and dissected terrain and valley floors. Glenn et al., (2006) employed the standard deviation of elevation differences from a hypothetical spline plain, semivariograms, and fractal dimensions to characterize the mechanisms of deep-seated slides. Using different filter size allowed them to define different landslide activity stages. Also Kasai et al., (2009)characterized geomorphic features of deep-seated landslides at various stages of evolution and activity. They combined the LiDAR-derived Eigenvalue Ratio filter and slope angle, and assessed relationships between the ranges of filter values and actual surface features.

Luca Tanteri — *"Integration of Remote-Sensing techniques and geomorphological analysis for the characterization and mapping of ground instability at regional scale"*

2.2. Multi-sensor data fusion methods

Multi-spectral and Hyperspectral images are commonly used in order to perform analyses with semi-automated pixel-based methods including unsupervised and supervised classification, as well as change detection. The significance of providing accurate fine-scale land cover maps is emphasized by the evidence of marked impacts of land cover changes on local surface dynamics (Claessens *et al.*, 2009). *Remote-sensing* data classification represents an essential tool for environmental monitoring and sustainable land use management (Melesse *et al.*, 2007), especially in heterogeneous landscapes characterized by many interconnected natural- and human-induced processes (Forzieri & Catani, 2011).

If multi-temporal imagery of a given area can be provided, change detection is a promising approach for landslide mapping and monitoring. Despite the great variety of proposed approaches, change-detection methods usually comprise a modelling phase and a subtraction phase. While there is no general agreement on the best available method differencing, PCA, Change Vector Analysis (CVA) and Post-Classification Comparison are at present most frequently used.

Modern space-borne hyperspectral (e.g., HYPERION, CHRIS/PROBA) and laser scanner (ICESat/GLAS) sensors recently offered an interesting potential in land surface characterization (Duca & Del Frate, 2008; Goodenough *et al.*, 2003), but may still exhibit possible inaccuracies in monitoring environments that are highly variable in space (Cavalli *et al.*, 2008; Pignatti *et al.*, 2009). In this context, high-resolution airborne sensors represent enhanced mapping tools (Gianinetto & Lechi, 2004; Lu *et al.*, 2007; Melgani & Bruzzone, 2004) and also preliminary tests to drive planned satellite-based systems (e.g., PRISMA, EnMAP, HyspIRI, Sentinel). High spatial resolution airborne color-infrared sensors (e.g., Intergraph DMC, ADS40, RC30) provided encouraging classification performances especially in antrophic areas, such as agricultural and urban zones (Belluco *et al.*, 2006; Tansey *et al.*, 2009). Airborne hyperspectral data, such as Multi-spectral Infrared Visible Imaging Spectrometer (MIVIS), Airborne Visible InfraRed Imaging Spectrometer (AVIRIS), and HyMap, thanks to their high spectral resolutions, have demonstrated to be powerful tools to discriminate land cover classes with partially overlapping of spectral signatures in the feature space, such as forest and wetland ecosystems (Colombo *et al.*, 2008; Hirano *et al.*, 2003) and geologic features (Van Der Meer *et al.*, 2012). Light Detection

and Ranging (LiDAR) data have been extensively used for mapping tasks due to their ability to capture the 3D structure of the monitored surfaces, especially in vegetated and built-up areas (Forzieri *et al.*, 2009; Priestnall *et al.*, 2000).

Several data fusion methods have been successfully tested for classification of different landscape scenarios. Here, we point out that the terms "data fusion" and "multi-source (multi-sensor)" classification are used in this work as synonymous with the meaning of labeling pixels by drawing inferences from several input data sources, according to the definition given by Richards and Jia (2006).

A common technique of data fusion for multi-source classification is the stacked vector approach that consists in generating extended pixel vectors stacking together the individual vectors that correspond to each input data source (Richards and Jia, 2006; Tso & Mather, 2000). The fusion of LiDAR and hyperspectral/multi-spectral data exhibited an interesting potential in several application fields including the retrieval of biophysical and geological properties of land surfaces (Anderson *et al.*, 2008; Forzieri *et al.*, 2012a; Spinetti *et al.*, 2009). The combined use of laser scanner and spectral data was particularly effective in classification tasks to distinguish vegetation types (Dalponte *et al.*, 2008; Elaksher, 2008; Mundt *et al.*, 2006), anthropogenic surfaces (Chen *et al.*, 2009), and land cover changes (Forzieri *et al.*, 2012b). Additional derived features, such as texture or DTM-based layers, have been used to improve class discrimination over cropfields and riparian corridors (Forzieri *et al.*, 2010; Herold *et al.*, 2003).

Mapping approaches based on multisource data can be either contextual or noncontextual depending on the possible use of spatial information. Region- and object-based methods represent a primary subcategory of contextual classification methods. Noncontextual classifiers label the (multi-source) signature of each pixel regardless of all other pixels (Richards & Jia, 2006), thus discarding the spatial information associated with the image.

Contextual approaches use both spectral and spatial information (Moser and Serpico, 2013; Moser *et al.*, 2013). The former approach bears the obvious advantage of simplicity, but the latter generally includes more powerful classification techniques.

Region-based and object-based methods currently play a primary role in the literature of contextual classification, especially when high-resolution data are concerned. A basic region-based approach may be two-step process involving: (1) segmentation of the image into homogeneous regions, possibly representing objects or parts of objects, and (2) classification of

those regions (De Jong & Van der Meer, 2004; Navulur, 2007). However, more sophisticated region-based architectures can be devised, depending on the nature of data being analyzed, their spatial resolutions, the computational resource available, and the intended application of the classified data (Lillesand *et al.*, 2008; Moser *et al.*, 2013).

Even though the costs of airborne image acquisition are high compared to satellite *remote-sensing* image procurement and may represent an operational constraint in several environmental applications, their exploitation can be viewed both as a preliminary step toward the development of spaceborne advanced monitoring systems and in the perspective of the application to specific monitored areas of particular environmental interest. In light of the recent advances in sensor technology, additional fusion experiments on modern airborne *remote-sensing* data serve for a better understanding of the potential and limitations of current Earth Observation systems. In particular, there is a great need for assessing optimized exploitation strategies of multi-sensor *remote-sensing* data to maximize the inter-class separability in heterogeneous landscape scenarios. In this context, hyperspectral MIVIS, color-infrared ADS40 and LiDAR data represent useful datasets to quantify multi-source synergies for image classification tasks.

3. Materials and Methods

3.1.   Available *radar* interferometric data

In this work different satellite InSAR datasets have been exploited as an important tool for ground movement mapping and characterization, in particular:

- Data from satellite TerraSAR-X have been processed and analyzed in order to detect all the areas affected by ground deformation over the urban area of Barcelona and in correspondence of the village of El Papiol (Catalonia - Spain).

- data from satellites ERS-1, ERS-2 (Earth Resources Satellite) and ENVISAT (ENVIronmental SATellite) have been utilized for the update of Tuscany landslides and subsidence inventory map, providing informations on the velocity, state of activity and deformation rate of the monitorable phenomena and allowing to detect new areas not included in the original inventory map.

3.1.1. *Radar* Interferometry basics

Radar is the commonly used acronym for *Radio Detection and Ranging* and is an active object-detection system which operates with a beam of microwaves of the electromagnetic spectrum. Imaging *radar* is an active illumination system, in contrast to passive optical imaging systems that require the sun's illumination. An antenna, mounted on an aircraft or spacecraft, transmits a *radar* signal in a side-looking direction towards the earth's surface.

Radio waves are that part of the electromagnetic spectrum that have wavelengths considerably longer than visible light, as shown in Figure 4.
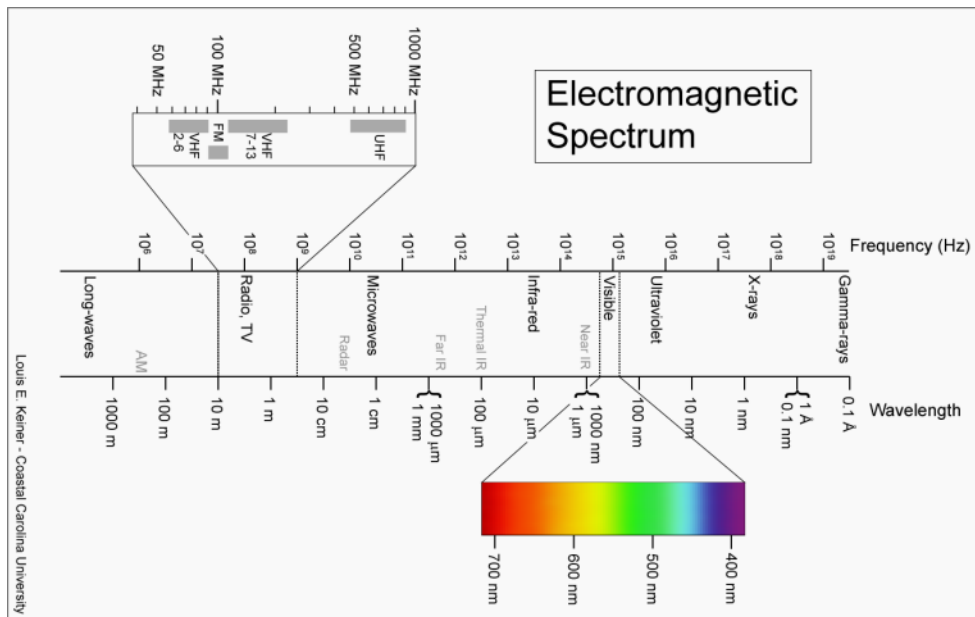
Figure 4. Main regions of the electromagnetic spectrum

The reflected signal, known as the echo, is backscattered from the surface and received a fraction of a second later at the same antenna, as shown in Figure 5.

The brightness, or amplitude, of this received echo is measured and recorded and the data are then used to construct an image. For coherent *Radar* systems such as *Synthetic Aperture Radar* (SAR), the phase of the received echo is also measured and used to construct the image. *Radar* provides at least two significant benefits from not being dependent on natural light: the ability to image through clouds, and the ability to image at night.

The wavelength of the microwaves used in *Radar* are longer than those of visible light, and are less responsive to the boundaries between air and the water droplets within the clouds. The result is that, for *Radar*, the clouds appear homogeneous with only slight distortions occurring when the waves enter and leave the clouds.

Figure 5. a) *Radar* pulse transmitted from the antenna to the ground. b) *Radar* pulse scattered by the ground targets bock to the antenna. From http://www.crisp.nus.edu.sg/~research/tutorial/mw.htm modified.

The *radar* devices of the SAR type exploit a long array of successive and coherent *radar* signals that are transmitted and received by a physically short (real) antenna as it moves along a predetermined flight or orbital path.

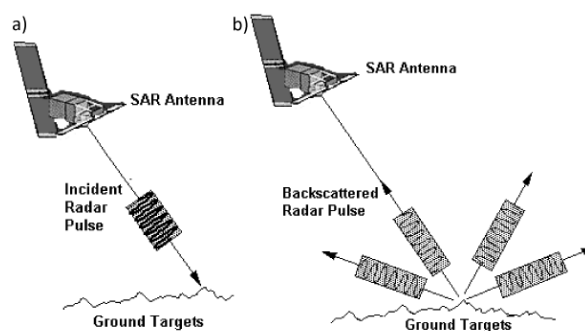The synthetic aperture is formed by pointing the real *radar* antenna of relatively small dimensions, which are restricted in size by the satellite platform, broadside to the direction of forward motion of that platform.

As the line of sight direction changes along the *radar* platform trajectory, the synthetic aperture is produced by signal processing that has the effect of lengthening the antenna.

This long virtual antenna concept is the basis for synthetic aperture *radar*, or SAR.

A SAR sensor generates high-resolution *remote-sensing* imagery. Signal processing uses magnitude and phase of the received signals over successive pulses from elements of a synthetic aperture to create an image.

The achievable azimuth resolution of a SAR is approximately equal to one-half the length of the actual (real) antenna and does not depend on the platform altitude (distance). High range resolution is achieved through pulse compression techniques.

The synthetic aperture information acquired by the antenna is saved as a complex SAR image. This image has a complex number in each pixel, that is, a number, $z = a + b_i$, with a real part a and a complex part b, and where $i^2 = -1$. For each complex number, the amplitude, A, can be extracted:

$$A = \sqrt{a^2 + b^2} \qquad (1)$$

Doing this operation for each pixel of the complex image, an image of amplitude can be derived. In Figure 6 shows an example of an amplitude image; since the amplitude image reflects the power where upon signal SAR is reflected, there are pixels of the amplitude image darker and others clearer due to the surface has different characteristics.

Figure 6. Amplitude of a SAR complex image. Example covering the Catalan coast from Calella to Torredembarra (image provided by Institute of Geomatics in Castelldefels).

For example, the urban areas have high values of amplitude, because of the metallic elements and the geometric forms, the forests have medium values of amplitude, and the smooth surfaces have low values of amplitude.

From the SAR images, the phase can be extracted, too. The phase of each complex number of a SAR image, φ, can be calculated:

$$\varphi = arctan\frac{b}{a} \qquad (2)$$

Doing this operation for each pixel of the complex image, a phase image can be derived.
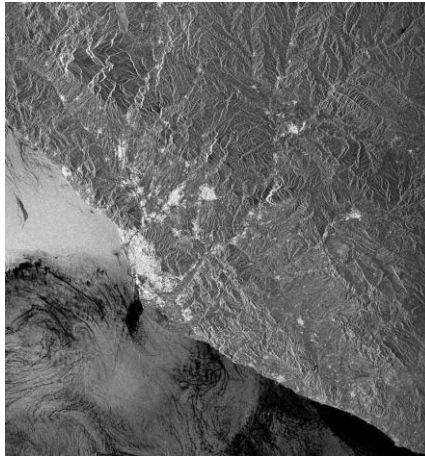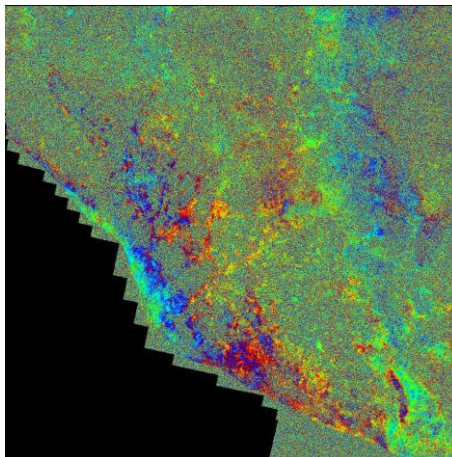

Figure 7. Phase of an InSAR complex image. Example covering the Catalan coast from Calella to Torredembarra (image processed by the Institute of Geomatics in Castelldefels).

Information can be extracted from the phase data of a *synthetic aperture radar* system, in particular exploiting carefully engineered differences between SAR images: the principle of SAR interferometry or InSAR.

A scheme of InSAR acquisition image is shown in Figure 8: the sensor acquires a first SAR image at the time T_0, measuring the distance in terms of phase (R_1). The first image are usually referred as the *master*, M.

Assuming that a land deformation occurs between times T_0 and T_1 ($T+\Delta t$), the target moves on a distance Δr.

The sensor acquires a second image at the time T_1 ($T+\Delta t$), measuring the phase R_2. The second image is usually referred as the *slave*, S.
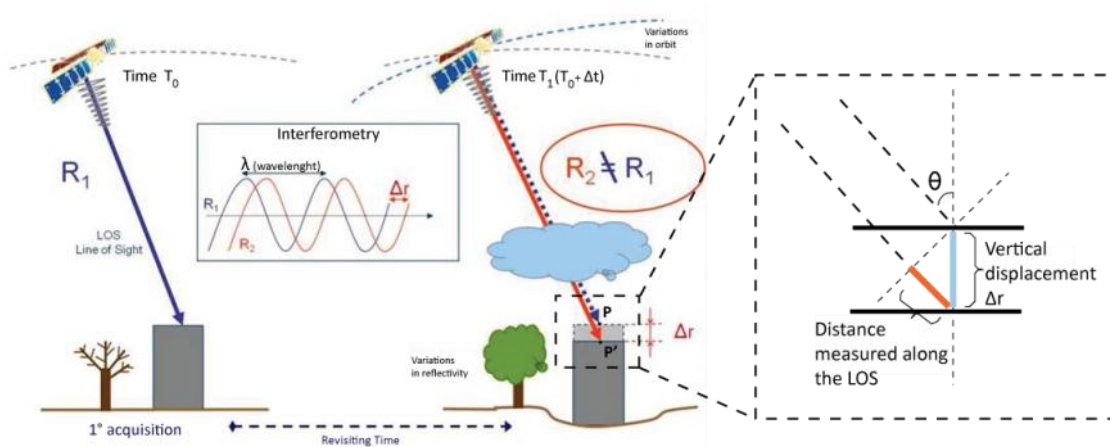
Figure 8. Scheme of InSAR acquisition

The phases of images with a difference of position (e.g., two antennae on one plane acquire images simultaneously) or with a difference of time (e.g., one antenna acquires images at two distinct times) can be compared after proper image registration.

This image has a complex number in each pixel, therefore, just as in the SAR images, the amplitude and the phase of each pixel can be extracted. In this case the phase value is of interest, since it gives information about the different distances between the terrain and the *master* and *slave* satellites, and therefore information about the terrain.

The InSAR techniques exploit the phase difference $\phi_S - \phi_M$ ($R_2 - R_1$), named interferometric phase ϕ_{Int}.

The image that contains the differential interferometric phase is called an **interferogram**.

Assuming that the terrain is stable and $P(T_1)$ coincides with $P(T_0)$, this phase is related to the distance difference SP - MP , which is the key element for the InSAR DEM generation. When the point moves from $P(T_0)$ to $P_0(T_1)$ between two image acquisitions, besides the topographic phase component ϕ_{Topo}, the phase includes the terrain movement contribution, ϕ_{Mov}:

$$\Delta\phi = \phi_S - \phi_M = \frac{SP-MP}{\frac{\lambda}{4\pi}} + \frac{SP'-MP}{\frac{\lambda}{4\pi}} + \phi_{Atm} + \phi_{Noise} = \phi_{Topo} + \phi_{Mov} + \phi_{Atm} + \phi_{Noise} \qquad (3)$$

where ϕ_{Atm} is the atmospheric contribution; ϕ_{Noise} is the phase noise; SP' is the slave-to-P' distance; and λ is the *radar* wavelength.

If the two samples, M and S, are obtained simultaneously (by placing two antennas on the same platform, some distance apart), then any phase difference will contain information about the angle from which the *radar* echo returned. Combining this with the distance information, the position in three dimensions of the image pixel footprint can be determined. In other words, the terrain altitude can be extracted, producing a digital elevation model with a single satellite pass.

There are two important parameters related to interferogram generation. The first is the incremental time, Δt, that is, the difference of time between the two images that form the interferogram. Secondly, the perpendicular baseline, B_{Perp}, that is, the distance between the position of the satellite at the moment of acquisition of each image. The incremental time and the perpendicular baseline are related to ϕ_{Mov} and ϕ_{Topo} respectively. So these both parameters are essential for the study of ϕ_{Mov} and ϕ_{Topo}.

Each interferogram has an associated image called *coherence*. This image gives information of the quality of the phase to every pixel. It is calculated using the next formula:

$$\alpha = \frac{E\{y_1 y_2^*\}}{\sqrt{E|y_1|^2 + E|y_2|^2}}, 0 \leq \alpha \leq 1 \qquad (4)$$

The coherence image can be used to select those pixels of the phase with good quality. The value of the coherence is affected by interferometric phase variation due to noise in the data and/or to systematic phase variation within the coherence estimation window.

The formula used to obtain the phase image (2), provides values included in the interval [-π, π], since $\arctan x \in [-\pi, \pi] \forall x \in \mathcal{R}$. Therefore, the values of the phase are known module 2π. This phase is called wrapped phase. For that reason, an ambiguity exists in the determination of the phase value.

The problem is to determine k(i; j), so that:

$$\phi(i,j) = \psi(i,j) + 2\pi k(i,j) \qquad (5)$$

where: $k(i,j)$ is an integer function, $\phi(i,j)$ is the unwrapped phase, and $\psi(i,j)$ is the wrapped phase.

There are several techniques to unwrap the phase, although anyone works correctly under all conditions.

Differential interferometric SAR or DInSAR is a technique developed to land deformation measurement. It requires taking at least two SAR images and a Digital Elevation Model (DEM). In the DInSAR techniques ϕ_{Topo} is simulated and subtracted from $\Delta\phi_{Int}$, obtaining the so-called DInSAR phase $\Delta\phi_{DInt}$:

$$\Delta\phi_{DInt} = \phi_{Int} - \phi_{TopoSim} = \phi_{eTopo} + \phi_{Mov} + \phi_{Atm} + \phi_{Noise} \qquad (6)$$

where $\phi_{TopoSim}$ is the simulated topographic component, and ϕ_{eTopo} is the residual component due to errors in the simulation of ϕ_{Topo}, i.e., due to a disagreement between the used DEM and the surface that responds to the *radar* (can be different because the buildings or because some errors of the DEM in the heights).

In order to extract information of the terrain movement, ϕ_{Mov} must be isolated (see Equation 6) from the other phase components. The present approaches use several interferograms to identify the different components of $\Delta\phi_{DInt}$. Moreover, the physic characteristics of each component are used (as the temporal and spatial correlation).

The information on the phase allows to elaborate displacement maps, in which the phase information could be converted in terms of distance.

Theoretically, it has the potential to detect millimetric target motion phenomena along the sensor-target (Line-of-Sight, LOS) direction. In particular, significant results have been obtained in mapping volcano dynamics (Massonnet *et al.*, 1995), coseismic (Massonnet *et al.*, 1993) and postseismic (Massonnet *et al.*, 1994; Massonnet *et al.*, 1996) deformation along active seismic faults, as well as slope instability and failure (Fruneau *et al.*, 1995) phenomena.

In this research *radar* interferometric datasets have been utilized, in particular ERS 1/2 and ENVISAT for the case study of Tuscany and TerraSAR-X data for the analysis performed on the area of Barcelona.

The term PSI (Persistent Scatterer Interferometry) refers to a family of different approaches based on processing of several (at least 15, or more), co-registered, multi-temporal spaceborne SAR imageges of the same target area. In general, larger the number of images, more precise and robust the results. The main idea behind this method is to analyze the backscattered signal

Luca Tanteri − *"Integration of Remote-Sensing techniques and geomorphological analysis for the characterization and mapping of ground instability at regional scale"*

from the observed scene, to identify ground elements (temporally stable from an electromagnetic point of view) dominated by highly reflective single scatterers: the socalled PS (Persistent Scatterers) (Ferretti *et al*. (2000); (2001); Werner *et al*. 2003).

In this thesis the TerraSAR-x PSs have been obtained using an PSI approach defined described in Biescas *et al.,* (*2007*) and Crosetto *et al.* (2011).

3.1.2. TerraSAR-x data

Study area: Barcelona

Barcelona is a Spanish city, capital of the autonomous community of Catalonia and the second largest city in the country as well as the largest metropolis on the Mediterranean Sea.

Barcelona is located on the northeast coast of the Iberian Peninsula (Figure 9), facing the Mediterranean Sea, on a plain approximately 5 km wide limited by the mountain range of Collserola at west, the Llobregat river delta to the southwest and the Besòs river to the north. This plain covers an area of 170 km^2 of which 101 km^2 are occupied by the city itself.

Figure 9. Geographic position of Barcelona and the village of El Papiol, up-country.

The main relief that borders the city is the Tibidabo, a 512 m high hill part of the Collserola range, offers striking views over the city.

Barcelona is peppered with small hills, most of them urbanised, that gave their name to the neighbourhoods built upon them, such as Carmel (267 m), Putxet (181 m) and Rovira (261 m).

The escarpment of Montjuïc (173 m), one subject matter of the research, is situated to the southeast, overlooking the harbour and topped by Montjuïc castle and some of the most important sports structures and monuments (built for the 1992 olympic games) such as the sports arena "Palau St. Jordi", the Olympic Stadium and other sports venues.

Montjuic houses also some of the biggest park and gardens of the city, such as the botanical gardens of "Jardins de Costa I Llobera", matter of study in this research as affected by slope movements.

Barcelona has a Mediterranean climate (Köppen climate classification: Csa) with mild, humid winters and warm, dry summers (Kottek *et al.,* 2006).

The average amount of precipitation per year is about 640 millimeters (Agencia Estatal de Meteorología) and the annual average distribution of rainfall and rainy days highlight the peculiarities of the type Csa in Köppen classification (Figure 10).
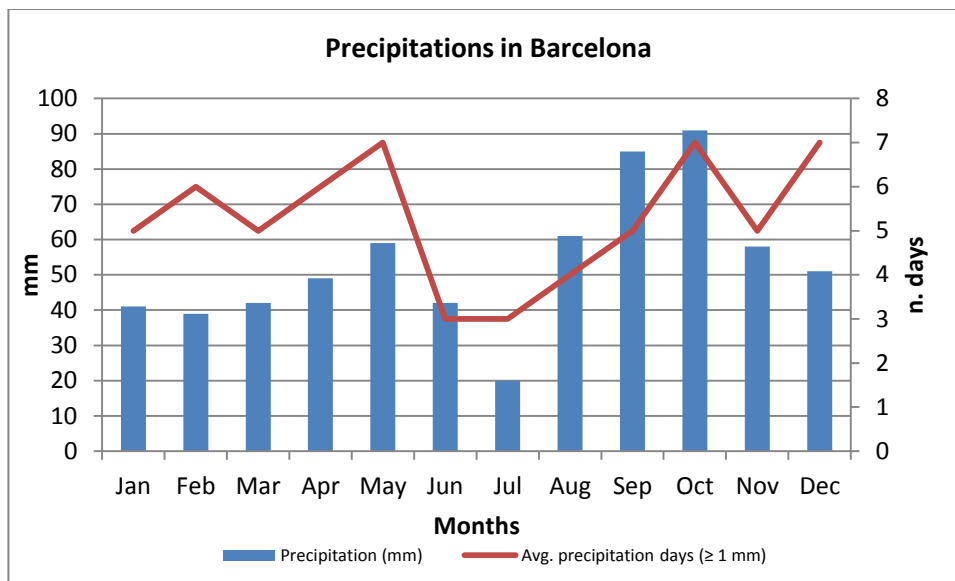
Figure 10. Distribution of average rainfall and number of rainy days per month.

From a geological point of view the urban area of Barcelona is placed on sediments with flat topography, originated by the deltaic deposits of the two main rivers Llobregat (south) and Besòs (north), and deposits of other minor streams coming down from the upper serra de Collserola range (Figure 11).

The airport is entirely built on the deltaic sediments of the river Llobregat while the center of the city is built on the Besòs delta and on the sediments coming from serra de Collserola.

Figure 11. Geological setting of Barcelona, from the southern part of Llobregat delta to the Besòs delta up north.

The intrinsic permeability of such deposits and the consequent conspicuous underground water circulation make this area very prone to subsidence areas, mainly due to the exploitation or artificial drainage of the subterranean water.

The hill of montjuic is almost entirely characterised by a recent sandstone formation with the exception of a small area with superficial sediments of alluvial terrace.

Available TerraSAR-x data

The TerraSAR-X data exploited in this work are of exclusive property of the Institute of Geomatics in Castelldefels (Catalonia - Spain) and have been processed at the same institute using the procedure described in Biescas *et al.,* (2007) and Crosetto *et al.,* (2011).

TerraSAR-X is a satellite equipped with an active phased array X-band SAR antenna (wavelength 31 mm, frequency 9.6 GHz) and acquires new high-quality *radar* images of the entire planet whilst circling Earth in a polar orbit at 514 km of altitude. The orbit is selected such that the satellite flies in a sun-synchronous dusk-dawn orbit, which means that it moves along the day-night boundary of the Earth and always presents the same face to the sun, ensuring an optimum energy supply via the solar cells.

In this study 28 StripMap images (up to 3 m resolution, scene size 30 km in width x 50 km in length), acquired in ascending orbit, have been involved in the processing chain, generating 56 interferograms and covering a time span between December 2007 and November 2009.

The elaborations have been performed on the urban area of Barcelona (and on the village of El Papiol) in order to detect all the areas in the city affected by superficial displacement and potentially at risk.

The data have been processed using a PSI technique with linear deformation model.

The data have been cut using the borders of the urban area of Barcelona and divided in tiles of 1Km x 1Km, each of which processed obtaining a raster velocity map, in order to better manage the huge amount of data memory and focus the further point densification processes only in areas considered of interest, optimizing the computational time (Figure 12).
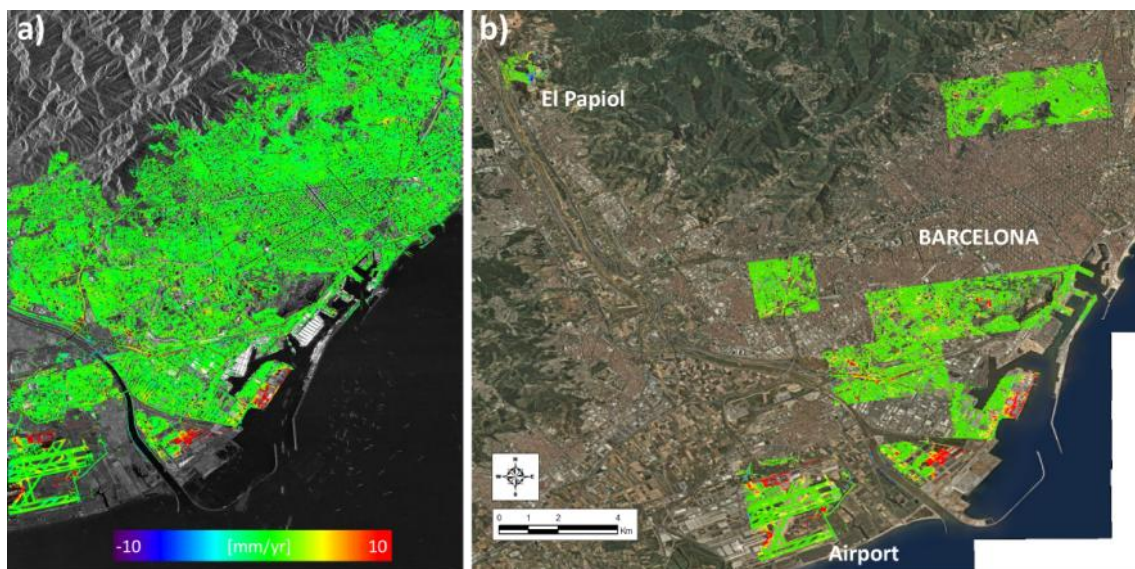
Figure 12. a) Velocity map over the urban area of Barcelona, obtained by processing TerraSAR-X stripmap images. b) Tiles selected for the post-processing densification.

The densification process has permitted to increase considerably the spatial coverage of points, allowing to better delimit and characterize the detected phenomena.

Processing chain

The atmospheric component of DInSAR observations is considerably low in areas up to a few square kilometers. Over small areas, where the atmospheric component has a negligible impact, it is often sufficient to run a simplified PSI data analysis procedure, which does not directly involve the estimation of the atmospheric component.

The procedure includes four main parts. First, the more suitable pixels of an interferogram stack are selected and connected by a network (Figure 13) For each edge of the network a phase difference is computed by differenciating the phases of the two corresponding pixels. Then, the differential terrain deformation and the differential topographic error are estimated for each edge. Finally, these differential values are integrated over the entire set of selected pixels. The most relevant stages of the procedure are briefly described in the following (Biescas et al., 2007; Crosetto et al., 2011):

- Stage 1: **Selection of the pixels of interest**. This step guarantees a good quality of the input phases, discarding the bad pixels in terms of phase noise. If the interferograms are at the maximum SAR resolution, the best selection criterion is the amplitude dispersion (DA), while if they are compressed (multilook Images) the coherence criterion is applied.

- Stage 2: **Pixels connection**. The result of the previous step is an irregular set of pixels. As the information contained in the DInSAR phase is differential, it can be exploited only by considering pairs of the previous pixels. For this reason the pixels are connected by edges, computing the phase difference of each edge. These edges have to be as short as possible in order to minimize the atmospheric effects in the phase difference. Several methods to connect an irregular set of points can be used, e.g., the Delaunay triangulation.

- Stage 3: **Differential phase calculation**. A differential wrapped phase value is assigned for each edge and for each interferogram, obtaining for each edge a stack of N differential interferometric wrapped phases. As it is shown in Figure 13, this is done by computing for the edge $e = \overline{p_1 p_2}$ the difference of the wrapped phases over p_1 and p_2.
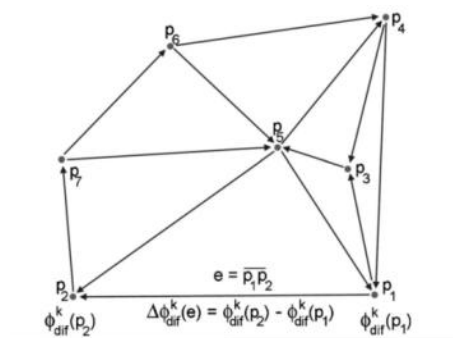

Figure 13. Pixels connection. The selected pixels are connected by edges. The differential wrapped phase value over each edge is calculated by subtracting the wrapped phase values over its extremes. Each edge has one differential phase value for each of the N interferograms (figure from *Biescas et al., 2007*).

- Stage 4: **Reordering.** In the previous step, a set of pixels and edges is obtained. Each edge has associated a *gamma* value which indicates the quality of the Δte and the Δv. The edges with a low *gamma* value are not used in the reconstruction of te and v for each pixel. A minimum number of edges associated to a single point are also set as condition for reordering. This process is needed in order to obtain a connected network of pixels (groups). Besides, results obtained in different tests can be joined in this process. In greater detail the differential values of Δte and Δv are computed over each edge by using the *N* differential wrapped phases and some geometrical parameters of each interferogram. For each edge *e* the goal is to get the differential velocity $\Delta v_e(e)$ and the differential topographic error $\Delta te(e)$ that minimize the function:

$$\Delta\varepsilon^k(e) = \Delta\phi_{obs}^k(e) - \Delta\phi_m^k\big(\Delta v(e), \Delta te(e)\big) \qquad (\text{mod } 2\pi) \qquad (7)$$

where $\Delta\phi_{obs}^k(e)$ is the differential wrapped phase of edge e and interferogram k, and

$$\Delta\phi_m^k\big(\Delta v(e), \Delta te(e)\big) = \frac{4\pi}{\lambda}\Delta T^k \Delta v(e) + \frac{4\pi}{\lambda}\frac{B^k}{R^k \sin\theta^k}\Delta te(e) \qquad (8)$$

is the modeled differential phase, where $\Delta v(e)$ and $\Delta te(e)$ unknowns associated to the edge e; ΔT^k, B^k= temporal baseline and the normal baseline of the interferogram k; R^k, and θ^k= mean slant range and mean incidence angle of the interferogram k; and λ= radar wavelength. The previous equations are the same proposed by Ferretti *et al.* (2001). It is worth stressing that in Eq. 8 a linear model for terrain deformation is considered. Depending on the expected temporal evolution of deformation, more complex models can be chosen. In order to find the unknowns $\Delta v(e)$ and $\Delta te(e)$the following function is maximized:

$$\gamma(e) = \frac{1}{N}\sum_{k=1}^{N}\exp\big(j(\Delta\phi_{obs}^k(e) - \Delta\phi_m^k\big(\Delta v(e), \Delta te(e)\big))\big) \qquad (9)$$

where N is the number of interferograms, see Mora *et al.* (2003). In this work, the maximization of function 9 is done numerically. To find the values $\overline{\Delta v(e)}$ and $\overline{\Delta te(e)}$ that give the maximum $\gamma(e)$, a discrete grid is used, see Figure 14. For each edge this maximum is used to assess the goodness of fit of the model with the given set of wrapped phases (observations).
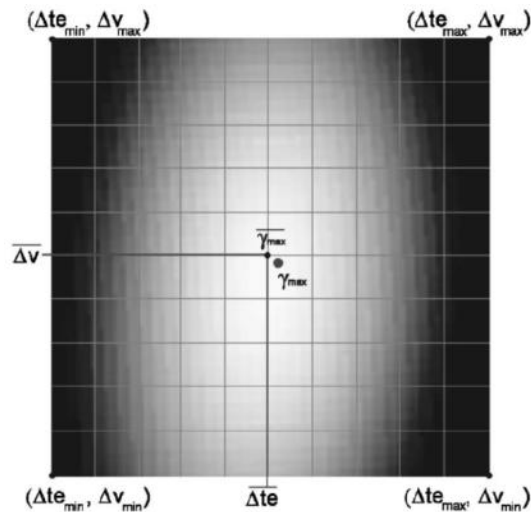
Figure 14. Estimation of the differential velocity and the differential topographic error. For each edge, γ is a function which depends on the variables Δte and Δv. To find the maximum value of γ several pairs (Δte, Δv) are proved, where Δte ∈ Δte_min, Δte_max and Δv ∈ Δv_min, Δv_max. The estimated values $\overline{\Delta te}$, $\overline{\Delta v}$ are given by the pair which gives the maximum value of γ. This solution doesn't give exactly the absolute maximum γ_max but the best approximation $\overline{\gamma_{max}}$ due to the used discrete network. As much dense is the discrete network, better is the approximation, but at the same time, more expensive is the computation time (figure from *Biescas et al., 2007*).

- Stage 5: **Integration**. This stage consists on the reconstruction of the velocity and the topographic error on the selected pixels using the results obtained over the edges. This is done by least squares adjustment, considering the linear velocity and the topographic error over each pixel as unknowns, and the estimated differential velocities and differential topographies as observations. This step takes advantage of the classical tools used in geodesy and surveying (outlier rejection procedures, estimation of the precision, etc.). The larger the ratio is between edges and pixels the more reliable are the integration results. Since the integration only involves differential values, it is necessary to fix the velocity value of at least one pixel (*reference point*). The same has to be done for the topographic error. The outcomes of this stage are a velocity map and a topographic error map, whose values are relative to the chosen reference point.

- Stage 6: **Gamma Calculation**

  The gamma value must be computed after each integration process. The value of gamma is related to a stable point which phase is theoretically noise-free and deformation-free (reference point). The choice of this point is done by a software for automatic selection of the stable point. It is necessary to minimize the temporal series noise of the PS's set based on the statistical computation of gamma. The automatic selection is computed with an exhaustive research of the point able to minimize the

gamma value for all the points. In that way topographic error and velocity will be the minimum. The problem of this solution is the computational time cost. To minimize it the number of points to process has to be chosen according to the total number of points as explained in the follows.

Note: Processing time depends on the number of points set in the batch file for the search of the reference point. The number of points to process is correlated to the total number of points, and acceptable values are:

- Ntotal_point < 5000 → Npoint_to_process = Ntotal_points
- 5000 < Ntotal_point < 30000 → Npoint_to_process = 3000
- Ntotal_point > 30000 → Npoint_to_process = 5000

The software will be able to automatically generate a gamma map with minimum gamma for all the PS's.

- Stage 7: **Geocoding.**

To have a representation of the PS's in ground geometry a geocoding of the results is needed. This process is essential for the interpretation of the data, inasmuch allows the visualization of the results on a web map service (such as GoogleEarth) or the implementation of further analyses in GIS environment (Figure 15).

In practice the geocoding process consists in the coordinate transformation from *radar* geometry to ground geometry.

In order to perform this, a "ground control point" (GCP) with precise geographic coordinates is needed for a first shift calculation, converting the *radar* image coordinates (lines and columns) in ground coordinates.
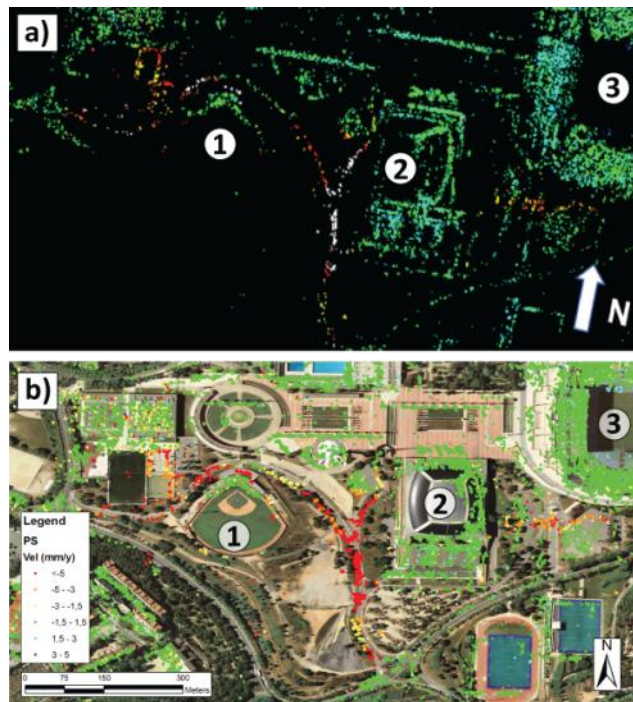
Figure 15. a) Velocity map obtained by the processing of 28 TerraSAR-X StripMap images, acquired from December 2007 to November 2009 on the hill of Montjuich (Barcelona - Spain). b) Geocoding results of the Velocity Map. In the picture the positions of the "Pèrez de Rozas" baseball stadium (1), the "Palau St.Jordi" (2) and the Olympic Stadium (3) are indicated.

- Stage 8: **Densification** (optional)

  In this study a further densification was needed for some tiles in which significant ground movements were present. In this case the densification have been performed running again the reordering process, starting from the original Δv and Δt values and lowering the *gamma* threshold in input. Afterwards the steps 4,5,6 and 7 have been repeated, therefore some edges, initially discarded due to the low gamma value, are now considered and more point can be processed (Figure 16).

  Thus, this process has permitted to increase considerably the spatial coverage of points, allowing to better delimit and characterize the detected phenomena.
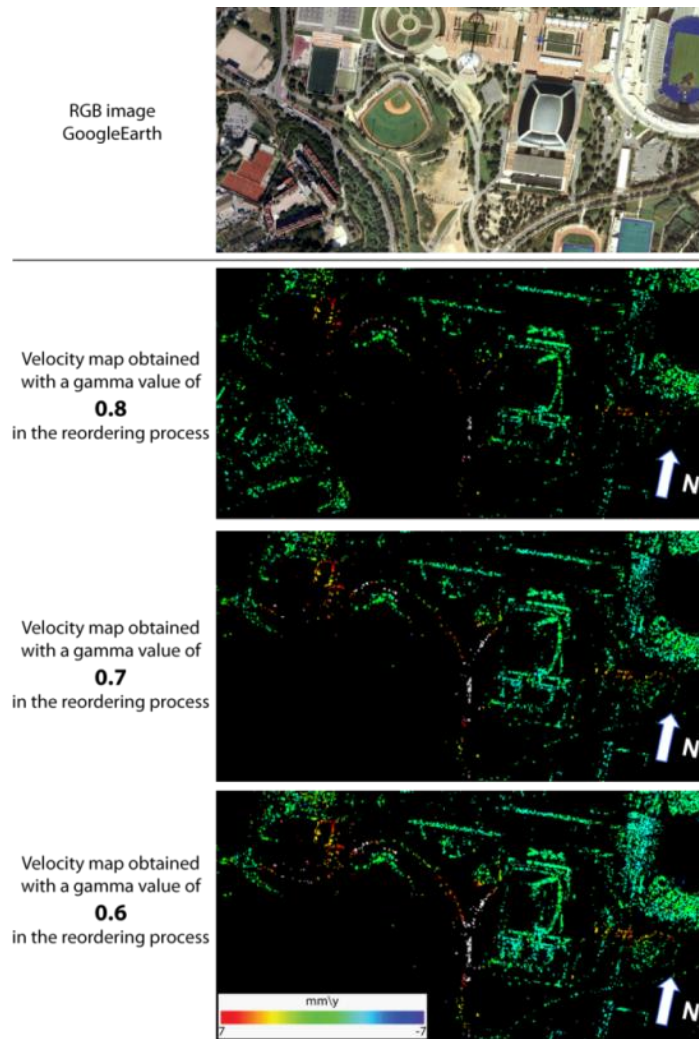
Figure 16. Results of the densification process in the area on top of Montjuic hill, performed using different input *gamma* value in the reordering process.

To conclude, it is worth underlying the most significant characteristics of the proposed procedure:

1. It is a simplified A-DInSAR approach that does not directly involve the estimation of the atmospheric component. For this reason it can be applied to study areas of limited spatial extension, say a few kilometers wide, where the atmospheric component has a negligible impact. This aspect considerably simplifies the implementation of the proposed approach.

2. It can work with both amplitude- and coherence-based pixel selection criteria.

3. It can be used with a limited number of SAR images, say at least ten.

This represents a key feature, especially to study current or recent phenomena, where it is usually difficult to obtain large sets of SAR images.

3.1.3. ERS and ENVISAT data

During the research programme ERS and ENVISAT PS data have been utilized for subsidence and landslide detection purposes.

In particular a new landslide inventory map have been achieved, on the whole regional territory, by updating a pre-existing inventory through the ground movement measurements provided by the *radar* data.

This process leaded to a new inventory in which new landslides have been detected and further new informations about the state of activity, perimeter, velocity and temporal evolution of movement, have been added to several already reported phenomena.

Moreover, the available PS data have been exploited in order to achieve automatically a new database in which the more important subsidence areas of the region are reported and characterized.

Study Area: Tuscany
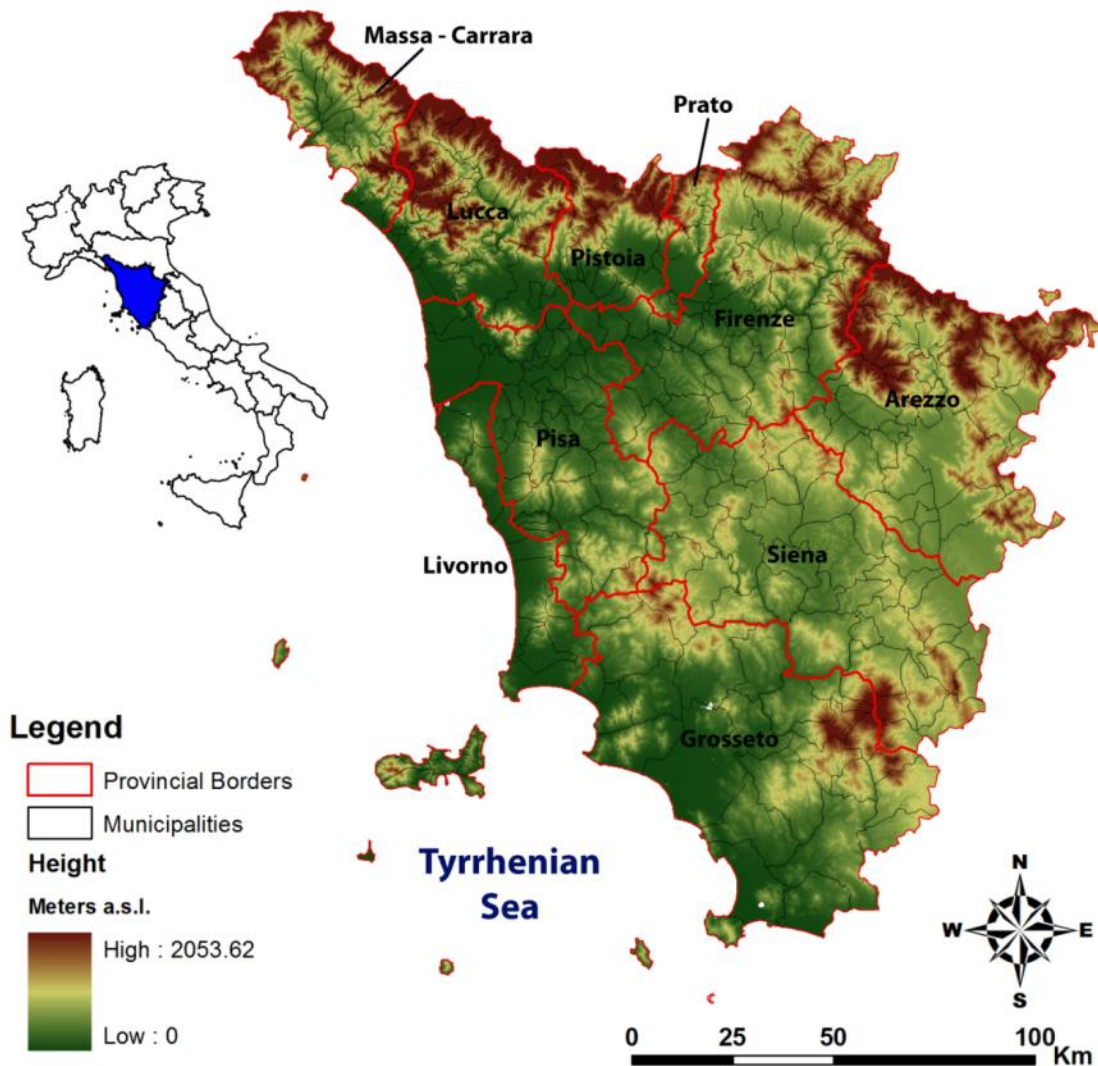
Figure 17. Tuscany region, position within the Italian peninsula and distribution of the relief (DTM)

The study about the development of ground movements databases was conducted on the whole extension of Tuscany region, in central Italy (43°46'17"N 11°15'15"E). Tuscany extends on 22.994 Km^2 between the regions of Emilia-Romagna, Marche, Umbria and Lazio, also including a little island archipelago composed by 6 main islands and other small ones.

Tuscany is divided administratively into 10 provinces and 287 municipalities, the regional capital is Florence (the most populated city with about 373.000 inhabitants) and the others provincial capital are Arezzo, Siena, Grosseto, Pisa, Livorno, Massa, Pistoia, Prato and Lucca (Figure 17).

The territory is characterized by extremely various landscape morphology, from the Thyrrenian coastal plains, in the western part, up to the Apenninic ridge that runs on the border of the region from NW to SE, with heights even greater than 2000 meters a.s.l. (Monte Prado, 2054 m a.s.l., where the topography pattern is typical of mountainous areas. The central part of the region includes hilly areas and flat territories or wide valley floors where the main rivers such as Arno, Ombrone and Serchio run.

As a whole the climate of Tuscany is typically Mediterranean (Köppen classification, **Csa**) but it is possible to recognize several areas with different climatic peculiarities, depending on the position with respect to orographic elements and the coast, as well as vegetation coverage and internal water bodies. The annual average temperatures range between 16°C, along the coast, to lower values in the internal areas and the mountain ridges. In the internal flat areas the temperature reach the maximum in summer, sometimes exceeding 40°C. The major rainfall and snowfall values are concentrated in the Northern part, along the Apennine ridge, reaching values of over 2000 millimeters per year in correspondence of the Apuan Alps and the Garfagnana zone (provinces of Lucca and Massa-Carrara). Indeed these areas, as well as the Amiata mount and surroundings, show the major concentration of landslide phenomena.

The geological setting of the region is strictly correlated with the overall Northern Apenninic scenario. The Apennines mountain range was originated by the overlapping of three main geological units: the Ligurian unit that overlaps the Tuscan unit that, in turn, overlaps the Umbro-Marchigian unit. (Bertini *et al.*, 1991; Bortolotti, 1992; Vai & Martini, 2001).

The aforementioned units belong to different paleo-geographic domains, called Ligurian, Sub-Ligurian, Tuscan and Umbro-Marchigian (Figure 18), related to their position with respect to the Giurassic ocean Ligurian-Piedmontese.

The Ligurian domain consists in several tectonic units which deposits are parts of giurassic oceanic lithosphere (ophiolites, gabbric rocks and pillow basalts) and its sedimentary coverage, deposed between Malm and middle Eocene.
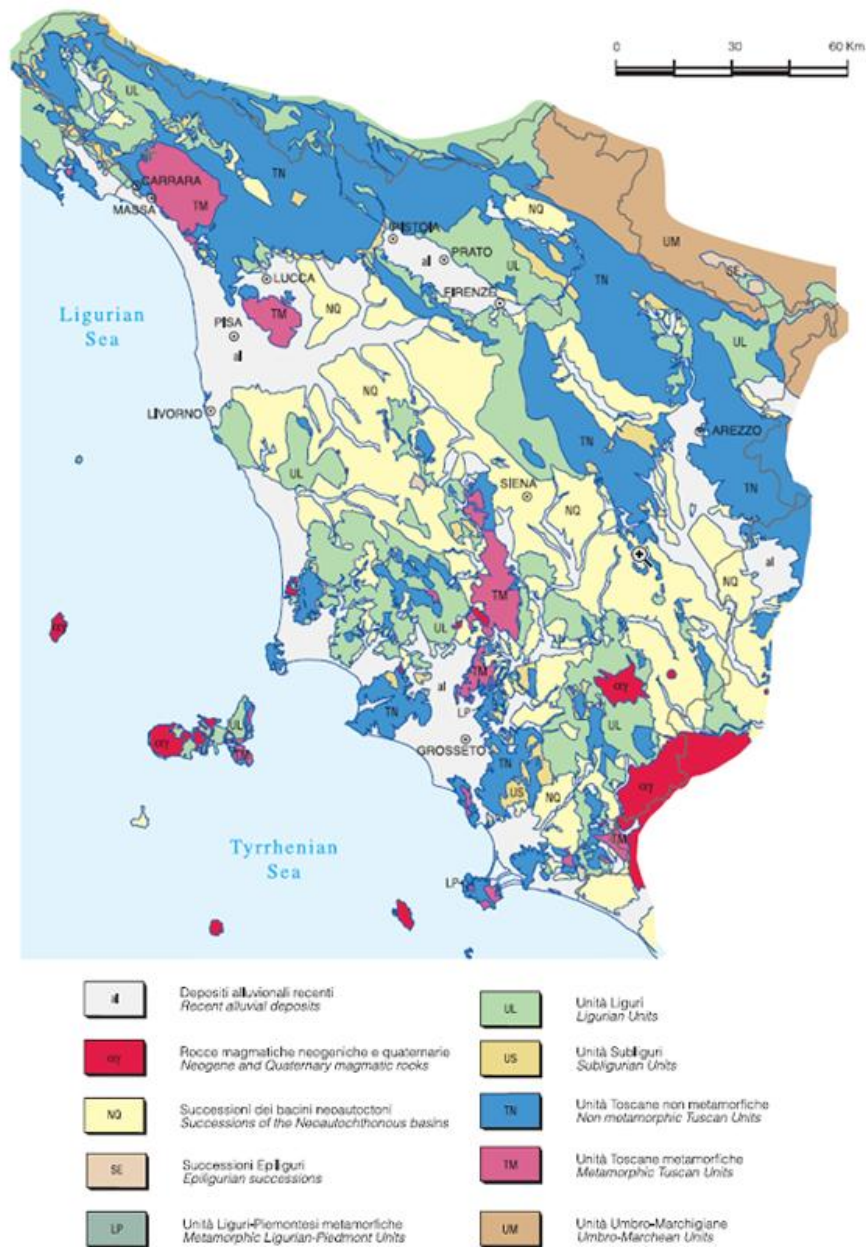
Figure 18 Scheme of the main stratigraphic and structural units in tuscany. (Carmignani *et al*., 2004): Geological Map of Tuscany.

The Sub-Ligurian domain is characterized by sedimentary rocks with unknown substratum. On the base of the geometrical position within the structure of the Apennines and stratigraphical considerations, these units are considered as the results of the deposition of sediments in a transition area between the Ligurian ocean crust and the continental crust (Adria tectonic plate).

The Tuscan domain is substantially composed by two units: the Metamorphic Tuscan Units and the Non-Metamorphic Tuscan Units.

The Non-Metamorphic are Mesozoic-Tertiary deposits of various kind, originated on a continental basement, such as coral reef limestones, pelagic sediments, turbidites

The Metamorphic units are underlying the previous and outcrop in the vicinity of the "Apuan tectonic window", in the Apuan Alps.

The Umbro-Marchigian units consist in a sedimentary sequence that lies on continental crust of the Adria plate but unstuck from it in correspondence of the basal evaporitic layers.

Available ERS and ENVISAT data

The ERS and ENVISAT data (provided by ESA), used for the detection of slow kinematics ground movements in Tuscany, were included in the "Piano Straordinario di Telerilevamento Ambientale" (Extraordinary Plan of Environmental *Remote-sensing*), pursuant to italian Law 179 of 31 July 2002 art. 27. The plan is an agreement programme between the Ministry of Environment and Territory of the Sea (METS), Chairperson of the Council of Ministers - Department of Civil Protection (DCP) and the Ministry of Defense (MD) in agreement with the Regions and Autonomous Provinces.

The data have been processed using the *Persistent Scatterers Technique* (PSI) by *T.R.E* (Tele-Rilevamento Europa) and *e-geos* (Telespazio company), covering almost entirely the Italian territory.

Since ERS 1/2 satellites have been active between 1992 and 2000 while ENVISAT from 2002 to 2010, it has been possible to have 18 years of almost continuous information about the temporal evolution of the displacements, in all the areas in which PS were present.

Unfortunately the overall spatial coverage on the Tuscany region is widely incomplete regarding ERS satellites data, that cover the whole region in descending orbit but only a small area in ascending orbit (Figure 19).

On the other hand ENVISAT data cover the entire regional territory, allowing to carry out a complete analysis on the whole study area.

Luca Tanteri – "Integration of Remote-Sensing techniques and geomorphological analysis for the characterization and mapping of ground instability at regional scale"
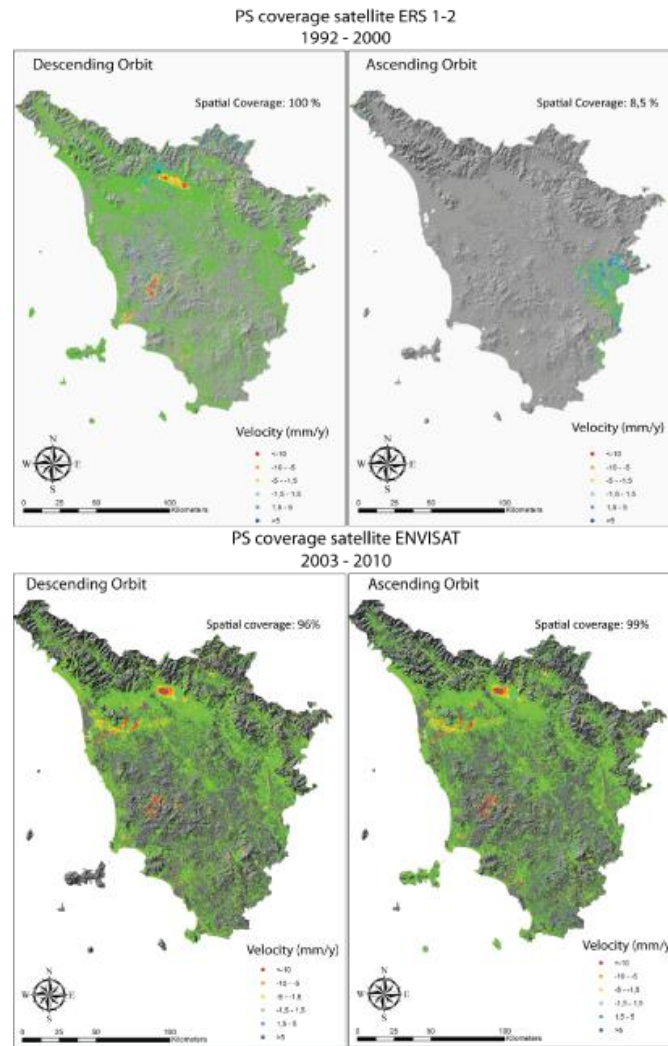
Figure 19. ERS and ENVISAT spatial coverage over Tuscany region.

In Table 1 some numerical information about the distribution of PS data over the region are shown, in particular regarding the number and the density of available points respectively in total and for each satellite and orbit.

Table 1. Spatial distribution and density of the available ERS and ENVISAT data over Tuscany region

	Regional Territory		Hilly-Mountanious areas (slope >5°)		Spatial Coverage	
AREA (Km^2)	22'988.1		19'163.6			
	N. of PS	PS density (PS/km^2)	N. of PS	PS density (PS/km^2)	PS Area (Km^2)	PS coverage
ENVISAT Desc	1'353'732	58.9	606'831	31.7	22'700	98.7%
ENVISAT Asc	1'142'698	49.7	514'205	26.8	22'950	99.8%
ERS Desc	404'850	17.6	199'987	10.4	22'988	100.0%
ERS Asc	9'618	0.4	5'994	0.3	2'100	9.1%
TOTAL	2'910'898	126.6	1'327'017	69.2		

An analysis about the distribution of PS has been conducted separately for flat and mountainous areas, by dividing the region on the base of the slope angle, using a threshold of 5 degrees. The result is that the PS density is much lower in the mountainous area, due to the presence of vegetation and the lack of strongly reflective surfaces such as buildings and infrastructures. On the other hand, flat areas are more densely populated with widely diffuse buildings, roads and urban areas, allowing to process more PS on the *radar* image-stacks (more pixels with high coherence and amplitude).

The data have been classified on the base of the registered velocity values and visualized in GIS environment according to a colourbar as shown in Figure 19.

For the PSI data interpretation, an 8 class subdivision of the velocity range of the PSI frames has been applied, in which the class with values between 1,5 mm/year and -1,5 mm/year is considered as stable.

The velocity values are measured along the Line Of Sight (LOS) of the satellite and are considered as positive where the displacement direction is towards the satellite and negative in case the *radar* target is moving away from the satellite.

Applications in landslide mapping

Radar satellite data are widely used in mapping and characterizing ground motions on the earth surface (Colesanti & Wasowski, 2006; Colesanti *et al.*, 2003; Farina *et al.*, 2006; Lu *et al.*, 2012, Tomas *et al.*, 2010; Vilardo *et al.*, 2009).

Figure 20 shows the methodology adopted for the updating of the Tuscany Landslide Inventory Map, starting from the acquisition and integration of the avalilable data, through the interpretative stages, until the results validation based on field surveys.
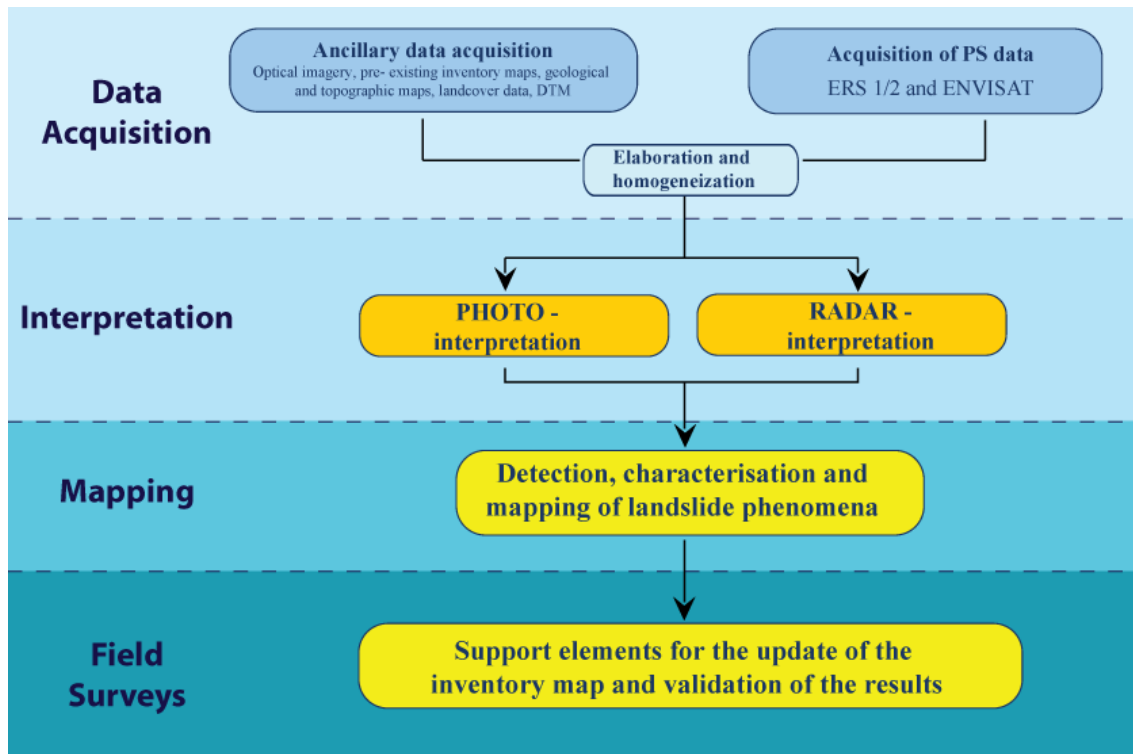
Figure 20. Schematic flowchart of the methodology adopted for the updating of Tuscany Landslide Inventory using ERS and ENVISAT PSI data.

By integrating PSI and ancillary data, it has been possible to modify the features of the landslides already included in the inventory or to detect new phenomena.

A deep knowledge of the morphologic features related to landslides, highlighted by comparing topographic maps and optical images is a key point in the achievement of landslide inventory maps.

For this purpose the ancillary data are necessary, they are typically topographic maps, terrain models and other thematic maps that can allow the operator to understand and interpret the information provided by the satellite data.

In particular, the importance of the ancillary data is due to the intrinsic characteristics of the measurements obtained by SAR techniques, such as the capability to observe the displacement components along the *Line Of Sight* of the satellite and the irregular spatial distribution of the points.

The data used to develop the Tuscany Landslide Inventory Map (Figure 21) were:

- A *Digital Terrain Model* (DTM) covering the entire Tuscany Region with 10 meters of spatial resolution.
- RGB images covering the entire Tuscany Region with 1 meter of spatial resolution.

- Regional Topographic Map (CTR) at scale 1:10.000.

- Regional Geological Map (developed in the CARG project).
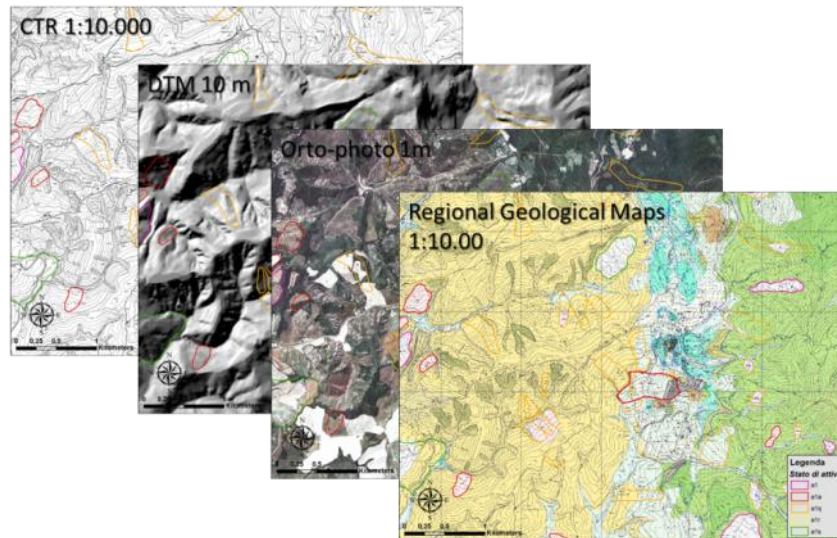
Figure 21. Ancillary data utilized for the interpretation of PSInSAR information.

Once the available data are visualized and homogenized is possible to go on to the interpretative stage and the update of the inventory map.

The preliminary mapping of hydrogeological instable areas have been carried out through *photo-interpretation* and *radar-interpretation*, two very different but essential activities.

The *photo-interpretative* analysis represents a fundamental tool in performing geomorphological surveys on wide scale, allowing to detect and delimit areas prone to instability.

For this purpose the analysis of optical images, combined with equally detailed cartographic data, are extremely useful to detect morphological and topographic evidences on the slopes, related to ground movements.

Materials and Methods
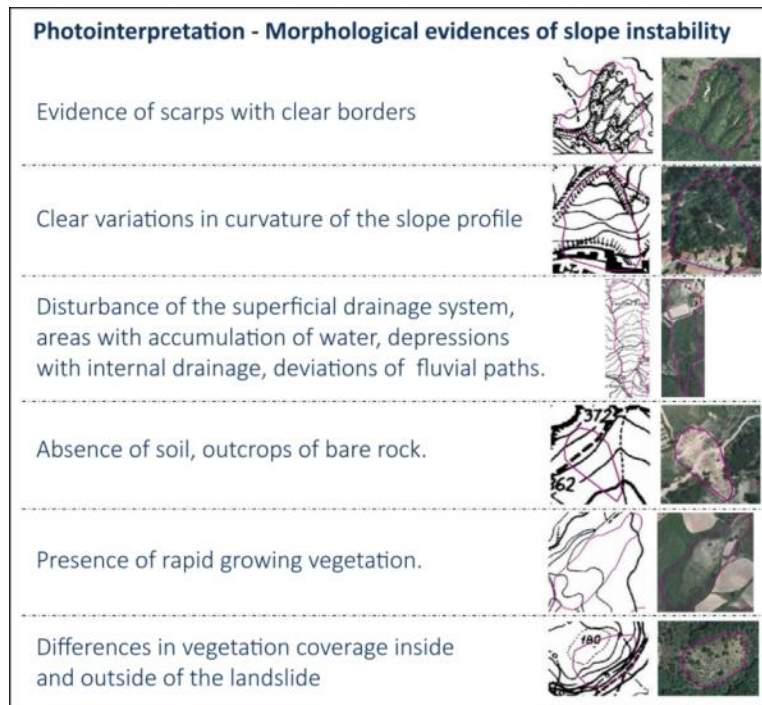
Figure 22. Examples of morphological evidences related to slope instability (Guerri, 2008. Modified)

Generally the *photo-interpretation* is performed simply by visualizing and examining orto-photos of the area of interest or analyzing couples of stereographic images taken over an area of interest, in order to have available a three-dimensional view of the scene.

This kind of approach has been very useful in all the cases where the intrinsic limits of the PSInSAR technique did not allow to have points, such as in densely vegetated areas of presence of very rapid movements such as flow landslides or rock falls.

In Figure 22 some examples of elements of the territory that can be related to the presence of landslides are shown by comparing the regional topographic map and RGB images.

The *radar-interpretative* analysis is the main activity carried out in this project and consists in the integration of the interferometric measurement of ground motion and the informations contained in the ancillary data and a following synthetic assessment of the scenarios.

For the interpretation of PSs measurements, as mentioned before, velocity values that range between +1,5 and -1,5 millimeters per year are conventionally considered as stable.

Such threshold values have been chosen on the base of the characteristics of the satellite images and the evolutive characteristics (velocity and displacement ratios) of the phenomena, that could be extremely slow.

The velocity have been estimated taking into account the spatial distribution of the PSs on the slopes and the orientation of the slope itself with respect to the direction of the satellite LOS.

Once defined the average velocity value and the perimeter of an area of interest, is possible to establish its state of activity on the base of an activity matrix (Figure 23)
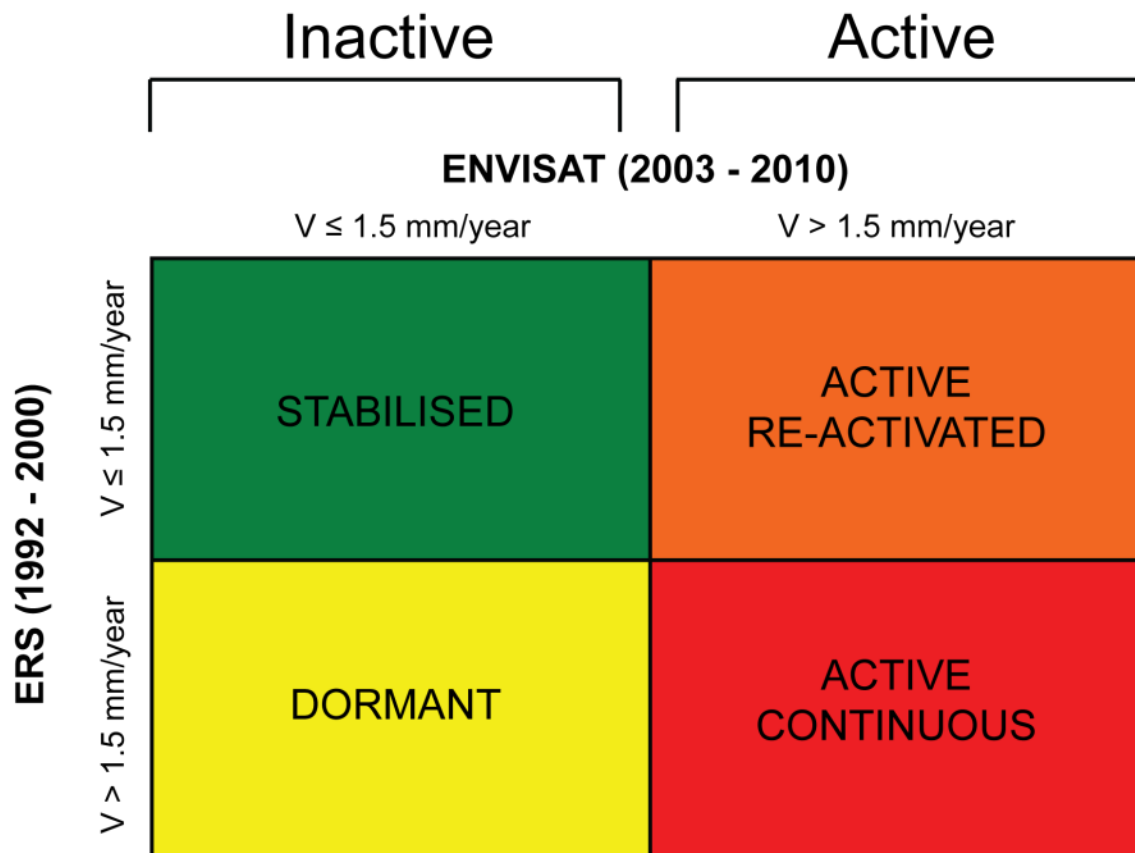
Figure 23. Activity matrix used for the assignment of the state of activity to the mapped phenomena.

The activity matrix is obtained by combining the velocity values measured in the acquisition time intervals of the two *radar* datasets.

According to the matrix, 4 activity classes are established: Stabilised, Active Reactivated, Dormant, Active Continuous. Such classes are defined according to the Multilingual Landslide Glossary (WP/WLI, 1993) and separated by the threshold value ±1,5 mm/year.

Taking into account such threshold velocity value, the different states of activity have been assigned as follows:

ACTIVE LANDSLIDE

- **Continuous**

    The threshold value is exceeded in both acquisition periods (1992-2000 and 2003-2010)

- **Reactivated**

    The phenomenon shows velocity values below the threshold in the 1992-2000 period and above the threshold in the interval 2003-2010.

INACTIVE LANDSLIDE

- **Stabilised**

  The phenomenon shows velocity values below the threshold in both the time intervals.

- **Dormant**

  The threshold velocity value are exceeded only during the time interval between 1992 and 2000.

Worth to underline that the class "relict" is not considered in the matrix. This because, according to the definition of *relict* proposed by the WP/WLI (1993), a relict landslide is an inactive landslide which occurred under climatic or geomorphological conditions considerably different from those at present. It is clearly impossible to formulate such considerations, only using the available ancillary data and without very specific *in situ* surveys.

For the same reasons, even though the category "stabilised" is included in the matrix, no new landslides have been classified with such class of activity. This because, according with the WP/WLI (1993), a stabilised landslide is an inactive landslide which has been protected from its original causes by remedial measures, condition unverifiable with the available data.

Using the proposed methodology some pre-existing polygons have been modified there where PS data were present and new ones have been delimited and characterized.

Some examples of modifications are following shown.

Modifications of already mapped phenomena

Checking the distribution and the velocity values of the PSs inside or in the vicinity of a landslide, the state of activity of a landslide has been possibly modified.
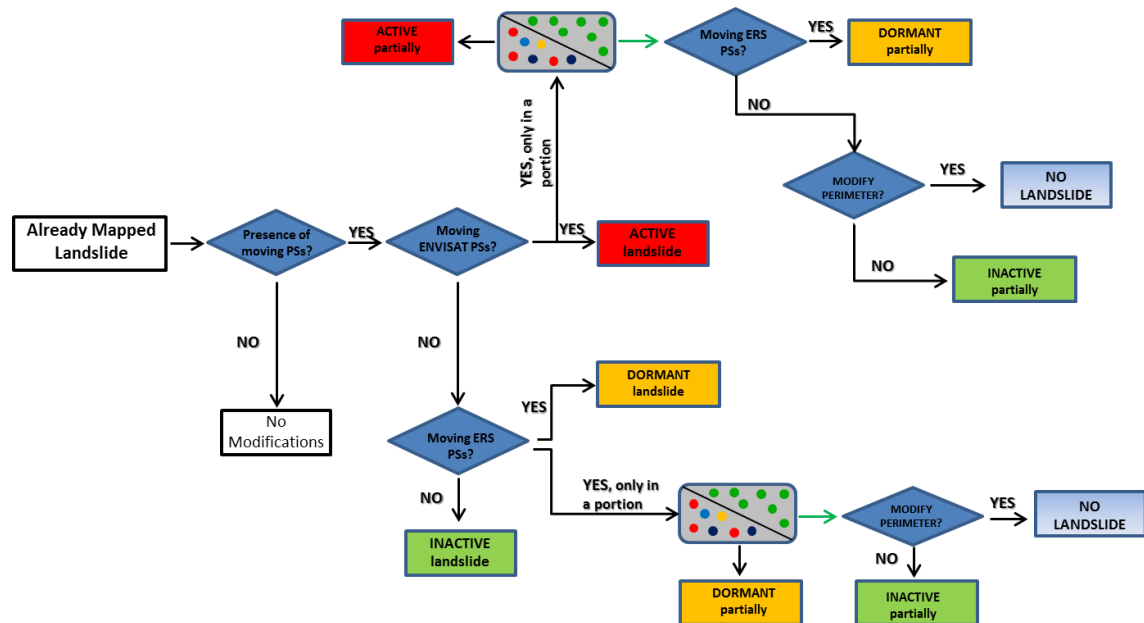
Figure 24. General flowchart showing the procedure utilized for the modification of landslides perimeter and state of activity, using ERS and ENVISAT data.

In Figure 24 a schematic procedure for the modification of the state of activity of landslides that already exist in the inventory.

If PSs indicate velocity of more than 1,5 mm/y only in a portion of a landslide, the state of activity has been modified only in that portion and the polygon is subdivided in two or more areas with different state of activity.

In some cases the PSs have allowed to modify the perimeter changing the areal extent and the shape of the polygon, according to the morphology, the velocity values, other indicators visible on the ancillary data and, in some cases, field surveys.

Figure 25 shows a graphic example of a modification of the state of activity, applied to some landslides already included in the original inventory and classified as indeterminate.

This is a wide area affected by complex slope processes placed in the municipality of Sambuca Pistoiese (province of Pistoia), where the interferometric data have highlighted significant displacement on the surface.
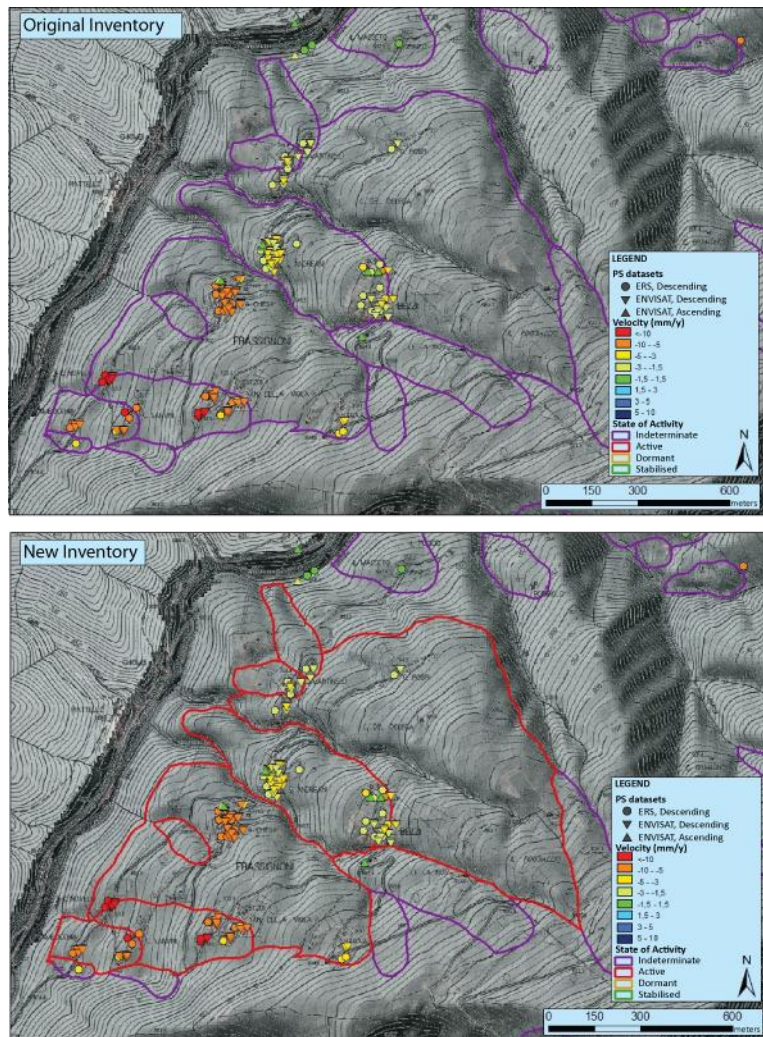
Figure 25. Example of change in state of activity, from indeterminate to active. Landslide placed in the municipality of Sambuca Pistoiese (province of Pistoia)

In this case, the displacement measurements obtained by PS, inside and in proximity of the area have highlighted velocity values that range between 3 mm/y and 5 mm/y in the NE portion, between 10 mm/y in the central portion of the slope and up to more than 10 mm/y in the SW part.

Such values are measured along the LOS of the ENVISAT satellite and referred to the descending orbital configuration, for this reason the negative values indicate a movement moving away from the satellite, according to the mean slope angle.

According to the PS data the state of activity of the landslides in Figure 25 have been changed from "indeterminate" to "Active", attributing a velocity to the different polygons by averaging the values of the PSs, weighting the resulting velocity taking into account the slope orientation and the displacement time series of the points.

The distribution of the PSs and the morphological pattern of the area, assessed by the exam of the ancillary data, have confirmed the effectiveness of the delimitation, making unnecessary a further modification of the shape and area of the mapped phenomena.

Depending on the entity of the velocities and the spatial distribution indicated by the PSs, the perimeter of landslide polygon could be modified. In Figure 26 some landslides in the municipality of Marliana (Pistoia) are shown. The PS data have been useful in order to modify the perimeter of the polygons 1 and 2, including surrounding portions of the slope, where points with LOS velocities greater than 1,5 mm/y (in direction away from the satellite) were present.
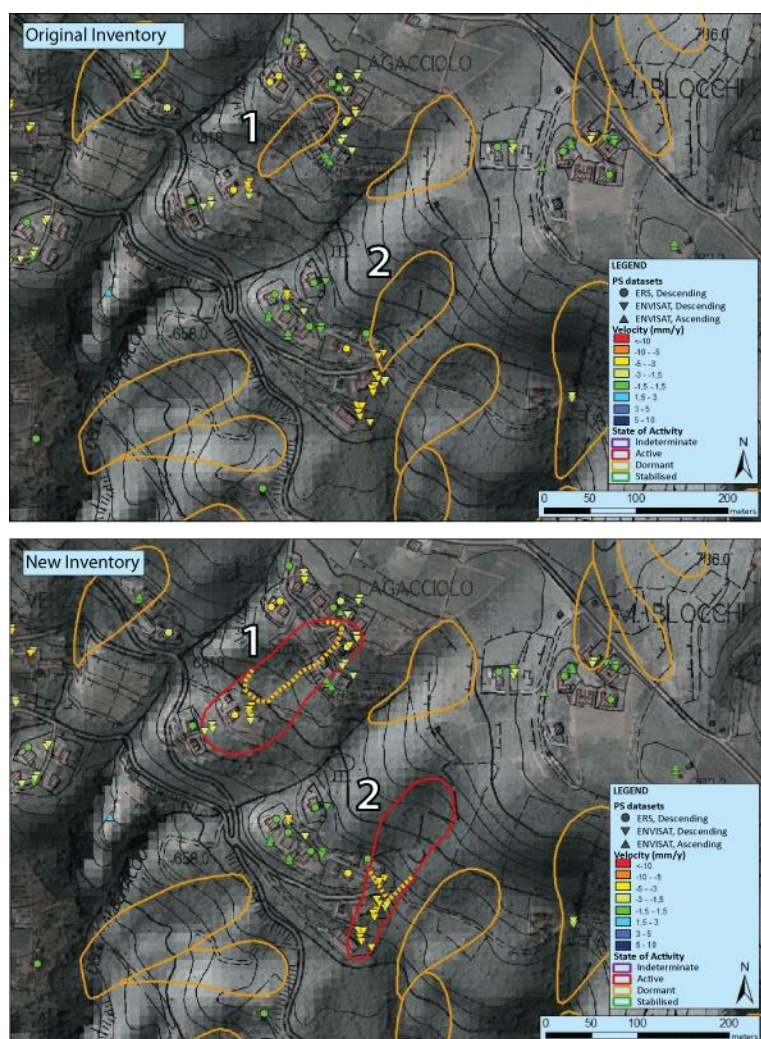
Figure 26. Example of change in perimeter and in state of activity (from dormant to active). Landslide placed in the municipality of Marliana (province of Pistoia)

For the modification of the perimeters the PS spatial distribution and the morphological features of the slope have been considered, using DTM and topographic maps.

Along with the change of perimeter, also the state of activity has been changed, according to the activity matrix and a velocity value have been attributed. In particular a velocity of 3,2 mm/year has been assigned to the polygon 1 and 3,5 mm/year to the polygon 2.

As mentioned before the landslide velocities are the results of an average of the values of the involved PSs, weighted by the operator considering the satellite LOS direction with respect to the global slope orientation.

In Figure 27 shows a case in which some slope movements already contained in the original inventory have been modified in their extent, splitted and classified with a different state of activity
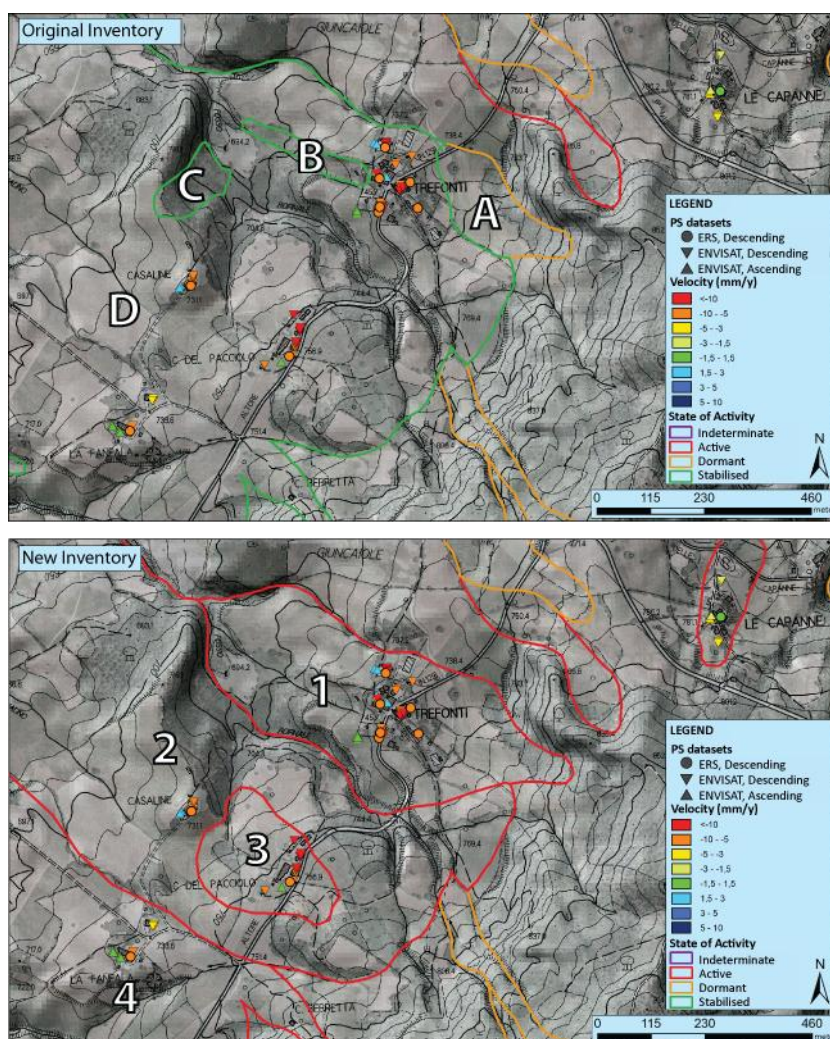
Figure 27. Example of new subdivision (pro-parte) of an already mapped phenomenon. Changes in state of activity (from dormant to active) have been also applied. Landslide placed in the municipality of Seggiano (province of Grosseto)

Figure 27 shows a detail of a wide area near Seggiano (province of Grosseto) affected by some slope movements classified as "dormant" or "stabilised" in the original inventory.

According to the PS measurements and the morphology, the polygons have been merged or splitted splitted and associated with a representative velocity value.

New phenomena

In case some moving points are placed where no landslide were previously mapped, the delimitation of new phenomena have been performed taking into account the spatial distribution of the PSs and the geomorphological features of the slope.

Worth to underline that only the areas with a good density, spatial distribution and good coherence in the deformation rates, have been considered in the analysis.
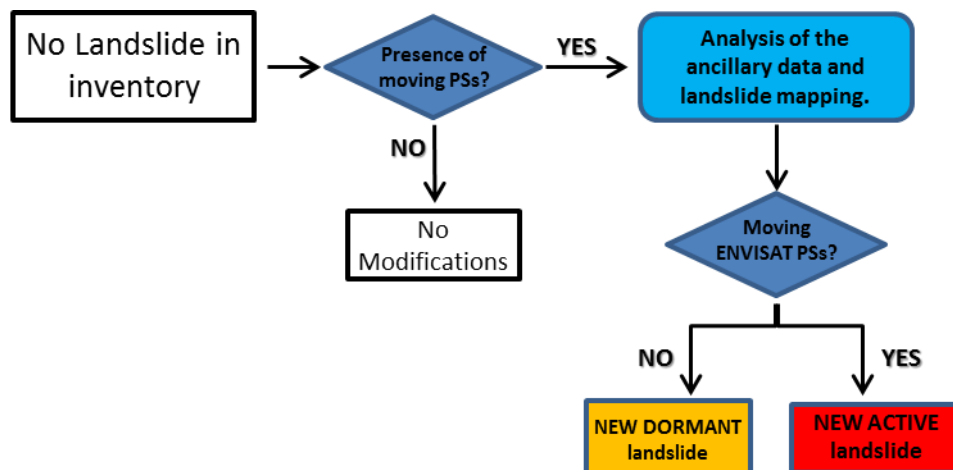
Figure 28. Flowchart showing the procedure utilized for the delimitation and assignment of the state of activity to a new detected landlside, using ERS and ENVISAT data.

Figure 28 shows schematically the methodology adopted in mapping new landslides. In particular, in case that only ERS 1/2 data with velocities higher than 1,5 mm/year are present, a landslide have been delimited but classified as "dormant", since the lack of ENVISAT data doesn't allow to establish if there have been movement until 2010.

If ENVISAT data with velocities higher than 1,5 mm/year are present, the landslide is classified as "active", whereas in all other cases the state of activity is assigned according to the matrix.
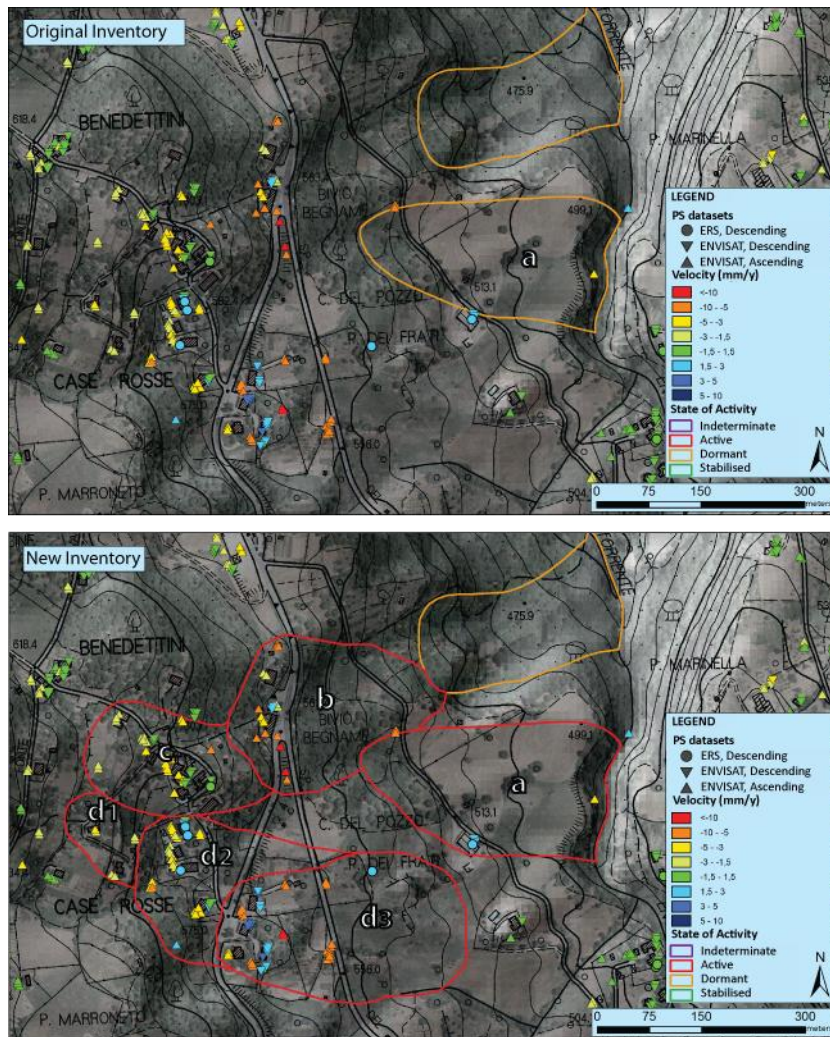
Figure 29. Example of the delimitation of new detected landlsides. Area placed in the municipality of Arcidosso (province of Grosseto)

In Figure 29 an area affected by slope movements is shown, in such area the *radar* data have allowed to detect and characterize a wide and complex scenario of active landslides.

The area is placed in the municipality of Arcidosso (province of Grosseto), and shows a good point density and spatial distribution. Due to the average aspect angle of the slope, and consequently the mean direction of displacement, the measured velocity values are negative (away from the satellite) in ascending orbit and positive (towards the satellite) in descending orbit.

Considering the medium orientation of the slope (East-North-East) the real displacement vector is more underestimated in the descending orbit.

In the case shown in Figure 29 the perimeter and the state of activity of the landslide "a" have been modified (classified as active) and a new area affected by some phenomena with different velocities have been delimited (areas "b", "c", "d$_1$", "d$_2$" e "d$_3$").

A velocity value have been attributed to the phenomena mapped *ex-novo,* considering mainly the velocity values measured by the ENVISAT in ascending orbit, less underestimated due to the slope orientation:

- Polygon **a**: 3 mm/year
- Polygon **b**: 8 mm/year
- Polygon **c**: 3 mm/year
- Polygon d_1: 2,5 mm/year
- Polygon d_2: 4 mm/year
- Polygon d_3: 8 mm/year

Taking into account the aforementioned approach the Tuscany Regional Database of Landslides at scale 1:10.00 have been revised and updated.

The final product is a new landslide inventory map in *shapefile* format, similar to the original one, with new fields in the attribute table (see Appendix 1), related to the modifications applied to each polygon.

In particular, in all the cases in which the PSI technique has proved to be efficient, the *radar-interpretation* approach have allowed to modify or assess (in case of new detected phenomena) the following attributes:

- Area and perimeter (shape)
- Landslide Type (according to Cruden & Varnes, 1996)
- Displacement velocity, during the acquisition period.
- State of activity, according to the activity matrix.
- Displacement direction

Worth to specify that, in most cases, it has been impossible to modify or characterize the attribute "Landslide Type" inasmuch it has been considered that such consideration needs for further and more detailed analyses.

In order to perform an sufficiently robust analysis, only areas in close proximity of at least 2-3 *persistent scatterers* have been taken into account along with some morphological indicators visible in the ancillary data.

The attributes of the database are listed and described in Appendix 1.

Applications in subsidence mapping

Since all the satellites acquire images broadside the direction of movement, they illuminate earth's surface from different angles when they move on ascending or descending orbit.

Thus, the real displacements of an area will be measured as projected along the LOS in a different way for the two orbital configurations (Figure 30).

Given that ERS and ENVISAT satellites moves on a *quasi-polar* trajectory, acquiring images on the right side and with an angle of incidence on the earth surface equal to 23 degrees with respect to the vertical plane, movements with a strong component in the N-S direction are not well detectable.
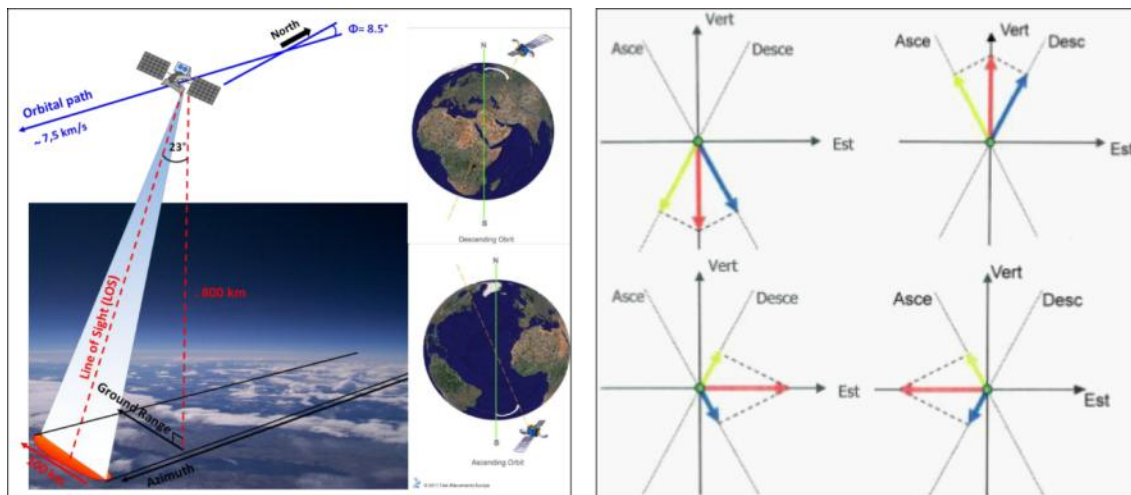
Figure 30. Left box: orbital configuration for *radar* satellite acquisitions. Right box: projections of the real displacement vector along the satellite LOS in the two orbits.

Considering that, combining geometrically the velocity values from the two orbits is possible to calculate the horizontal (EW) and vertical (V) component of the displacement vector.

This process is important to distinguish areas with movements mainly in the vertical direction (subsidence) and areas with a strong horizontal component (landslides), detectable in the East-West direction.
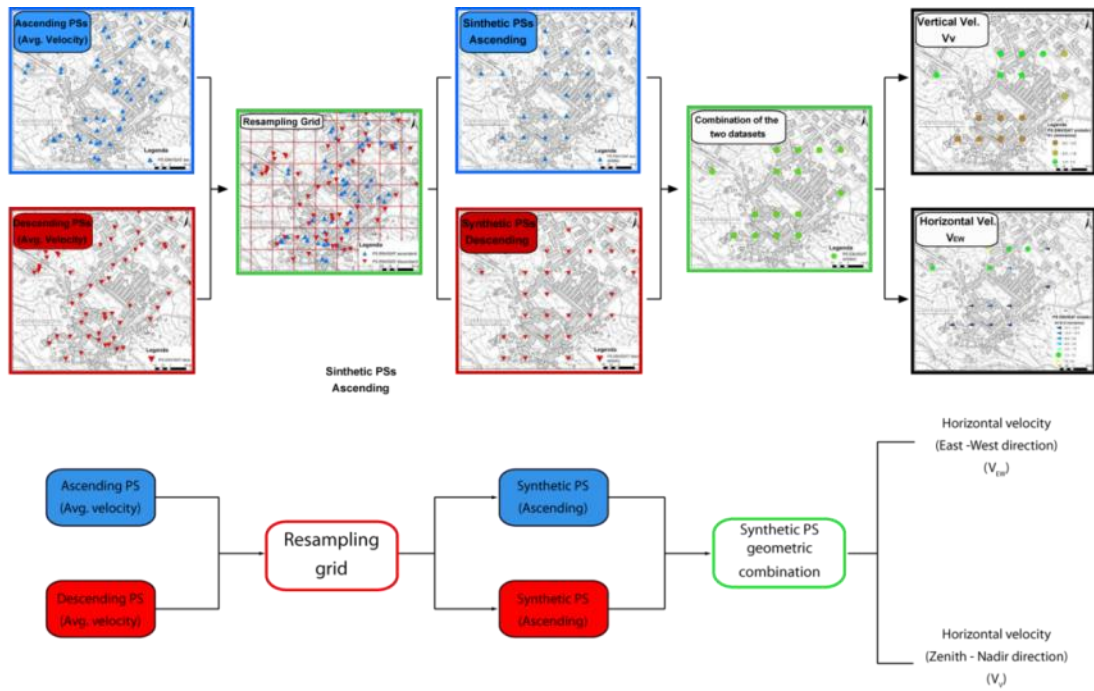
Figure 31. Flowchart showing the adopted procedure for the resampling and combination of ascending and descending PSs. The result are two maps with synthetic PSs respectively for vertical and EW components of the displacement vectors.

Since it is a *point-wise* approach, it would be essential that every *radar* target is detected by the sensor in both acquisition geometries. Unfortunately this hypothesis is rarely verified, therefore a resampling of the PSs is needed, performed using a regular grid, which dimensions must be calibrated according to the point density at the scale of analysis (Figure 31).

For the two datasets a mean velocity value is calculated in each cell by averaging the values of the PSs inside it obtaining two sets of synthetic PSs on which a reconstruction of the horizontal (V_{EW} in E-W direction) and vertical (V_v in Zenith-Nadir direction) components of movement can be evaluated.

The velocity values can be integrated as follows:

$$\begin{cases} V_a = V_V \cos \Theta_a + V_{EW} \sin \Theta_a \\ V_d = V_V \cos \Theta_d + V_{EW} \sin \Theta_d \end{cases} \qquad (10)$$

Where V_a and V_d are respectively the velocities measured in ascending and descending orbit and Θ is the LOS angle of incidence with respect to the vertical plane (23° for both ERS 1/2 and ENVISAT sensors, 35,5° for TerraSAR-x) (Figure 32).
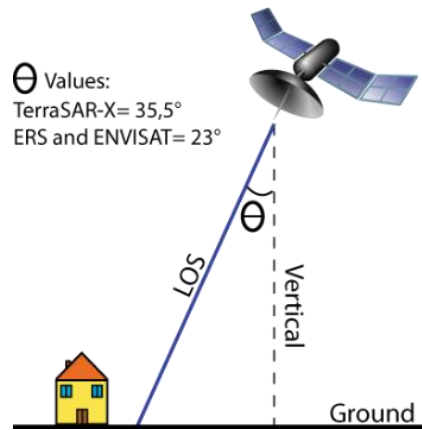
Figure 32. LOS angle with respect to the vertical.

The outcome of this process consists in two maps in which, respectively, the horizontal (EW) and vertical (Z) components of the displacements are represented, making the overall results not easy to appreciate.

To avoid this problem the resulting vector of the two components V_V and V_{EW} have been calculated in order to have, for every synthetic PS, a deformation value and direction on the vertical plane.

3.2.   Airborne multi-sensor data fusion

The exploitation of multi-spectral, hyperspectral and LiDAR data synergies have been used in this research in order to detect slope processes with rapid kinematic, not detectable with the previously described PSI technique.

Indeed, slope movements have to be necessarily slow and rather constant in time (coherent) to allow the processing of PSs inside them. For this reason a different approach is needed in order to detect and delimit phenomena that occurs in a very short time, like landslides of the flow type (Hungr *et al.* 2001), erosion phenomena or changes in fluvial morphology.

Here an approach based on a *change-detection* technique have been used, comparing multi-source data acquired during two different flights, carried out respectively in 2009 and 2010, over the area of Valmarecchia (province of Rimini).

Furthermore, this kind of data has proven to be very suitable for the automatic development of land cover maps, classifying the landscape by combining the spectral signature of the elements on the ground with height informations derived by the LiDAR high-resolution DEM.

This approach have been used for a *pixel-based* land cover classification, performed using the data acquired on the 2009 survey over a 80 Km section of the valley, that resulted in a detailed map of the elements present on the territory (i.e. houses, industries, roads, vegetation and water).

3.2.1. Study area: Valmarecchia

The studies carried out using Multi-spectral and LiDAR data were conducted on an area including the most part of the fluvial reach of Marecchia river, that sources in Eastern Tuscany and runs at the border between the regions of Emilia-Romagna and Marche, and an area along the coastline between the cities of Cattolica and Ravenna in North-Eastern Italy (Figure 33).

Figure 33. Geographic position of the Valmarecchia basin (province of Rimini)

Such area is characterized by complex land cover patterns and geomorphological spatial variability, for this reason it represents an interesting site to test the proposed technologies.

Indeed, the area is morphologically characterized by a wide variety of scenarios such as an extremely dynamic fluvial system and diffused erosive and landslide processes on the hillslopes.

Streamside dredges for fluvial sediment extraction with related decantation basins are widely present along the floodplain. The valley floor, along the Marecchia river, is prevalently made up of factory/industrial units, agricultural fields such as croplands and olive groves and semi-natural vegetation such as meadows.

The hilly and mountainous part of the area is characterized by steep slopes due to the alternation of competent and more erodible lithological units. Those condition are suitable for the occurring of landslide phenomena, correctly detected applying the proposed method.

Furthermore the territory along the Marecchia river is extensively characterized by the presence of endemic vegetation both on the hillslopes and on the fluvial domain.

The reach along the coastline is almost totally flat and widely cultivated with the presence of several villages and industrial areas.

From a geological viewpoint the area belongs to the general Northern Apennine structure described for Tuscany. The Ligurian and Epi-Ligurian units (deposed on *piggy back* basins on the frontal part of the moving Ligurian units) are prevalent, along with some formation of Umbro-Marchigian pertinence (such as the *Formazione Marnoso-Arenacea della Valmarecchia*).

In general the area shows very *"young"* morphological features, with abundant clay formations, prone to instability and marked erosive processes (Figure 34).

In addition to the natural instability the area have been affected, in some cases, by incorrect human management such as riverbed dredging up and the construction of river dykes, that have seriously modified the natural sedimentation/deposit balance creating weakness on river banks and bridges, as well as significant changes in fluvial morphology.

Figure 34. A panoramic view of the village of Pietracuta, placed on the right side of the Marecchia river. The picture shows the characteristic morphological features of the area, with the contrast between gentle slopes in the clayey areas (in the foreground) and sandstone rocky cliffs (in the background).

3.2.2. Available data

In this work multi-spectral and LiDAR have been utilized for the following two purposes:

- develop semi-automatic procedures for the detection of rapidly moving slope processes
- explore the potential of some existing image classification algorithms, for a rapid and automatic landscape mapping.

The development of a method for rapid kinematics processes detection is an important topic. Indeed, due to the intrinsic limitations of the abovementioned *radar* techniques to measure rapid movements without losing coherence, a different method is needed.

For this reason, the proposed methodology is based on the exploitation of a change-detection procedure on data acquired on the same area in two different surveys, respectively in 2009 and 2010.

Furthermore, the data acquired December 2009 have been exploited to carry out an optimized landscape mapping based on the choice of the most suitable classification algorithm , multi-source data combination and number of hyperspectral channels of the MIVIS sensor.

The three different sensors were placed on an aircraft equipped for *remote-sensing*: we select the sensors with the most advanced technology.

These sensors were:

- A multi-spectral camera
- A hyperspectral sensor
- An airborne laser scanning device (LiDAR)

The sensor listed above are briefly described in the following paragraph.

Multi-spectral sensor ADS40

Optical sensors have replaced the traditional film cameras and provide an important opportunity to acquire panchromatic images and multi-spectral images. Panchromatic and multi-spectral sensors use wavelength of the visible and near infrared, allowing very high spatial resolutions providing the fundamental basis for the analysis and description of the territory. In this experiment the digital camera system Leica ADS 40 LH (now referred as ADS40) was used (Figure 35). ADS40 is a photogrammetric camera that registers with

continuity along the line of flight (pushbroom type). It has 4 spectral bands between 420 and 885 nm: through this camera we can obtain images of the territory in the visible and near infrared. ADS40 is placed on a stabilized platform (Wild PAV30) and inside contains the opto-electronic apparatuses and the inertial measurement unit, so pixels are geo-referenced directly in the acquisition phase. ADS40 creates continuous image that covers an entire strip. Every strip is composed by the succession of scan lines of 12000 pixels.

Figure 35. High-resolution multi-spectral camera ADS40

The panchromatic sensors are arranged on the focal plane to register the same point in three corners of observations (forward, backward and nadir). This offers the possibility of three distinct stereoscopic visions. The four color visible and infrared sensors are placed in nadir position: in this way the perspective effect along the axis of flight is null, and in the transverse direction it is also attenuated.

All sensors have the same geometric resolution. All the acquired images (color and infrared) have the same resolution on the ground (unlike satellites images): 20 cm/pixel with a planimetric tolerance less than 1 meter.

Hyperspectral sensor MIVIS

In this experiment the MIVIS (Multi-spectral Infrared & Visible Imaging Spectrometer) scanner, produced by the U.S. company Daedalus, have been used. MIVIS is a scanning system that operates with a high spatial and spectral resolution and can be easily adapted to airplanes and flying platforms. The correct georeference is guaranteed by a PAS system (Position and Attitude Sensor): it consists of a GPS receiver to determine the position and speed of the aerial platform and a gyroscope to control of pitch and roll.
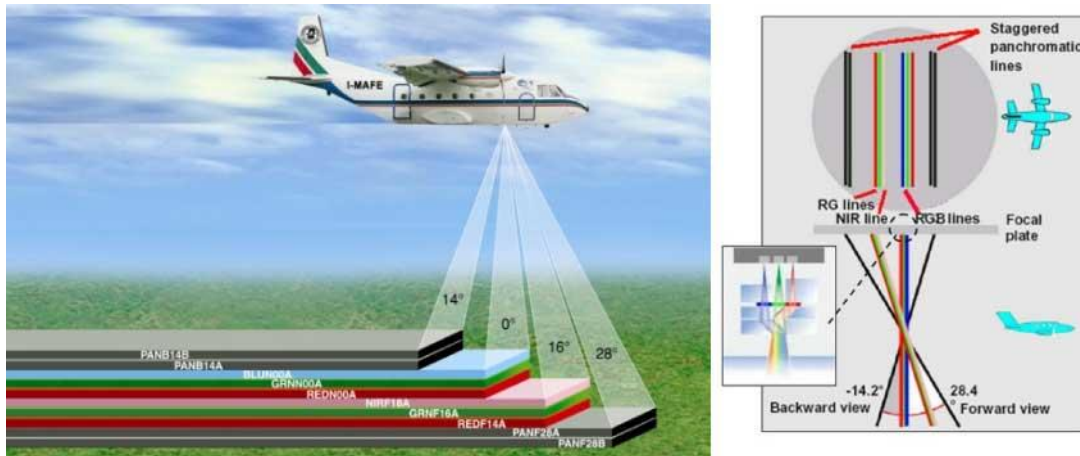
Figure 36. Scheme of the MIVIS acquisition parameters.

MIVIS is a modular instrument, consisting of four spectrometers which simultaneously measure the radiation from the Earth's surface in the visible, thermal infrared and medium infrared (Figure 36). MIVIS wavelengths, number of channels recorded and its spatial resolution can satisfy the needs of the research in various scientific disciplines such as Botany, Agronomy, Geology, Hydrology or Oceanography (Ciraolo *et al.*, 2006; Belluco *et al.*, 2006; Boschetti *et al.*, 2007; Pignatti *et al.*, 2009). MIVIS simultaneously records the information in 102 channels divided as described in Table 2

Table 2. MIVIS spectral range of acquisition and bands.

Spectrometer	Spectral Region (nm)	Bandwidth (nm)	Band Number
Visible - NIR	433 - 833	20	20
IR Middle	1150 - 1550	50	8
IR Middle	2000 - 2500	8	64
IR Termal	8200 - 12700	400	10

The flight characteristics have been established to obtain multi-spectral images with ground resolution equal to 3 m/pixels and with a tolerance planimetric below that resolution.

LiDAR data

The scanning systems that use the laser technique for ground modeling substantially measure the distance between the laser beam emanation point and the first obstacle which generates the reflection. These systems are called Light Detection and Ranging or Laser Imaging Detection and Ranging (acronym LIDAR).

The measurement is done through a very precise calculation of the time of return, allowing intrinsic accuracies of the order of centimeters. The LIDAR sensors are constructed to calculate a very high number of measures in the time unit.
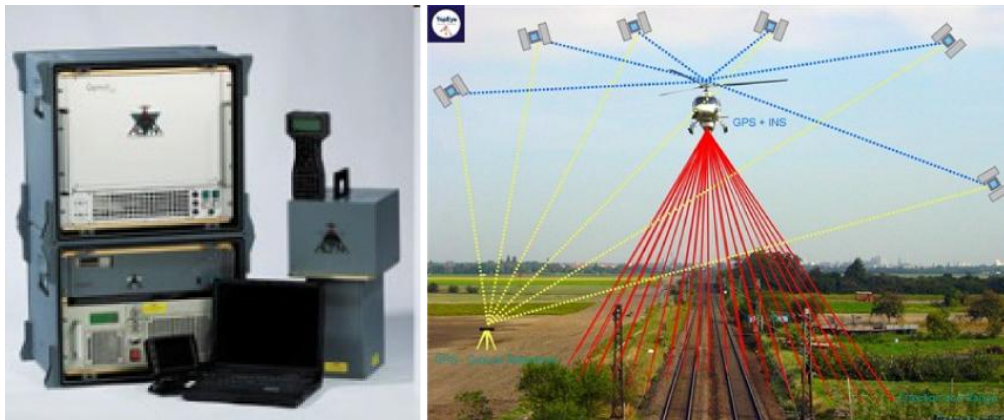
Figure 37. The LiDAR sensor Optech ALTM Gemini (left) and a schematic view or the acquisition mode.

A LIDAR sensor Optech ALTM Gemini was used (Figure 37). The system is characterized by a highly focused laser beam. The beam has a fixed frequency within the infrared wavelength range and the spokes are perpendicular with respect to the movement of the aircraft. Width and density of points is programmable and also depends on the flight altitude. The sensor can produce up to 167,000 pulses per second at its maximum operating height of 4000 meters , with opening angles of up to + / -25 °.

The correct absolute position of the instrument, which is fundamental for this type of acquisition, is ensured by a GPS receiver with integrated inertial sensor. This equipment is essentially a series of accelerometers and allows recording with a very high frequency to improve the positioning data obtained from the GPS. These elements are essential for the postprocessing of LIDAR data.

The laser pulse (or its portion) is reflected back to the instrument from the surface and it is collected by the receiver. Measuring the time difference between pulse and its response is possible to determine the distance from the object hit the ground. The intensity value of response of the laser beam is related to the reflectivity of the material struck by the laser: more the material responds at the laser frequency, higher is this value. The LIDAR system emits a laser beam in the infrared wavelength range. Since at these wavelengths water absorbs but does not reflect all of the signal, in general there is no return signals (and therefore measures) in correspondence of water.

The laser system can record multiple echoes (up to 4) of the return laser beam. This ability is mainly used in vegetated areas where, in general, the pulse get a first reflection at the first leaf surface encountered; part of the ray penetrates vegetation and get further reflections that give other responses. Thanks to this characteristic LIDAR allows measurements even below the layer of foliar vegetation.

The raw data obtained by this LIDAR instrument is a cloud of points with variable spacing estimated between 25 and 35 cm stored in LAS files. The LAS file format is a binary file format that maintains information specific to the LIDAR. Each point stores the characteristics of its acquisition (pulse number, intensity, minimum, maximum, standard deviation, etc.).

Raw data was processed in order to obtain a regular data grid with ground resolution of 1 m/pixels.

The planimetric tolerance of this products is within the size of the pixel, while the altimetric tolerance is estimated in 10-15 cm. Two models with this characteristics have been developed (Figure 38): the elevation model of the surfaces (DSM, Digital Surface Model), obtained the first response pulse, and elevation model adjusted removing possible vegetation, buildings or similar data (DTM, Digital Terrain Model).
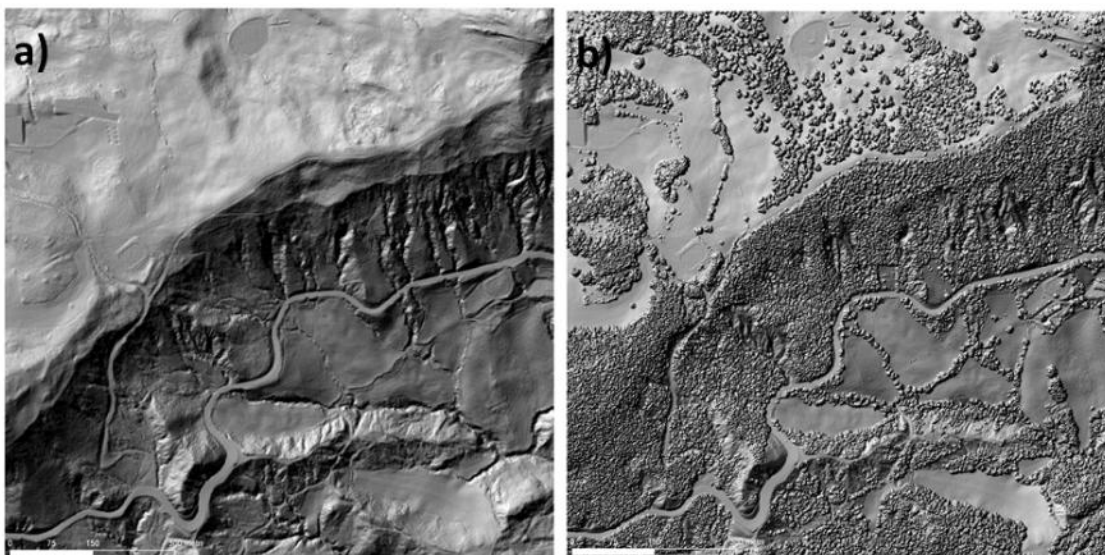
Figure 38. Difference between a DTM (a) and a DSM (b) on which the vegetation is visible.

The normalized Digital Surface Model (nDSM) has been calculated by using the following equation:

$$nDSM = DTM-DSM$$

To resolve the lack of resource problem in the processing of data with high informative content in such large area we have adopted a territorial subdivision in regular tiles: each one consist in a 1kmx1km square with an overlapping border of 20m (Forzieri *et al.* 2012b). Overall the area is subdivided in 455 tiles as shown in Figure 39.

Figure 39. View of the entire area surveyed using airborne sensors and the tiles used for processing

3.2.3. Automated landcover classification method (Annex 2)

Land cover is a crucial variable, which plays an important role in most soil–atmosphere interactions (Feddema *et al.*, 2005). The significance of providing accurate fine-scale land cover maps is emphasized by the evidence of marked impacts of land cover changes on local surface dynamics (Claessens *et al.*, 2009).

Remote-sensing data classification represents an essential tool for environmental monitoring and sustainable land use management (Melesse *et al.*, 2007), especially in heterogeneous landscapes characterized by many interconnected natural- and human induced processes (Forzieri & Catani, 2011).

Furthermore, the possibility to obtain automatically a detailed map of the elements of territory represents a fundamental tool in the optic of a Hydrogeological Risk Evaluation, providing a high-resolution datasets in a *time-* and *cost-effective* way.

In this study all the available data, including optical ADS40, hyperspectral MIVIS, and LiDAR, have been used for a detailed land use classification.

The proposed procedure explores different strategies of exploitation of multi-sensor *remote-sensing* data for fine-scale mapping of 17 land cover classes. The method generates a large array of classification scenarios obtained with different sensor/ setting combinations and, similar to a model identification problem, identifies the combination which maximizes the classification accuracy.

The configuration to identify include: (1) classification algorithm (*al*); (2) multi-source data combination (*FS*); and (3) numberof hyperspectral channels (*n*). The array of the classification maps can be described by the following mathematical notation:

$$H = K(al, FS, n) \qquad (11)$$

where H is the classification accuracy associated with the triplet (al, FS, n) used as input in the classification routine (K).
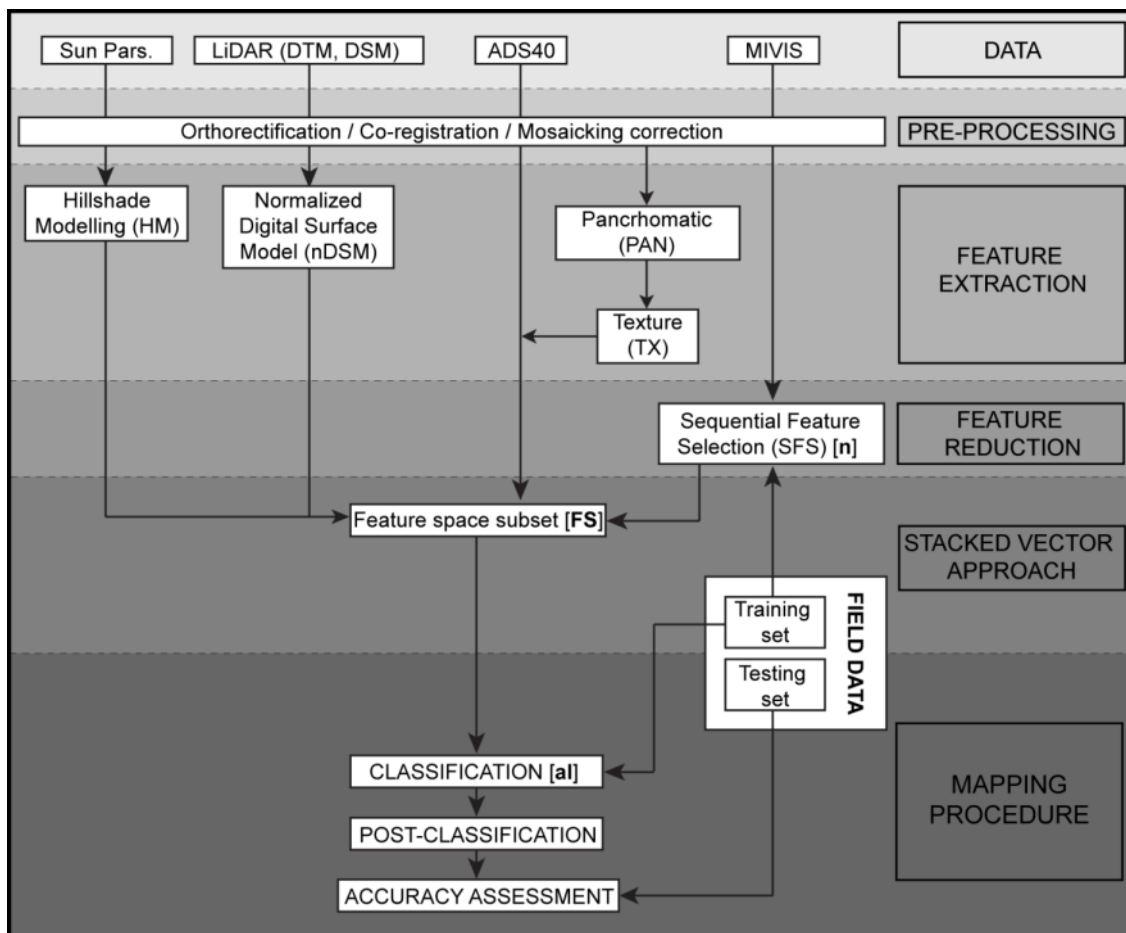

Figure 40. Flowchart of the developed classification scheme. Data, pre-processing, feature extraction, feature reduction, stacked vector and mapping procedures are differently displayed according to the reference shaded color.

Figure 40 displays the flowchart of the generation of the explored array of classification results. This generation is organized in five sequential steps.

- **Pre-processing**: The remotely sensed data were orthorectified and co-registered in the UTM-WGS84 projection by ground control points.
- **Feature extraction**: calculation of hillshade modeling (HM), normalized Digital Surface Model (nDSM), texture (TX) using the remotely-sensed data
- **Feature reduction**: sequential selection of the most suitable MIVIS bands (n in Figure 40) using the Sequential Feature Selection method (SFS) (Serpico *et al.*, 2002)
- **Stacked vector approach**: a straightforward approach to classify mixed data is to form extended pixel vectors stacking together the individual vectors that correspond to each input data source (stacked vector method; Richards and Jia, 2006; Tso and Mather, 2000). Here, 16 options for stacking the original (ADS40, MIVIS) and derived information (nDSM, HM, TX) were explored.
- **Mapping procedure**: The generated multi-stacks were classified by means of three popular classifiers (*al* in Figure 40) that have been chosen in this study for their simple implementations and computational efficiencies: the well-known Maximum Likelihood (ML, Richards & Jia, 2006), Spectral Angle Mapper (SAM, Kruse *et al.*, 1993), and Spectral Information Divergence (SID, Chang, 2000) classifiers.

The training/testing samples represented the *ground-truth* of the images and have been collected by applying ROIs (Regions Of Interest), drawn on the base of a visual interpretation of the RGB data and some focused field surveys.

Training/testing samples were used to calibrate/validate each generated configuration. The classification performances were quantified in terms of confusion matrix (M), overall accuracy (OA), commission (COM)/omission (OMI) errors and kappa conditional statistics (K_s) (see Annex 1).

As a whole 17 main target land cover classes have been discriminated: water river (WR), water lagoon (WL), bare soil (BS), asphalt (AS), plowed field (PF), urban fabric (UF), industrial unit (IU), herbaceous (HE), heatland (HL), arundo donax (AD), poplar (PL), oak (OK), pine (PN), cypressus (CY), spruce (SP), willow (WI), and olive (OV).

In order to highlight specific parameter-dependent improvements and to define possible sub-optimal alternatives we described the classification scheme identification through 3 sequential steps, by progressively fixing one optimal configuration variable at a time and by accordingly reducing the size of the search space:

1. classifier choice:

$$H_{al}(FS, n) = \max_{al}[K(al, FS, n)] \qquad (12)$$

2. choice of the stacked vector configuration:

$$H_{al,FS}(n) = \max_{FS}[H_{al}(FS, n)] \qquad (13)$$

3. array subset, choice of the number of hyperspectral channels.

$$H_{al,FS,n} = \max_{n}[H_{al,FS}(n)] \qquad (14)$$

The variability of the three key parameters (al, FS, n) across the investigated land covers has been investigated to assess possible sub-optimal classification solutions more suited to specific environments, such as mixed forest, floodplain, urban, and agricultural zones.

3.2.4. Landslide detection: a change-detection approach (Annex1)

The changes in ground morphology registered through the two LIDAR acquisitions have been analyzed.

The purpose is to provide a probability map to establish if a landcover change, detected during a change detection process on the remotely sensed datasets, could be related to a landslide.

The method is structured in 6 steps as follows:

- Development of a change detection map.
- Choice of specific classes in the change detection map on which the model can be implemented.
- Production of an inventory map of landslides occurred between the two *remote-sensing* surveys.

- Choice of geomorphological features (or indices), which varations could be related to a landslide.
- Statistical analyses on the correlation between the observed landslides and the values variations of the selected morphological features.
- Analyses of the specificity of such variations with respect to landslides.
- Developement of a landslide probability map.

In order to consider the changes in the land cover between the two acquisitions, a pixel-oriented approach based on a tree-decision classifier has been adopted (Figure 41).

This approach takes into account the changes of spectral and geomorphological parameters, such as NDVI (Normalized Difference Vegetation Index)(Tucker, 1979) and height differences. NDVI index is widely used to monitor, using multi-spectral satellite data, the growth of plants, vegetation cover and biomass production. It is a simple graphical indicator that can be used to analyze *remote-sensing* measurements and assess whether the target being observed contains live green vegetation or not (Myneni *et al.*, 1995). It permits to distinguish different tree species, making vegetation carts and, more generally, the use soil.

The NDVI is calculated from the measurements as follows:

$$NDVI=(NIR-VIS)/(NIR+VIS)$$

where VIS and NIR stand for the spectral reflectance measurements acquired in the visible (red) and near-infrared regions. The capacity of the digital camera to generate infrared images was essential for our purposes in *remote-sensing* related to the study and monitoring of the territory: the NDVI index was obtained using very high definition ADS40 images (0.2 m/pixel) instead of low resolution MIVIS images.

The tree-decision classifier is based on a set of rules in order to detect the target variables generating a binary branch structure. The threshold values have been a priori defined on the base of a try-and-error procedure.

The other parameters considered in the *change-detection* are listed and described in the Appendix 2.

Figure 41. Structure of the adopted *tree-decision* classifier used for the change-detection process.

4. Results and discussion

4.1. Detection of slow kinematic processes using TerraSAR-x data: Barcelona

By processing 28 TerraSAR-x *stripmap* image over the urban area of Barcelona, acquired and elaborated at the *Institut de Geomàtica* in Castelldefels, 56 interferograms have been developed and a PSI datastack has been computed making possible to carry out an accurate detection of all the main ground deformation processes active in the area between 2007 and 2009 (cfr.§ 3.1.2).

In addition, the same processing procedure have been applied on a small area in correspondence of the village of El Papiol, placed in the Llobregat river valley, at about 15 Kilometers North-West of Barcelona.

In the following paragraph some results of the analysis are reported and briefly described, in particular regarding the village of El Papiol, some processes ongoing on the hill of Montjuïc and some local subsidences occurred in the urban area of Barcelona and in correspondence of "El Prat" airport between 2007 and 2009.

4.1.1. The village of El Papiol

El Papiol is a village and a municipality in the province of Barcelona in the autonomous community of Catalonia (Figure 42).

The village is placed on the hydrographic left side of the Llobregat river valley at an averaged altitude of 110 meters a.s.l. and it is composed by an old village centre and other recently built areas.

An industrial zone and an important cement plant are placed downslope the village in

The most part of the urban area of El Papiol is affected by old landslides, reactivated during a flood in October 1962. All the further reactivations have occurred following intense rainfall events such as in 1971, November 1983 and March 1984.

In all of this cases the massive rainfalls have been the triggering factor but the effects have been accelerated by the diffuse water losses from the flawed sewage system (Ramon Copons, Project RISK-CAT 2008)
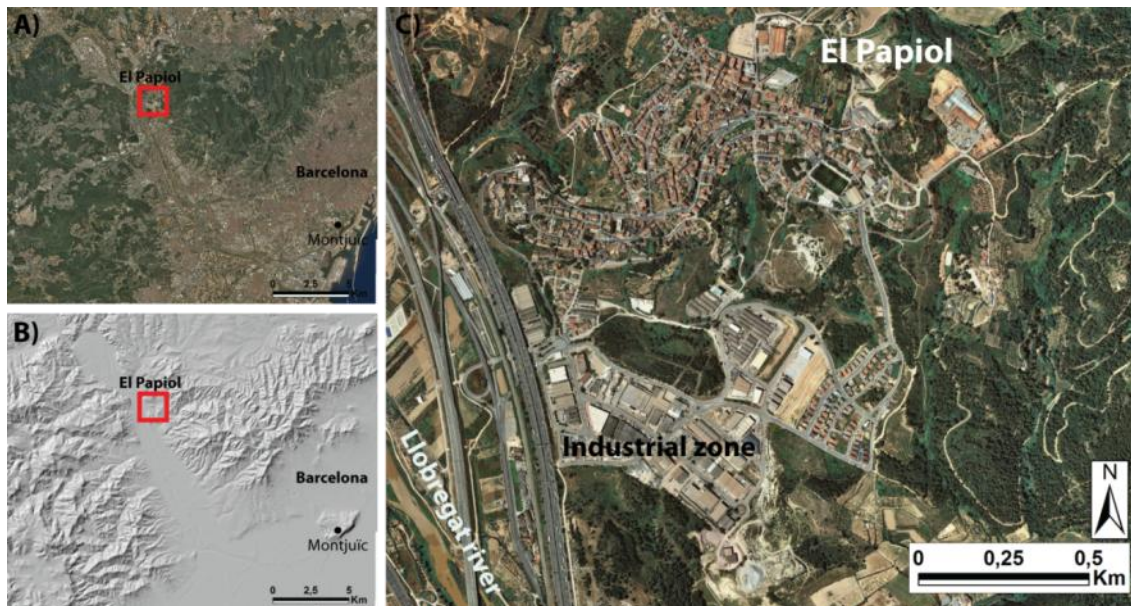
Figure 42. Geographic position of El Papiol.

The area of El Papiol shows a geological setting where the marine and fluvial pliocenic sediments are prevalent (Figure 43). In particular on the valley floor, near to the industrial area, the subsoil is characterized by very plastic clays whereas the main part of the village is built on an older sandstone formation, on which the aforementioned landslides have occurred.
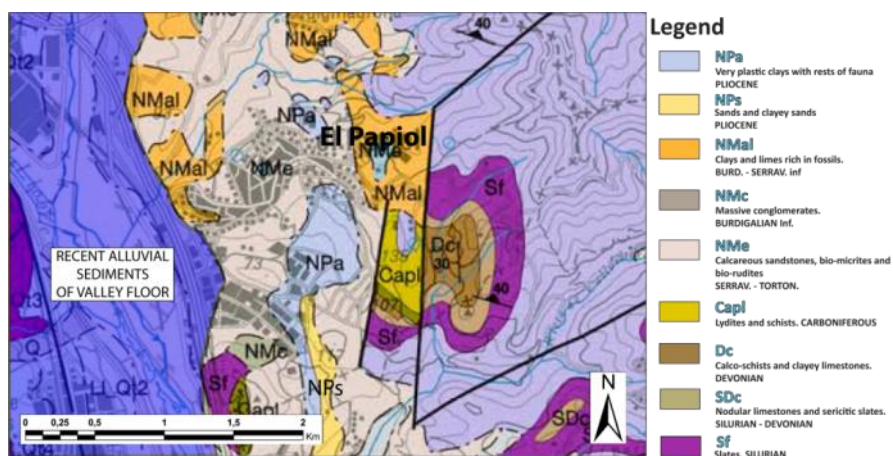
Figure 43. Geological setting of EL Papiol. Extract from the Geological Map of Catalunya 1:50.000

The processing of TerraSAR-X data have allowed to delimit four main areas affected by slope processes (Figure 44), the negative velocity values are movements on direction away from the satellite whereas the positive ones have a strong component toward the satellite LOS.

Taking into account the morphological features of the slopes, the damages distribution and the velocity values measured by the PSs the phenomena have been delimited and characterized with an average velocity value.

The industrial area placed on the valley floor is affected by an uplift with displacement ratios up to 8-9 mm/year, that could be due to the swelling of the underlying plastic clays resulting from a suspension of underground water extraction.
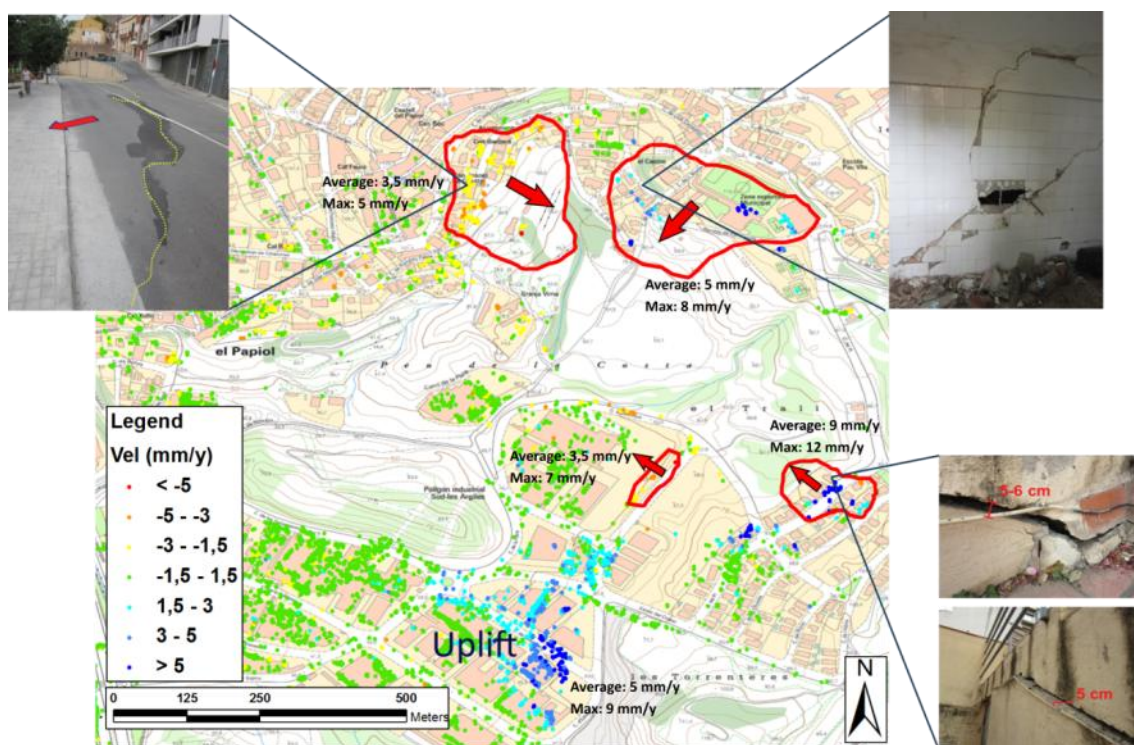
Figure 44. Slope processes delimited on the village of El Papiol. The pictured were taken during a field survey when diffuse damages to the buildings and roads have been detected.

In the other four areas diffuse damages to the buildings and roads have been detected during the validation field survey (Figure 44).

Luca Tanteri — *"Integration of Remote-Sensing techniques and geomorphological analysis for the characterization and mapping of ground instability at regional scale"*

4.1.2. Montjuïc

Barcelona's Montjuïc is a broad shallow hill (height 184,8 m) with a relatively flat top overlooking the harbour, to the southwest of the city centre.

The eastern side of the hill is almost a sheer cliff, giving it a commanding view over the city's harbour immediately below.

From a geological point of view Montjuïc represent an "island" among the surrounding areas, that are characterized by recent alluvial sediments, mainly of the Llobregat river delta in the southern part and other minor streams coming from the surrounding hills (Serra de Collserola) in the northern part.
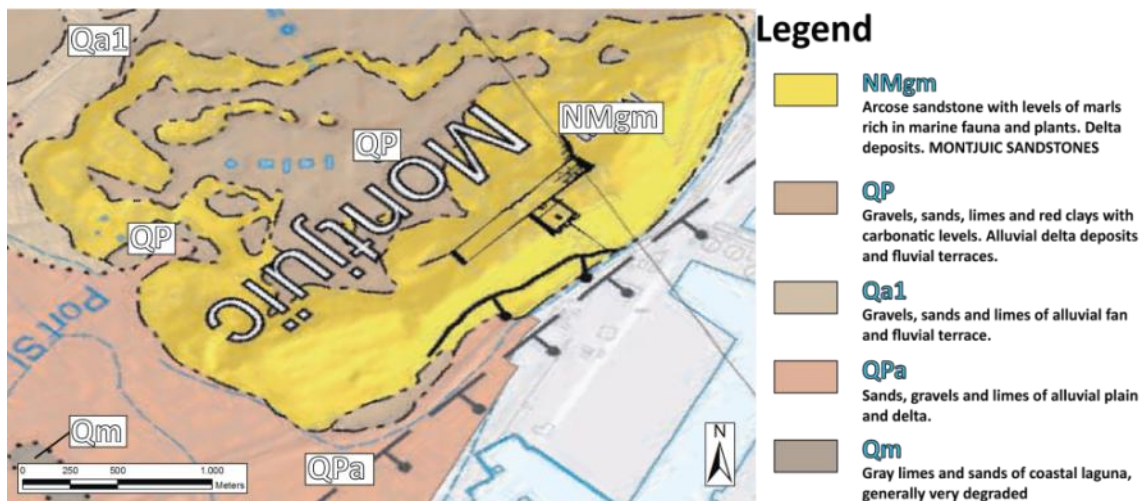
Figure 45. Extract of the 1:25.000 geological map of the area of Barcelona (IGC, 2010; www.igc.cat)

The lithology of the hill is characteristic and different from the surrounding reliefs like Serra de Collserola, the hills of Monterols, El Putget and El Carmel i la Rovira, that are composed by metamorphic rocks and sandstones of the Paleozoic age (between 500 and 300 millions of year). In fact Montjuïc is composed by more recent (Neogenic) sedimentary rocks (Figure 45), in particular Miocenic arcose sandstones with levels of marls with abundant fossils of marine fauna and plants, locally covered by more recent fluvial terrace deposits.

Due to this lithological setting and composition an intense mining activity have been performed until the early seventies of '900 with the development of many sandstone quarries, some of which visible even now, that have been for a long time the main source of building material of the city (Figure 46).

Figure 46. Montjuïc quarry "El Pantano" an historical picture (left) and present appearance (right)

By analysing the SAR data several areas with remarkable surface displacement have been detected on the hill, in particular near Palau Sant Jordi and the Pèrez de Rozas baseball stadium, structures built on the occasion of the 1992 Olympic Games, and on the east side in correspondence with the area of Jardins de Costa i Llobera (Figure 47).
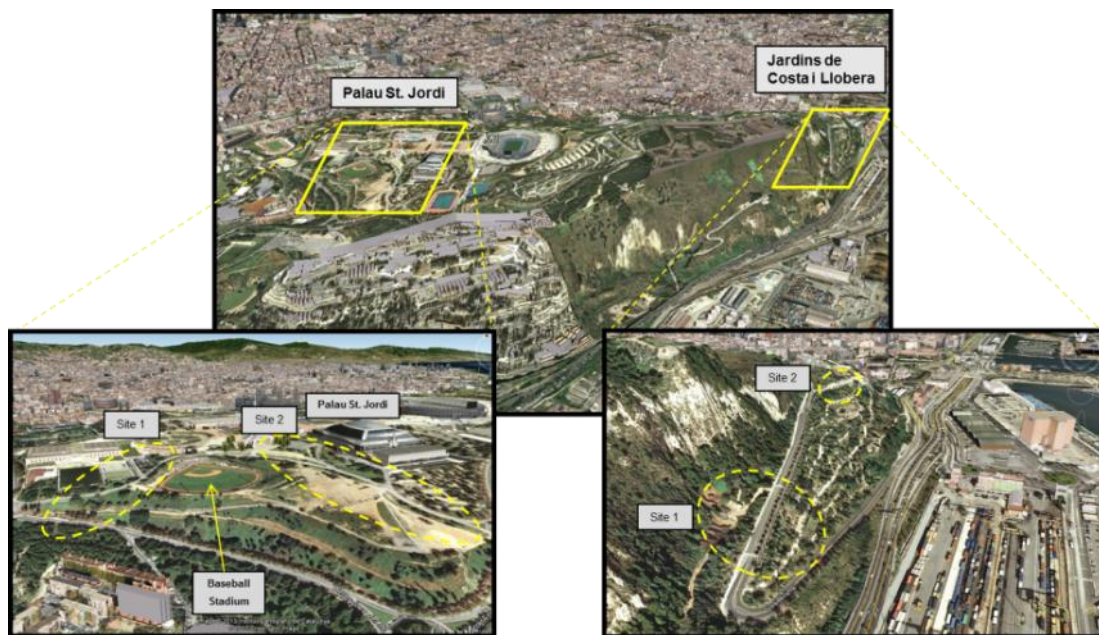
Figure 47. Perspective images of the hill of Montjuïc with focus on the areas of Palau St. Jordi (low left) and Jardins de Costa i Llobera (low right)

In such areas an accurate exam on the SAR data has highlighted displacements with velocity values up to several millimetres per year, measured along the Line-Of-Sight (LOS) of the satellite, and in direction away from the satellite (orange and reddish points in Figure 48).
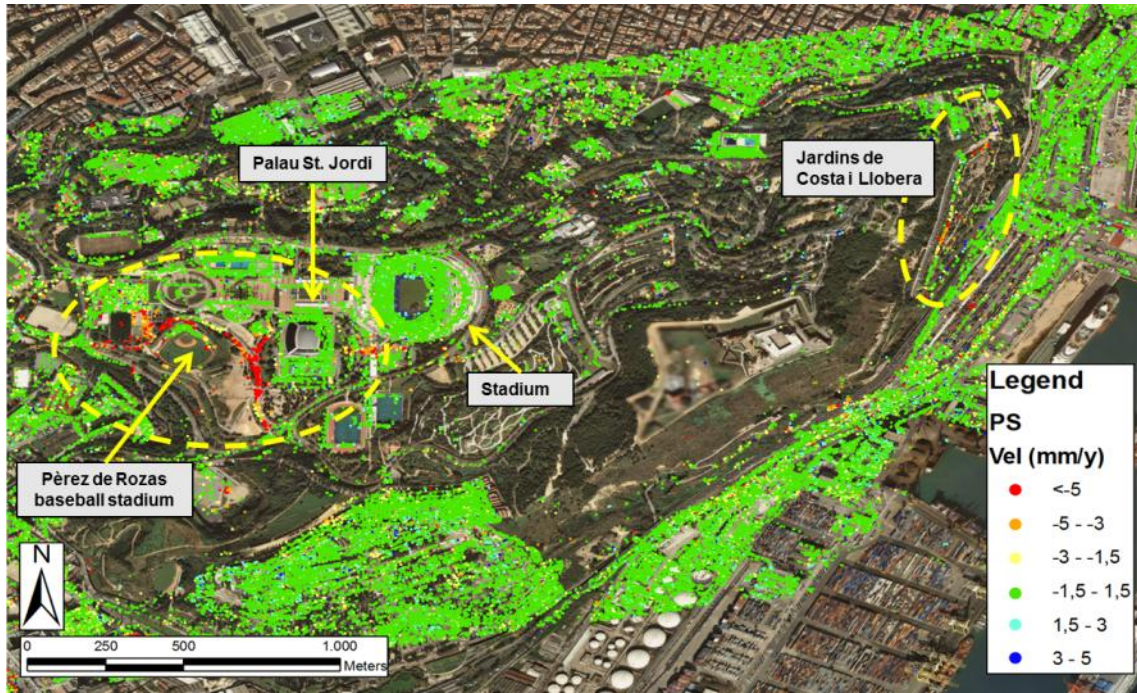
Figure 48. Geocoded velocity map obtained by processing TerraSAR-X imagery on the area of Montjuïc.

Area near Palau St. Jordi

In the area next to Palau St. Jordi, LOS velocity values up to 12 mm/yr have been measured along the satellite LOS by the PSs, highlighting a complex deformation pattern that interests all the area surrounding the Pèrez de Rozas baseball stadium (Figure 49).

Given that the general slope angle of the area is less than 4°(Figure 49) the observed deformation could be in principle due to a landslide or a subsidence phenomenon. The cause of these deformation cannot be determined by only using the PSI because they only provide deformation along the LOS direction.

In addition, the morphological features of the area did not help to evaluate if the displacement are related to a landslide (strongest horizontal component of the movement) or to a local subsidence phenomenon (mainly vertical displacement).
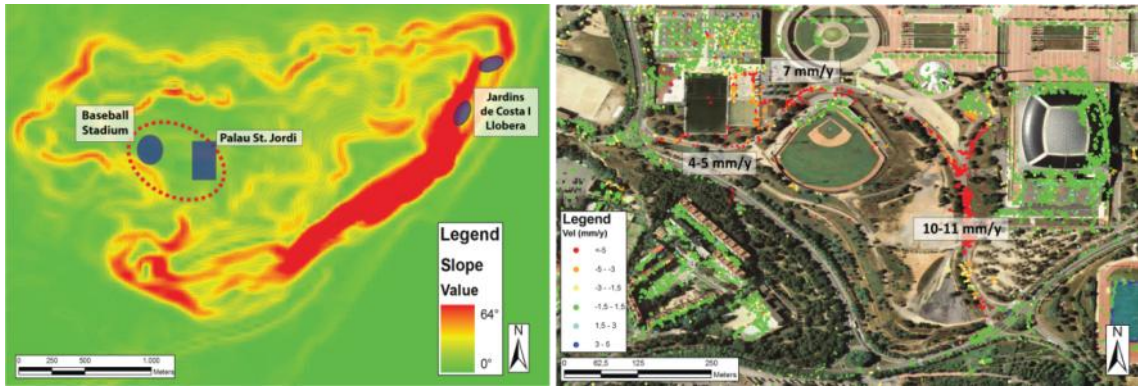
Figure 49. Slope map of the hill of Montjuïc (left) and focus on the PSI velocity values on the area of Palau St.Jordi and Pèrez De Rozas baseball stadium (right).

We needed further informations in order to establish what kind of phenomenon is at the base of these surface displacements.

For this purpose a field survey has been performed both to validate the results of the PSI processing and to assess the real state of activity and extent of the deformation.
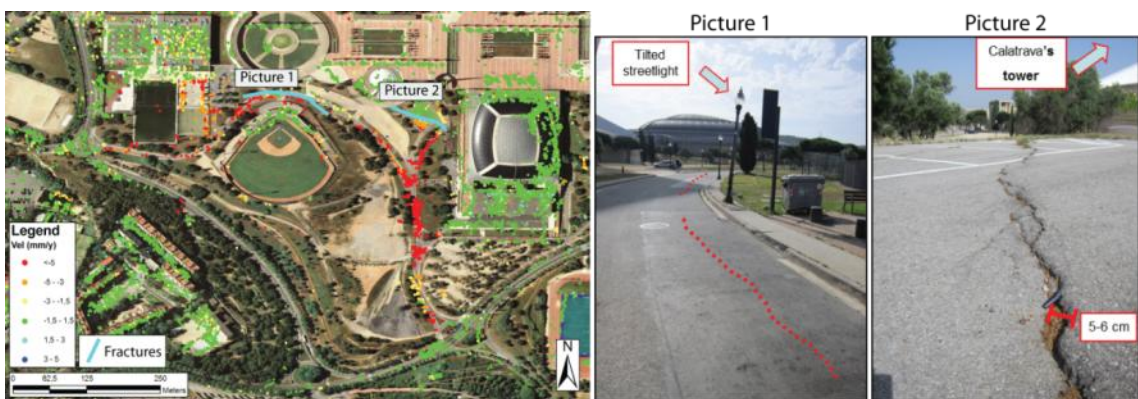
Figure 50. Focus on the velocity values measured with the PSs on the area at west of Palau St.Jordi with location and pictures of two fracture systems detected during the field survey.

During the field survey two main fracture systems have been detected on the asphalt as shown in Figure 50, that indicate a ground displacement directly downline of the area. Such fracture systems follow perfectly the limit between the moving and the stable PSs areas.

By collecting hystorical data and imagery the area, it has been discovered that it was occupied by a sandstone quarry called Cantera Mussol, active until middle '900 (Figure 51). Subsequently it began to be refilled by garbage becoming the main dump of the city until 1971, when intense rainfall event literally generated a garbage landslide that seriously affected the little borough of Can Clos (Castillo I., 2011). The dump was closed and totally refilled only in 1974 and today the area is occupied by some of the most important structures built for the 1992 Olympic Games.
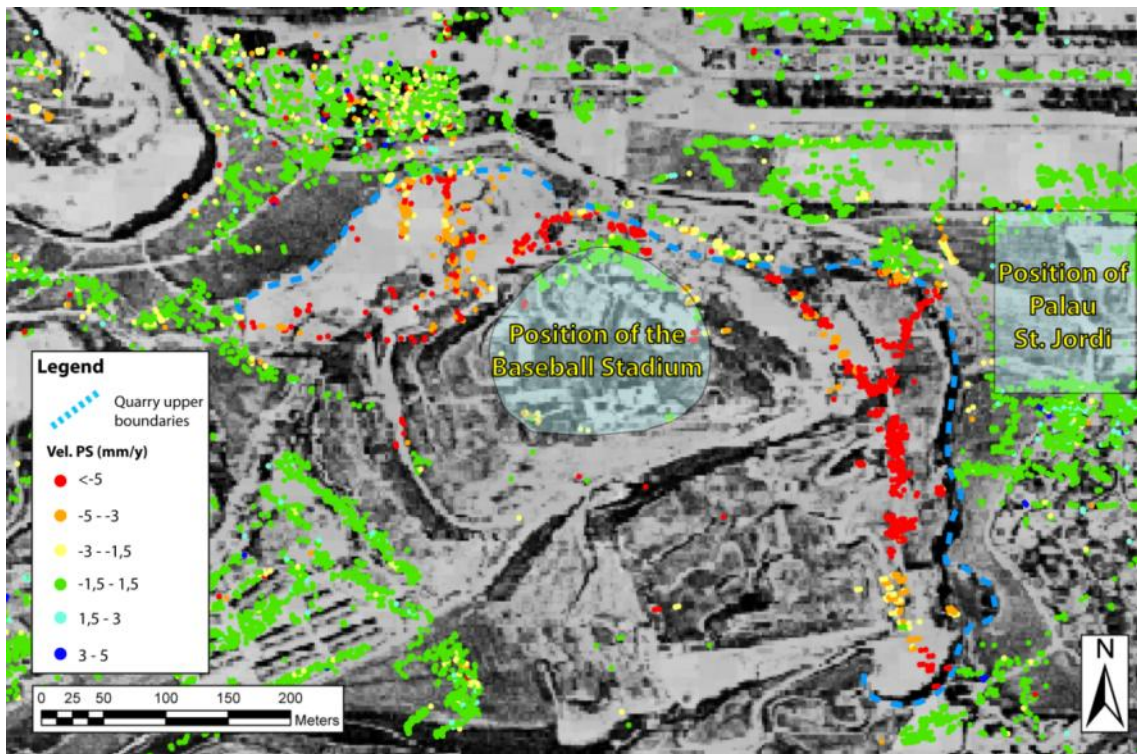
Figure 51. A 1956 ortophoto of the area of the quarries. In the picture the quarry boundaries are drawn in order to highlight the perfect spatial correspondence between the moving area detected by the PSs and and the location of the old mines. To facilitate the interpretation the positions of Palau St. Jordi and the baseball stadium are indicated (source: Diputaciò de Barcelona, WMS service).

As shown in Figure 51, the quarry boundaries, drawn from the ortophoto of 1956, perfectly delimit the area characterised by remarkable PSI displacements.

Therefore, these displacements can be interpreted as a result of the garbage and landfill compaction that originate diffuse ground movements mainly in the vertical direction.

The velocity values are generally higher next to the quarry boundaries, where the thickness of the landfill is likely greater and the compaction phenomenon is more evident.

The bleachers of the baseball stadium are almost completely stable, probably due to their foundation that lie directly on the underlying bedrock.

Jardins de Costa I Llobera

In the area of Jardins de Costa i Llobera evidences of superficial displacements have been detected in two sites (Figure 52).
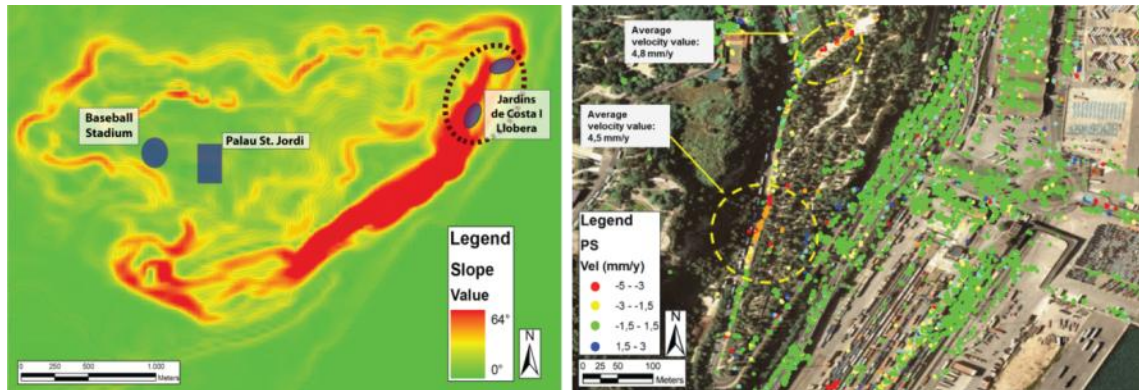
Figure 52. Slope map of the hill of Montjuïc (left) and focus on the PSI velocity values on the area of Jardins de Costa i Llobera (right).

The first one (the lower in the right box of Figure 52 near the gardens) interests the Carretera Miramar and a portion fo the underlying gardens. The average LOS velocity values are around 4-5 mm/yr measured along the LOS of the satellite but unfortunately the presence of a dense vegetation did not allow to increase the density of PSI points in the area of the gardens, but only on the road.

The second site (the upper in the right box of Figure 52) is placed in the vicinity of a small car park next to the entrance of the tunnel on Carretera Miramar. In this site the measured velocities are around 4,8 mm/y.

It is worth to underline that the displacement direction in this side of the hill is particularly favourable to be detected by a satellite with a polar orbit like TerraSAR-X, indeed in this case the velocity values could be considered as very near to the real ones.

Figure 53. View of the outcrop of sandstone deposits on the east side of Montjuïc, above the Jardins de Costa I Llobera.

This side of Montjuïc is characterized by a rocky cliff (Figure 53) and an underlying steep slope where the gardens are located. As seen during a field survey performed in June 2013, the cliff is a wide outcrop of weakly consolidated sandstones, sands and clays, whose rockfall sediment have originated a large deposit at the foot. Furthermore, in some parts of the cliff, quarry activities have took place in the past, whose waste materials have contributed to increase the thickness of the deposits at the foot.

Even though during the field survey no evident damages have been detected neither on the road floor nor on the sidewalk, on the basis of geological and geomorphological setting of the slope it's clear that those two landslides involve those instable slope deposits, which are moving with an extremely low deformation rate (Cruden & Varnes, 1996).

4.1.3. Subsidences in Barcelona

The available TerraSAR-X data have allowed to detect some local subsidence phenomena that occurred in Barcelona during the satellite acquisition time (2007-2009).
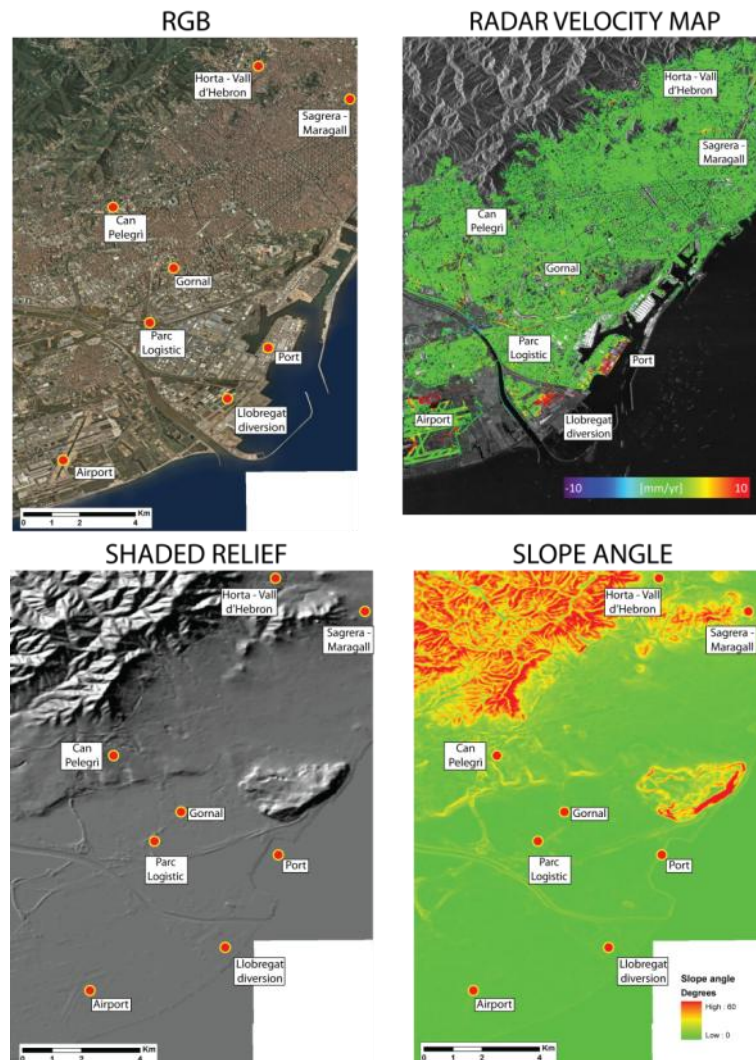
Figure 54. Subsidences in the urban area of Barcelona. The topography of the area is shown by the *shaded relief* and the *slope* map (bottom left and right).

In Figure 54 some *hotspots* are visible and have been chosen to be studied for their importance for the safety of the city.

In the urban area of Barcelona, the analysis of the velocity map obtained by the interferometric analysis of the TerraSAR-x images have highlighted 8 spots where significant ground deformations were ongoing during the acquisition period.

This analysis have been very important in order to point out how some human activities, contrary to the collective imaginary, can imperceptibly but deeply modify the environment, generating risk conditions especially in densely populated urban areas.

Due to the gentle and flat topography of the urban area (except Montjuic), almost the detected ground motions have been easily classified as subsidence, relative to underground works for the achievement of new lines of the Tube, underground water exploitation and some other local causes.

The capability of the Satellite SAR *remote-sensing* technique to detect millimetric displacements have proven itself as a perfect tool to monitor and map areas affected by slow ground motions that can cause serious injuries to the building and structures on the surface, generating potential situations of risk.

As mentioned previously, the city of Barcelona , in its majority, is placed on a flat territory characterized by fluvial sediments related to all the river streams that runs from the Collserola mountain ridge to the Llobregat river delta.

The underground geological setting of the city is therefore characterized by a complex pattern of *paleo-* and recent riverbeds, in many instances occupied by roads (the *Ramblas*) or obliterated by buildings and structures.

This complex system and the intrinsic high permeability of fluvial sediments represent an ideal condition for the development of a dense sub-surface flow net and potentially exploitable aquifers.

The underground water exploitation is one of the most common causes of subsidence in flat areas and valley floors, as a consequence of the compaction of the sediments due to the removal of the internal water.

Here, in addition to the exploitation for the water supply and the aqueduct/network one other cause of sub-surface drainage is tunnel excavation: indeed one of the main problems of this kind of works is seepage, that can considerably weaken the sides and face of the gallery (Lee *et al.,* 1992).

The groundwater flow passing through soil grains occurs in response to an energy gradient and a measure of this gradient is provided by the difference in hydraulic head (Freeze and Cherry, 1979). When a tunnel is excavated below the groundwater level, the groundwater flows into the excavated surface of the tunnel and there exists a difference in hydraulic head around the tunnel (Lee & Nam, 2004).

In the whole, 8 areas affected by significant subsidence motions have been detected; some of them related to the underground works for the new tube lines L5 and L9 and some others related to other causes such as underground water exploitation or soil compaction due to superficial weights.

In particular the areas are:

1. The airport of El Prat de Llobregat

2. An area next to the new Llobregat river mouth

3. A new industrial unit called Parc Logistic

4. The area around the new underground station Gornal (line L9)

5. An new embankment area near the harbor

6. The district of Can Pelegrì

7. The new section underground line L9, between the stations Sagrera and Maragall

8. The new section underground line L5, between the stations Horta and Vall d'Hebron.

In some of these areas a further densification of PSs have been performed modifying the setting values in the *reordering* and *geocoding* processes.

In that case a set with an higher number of PSs have been obtained, starting from the *linear velocity* map, by lowering the *gamma* threshold in the *reordering* process and performing again the *integration* and *geocoding steps.* In this way an higher number of edges (even with a lower *gamma* value) are considered in the reconstruction of *te* and v for each pixel.

Furthermore an accurate exam of some selected interferograms have been carried out in order to try to reconstruct the general evolution of the ground deformation.

Since only data acquired in ascending orbit were available, a combination of the velocity vectors (as shown in paragraph 3.1.3) in both the acquisition geometries is impossible.

In order to solve this problem, the ground motions in these areas have been assumed as vertical due to the flat topography. Hence the measured velocity vectors in each point, parallel to the sar line of sight, have been projected on the vertical plane, solving the same system of equation utilised for Tuscany (riferimento alla formula) but assuming that the component V_{EW} is equal to zero, obtaining:

$$V_a = V_V \cos\theta_a \qquad (15)$$

where θ_a = 35,5°.

An analysis of the temporal and spatial evolution of some areas have been carried out by comparing interferograms related to progressively larger time interval and computed using images with short geometric baselines.

This because the larger is the baseline value and the larger will be the contribution of ground topography on the deformation measured by the interferometric pairs.

In general the 8 subsidences are related to two main causes: underground works for the extension of the metropolitan train network and ground settlement due to the weight of new structures on the surface.

Some interesting results are shown below.

Metro excavation: Sagrera-Maragall

Some of the subsidence areas in Barcelona, highlighted by the velocity map, are placed where there were active underground works during the acquisition time.

Barcelona has a very efficient underground railway network that, at the moment, is still growing. In particular the works carried out during the satellite acquisition time, concern a new section of the pre-existing line 5 (L5) and the construction of a new important line that connect the north-eastern part with the south-western: line 9 (L9).

In these areas, significant ground displacement have affected the surface according to the progresses of underground excavation works.

In some of these areas the available PSs have been densified in order to have available an higher number of points with a better spatial coverage.

The area in correspondence of the new line L9, between the stations of Sagrera and Maragall is placed in the northern part of the city, in a densely built-up area (Figure 55).

Figure 55. Position of the area of Sagrera-Maragall in the urban area of Barcelona.

83

The PS data resulted very useful to delimit the ground motion area that corresponds to the path of the new metro line 9. The processed dataset has given a satisfying points density that has highlighted the extent of the area (Figure 56)
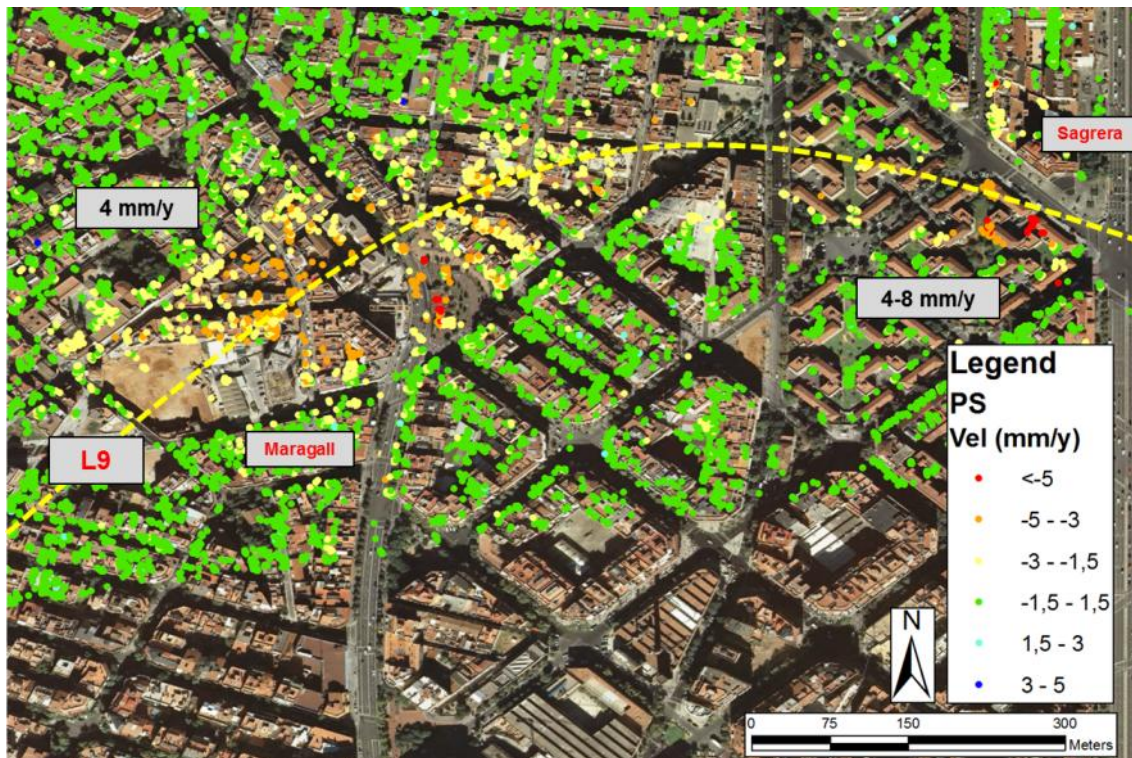
Figure 56. Geocoded PSs on the subsidence area in correspondence of the Metro line L9, between Sagrera and Maragall.

The overall deformation pattern measured during the entire time of acquisition shows two large areas where the subsidence phenomenon reach velocity values that range between 4 and 8 mm/y, the one in proximity of Maragall station and the other in Sagrera.

In particular, in the first one, the measured values are around 4 mm/y, so slightly lower than the 7-8 mm/y measured in Sagrera, but the area interested by deformation near Maragall is wider than the other.

The two hotspots are connected by a belt in which the velocity values are diffusely above 3 mm/y, that runs in correspondence to the underground path of line 9.

The area affected by subsidence is located on the path of the new reach of the metro line L9. The deformation is therefore due to the tunneling works.

Several interferograms obtained by the satellite images have been examined in order to better characterize the temporal evolution of the deformation. For this purpose only the interferometric couples with normal baseline extremely short (<40m) have been taken into account.

In addition to a general study on interferograms that cover the entire acquisition time two further analyses have been carried out separately for the years 2008 and 2009, in order to understand the temporal evolution of the deformation (Figure 57).
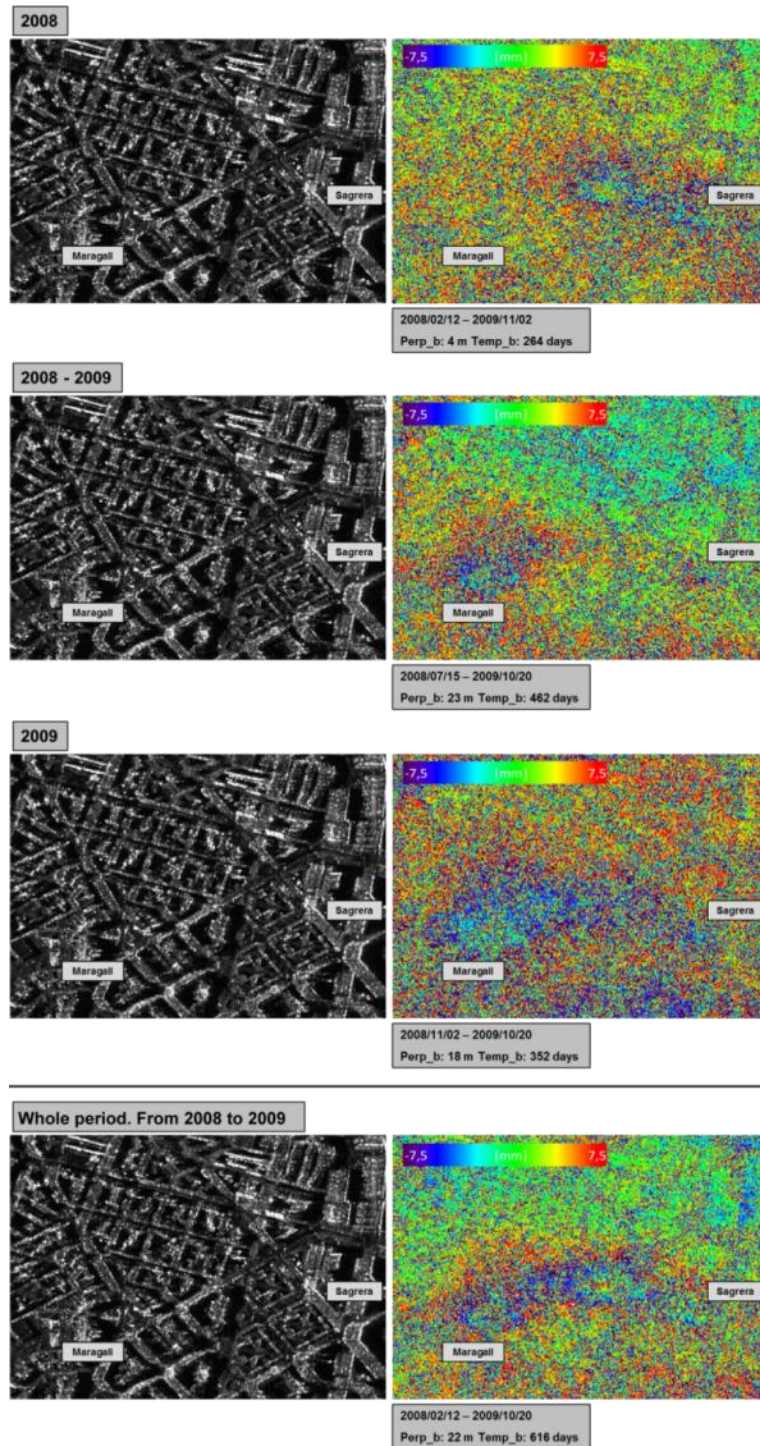
Figure 57. Subsidence on the Metro line L9 between Sagrera and Maragall: interferogram analysis.
The interferogram analysis was carried out only in the area where the subsidence phenomenon was highlighted by the PS data.

The interferograms show a "belt-shaped" area between the two underground stations of Sagrera and Maragall, corresponding to the two areas of maximum displacement in the deformation map.

In addition to a general analysis of interferograms that cover the entire period of observations, further analyses were carried out independently for the years 2008 and 2009, and the period between the two years, in order to understand the temporal evolution of the deformation.

Figure 57 shows some selected interferogram in wich the temporal evolution is particularly clear, separately for the year 2008, for a period of 462 days between 2008 and 2009, an interferogram of 352 days within the year 2009 and an interferogram that covers the entire acquisition period.

The maximum measurable displacement is ≈15 mm, value that is a half of the wavelenght used by the TerraSAR-X antenna (≈31 mm), for this reason the colorbar associated to a complete fringe cycle, ranges between -7,5 and 7,5 mm.

Unfortunately all the interferograms were considerably affected by atmospheric noise and in some cases the too large normal baseline value have made a minimum topographic contribution visible along with the real deformation.

However the results show that at the beginning of 2008 the displacement was exclusively in correspondence of the Sagrera station, subsequently it progressively moved towards Maragall at the end of 2008 and January 2009. The displacements were solely detected around Maragall station during the last months of 2009.

The displacement values visible on the interferograms are perfectly compatible with those measured with the PS technique.

Airport El Prat

The area is placed directly on the Lobregat river delta and the hydrogeological setting of the area is almost completely characterized by fluvial sediments of delta system (Figure 58), with the exception of the area near the coastline occupied by litoral sands. Furthermore, the construction of the airport have severely modified the surface drainage system that was composed by a complex fluvial channel network.
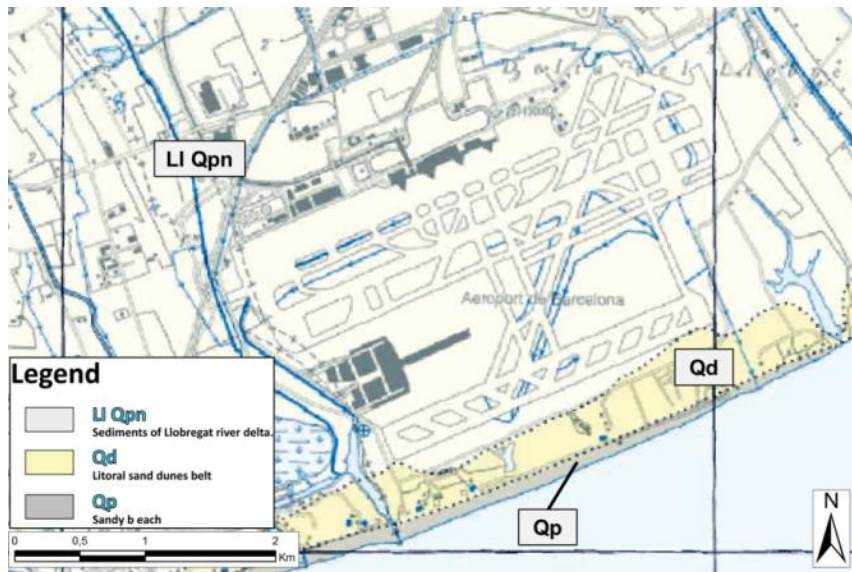
Figure 58. Geological setting of the airport area.

The airport El Prat de Llobregat is affected by diffuse vertical displacements, concentrated in 4 main zones (Figure 59).

The velocity values measured by the PS indicate evident deformations around the terminals (zones 1 and 2), outside of the landing area, where the control tower is placed (zone 3) and directly on the landing stripes (zone 4).
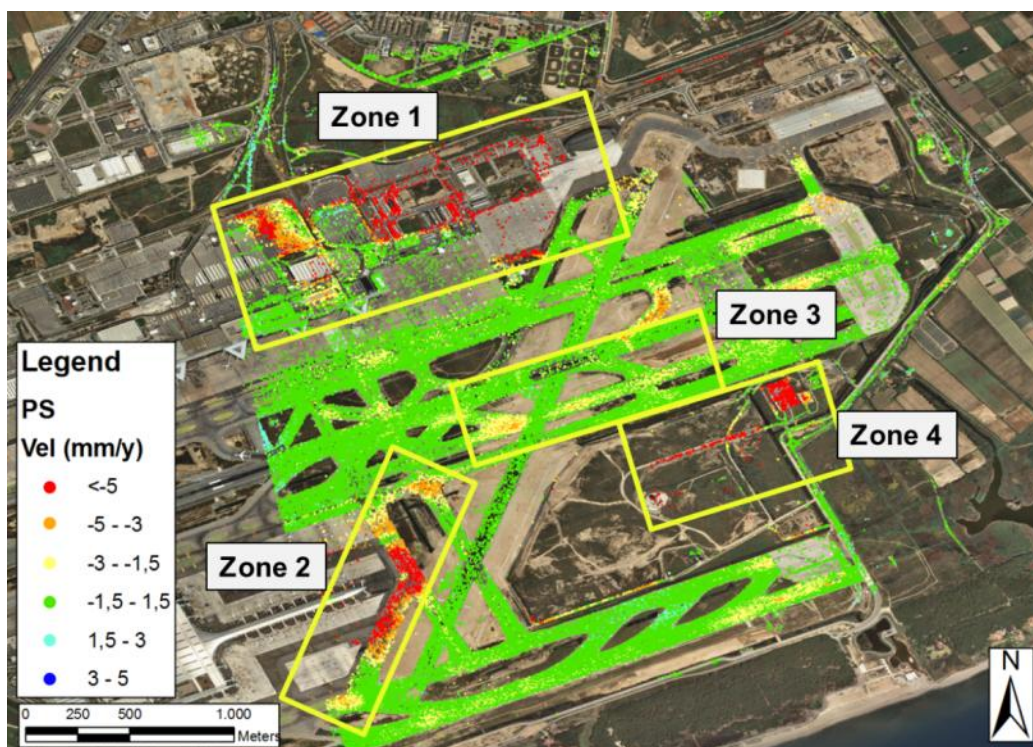
Figure 59. Geocoded PSs on the area of El Prat airport.

The Zone 1 is characterized by a complex superficial deformation pattern.

The velocity map shows values up to 11-12 mm/y in correspondence with some areas on which new structures have been built recently.

The extremely complex distribution of the areas in deformation and the lack of further informations about the subsoil structure and the underground water pattern, do not allow to establish the exact causes of the displacement.

Most likely the subsidences could locally be due to the presence of wells where remarkable quantity of water have been pumped out during the acquisition time.

The Zone 2 is characterized by a wide area in deformation that surrounds the recently built Terminal 1 of the airport (Figure 60).
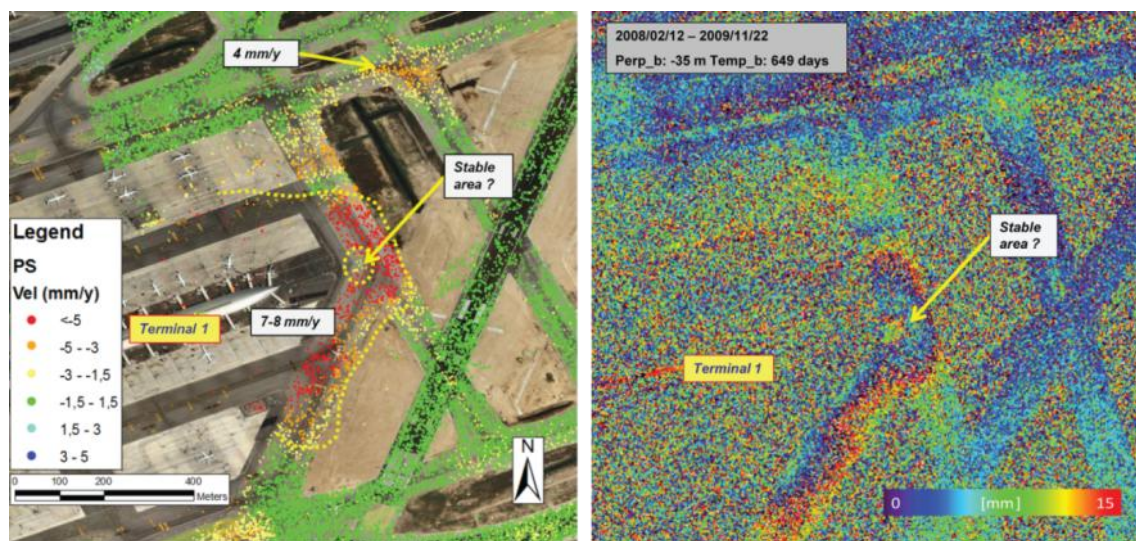
Figure 60. Zoom of the zone 1, near the recently built Terminal 1. The left box shows the geocoded velocities obtained by the TerraSAR-X data and the right box a two-years interferogram covering the area.

Initially 4 hypotesis have been advanced:

1. Aquifer exploitation
2. Weight of the new Terminal
3. Weight of the aircrafts
4. Combination of 2 and 3

After an accurate exam of the distribution of the velocity indicated by the PSs the fourth hypotesis have been considered as the most likely.

The deformative contribution related to the weight of the aircraft is evident analyzing the deformation pattern, that shows the major values on the center of the strip where all the aircrafts pass and stand.

Luca Tanteri — "Integration of Remote-Sensing techniques and geomorphological analysis for the characterization and mapping of ground instability at regional scale"

Furthermore, a non-moving spot (stable area in Figure 60) is visible at the center of the area, highlighting the fact that the phenomenon does not consist in an uniform subsidence zone centered on the terminal but rather in a deformation situated on the stripes.

The average weight of the aircrafts (±80 tons) is probably sufficient to produce such deformation rates on the asphalt.

This hypotesis is confirmed by the exam of the zone 3, in which some areas affected by subsidence, located in the central part of the stripes, show a very peculiar shape and deformation pattern.

As supposed for the Zone 2 here the effects of the weight of the aircrafts on the asphalt are clearly visible (Figure 61).

Indeed, in all of those areas, the velocity values increase progressively from near zero (at the borders of the stripes) to the maximum values in the center.

Obviously this effect is not visible in all the landing stripes of the airport due to the periodic replacement of the asphalt, performed for maintenance and to the differential subsoil resistance properties.

Furthermore the areas with older asphalt have been proved as more affected by displacement as well as the areas where the aircraft usually stand or move at "crowling speed".

Figure 61. Zoom of the zone 3 showing deformation detected on the landing stripes.

The Zone 4 is still almost free from great structures and characterized by grassland, for this reason, it has not been possible to process a satisfying number of PS (Figure 62).
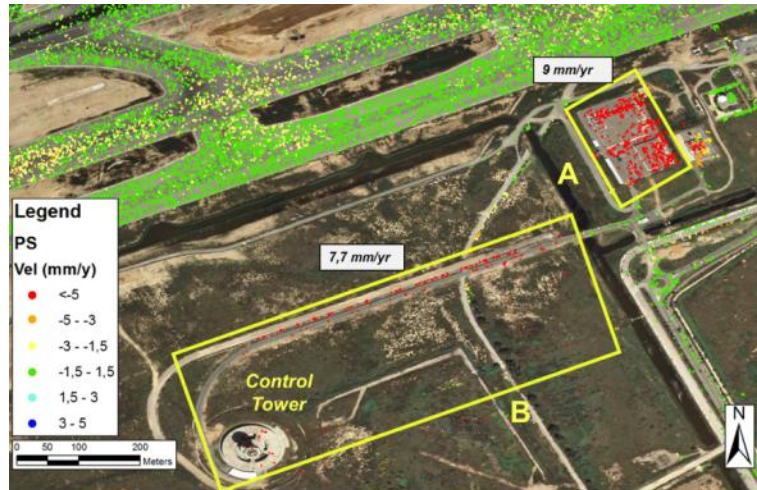
Figure 62. Zoom of the zone 4 showing deformation in the vicinity of the control tower.

Through a general overview of the zone, two micro-areas affected by subsidence are visible:

- Micro-area A: with velocity up to 9 mm/y measured along the LOS. In this area the deformation is likely due to the weight of the buildings, together with a probable presence and activity of wells for the water supply.

- Micro-area B: with velocity up to 7,7 mm/y measured along the LOS. In this area is situated the control tower of the airport and, likely, the subsidence phenomenon have the same causes that the micro-area A. Nevertheless, for the presence of the control tower, could worth to conduct some further analyses.

Unfortunately it has been impossible to detect the displacement on the interferograms, due to the low coherence and the high noise in the area.

4.2. Mapping slow kinematic processes using ERS and ENVISAT data: Tuscany

4.2.1. Tuscany Landslide Inventory

During the research programme the landslide inventory map of the Tuscany region have been updated, integrating available ancillary data and ERS/ENVISAT PS data with the procedure illustrated in paragraph 3.1.3 .

The new landslide inventory have been developed in *shapefile* format and is similar to the original one, with new fields in the attribute table (see appendix 1), related to the modifications applied to each polygon.
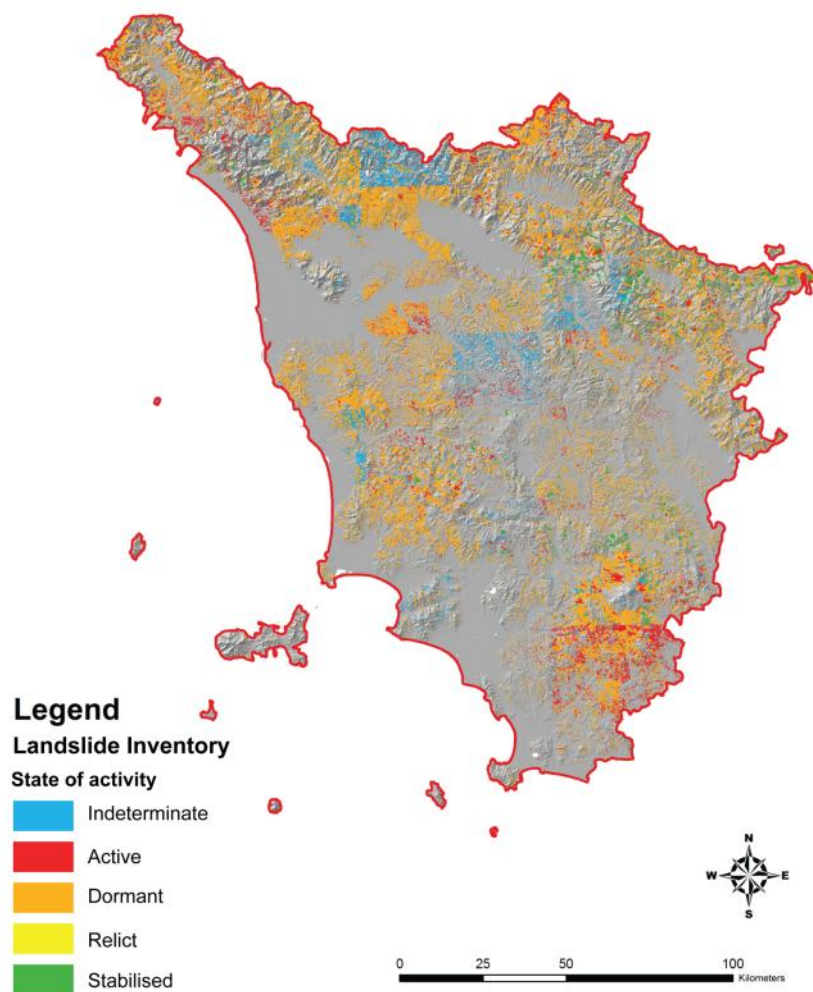
Figure 63. The new Tuscany Landslide Inventory in *shapefile* format. The polygons are coloured on the base of the landslides state of activity.

91

Figure 63 shows the Tuscany landslide inventory map, in which all the phenomena have been delimited with a polygon and classified on the base of the state of activity.

The work have involved the whole regional area (22.988,1 Km^2) and had leaded to the final census of 91.730 landslides.
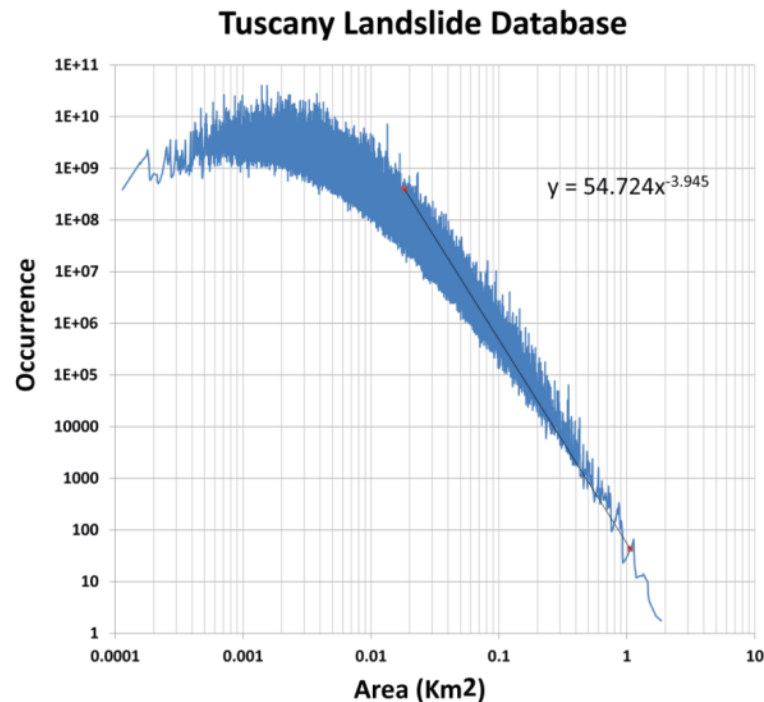
Figure 64. Frequency/area distribution of the new inventory.

Figure 64 shows the frequency/area distribution of all the landslides contained in the inventory.

The distribution shows the extremely wide range of landslide dimension, highlighted by a very low negative exponent (-3,945) of the decaying power-law of the distribution (Malamud *et al.*, 2004; Van Den Eeckhaut *et al.*, 2007; Guzzetti *et al.*, 2002). This value is rather high but comparable with the majority of the historical inventories at regional scale (Van Den Eeckhaut *et al.*, 2007) which are characterized by an extreme variability in landslide dimensions and type. The distribution of the state of activity of landslides, referring to the number and their areal extension, is showed in Figure 65. In this figure is related in detail the information about that distributions evaluated on the inventory before (Pre-) and after (Post-) the update.

Landslides state of activity in Tuscany
Number of landslides

	Number of landslides		Percentage	
	Pre-	Post-	Pre-	Post-
Indeterminate	8477	7927	9.3%	8.6%
Dormant	68821	69116	75.3%	75.3%
Stabilised	2024	1964	2.2%	2.1%
Active	12048	12720	13.2%	13.9%
Relict	2	2	0.0%	0.0%

Landslides state of activity in Tuscany
Landslides area

	Landslide area (Km^2)		Areal Percentage	
	Pre-	Post-	Pre-	Post-
Indeterminate	174	142.8	8.3%	6.8%
Dormant	1576.7	1578.4	75.0%	74.9%
Stabilised	169.5	146.3	8.1%	6.9%
Active	180.7	239.1	8.6%	11.3%
Relict	0.2	0.2	0.0%	0.0%

Figure 65. Distribution of the landslides state of activity in Tuscany

It worth to underline that in the final product there is a significant decrease in the number of landslides classified as indeterminate (from 8477 to 7927) and an increase of active ones (from 12048 to 12720). This demonstrates the effectiveness of the technique as a tool for the identification and characterization of ground movements.

No landslides of categories stabilized or relict have been added to the final inventory. The reason is that a landslide could be classified as stabilized when does not exist potential conditions to reactivate it and as relict when it was generated in different climatic condition from the present (Cruden & Varnes, 1996). Thus, the interferometric analysis itself is not sufficient to identify relict or stabilized landslides and therefore we can't leave aside the analyses of further data or the inspections aimed to the identification of phenomena belonging to these categories.

The state of activities of landslides classified as indeterminate have been changed in dormant or active only when PS technique has allowed to apply the matrix of activity shown in paragraph 3.1.3.

The multi-interferometric technique employed in this work had allowed to append information on the state of activities of 1940 landslides. As pointed out in Figure 66, the 1,7% of the complete database of the total elements (equal to 1540 landslides) has been modified in one or more attributes and 0,4% (equal to 364 landslides) is newly identified.

The exploitation of the PS technique prove to be effective also in the confirmation of the attributes of the pre-existing landslides. The polygons who had confirmed the state of activity, after the examination of PS data inside of them, are 3654, equal to 4% of the total.

If we take account about polygons that fall in urbanized areas, the percentages of modified landslides with PS technique raise considerably (in Figure 66B). Particularly, considering 1845 elements falling in class 1 areas of 2006 CORINE LandCover map (developed in the venture of Fast Track Service on Land Monitoring, FTSP, of program Global Monitoring for Environment and Security, GMES), the percentage of modified landslides change from 1,7% to 11,8%, while newly identified landslides change from 0,4% to 2,8%. Finally the percentage of confirmed landslides change to 4% relative to the total to 24,4% relative to urbanized areas.
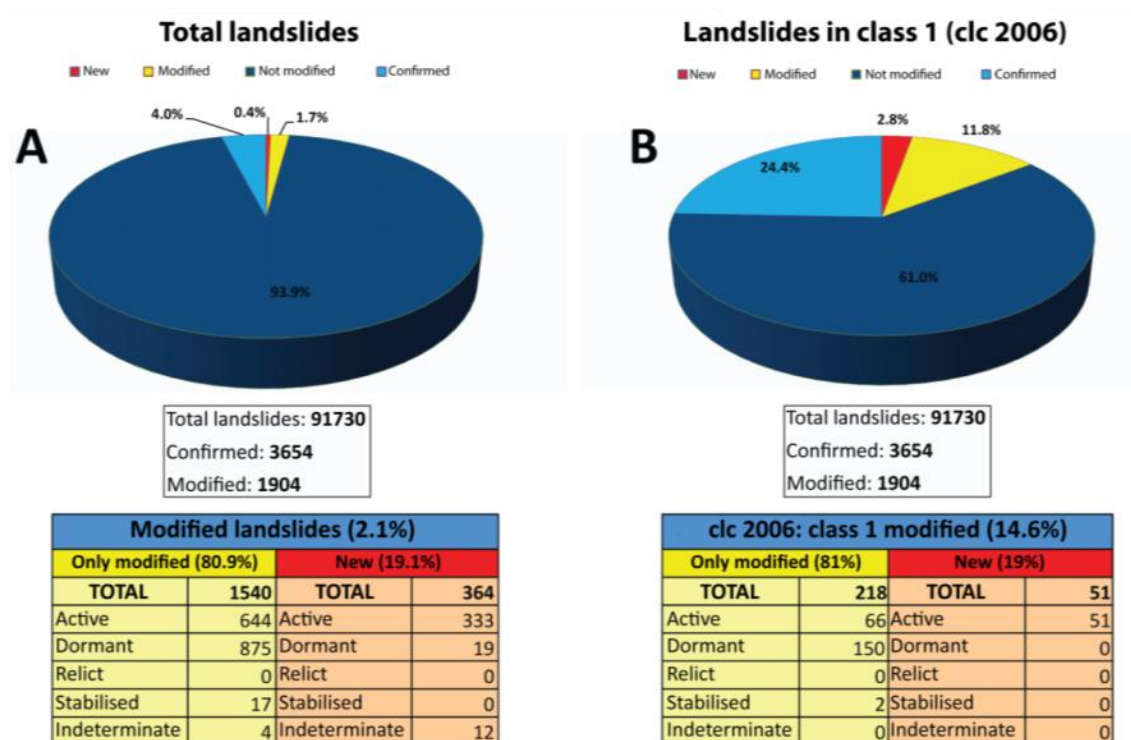
Figure 66. Modifications carried out considering the whole database (A) and considering only the phenomena that intersect areas classified in Class 1 in the map of CORINE Landcover Project (2006).

In summary the analysis of interferometric data has allowed to examine, to modify and to map about 6,1% of the total of landslides in the database and 39% of landslides that fall into class 1 of 2006 CLC.

Type of modification

All the modifications applied to the original landslide database have been reported in the attribute table of the polygon *shapefile*.

As shown in Figure 67 the modifications have been related to the perimeter boundaries of the landslides (p) the state of activity (a), the direction of movement (d) and the subdivision of a pre-existing polygon on the base of the available data.

All the polygons that derive entirely or partially from an already existing polygon are classified as partially modified "s".

MODIFIED POLYGONS		
New landslides	364	19.13%
s	67	3.52%
as	54	2.84%
a	943	49.61%
pas	27	1.42%
p	168	8.83%
ps	24	1.26%
d	13	0.58%
pa	131	6.88%
ds	5	0.26%
pd	8	0.42%
ad	11	0.58%
ads	24	1.26%
pds	6	0.32%
pad	9	0.47%
pads	11	0.58%
Only velocity	39	2.05%
Total	**1904**	**100%**

MODIFICATION CODE	
p	MOdified **perimeter**
a	Modified state of **activity**
d	Modified **direction**
s	Modified **partially** Part of a pre-existing polygon
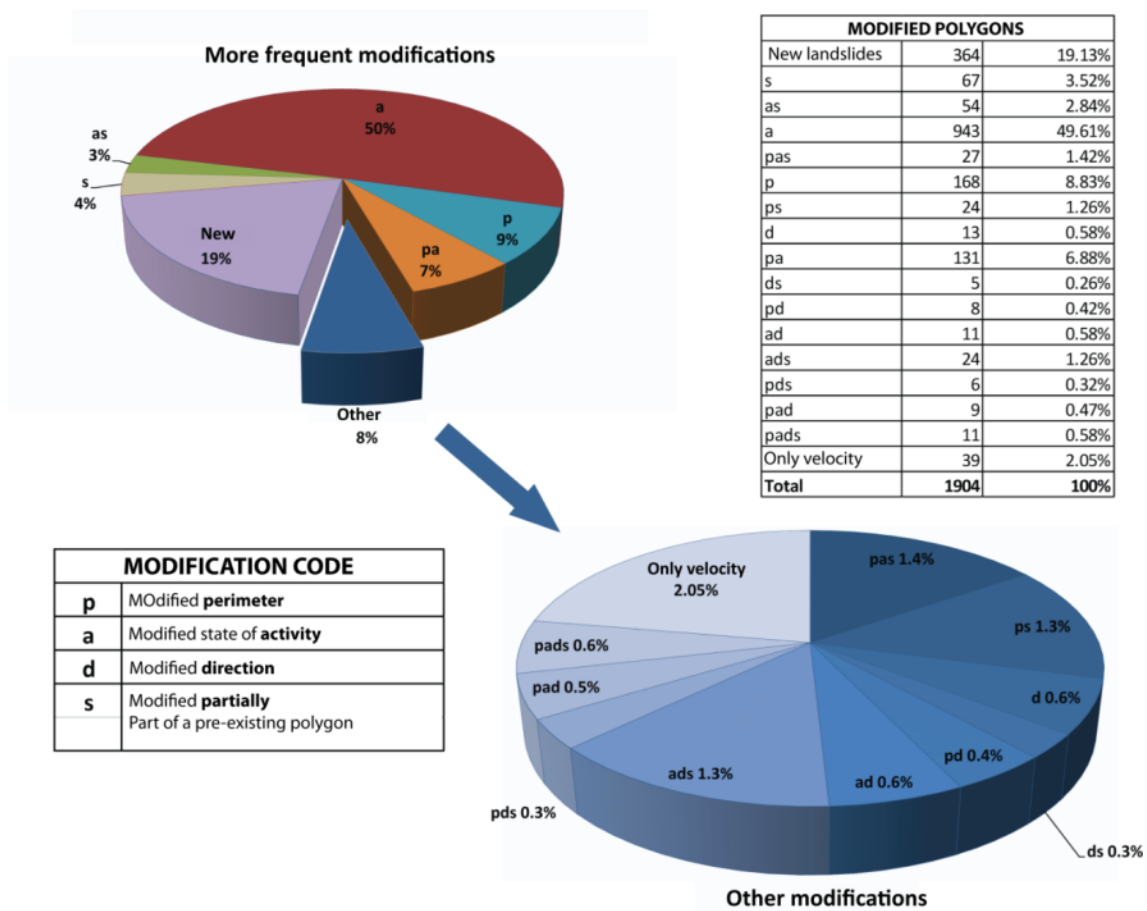
Figure 67. Modifications applied to the database polygons during the updating process.

Along with such categories, also the cases in which only the velocity value have been assigned to the polygons, without modifications other kind of modification.

As a whole, the modified polygons are 1903 and the distribution of the type of modifications is shown in Figure 67.

To about a half of the total number of modified polygons (51%) only the state of activity have been changed, whereas the 19% are new detected landslides, about the 9% of the polygons

have been re-delimited and the 7% have been modified in both their state of activity and perimeter.

In the pie chart bottom-right in Figure 67 the percentages of the less frequent modifications are shown, in the table at the top-right all the performed modifications are reported, both in terms of percentage and number.

The polygons with more than two different type of modification have lower percentages, due to the fact that PS from C-band satellites are not often adequately dense on the surface, not allowing a detailed and complete characterization with the only use of ancillary data.

Results at municipality scale

In the *Attribute Table* of the shapefiles the name of the municipality and the province where the landslide is placed have been associated to every polygon.

This has allowed to examine, at municipal scale both the distributions of the landslide phenomena and the relative modifications.

Table 3 shows some data of the municipalities with the higher number of modified polygons, in other words where the proposed approach have been more effective, but is only an extract of a table where the information about all the municipalities of the region are reported.

Table 3. Summary of some results at municipality scale

PROVINCE	MUNICIPALITY	N° landslides INITIAL	N° landslides FINAL	N° landslides MODIFIED	N° landslides NEW	Municipality area(km^2)	Landslide area (km^2)	Landslide index (%)
AREZZO	ANGHIARI	520	528	16	8	130,58	15,33	11,7%
AREZZO	CASTEL SAN NICCOLO'	309	313	20	4	83,33	21,32	25,6%
AREZZO	CHITIGNANO	36	46	1	10	14,56	3,49	23,9%
FIRENZE	FIGLINE VALDARNO	575	575	37	0	72,62	7,89	10,9%
FIRENZE	FIRENZUOLA	1308	1316	12	8	271,21	65,81	24,3%
GROSSETO	ARCIDOSSO	464	474	16	10	93,57	23,03	24,6%
GROSSETO	ROCCALBEGNA	747	760	21	13	123,53	30,49	24,7%
GROSSETO	SCANSANO	1128	1132	40	4	274,65	32,90	12,0%
LIVORNO	LIVORNO	365	366	6	1	103,89	10,26	9,9%
LIVORNO	MARCIANA	18	23	3	5	44,84	0,35	0,8%
LUCCA	CAPANNORI	581	583	26	2	155,01	7,71	5,0%
LUCCA	MINUCCIANO	431	435	12	4	56,70	5,68	10,0%
MASSA CARRARA	FIVIZZANO	1626	1637	13	11	179,64	23,55	13,1%
MASSA CARRARA	ZERI	852	857	23	5	73,40	15,03	20,5%
PISA	PALAIA	1543	1548	12	5	73,84	11,01	14,9%
PISA	RIPARBELLA	495	495	20	0	58,96	15,67	26,6%
PISTOIA	CUTIGLIANO	222	224	37	2	43,66	9,62	22,0%
PISTOIA	MARLIANA	784	790	4	6	43,03	7,64	17,8%

PROVINCE	MUNICIPALITY	N° landslides INITIAL	N° landslides FINAL	N° landslides MODIFIED	N° landslides NEW	Municipality area(km²)	Landslide area (km²)	Landslide index (%)
PISTOIA	PISTOIA	1879	1881	76	2	235,57	31,80	13,5%
PISTOIA	SAN MARCELLO PISTOIESE	488	489	91	1	84,69	14,32	16,9%
PRATO	CANTAGALLO	458	461	7	3	95,87	14,18	14,8%
PRATO	VAIANO	87	89	16	2	33,94	7,02	20,7%
SIENA	ABBADIA SAN SALVATORE	133	135	16	2	58,80	14,63	24,9%
SIENA	CASTIGLIONE D'ORCIA	662	669	7	7	141,26	32,09	22,7%

Starting from this table an two "updating coefficient" (UC) maps have been evaluated on municipality scale, referred respectively to the modified polygons and the new detected landslides.

This coefficient is expressed in percentage taking into account the number of new of modified polygons with respect to the total for every municipality at the end of the work and is calculated as follows:

$$UC = \frac{\text{Number of modified polygons in the municipality}}{\text{Total number of polygons in the municipality}} * 100$$

The results of the calculation are displayed in Figure 68 and Figure 69, respectively for new detected landslide polygons and modified polygons.
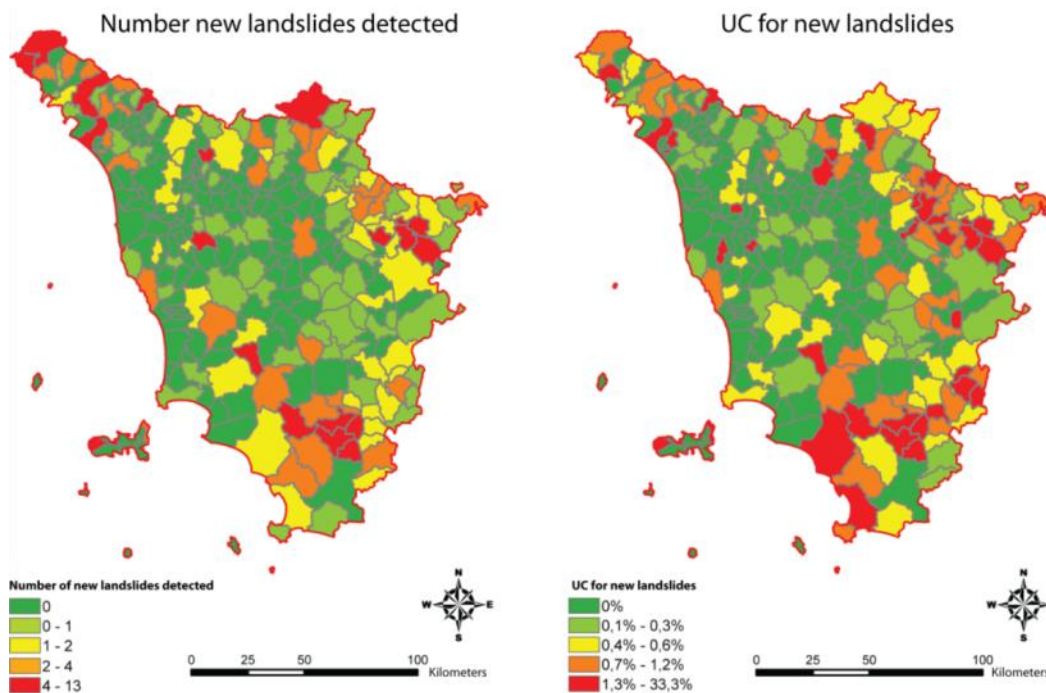
Figure 68. Number of new landslides (left) and updating coefficient in percentage, evaluated for each municipality.

97

In Figure 68 each municipality is classified on the base of the total number of landslides mapped *ex-novo* (left) and the UC values calculated with new polygons (right).
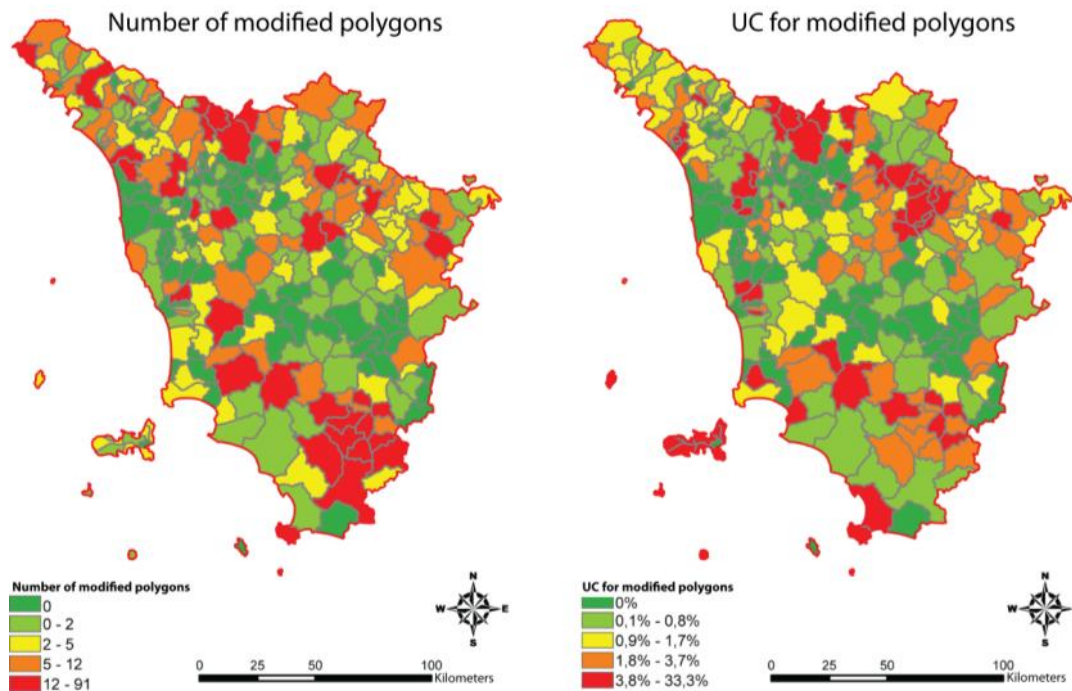
Figure 69. Number of landslides with at least one modified attribute (left) and the related UC percentages (right)

In Figure 69 each municipality is classified on the base of the total number of landslides of which at least one attribute have been modified (left) and of the relative values of UC for modified landslides (right).

Map of the landslide index

The availability of informations contained in the database have allowed to calculate the "landslide index" (LI) at municipality scale for the entire region:

$$LI = \frac{\text{Landslide area in the municipality}}{\text{Area of the municipality}} * 100$$

The results are displayed in Figure 70 where can be noted how the highest values of LI are concentrated on the Apennine mountain range, on the central part of the region occupied by the "Colline Metallifere" massif and the area around the Amiata mount.

In particulare the area of the Amiata mount, shows several very complex ground movement scenarios that required some *in-situ* surveys to be accurately defined.
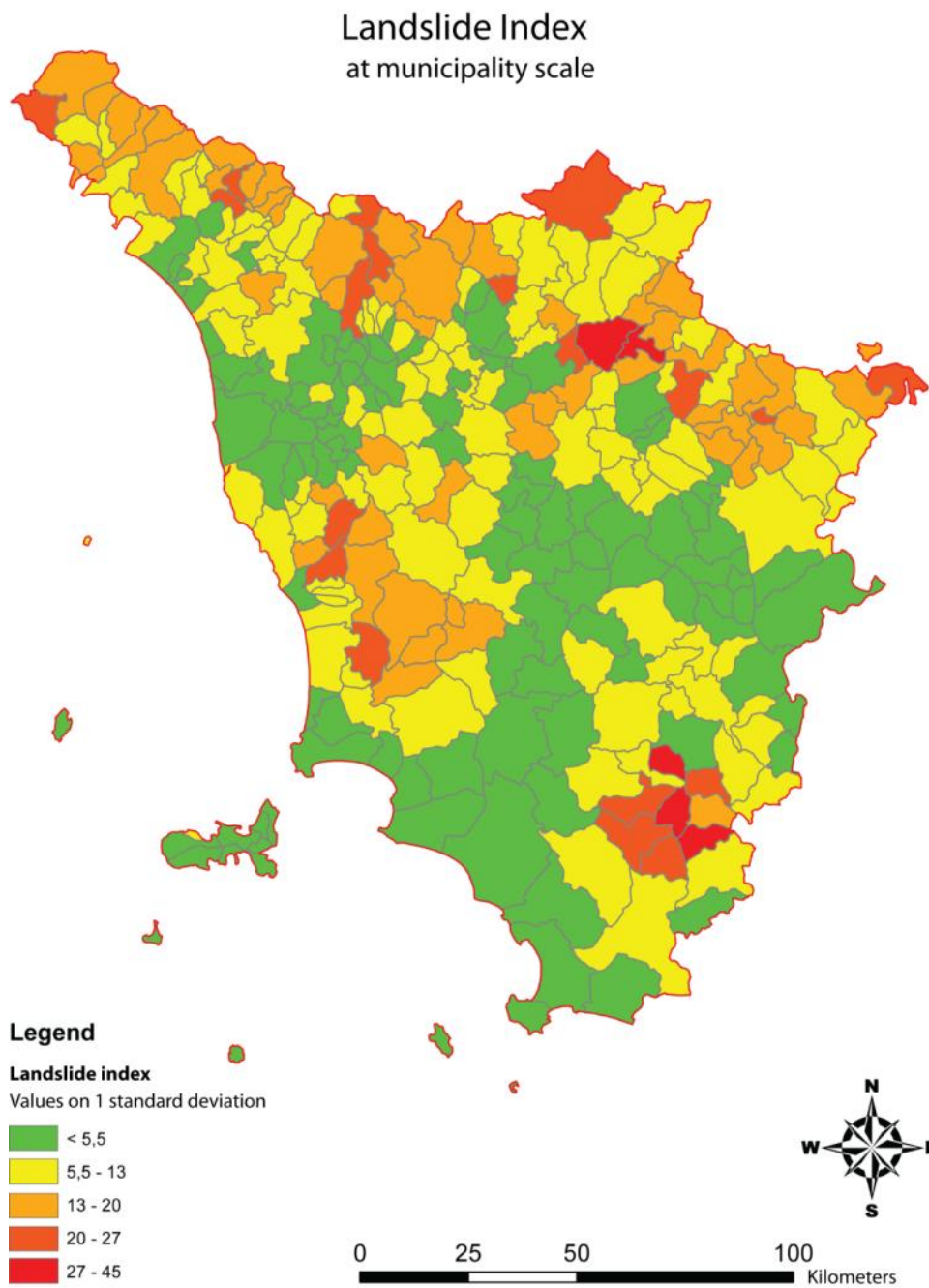
Figure 70. Distribution of the municipal Landslide Index

4.2.2. Tuscany Subsidence Inventory

According to the procedure described in paragraph 3.1.3 the ENVISAT PS data, acquired in the two orbital configurations have been combined geometrically in order to isolate wide areas with mainly vertical movements (uplifts and subsidences).

In order to perform the analysis on regional scale a resampling grid have been chosen with a 1Km x 1Km cell size. Such choice have permitted to obtain a good balance between results accuracy and computational load: using a larger cell size an excessive number of points would be averaged, points that could be related to different causes of displacement and different phenomena. Using a smaller cell size would have led to unbearable computational time.

Two maps have been developed, respectively one for the displacements measured on the vertical (Figure 71) and E-W component (Figure 72)
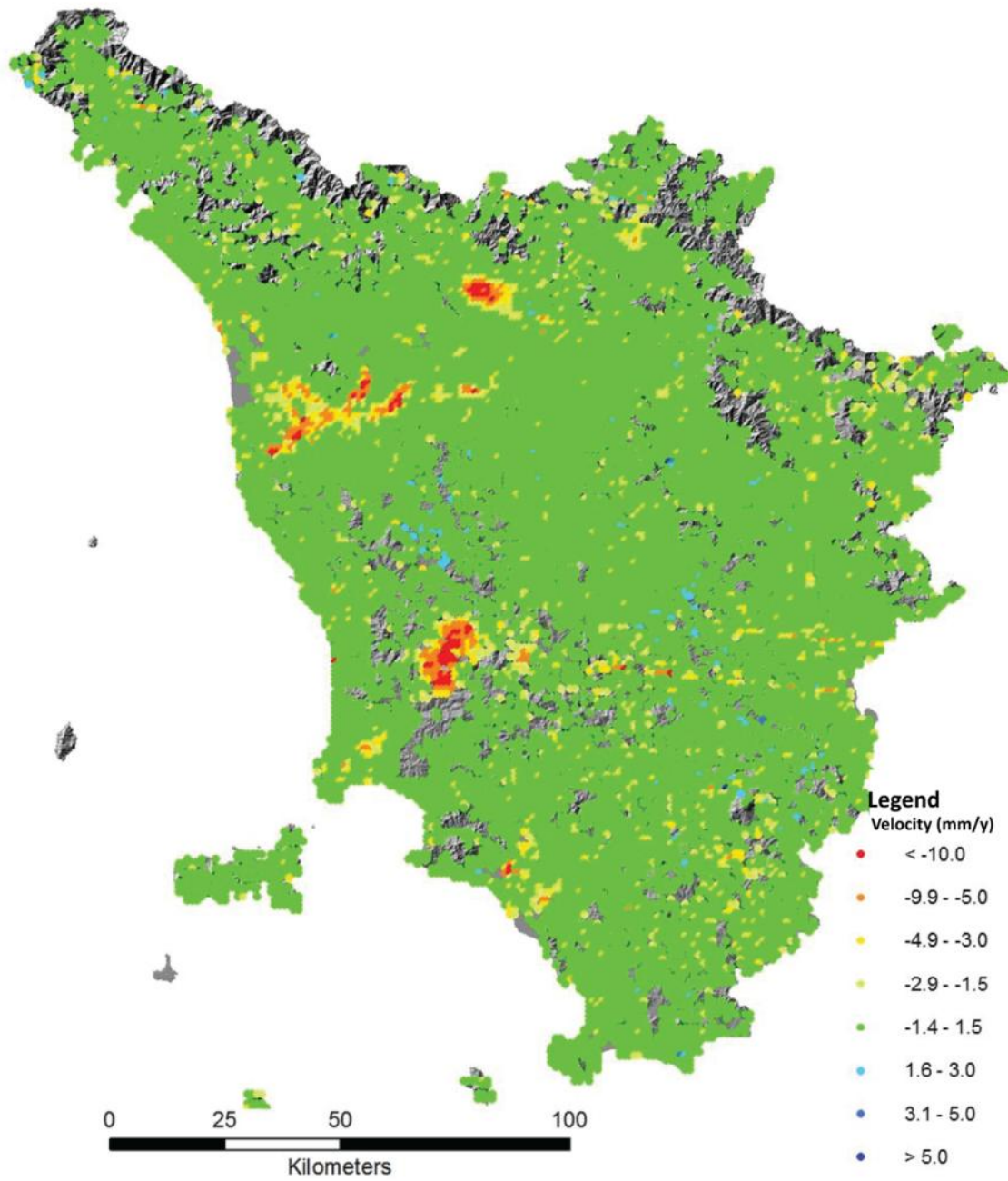
Figure 71. Vertical component of ground deformation velocities measured using ENVISAT PSs. Positive values indicate uplift, negative values indicate subsidence.
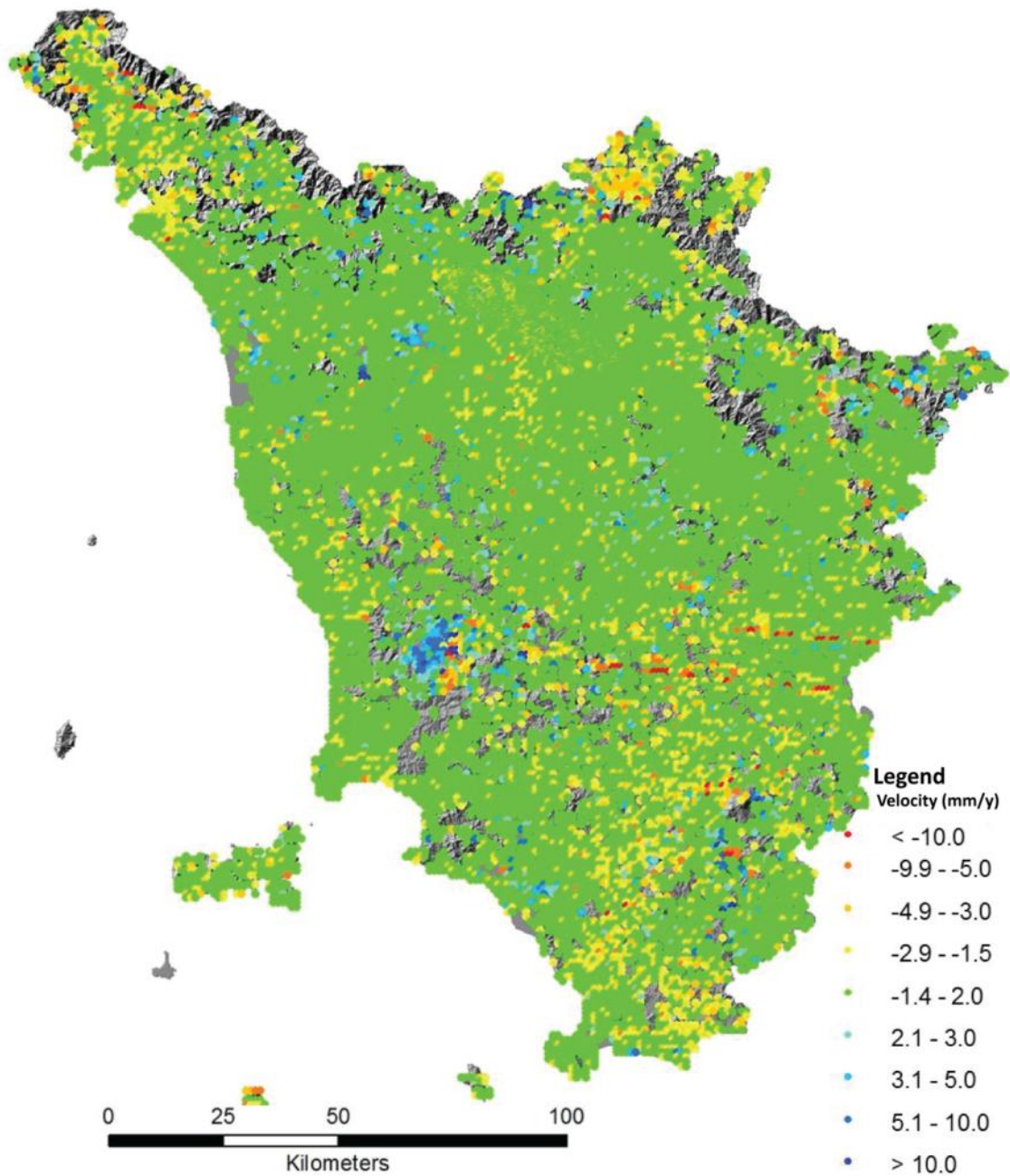
Figure 72. Horizontal component of ground deformation velocities measured using ENVISAT PSs. Positive values indicate eastward movements while negative values indicate westward movements..

In Figure 71 some area with more extended with vertical deformations are visible, such as the medium and lower Valdarno valley and an area in the upper part of the Cornia river basin.

In Figure 72 is visible the distribution of displacements in direction E-W indicating that deformative phenomena, with a strong horizontal component, are abundant and widespread but with small dimensions (slope processes).

Luca Tanteri − *"Integration of Remote-Sensing techniques and geomorphological analysis for the characterization and mapping of ground instability at regional scale"*

The two maps have been combined in order to reconstruct the displacement vector on the vertical plain on the East-West direction.

To better discern subsidences from slope deformative processes, the synthetic PSs obtained by the geometrical combination have been filtered, excluding all areas in which the horizontal component of movement is prevalent.

This operation have been performed computing the resulting displacement vector in the plane ZNEW (Zenith-Nadir and East-West) and taking into account all the areas characterized by mainly vertical displcements.

Considering the displacements projected in the ZNEW plane all the synthetic PSs associated with a displacement vector with orientation included in an angle of ±45° with respect to the Zenith-Nadir axis (Figure 73) are considered in the analysis.

In particular the synthetic PSs with resulting velocity vector on the upper quarters are considered as indicating uplift whereas PSs with resulting vector on the lower quarters are indicating subsidence.
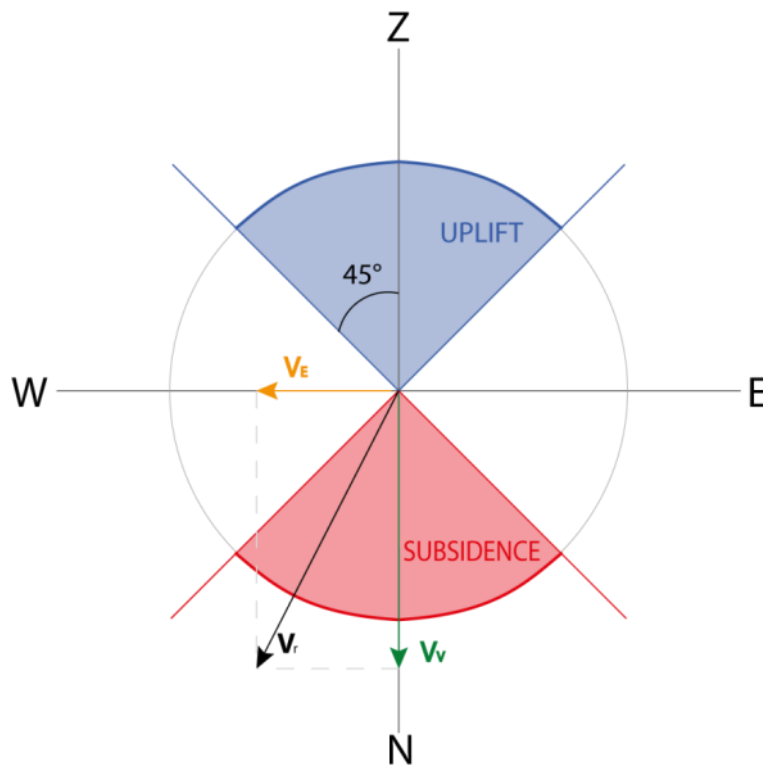
Figure 73. Schematic illustration of the vector angles considered for the subsidence and uplift mapping. V_e indicate the vector component on the horizontal (EW) plain; V_v indicates the component on the vertical (ZN) plain; V_r is the resulting vector.

In this way all the areas affected by mainly vertical ground movements are clearly visible, highlighting other wide areas in subsidence in addition to the already known areas such as the

middle Mugello basin, the Maremma plain near Grosseto and the coastal plain near Piombino (province of Livorno) (Figure 74).
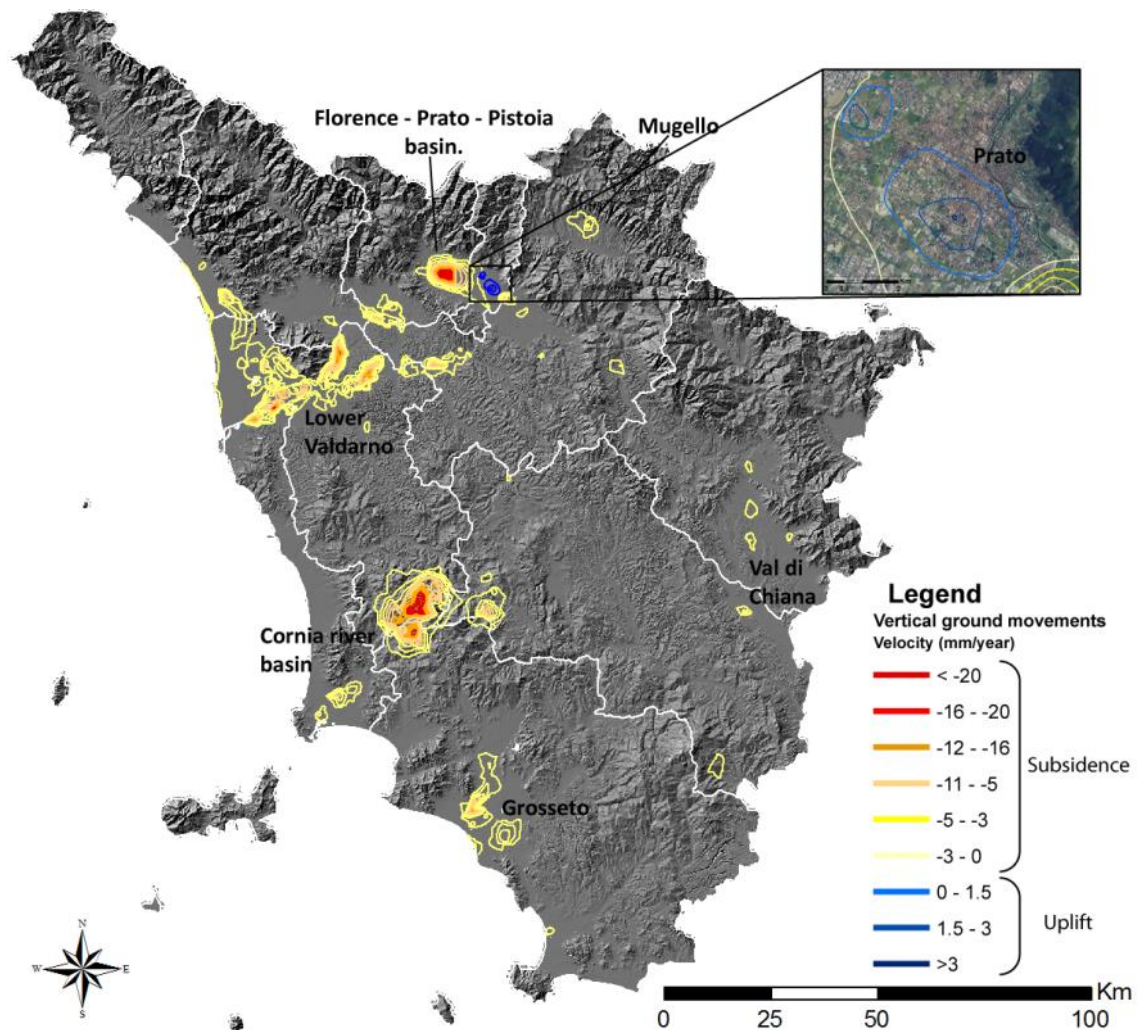
Figure 74. Map showing the main uplift and subsidence areas on regional scale. The unique uplift area with relevant extent is placed near the city of Prato, and shown in the upper zoom box.

In Figure 74 the more important subsidence areas in the region are visible; the area near Pistoia is characterized by extremely high velocity values (more than 20 mm/year), similar to those calculated for the geothermical area of Larderello, and represent the second subsidence area in Tuscany for deformation rate.

The lower Valdarno is affected by wider phenomena characterized by lower deformation rates (less than 20 mm/year) in correspondence of the municipality of Collesalvetti (province of Livorno).

Other important areas are the coastal plain of Versilia, with maximum velocities up to 10 mm/year and two areas at South and West of Grosseto, where vertical displacement velocities

range between 5 and 10 mm/year. Furthermore some smaller areas in the Val di Chiana basin have been recognized with this analysis.

In addition to the main phenomena some local ones have been detected using this approach, which dimensions are too small for an automatic mapping performed at regional scale. For this reason such areas have been delimited manually and included in a database in which an univocal identifying code, the areal extent, the average subsidence velocity and the geographic coordinates of the centroid of every polygon are reported (Figure 75).

ObjectID	Shape	ID	Avg Vel (mm/y)	Area (Km^2)	Longitude	Latitude	
1	Point	0	-5.338412	0.086175	606463.906921	4826918.24082	
2	Point	1	-13.601641	0.047382	625517.867599	4783020.31487	
3	Point	2	-3.445967	0.059052	605173.155197	4831547.37648	

Record: 1 ◄ ◄ 1 ► ►► Show: All Selected Records (0 out of 100) ▼
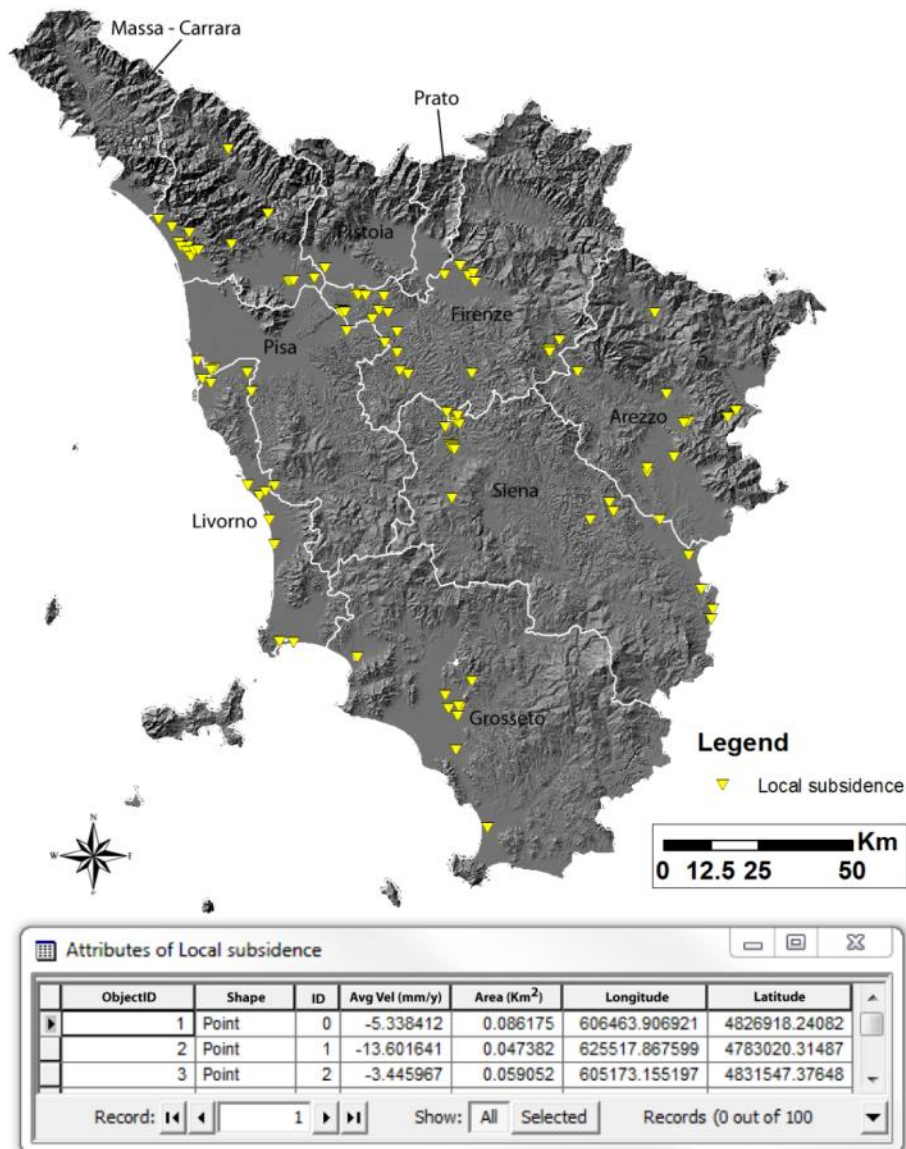
Figure 75. Database of local subsidences.

On the whole, one hundred zones affected by local subsidence have been detected and reported; those areas are placed in correspondence of valley floors and wide flat areas inland and in the vicinity of the coast and have an extent that range typically between 1 Km^2 and 2,6 Km^2.

The average displacement velocities range between 1,8 mm/year near Castelfiorentino (prov. Arezzo) and 13,6 mm/year in the municipality of Castagneto Carducci (prov. Livorno).

Relevant subsidences in Tuscany

Middle Valdarno valley (Florence-Prato-Pistoia basin)

As mentioned before, subsidence phenomena that affect the Middle Valdarno valley are well known and have been well documented in the last decade (Canuti *et al.*, 2005, 2006; Raucoules *et al.*, 2003) Here, in order to better characterize the area, the vertical velocities of the ground have been calculated for the two time interval 1992-2001 (Figure 76) and 2003-2010 (Figure 77), measured through the PS data.
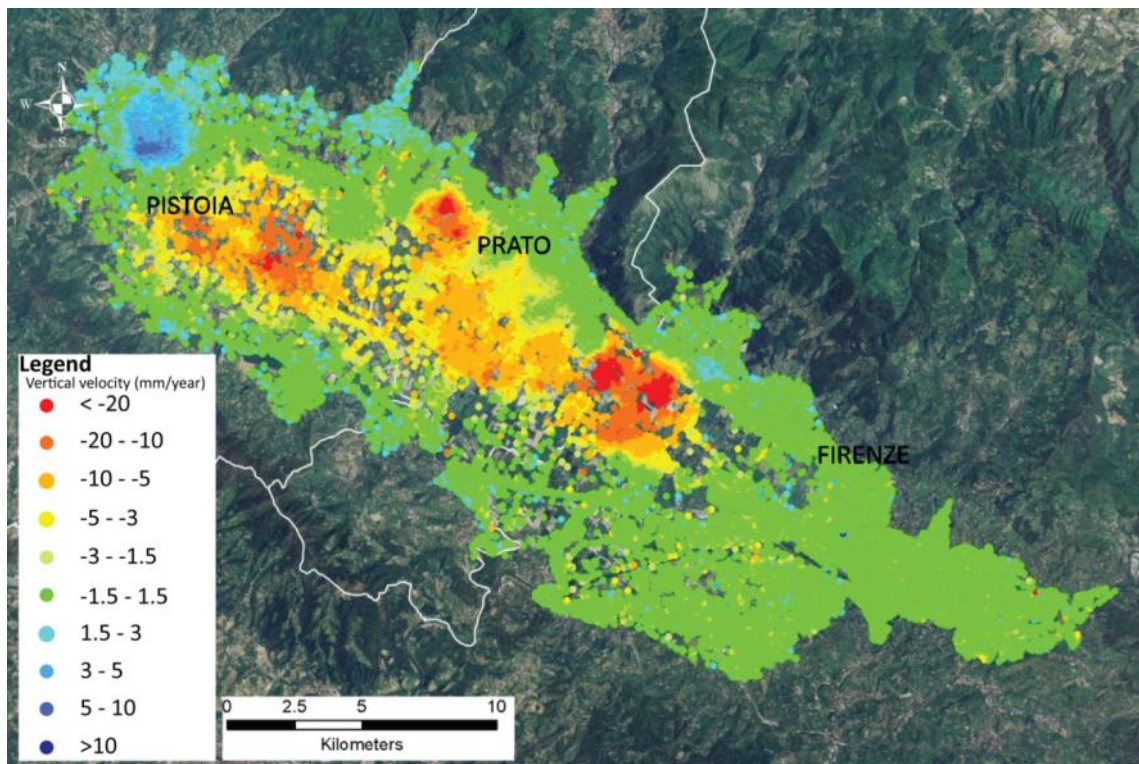
Figure 76. Vertical velocitiy map obtained by ERS data in descending orbit in the Middle Valdarno valley, covering the time interval between 1992 and 2001.

For the interval 1992-2001 only ERS data acquired in descending orbit are available but the vertical velocity have been calculated taking into account the flat topography and the previous works in which the main displacement component was already assessed as vertical.

Luca Tanteri – *"Integration of Remote-Sensing techniques and geomorphological analysis for the characterization and mapping of ground instability at regional scale"*

Such assumptions have not been necessary for the ENVISAT data, since they are available for both the orbital configurations and the presence of exclusively vertical displacements have been assessed by combining geometrically the ascending and descending data.

Observing the images in Figure 76 and Figure 77 a remarkable change in the overall deformative pattern is visible. Indeed, in the first decade of analysis a wide subsidence area that affected all the central portion of the valley was present whereas, starting from the early 2000s the scenario have changed with a reduction in extent of the big subsidence (limited to the northern part of the valley, with velocities up to 30mm/year) and the formation of some isolated and smaller ones.
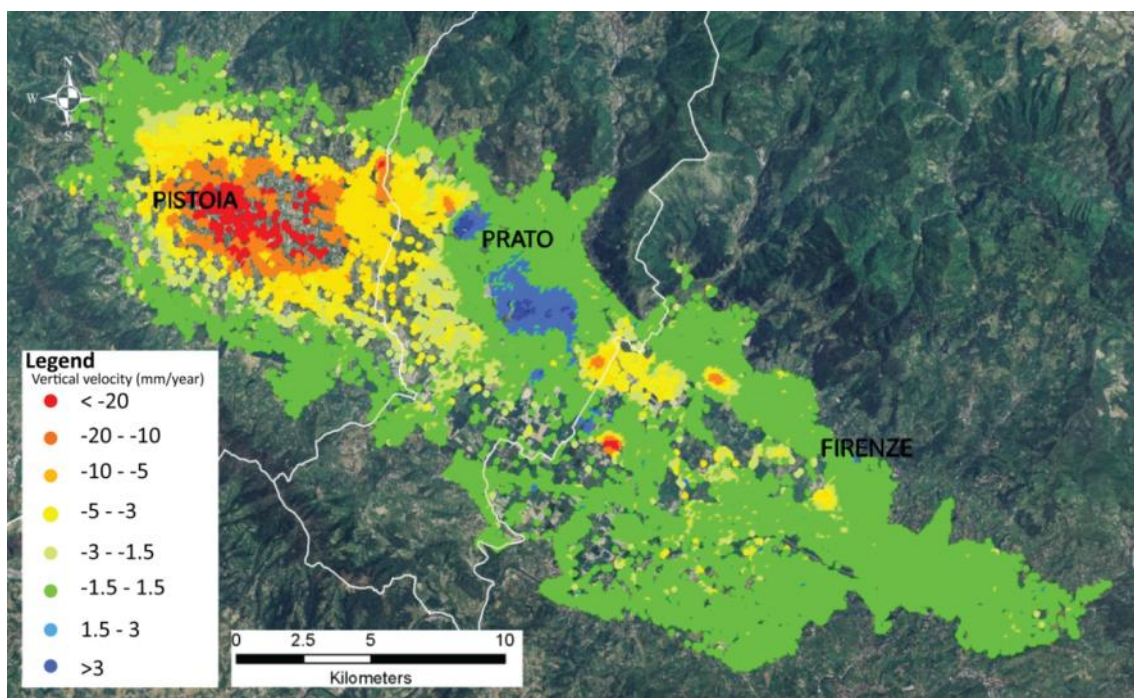
Figure 77. Vertical velocitiy map obtained by combining ascending and descending ENVISAT data in in the Middle Valdarno valley, covering the time interval between 2003 and 2010.

In the two datasets the vertical displacements in the area between the cities of Prato and Firenze have been decreased both in intensity, with velocities from 40 mm/year to 10-20 mm/year, and in spatial extent with an evident fragmentation and reduction of the areas affected by these phenomena.

Furthermore, it is very interesting how the subsidence in correspondence of the city of Prato has disappeared and have been replaced by a general uplift with average velocities from 3 mm/year up to 5 mm/year for the period 2003 – 2010 (Figure 77).

This general inversion in deformative pattern is mainly due to the suspension of the underground water exploitation, pursuant to the closure of most of the textile industries in the area during the first years of the 2000's.

In order to better highlight the deformative pattern the distribution of the velocities have been studied along three sections drawn on the valley floor, as shown in Figure 78. This have been useful to highlight the strong subsidence near Pistoia and its well defined conical shape.
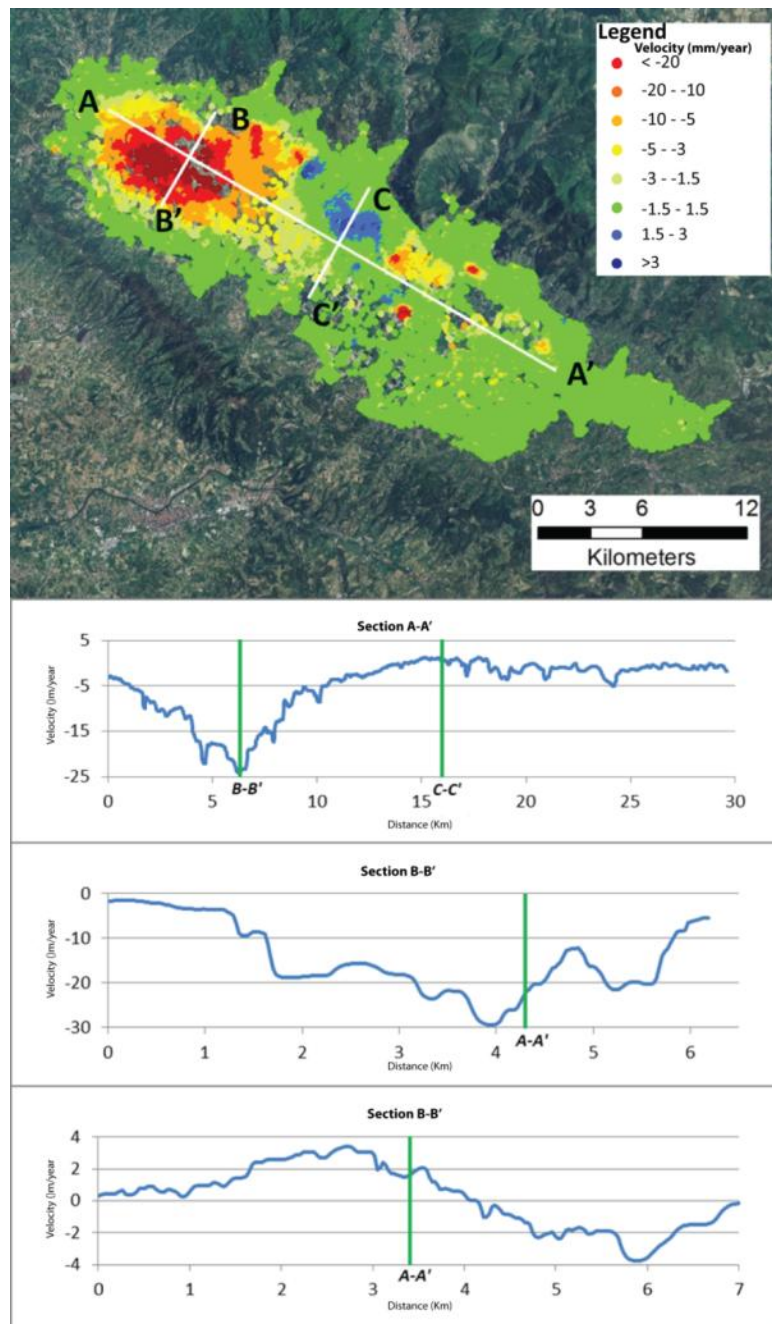
Figure 78. Velocity profiles plotted along three sections drawn on the basin. The picture shows the position of the sections, the three graphs show the vertical velocity values measured by NVISAT PSs along the sections.

Luca Tanteri – *"Integration of Remote-Sensing techniques and geomorphological analysis for the characterization and mapping of ground instability at regional scale"*

Lower Valdarno valley

The lower part of the Arno valley is placed in the provincial territory of Pisa, Lucca and Livorno and shows a rather complex deformative pattern, with several areas in subsidence affecting portions of the municipality of Empoli, an area between Santa Croce sull'Arno and Pontedera, where some tanneries are present ,and other areas near Cascina and Collesalvetti.
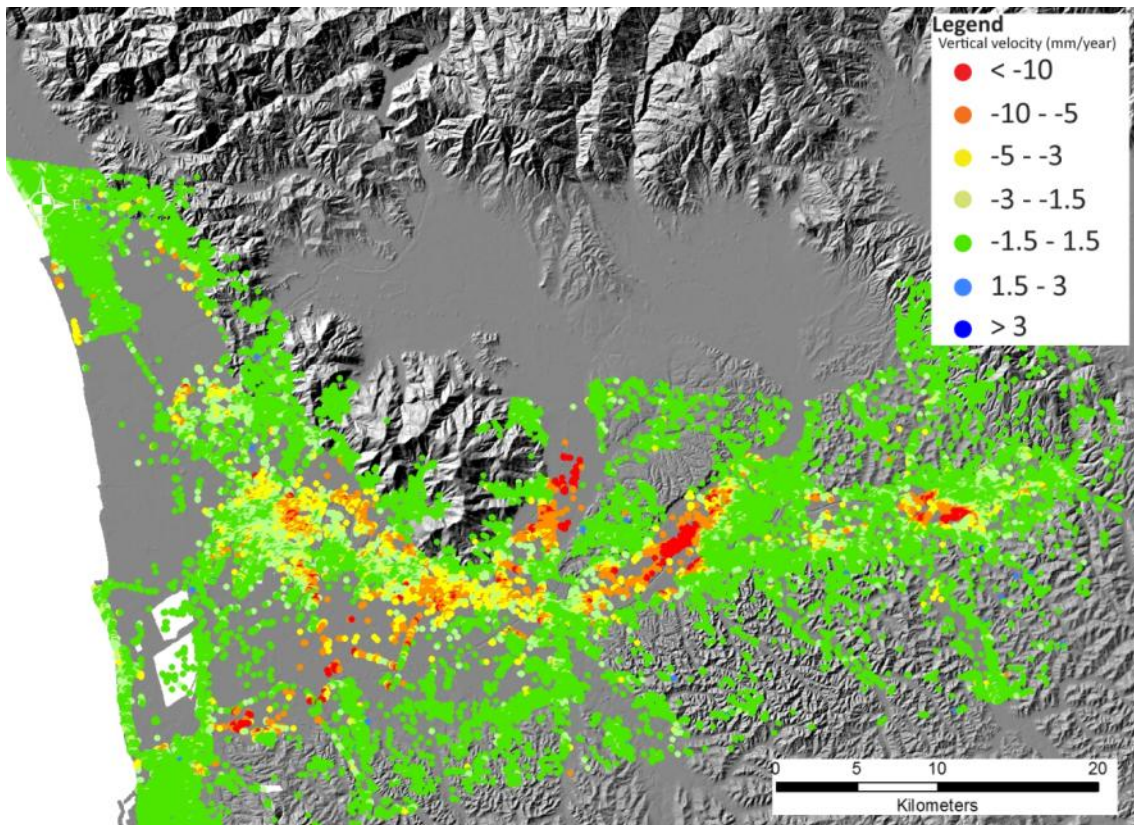
Figure 79. Vertical velocity map obtained by ENVISAT PSs on the lower Valdarno basin.

Besides the subsidence delimitation , in the area next to Bientina (prov. of Lucca), an historical reconstruction of the displacements have been performed along a section (Figure 80).

The analysis have been carried out by drawing in a plot the displacement time series of each synthetic PS along the section AB, with respect to the progressive distance from A to B.

The results have permitted to highlight that the ground settlement have progressively increased during the acquisition time, proving that the causes of the phenomenon are still active.

In this area the deformative pattern is different from that measured near Pistoia, which had a conical shape, indeed here the higher displacement values are not always in the center of the area, but sometimes are placed in the margins.
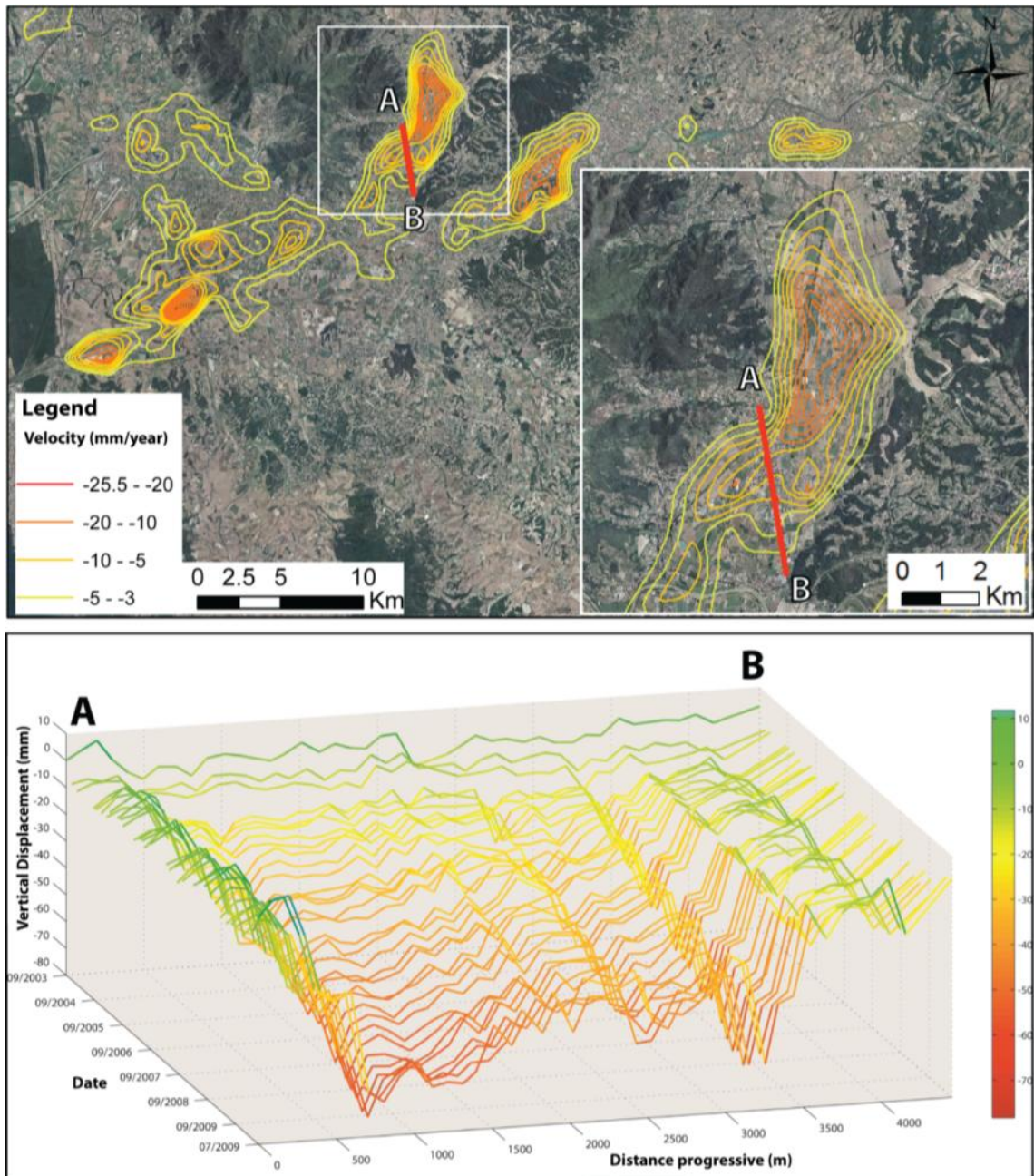
Figure 80. Subsidence mapped in lower Valdarno. The picture shows the contour applied in order to delimit and highlight the internal distribution of velocities. In the lower box the time series of some PSs placed along the section AB show the global settlement trend in the acquisition time, near Bientina. For this reconstruction ENVISAT data in descending orbit were used.

4.3. Detection of rapid kinematic processes (see Annex 1)

4.3.1. Landslide detection

The data acquired by the ADS40 and LiDAR sensors in the two flights (2009 and 2010) over the Valmarecchia have been combined in a *tree-decision classifier* (as shown in paragraph 3.2.4) in order to obtain a landscape classification that takes into account the changes occurred between the two surveys (Figure 81).

The output classified raster of has been sieved class by class applying a 3x3 sized kernel, in order to establish if an isolated pixel belongs to the same class of the 8 surrounding cells. The outcome is a map containing the information about the main natural/human-induced surface processes, such as urban planning (urbanization/ demolition/building), agricultural and forest management (rivegetation/ devegetation/bare soil/grass/shrub/forest), fluvial dynamics (permanent water/old river bed/new river bed) and slope instability (landslides) (Forzieri *et al.*, 2012b).
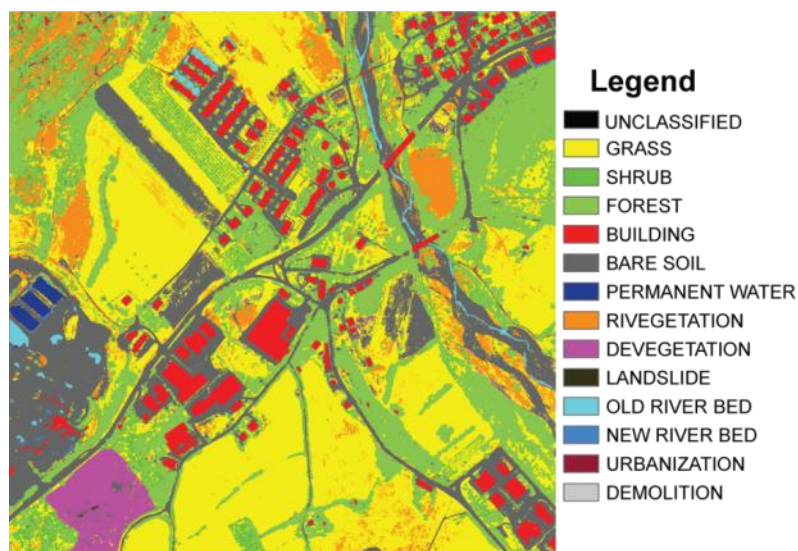
Figure 81. Classified *change-detection* map of the Valmarecchia, the visible 1Km x 1Km tile is placed near the village of Pietracuta.

The proposed model for the automatic detection of landslides occurred between the two acquisitions have been implemented to the general *change-detection* procedure only in correspondence of specific areas that have peculiar characteristics related to rapid slope

111

processes. For this purpose the model has been implemented in the following classes, retained as more representative of the presence of landslides:

- Bare soil
- Devegetation
- Landslide

As first step an inventory By comparing the optical images of 2009 and 2010 a landslide inventory map has been developed.

The inventory is at the base of all the statistical analyses proposed in this work.
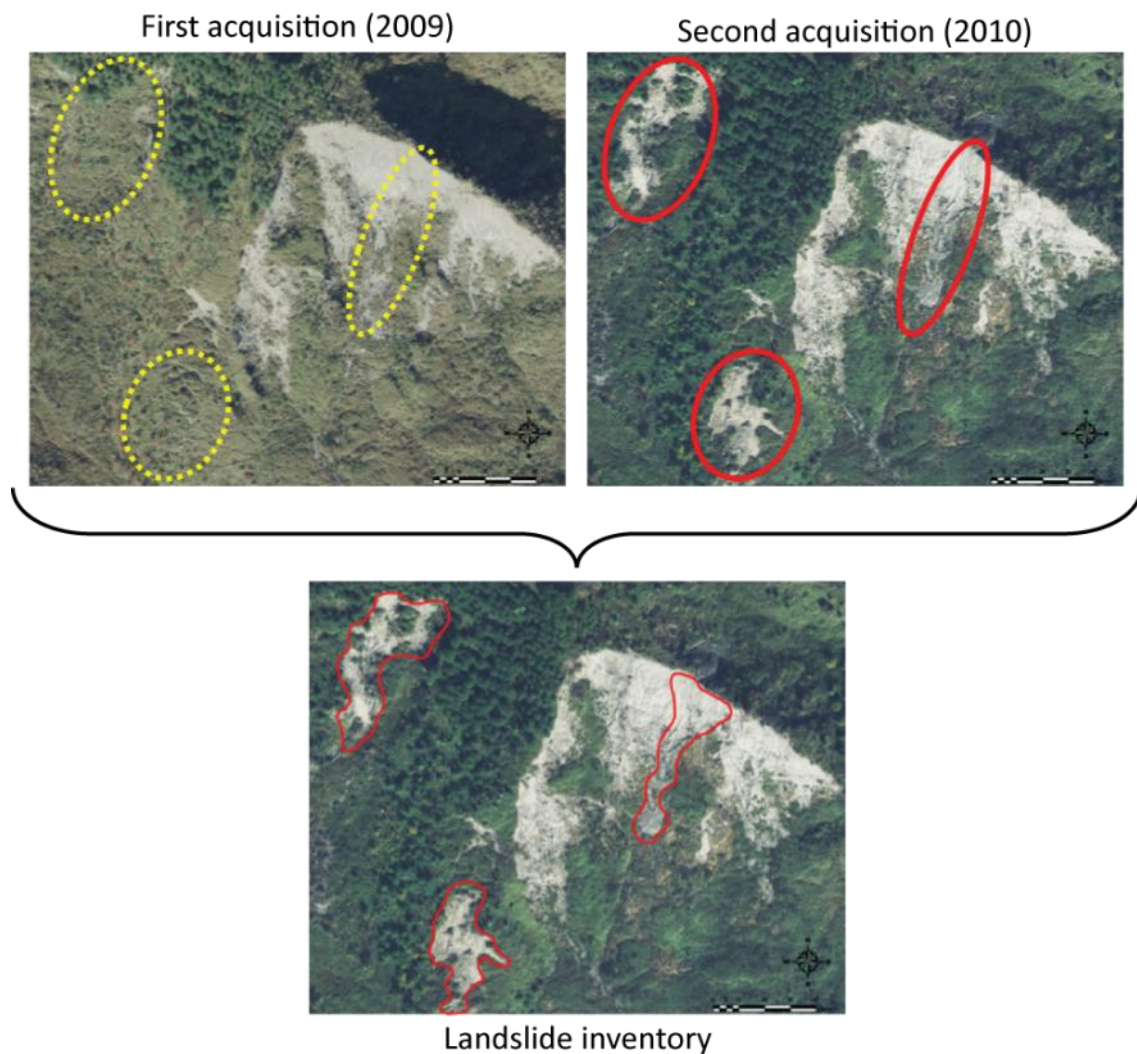
Figure 82. Comparison of the RGB (ADS40) images of 2009 and 2010, of a slope on which three landslides were occurred during the two surveys. The *photo-interpretation* of the RGB images from the two surveys is at the base of the achievement of the landslide inventory.

The automatic characterization of landslide areas could be implemented in the change detection process by considering a potentially wide range of factors. (Soeters & Van Westen, 1996).

In this study we consider the change occurred between the two LiDAR acquisitions of the factors listed in Table 4. All these surface parameters were derived from the LiDAR DTM.

Table 4. Factors and indices extracted from the LiDAR DEMs, whose variations between the two surveys have been taken into account in the firts stages of analysis.

Data source	Variable	Description
Lidar (DEM)	Altitude	
	Slope angle	Slope angle value in degrees.
	Planar curvature	Second derivative of the surface perpendicular to the slope direction.
	Profile curvature	Second derivative of the surface in the direction of slope
	Roughness	Divergence of vectors normal to pixel surface
	Specific catchment area	Upslope area per unit width of contour
Secondary indices	Topographic Wetness Index	Depends on specific catchment area and slope angle
	Steam Power Index	Depends on specific catchment area and slope angle
	Sediment transport capacity index	Depends on specific catchment area and slope angle

The changes that resulted most correlated to the landslides occurrence were changes in height values, slope angle and roughness between the two available LiDAR DTMs. The other parameters did not show any different variation between the landslides and their surrounding area.

The parameters in this table were calculated in the landslides zone and around it, identifying a circular buffer of 100 m radius. Then the difference between the first and the second acquisition was calculated. To investigate if the parameters variation trend was different between the two analyzed areas, statistical analyses were performed.

To establish If a factor variation was an exclusive characteristic of landslides zones, the trend of the difference was analyzed in specific areas, defined observing the RGB data: bare soil, erosion, herbaceous areas and others showing a vegetation reduction between the two acquisitions.

In order to establish if the distribution of each parameter was different inside the landslides area with respect to the others, the four statistical moments were calculated and a *t-test* was implemented. The results show that the DTM, the slope and the standard deviation of the DTM difference had a characteristic behavior inside the landslides zone.

The differences map was divided into several classes and, in order to verify the presence of prevailing classes, the frequency ratio model was used.
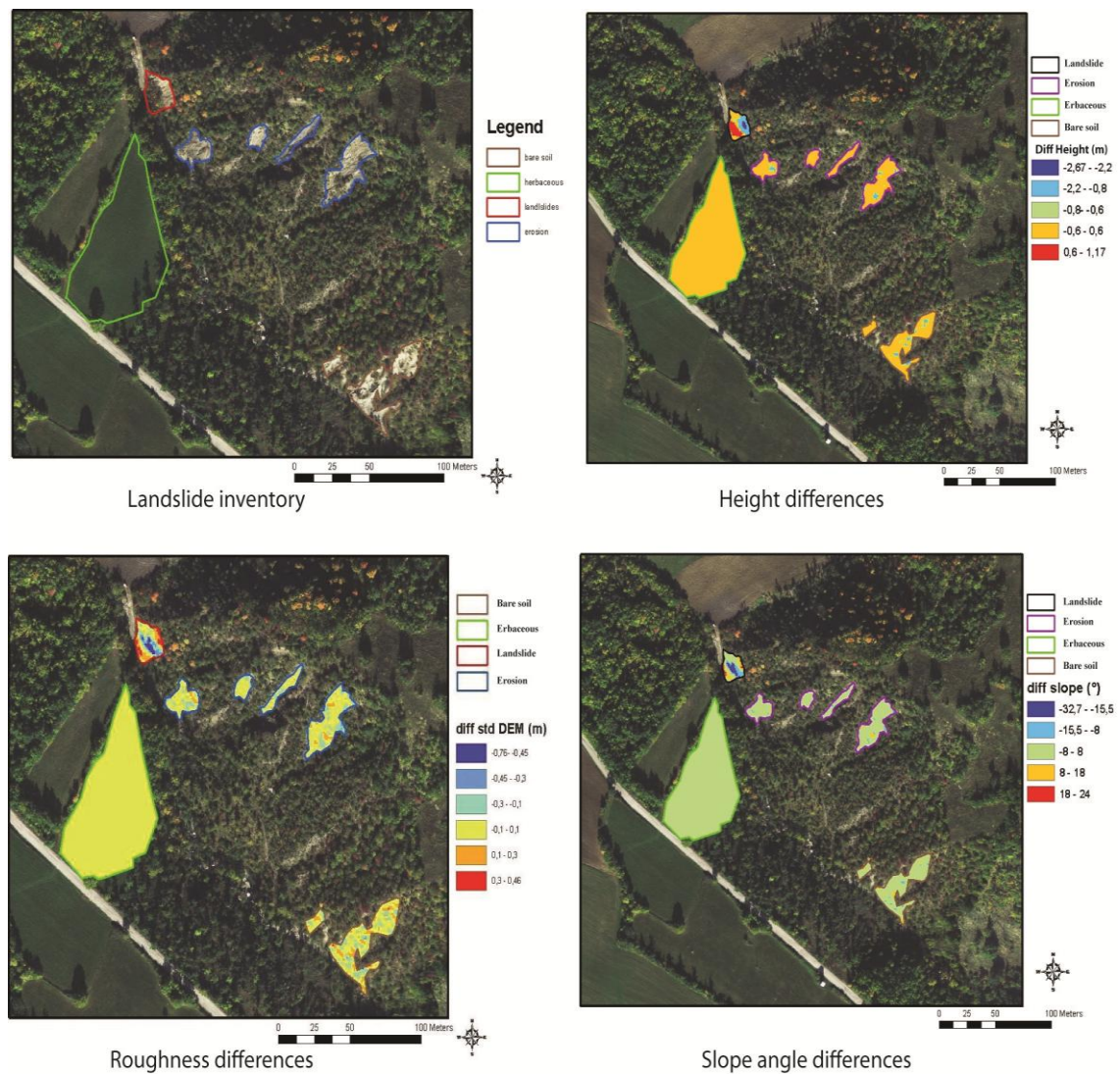

Figure 83. Study of the variations of the selected morphometric factors in the landslides and in other areas.

The factor difference values obtained inside the landslides area were compared to the difference calculated in the other analyzed zones. So, considering the change in that parameter, it is possible to discriminate between the areas.

The differences map was divided into several classes and, in order to verify the presence of prevailing classes, for such parameters the frequency ratio model was calculated (Lee & Tudan, 2005; Yilmaz, 2008):

$$FR_i = \frac{NpixX_i/(\sum NpixX)}{NpixN_i/(\sum NpixN)} \qquad (16)$$

where $NpixX_i$ is the number of pixels of the *i*-class falling within polygons representing landslides, $NpixN_i$ is the total number of pixels within the class *i*. According to this procedure, the factor difference values obtained inside the landslides area were compared with the difference calculated in the other analyzed zones separately.   If the analyzed geo-morphological factor variation would be independent by the investigated zone, the frequency ratio value would be 1: if this value is higher, the analysis suggests that there are some values characteristic of the landslides zone, so it has been possible to discriminate between the areas considering the change in that parameter. Considering the results of such analysis, a landslide classification scheme was developed taking into account increasing degrees of membership probability. The probability P that a pixel contains a landslide occurred between the two acquisition is then calculated as (Lee & Talib, 2005):

$$P = \sum_{j=1}^{N} FR_j \qquad (17)$$

where j is the considered morphometric parameter, N is the total number of considered parameters (DTM, slope and the DTM standard deviation) and FR is the corresponding value of Frequency Ratio. The result was then subdivided into 5 classes of probability: null, low, medium, high and very high.

Subsequently, post-processing refinements have been used to reduce misclassification errors and mapping inconsistencies, which conducted to a lower number of membership classes and a decrease in uncertainty accounting for the range in probability values of neighboring pixels. Furthermore it was decided to aggregate the probability classes, considering as landslides only that pixels that have a mean value, over a 3x3 m window, of at least 2.1, considering that it was assigned to the previously mentioned classes a numerical value from 1 to 5. In such way, a

probability map of occurred landslides, with only 2 classes was built. This map enables to better identify the perimeter of the detected landslides; furthermore the false alarms are strongly reduced.

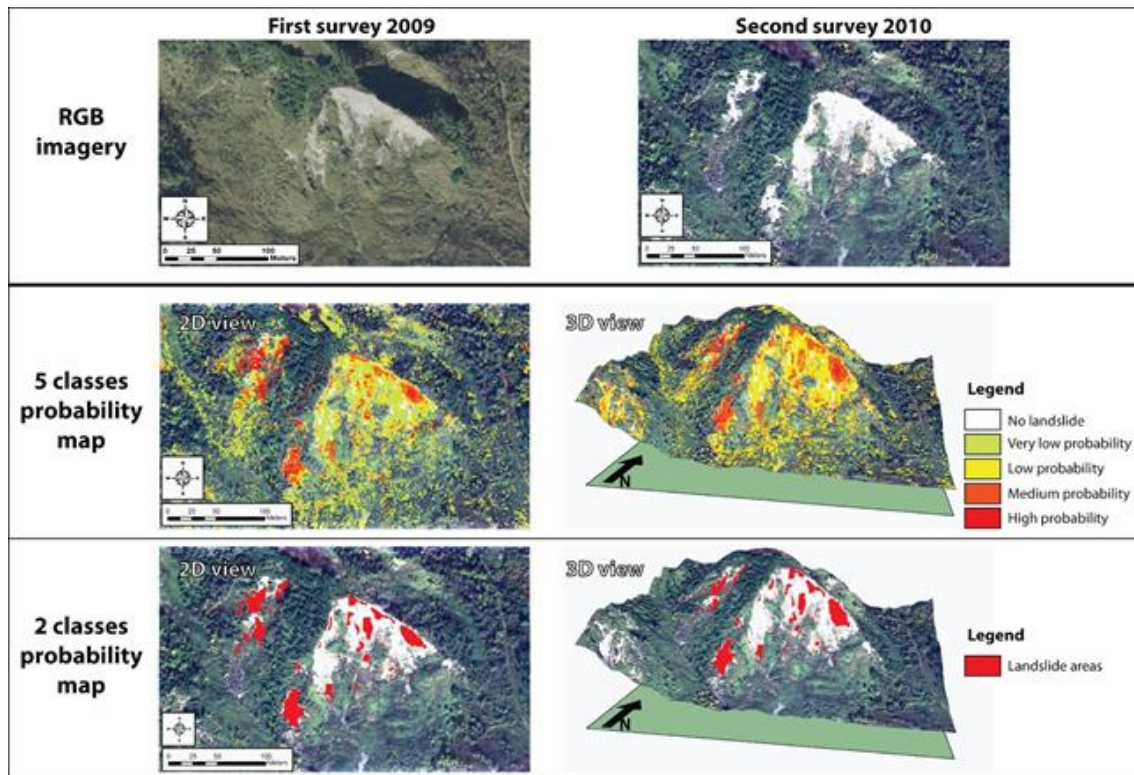Figure 84. Resulting probability map. The landslide areas are correctly detected.

Luca Tanteri — *"Integration of Remote-Sensing techniques and geomorphological analysis for the characterization and mapping of ground instability at regional scale"*

4.3.2. Changes in fluvial morphology

The available data have shown a high suitability for the detection of morphological elements related to variations in riverbed morphology.

Several previous studies, conducted using airborne LiDAR data in order to characterize and classify fluvial dynamics patterns (Cavalli *et al.*, 2008; Cavalli & Marchi, 2008; French, 2003), have highlighted the effectiveness of these kind of data in the analysis of river-bed morphology. Furthermore multi-spectral digital imagery can be suitable to this purpose, as shown by Wright *et al.* (2000).

In this study the use of both kind of remotely sensed data, referred respectively to two different acquisition times, have made possible to apply a multi-temporal approach in order to verify which are the most active areas of the river-bed in terms of morphological evolution.

As a whole the river can be classified as *braided channel* (Rosgen 1994) where the valley floor is wider and relatively straight where the valley floor is narrow and the river is entrenched between the hillslopes. In both cases, the lack of a strong human activity to control the river dynamics makes the fluvial domain considerably free to change its morphology, respectively in width and in depth.

Furthermore there are several river dykes that highly influence the present morphological pattern of the river reach, generally causing erosion areas downstream and deposition areas upstream.

Applying the proposed method all the morphological changes in the river path, especially on the river banks.

Figure 85 shows some evolutive stages of the river downstream of a dike placed near the village of Villa Verucchio (Rimini). Between 2002 and 2011 the riverbed has considerably deepened downstream the dike, as a consequence of the disturbance on the sediment/water ratio due to the dike itself, that originated deposition upstream and consequent erosion downstream.
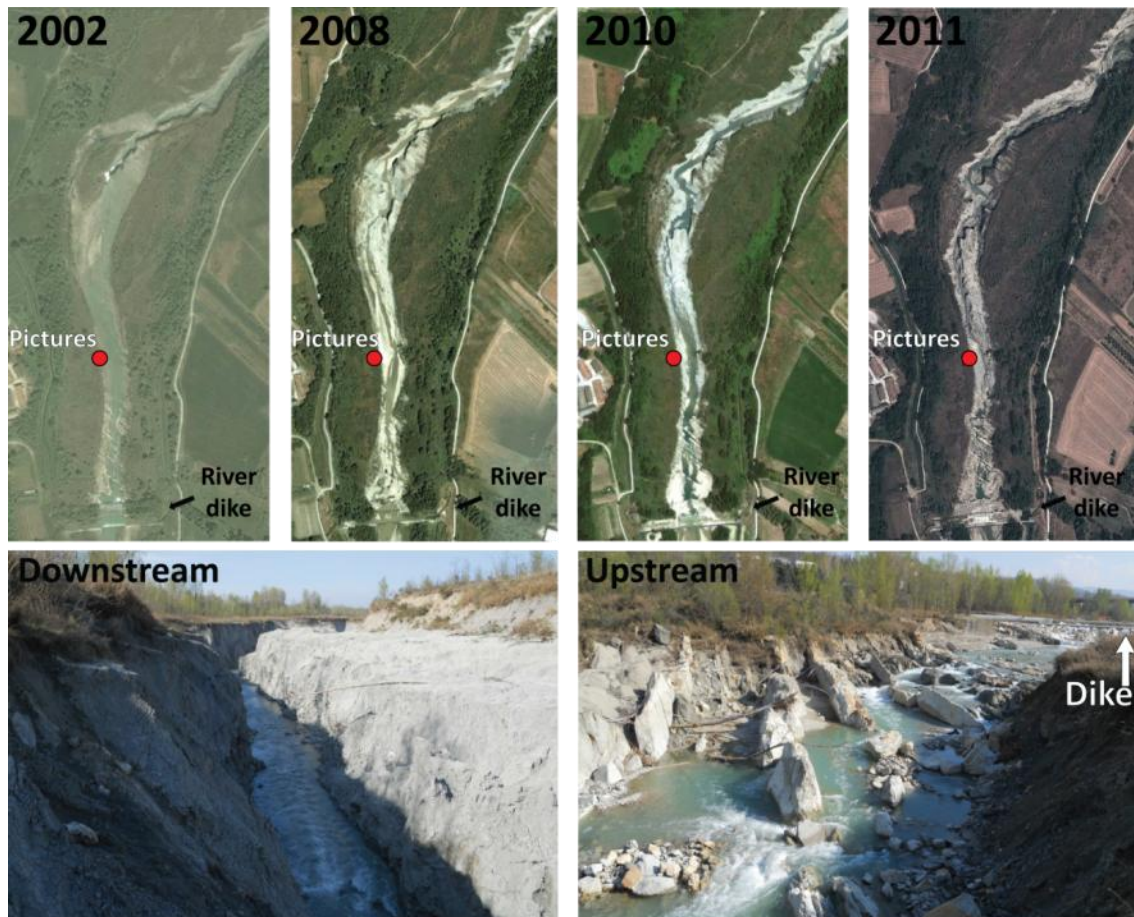
Figure 85. The upper four boxes are four aerial images (source Google Earth) taken from 2002 and 2011 over the dyke near Villa Verucchio showing the progressive deepening of the riverbed, downstream the dyke. The two lower boxes show two pictures taken in correspondence of the red dot, showing respectively the downstream reach (left) and the upstream reach (right).

Figure 86 shows the results of the model in correspondence of the river reach downstream the dike of Villa Verucchio.

In the inset box of the results all the areas eroded by the river between the two acquisition dates are highlighted by red pixels. The effectiveness of the results have been validated performing a field survey in situ. The two pictures in the bottom-left and bottom-right of Figure 85, show the deepening gorge with the steep banks, affected by diffuse instability.
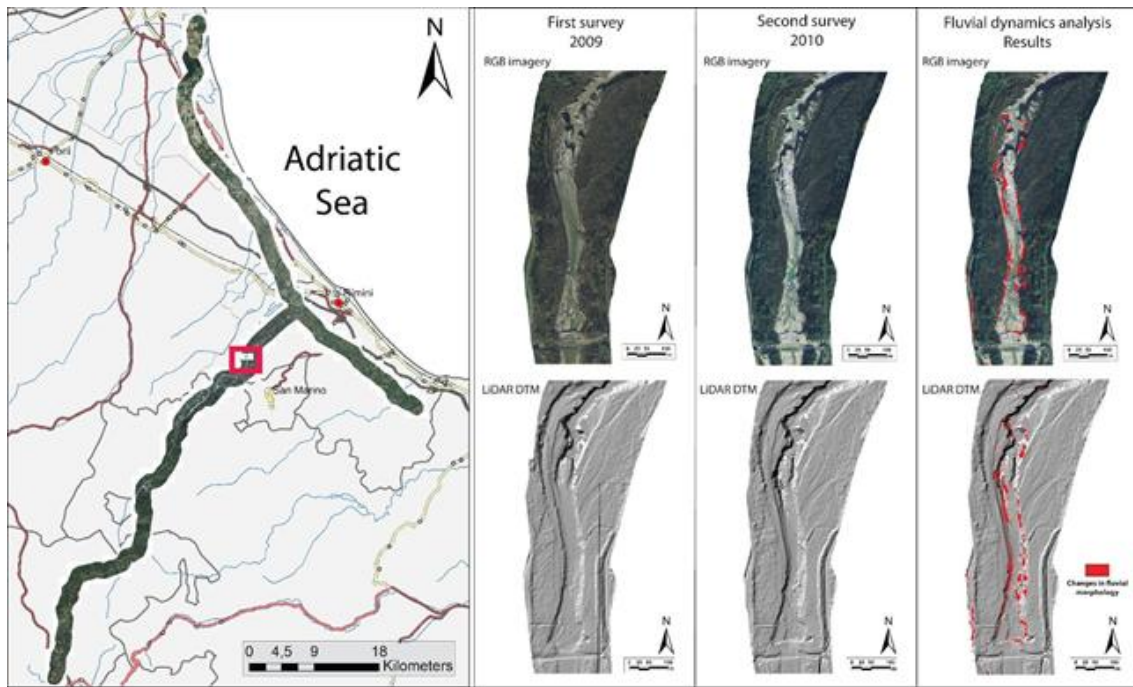
Figure 86. Results of the model for the detection of changes in fluvial morphology

4.4. Territory and landscape mapping (see Annex 2)

4.4.1. Classification results

In this paragraph the results of the automated landcover mapping procedure applied over an 20 Km transect of the Valmarecchia valley are briefly described.

In Figure 87 the resulting classified map of the area is displayed, the main box (upper map) shows a zoom of a 3-km × 3-km area in which the procedure has been trained and tested.

The optimized classification scheme represents the configuration that best performs on the considered 17-class set of land covers (see equation 11.).

The four inset boxes A,B,C and D show the four typical landscapes of the area chosen to explore further land cover-based optimized solutions.

For this purpose, the land cover classes have been grouped as:

- mixed forest;
- fluvial domain
- urban zone
- agricultural area
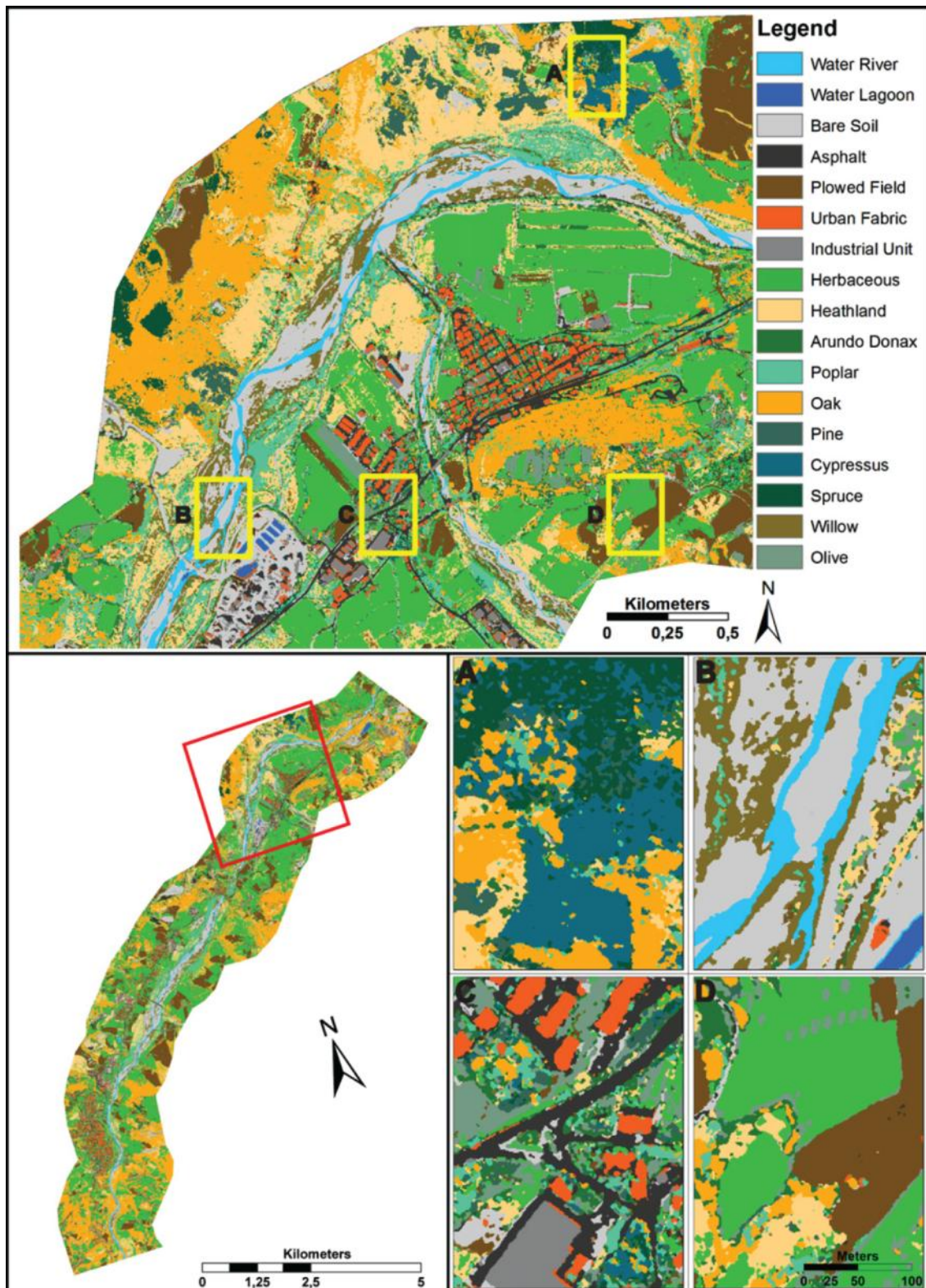
Figure 87. Classification map resulting from the proposed optimized exploitation of multi-source *remote-sensing* data, K(ML,FS15,24). Entire monitored 20-km stretch (bottom left map), reference 3-km × 3-km inset box (upper map), typical investigated landscapes including mixed forest (A), floodplain (B), urban zone (C) and agricultural area (D).

In order to optimize the classification ensemble (AI, FS, n) in the urban scenarios, the classes Asphalt (AS), Urban Fabric (UF) and Industrial Unit (IU) have been grouped (Figure 88).
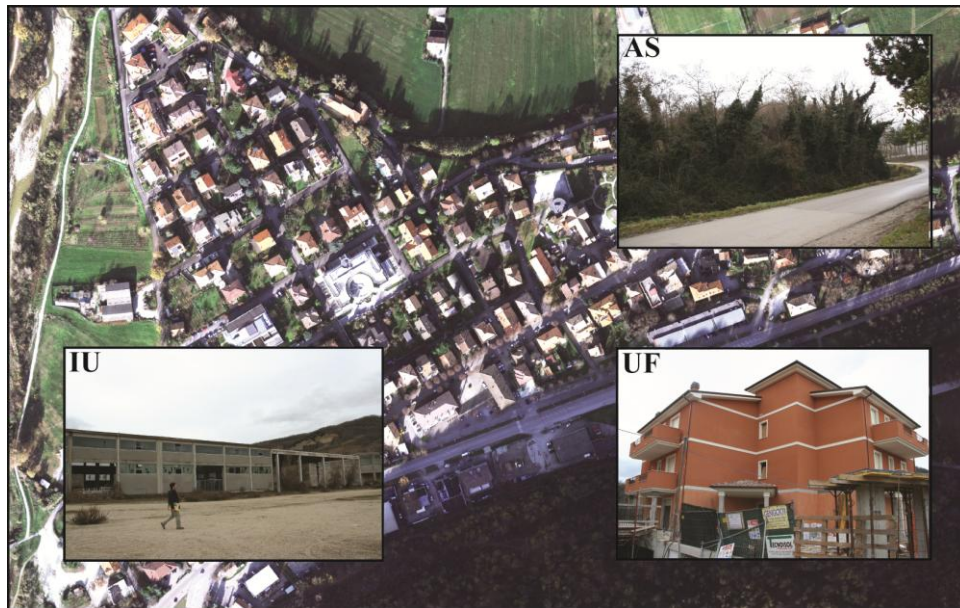
In the category "Asphalt" all the surfaces such as squares, roads and low-rise building with bituminous coverage. In the category "Urban Fabric" all the housing estate and built-up areas are included whereas all the industrial buildings, warehouses and prefabricated buildings.

Concerning the areas at agricultural use the classes Olive (OV), Plowed Field (PF) and herbaceous surfaces (HE) have been grouped (Figure 89)

The natural portions of the area, that is not influenced by human activity, show a strong biodiversity, correctly represented by the final classified map.

In order to characterize these features, the classes Heatland (HL), Poplar (PL), Oak (OK), Pine (PN), Cypressus (CY), Spruce (SP) and Arundo Donax (AD) have been chosen (Figure 89)
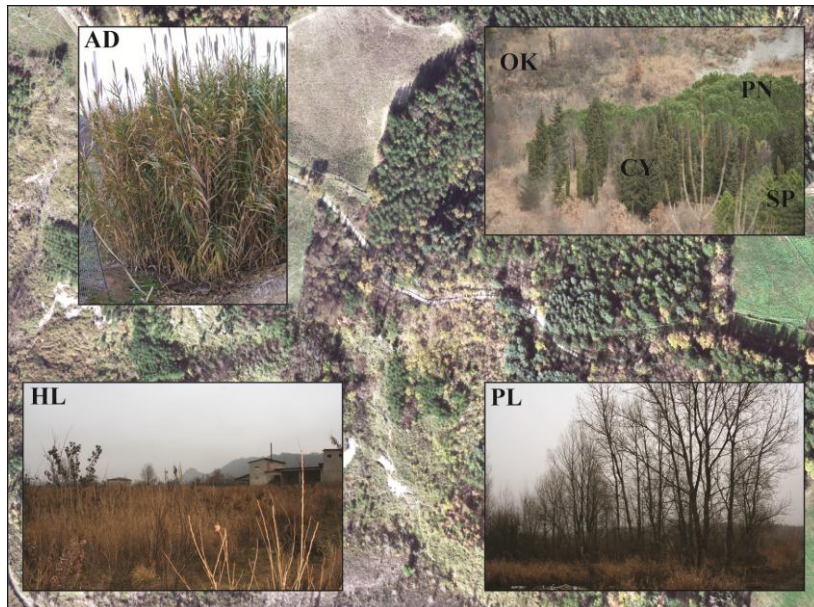
Figure 90. Focus on an area chraracterized by endemic vegetation. The inset boxes show particular of the classes chosen for the optimized classification ensemble for "spontaneous vegetation": Heatland (HL), Poplar (PL), Oak (OK), Pine (PN), Cypressus (CY), Spruce (SP) and Arundo Donax (AD).

Heatland areas (HL) are characterized in the majority by vegetal species such as *Arundo Pliniana, Spanish Broom,* and less diffuse small bushes, a vegetal association very typical for the area.

The particular species *Arundo Donax* have been classified inasmuch it resulted widely diffuse in the whole area and for its very peculiar dimensions and spectral properties.

Furthermore the distribution of this species is strictly correlated by the position of the main river Marecchia, that plays an important role on the evolutionary dynamics of the area concerning geomorphological setting, biodiversity and the areal distribution of anthropic elements.

The classes typical of this environment are: Water River (WR), Water Lagoon (WL), Bare Soil (BS) and Willows (WI), (Figure 91).

123

The class "Bare Soil" is a particular case inasmuch, in this class, all the ground portions without artificial coverage such as dirt patches, not paved squares, dirt piles and not vegetated fluvial bars.

The stagnant water pools (*Water Lagoon*) are present in little areas in the river bed and, in general, in natural or artificial lakes or ponds in the vicinity of construction sites or earth depots.
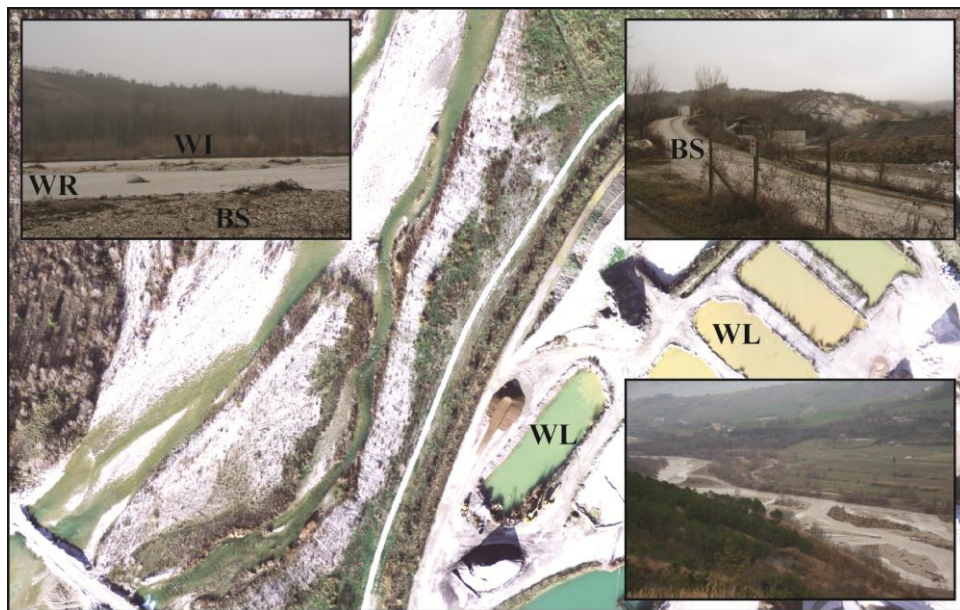
Figure 91. Focus on an area of fluvial pertinance. The inset boxes show particular of the classes chosen for the optimized classification ensemble for "fluvial domain Water River (WR), Water Lagoon (WL), Bare Soil (BS) and Willows (WI).

Luca Tanteri — *"Integration of Remote-Sensing techniques and geomorphological analysis for the characterization and mapping of ground instability at regional scale"*

5. Conclusions

Remote-sensing techniques represent a powerful tool to measure and map ground displacement as they offer a synoptic view that can be repeated at different time intervals and that is available at various scales.

The work is aimed to explore the potential of more recent *remote-sensing* techniques commonly applied in hydrogeological risk analysis, such as radar interferometric techniques and exploitation of high-resolution multi-temporal data, acquired using airborne LiDAR and multi-spectral/ hyperspectral sensors.

Within this PhD programme capability and potential of space-borne InSAR data as operational tool for the characterization of hydrogeological instability events has been tested and demonstrated.

The techniques have been exploited in relation with the kinematic of the processes that have to be analyzed, indeed, techniques such as radar interferometry have been used in presence of slow kinematic movements (slow moving landslides and land subsidence) whereas a multi-temporal approach based on change-detection on multi-spectral and LiDAR data have been proved to be more suitable for phenomena with rapid kinematic.

Such techniques have been exploited in three test sites in order to explore their effectiveness in detection and mapping of areas affected by ground movements (landslides and subsidence/uplift) along with the implementation of advanced classification procedures for a detailed mapping of the elements of territory.

In particular 28 SAR images acquired by the TerraSAR-x satellite over Barcelona (Spain) have been processed using a PSI approach and have allowed to detect and characterize 8 relevant subsidences in the urban area, mainly due to the underground excavation of new sections of the metro network, a complex landslide system that is affecting the village of El Papiol and significant ground deformations ongoing on the top of Montjuïc hill, due to the compaction of landfill over an old garbage dump. These results have been delivered to the Barcelona municipal authority and will be a part of a further publication, in progress at the moment.

Moreover ERS and ENVISAT PS data have been used in order to develop two inventory maps respectively for landslides and subsidence phenomena on the entire Tuscany regional territory. The inventories have been obtained integrating measurements of the ground displacements

with geomorphological expert knowledge, providing a powerful and up-to-date tool for a further hazard zonation on regional scale. The landslide inventory contains 91.730 polygons for which attributes such as areal extension, shape, activity, velocity, direction, type of movement are specified in detail. The subsidence inventory consists in two regional maps obtained by an analysis on the spatial distribution of vertical velocity measurements, evaluated by combining geometrically ENVISAT data (2002-2010) acquired in the two orbital configurations. With this approach two subsidence inventory maps have been developed: the first inventory includes the greater subsidence areas, highlighted with contours that shows the deformation pattern of the areas, whereas in the second map one hundred small subsidence (or upflift) areas (typically from 1 Km^2 to 2,6 Km^2) are reported with their geographic position, area and average velocity.

In order to detect rapid kinematic processes both on the slopes and on fluvial domain, the implementation of a change-detection process on airborne multi-sensor data acquired in two different surveys (2009-2010) has proven to be very suitable. The technique have allowed to detect correctly some shallow landslides occurred between the two acquisitions along with some changes of morphology within the riverbed of Marecchia, validated with some field surveys.

The results of this process have been published as shown in the annex 1.

Moreover, the possibility to obtain automatically a detailed map of the elements of territory represents a fundamental tool in the optic of a Hydrogeological Risk Evaluation, providing a high-resolution datasets in a time- and cost-effective way.

In this study the data acquired in 2010 over Valmarecchia, including optical ADS40, hyperspectral MIVIS, and LiDAR, have been used for a detailed land use classification.

The proposed procedure explored different strategies of exploitation of multi-sensor remotely sensed data for fine-scale mapping of 17 land cover classes, respectively related to vegetated, fluvial, urban and agricultural areas (see annex 2).

In sum, the proposed *remote-sensing* techniques, demonstrated their suitability for different activities dealing with risk investigations like geohazard (mapping, monitoring and modelling), for different typology of event (landslides and subsidence) and providing accurate fine-scale land cover maps, very important as a powerful tool for landscape elements mapping, and taking into account the marked impacts of land cover changes on local surface dynamics.

6. References

Abellan, A., Jaboyedoff, M., Oppikofer, T. and Vilaplana, J. M., (2009). *Detection of millimetric deformation using a terrestrial laser scanner: experiment and ap- plication to a rockfall event*. Natural Hazards and Earth System Sciences. 9, 365-372.

Agencia Estatal de Meteorología, "Valores Climatológicos Normales. Barcelona / Aeropuerto". Retrieved 16 June 2011. (*www.aemet.es/*)

Anderson, J.E., Plourde, L.C., Martin, M.E., Braswell, B.H., Smith, M.L., Dubayah, R.O., Hofton, M.A., Blair, J.B., (2008). *Integrating waveform lidar with hyperspectral imagery for inventory of a northern temperate forest*. Remote Sensing of Environment. 112, 1856–1870.

Barlow, J., Franklin, S., & Martin, Y., (2006). *High spatial resolution satellite imagery, DEM derivatives, and image segmentation for the detection of mass wasting processes*. Photogrammetric Engineering and Remote Sensing. 72, 687–692.

Belluco, E., Camuffo, M., Ferrari, S., Modenese, L., Silvestri, S., Marani, A., Marani, M., (2006). *Mapping salt-marsh vegetation by multi-spectral and hyperspectral remote sensing*. Remote Sensing of Environment. 105, 54–67.

Bertini, G., Cameli, G.M., Costantini, A., Decandia, F.A., Dini, I., Elter, F.M., Lazzarotto, A., Liotta, D., Pandeli, E., Sandrelli, F., (1994). *Structural features of southern Tuscany along the Monti di Campiglia-Rapolano Terme cross-section*. Mem. Soc. Geol. It., vol. 48, pp 51-59.

Besl, P.J., McKay, N.D., (1992). *A method for registration of 3-D shapes*. IEEE Transactions on pattern analysis and machine intelligence. 14 (2), 239 – 256.

Biescas, E., Crosetto, M., Agudo, M., Monserrat, O., and Crippa, B., (2007). *Two Radar Interferometric Approaches to Monitor Slow and Fast Land Deformation*. Journal Of Surveying Engineering. 133, 66-71.

Bitelli, G., Dubbini, M., Zanutta, A., (2004). *Terrestrial laser scanning and digital photogrammetry techniques to monitor landslide bodies*. In: Proceedings of the XXth ISPRS congress, Istanbul, Turkey, Commission V, WG V/2

Boschetti, M., Boschetti, L., Oliveri, S., Casati, L. and Canova, I., (2007). *Tree species mapping with airborne hyper-spectral MIVIS data: the Ticino Park study case*. International Journal of Remote Sensing. 28(6), 1251-1261.

Brenning, A., (2005). *Spatial prediction models for landslide hazards: review, comparison and evaluation*. Natural Hazards and Earth System Sciences. 5, 853–862.

Buchignani, V., Lombardi, S., Rizzo, S., Toro, B. (2004). *Il sinkhole di Camaiore*. Atti Conv. "Stato dell'arte sullo studio dei fenomeni di sinkhole", Roma, 139-157.

Canuti, P.,Casagli, N., Ermini, L., Fanti, R., and Farina P., (2004*). Landslide activity as a geoindicator in italy: significance and new perspectives from remote sensing*. Environmental Geology. 45, 907-919.

Canuti, P., Casagli, N., Farina, P., Ferretti, A., Marks, F., Menduni, G., (2005). *Land subsidence in the Arno river basin studied through SAR interferometry*. Proc. of SISOLS 2005, Seventh International Symposium on Land Subsidence. Shanghai, China, 23-28 October 2005, 1, 407-416.

Canuti, P., Casagli, N., Farina, P., Ferretti, A., Marks, F., Menduni, G., (2006). *Analisi dei fenomeni di subsidenza nel bacino del fiume Arno mediante interferometria radar*. Giornale di Geologia Applicata. 4, 131-136.

Canuti, P., Casagli, N., Catani, F., Falorni G. and Farina, P., (2007). *Integration of remote sensing techniques in different stages of landslide response*. In K. Sassa, H. Fukuoka, F. Wang, and G. Wang, editors, Progress in Landslide Science.

Castillo I., (2011). *La pútrida avalancha de Can Clos*.
http://ireneu.blogspot.com.es/2011/02/la-putrida-avalancha-de-can-clos.html

Catani, F., Farina, P., Moretti, S., Nico, G., Strozzi, T., (2005). *On the application of SAR interferometry to geomorphological studies: estimation of landform attributes and mass movements*. Geomorphology. 66, 119–131.

Cavalli, M., Tarolli, P., Marchi, L., Dalla Fontana, G., (2008). *The effectiveness of airborne LiDAR data in the recognition of channel-bed morphology*. Catena. 73, 249-260

Cavalli, M., Marchi, L., (2008). *Characterisation of the surface morphology of an alpine alluvial fan using airborne LiDAR*. Natural Hazards and Earth System Sciences. 8, 323-333.

Cavalli, R.M., Fusilli, L., Pascucci, S., Pignatti, S., Santini, F., (2008). *Hyperspectral sensor data capability for retrieving complex urban land cover in comparison with multi-spectral data: Venice city case study (Italy)*. Sensors. 8, 3299–3320.

Chang, C.I., (2000). *An information-theoretic approach to spectral variability, similarity, and discrimination for hyperspectral image analysis*. IEEE Transactions on Information Theory 46, 1927–1932.

Chen, R.F., Chang, K.J., Angelier, J., Chan, Y.C., Deffontaines, B., Lee, C.T., Lin, M.L., (2006). *Topographical changes revealed by high-resolution airborne LiDAR data: the 1999 Tsaoling landslide induced by the Chi-Chi earthquake*. Engineering Geology. 88, 160–172.

Chen, Y., Su, W., Li, J., Sun, Z., (2009). *Hierarchical object oriented classification using very high resolution imagery and LIDAR data over urban areas*. Advances in Space Research. 43, 1101–1110.

Cheng, K. S., Wei, C., & Chang, S. C., (2004). *Locating landslides using multi-temporal satellite images*. Advances in Space Research. 33, 96–301.

Ciraolo, G., Cox, E., La Loggia, G. and Maltese, A., (2006). *The classification of submerged vegetation using hyperspectral MIVIS data*. Annals of Geophysics. 49(1), 287-294.

Claessens, L., Schoorl, J.M., Verburg, P.H., Geraedts, L., Veldkamp, A., (2009). *Modelling interactions and feedback mechanisms between land use change and landscape processes*. Agriculture Ecosystems & Environment. 129, 157–170.

Colesanti, C., Ferretti, A., Locatelli, R., Novali, F., Savio, G., (2003). *Permanent Scatterers: Precision Assessment and Multi-platform Analysis*. IGARSS, Toulouse, France. 1-3.

Colesanti, C. & Wasowski, J., (2006). *Investigating landslides with space-borne Synthetic Aperture Radar (SAR) interferometry*. Engineering Geology. 88, 173–199.

Colombo, R., Meroni, M., Marchesi, A., Busetto, L., Rossini, M., Giardino, C., Panigada, C., (2008). *Estimation of leaf and canopy water content in poplar plantations by means of hyperspectral indices and inverse modeling*. Remote Sensing of Environment. 112, 1820–1834.

Copons, R., (2008). *El risc d'esllavissades a catalunya*. Document included in the RISKCAT project, committed by the CADS (Council for the sustainable development) to the research group RISKNAT of the University of Barcelona.

Corsini, A., Farina, P., Antonello, G., Barbieri, M., Casagli, N., Coren, F., Guerri, L., Ronchetti, F., Sterzai, P. and Tarchi. D., (2006). *Space-borne and ground-based sar interferometry as tools for landslide hazard management in civil protection*. International Journal of Remote Sensing. 27, 2351-2369.

Crosetto, M., Monserrat, O., Cuevas, M. and Crippa, B., (2011). *Spaceborne Differential SAR Interferometry: Data Analysis Tools for Deformation Measurement.* Remote Sensing. 3, 305-318

Cruden, D. M., (1991) *A simple definition of a landslide*. Bulletin of Engineering Geology and the Environment. 43, 27-29.

Cruden, D.M., Varnes, D.J., (1996). *Landslide types and processes*. In: Turner AK, Schuster RL (eds) Landslides: investigation and Mitigation, Sp. Rep. 247, Transportation Research Board, National research Council. National Academy Press, Washington DC, 36–75.

Dalponte, M., Bruzzone, L., Gianelle, D., (2008). *Fusion of hyperspectral and lidar remote sensing data for classification of complex forest areas*. IEEE Transactions on Geoscience and Remote Sensing. 48, 1416–1427.

D'Amato Avanzi, G., Giannecchini, R., Puccinelli, A., Verani, M., (2004). *Assetto geologico e pericolosità da sinkhole in aree urbane: il caso di Camaiore (Toscana, Italia) e ruolo delle amministrazioni statali e locali nel governo del territorio*. Atti Conv. "Stato dell'arte sullo studio dei fenomeni di sinkhole e ruolo delle amministrazioni statali e locali nel ruolo del territorio ", Roma, pp 331-346.

De Jong, Y.M., Van der Meer, F.D., (2004). *Remote Sensing Image Analysis Including the Spatial Domain*. Kluwer Academic Publishers, Dordrecht, Netherlands

Dewitte, O., Jasselette, J.-C., Cornet, Y., Van Den Eeckhaut, M., Collignon, A., Poesen, .J, Demoulin, A. (2008). *Tracking landslide displacements by multi-temporal DTMs: a combined aerial stereophotogrammetric and LIDAR approach in western Belgium*. Engineering Geology. 99, 11–22.

Duca, R., Del Frate, F., (2008). *Hyperspectral and multiangle CHRIS–PROBA Images for the generation of land cover maps*. IEEE Transactions on Geoscience and Remote Sensing. 46, 2857–2866.

Elaksher, A.F., (2008). *Fusion of hyperspectral images and LiDAR-based dems for coastal mapping*. Optical Laser Engineering. 46, 493–498.

Farina, P., Colombo, D., Fumagalli, A., Marks, F., Moretti, S., (2006). *Permanent Scatterers for landslide investigations: outcomes from the ESA-SLAM project*. Engineering Geology. 88, 200-217.

Feddema, J.J., Oleson, K.W., Bonan, G.B., Mearns, L.O., Buja, L., Meehl, G., Washington, W.M., (2005). *The importance of land cover change in simulating future climates*. Science. 310 (5754), 1674–1678.

Ferretti, A., Prati, C., Rocca, F., (2000). *Nonlinear subsidence rate estimation using Permanent Scatterers in differential SAR interferometry*. IEEE Transactions on Geoscience and Remote Sensing. 38 (5), 2202– 2212.

Ferretti, A., Prati, C., Rocca, F., (2001). *Permanent Scatterers in SAR interferometry*. IEEE Transactions on Geoscience and Remote Sensing. 39 (1), 8 –20.

Fiorucci, F., Cardinali, M., Carlà, R., Rossi, M., Mondini, A. C., Santurri, L., Ardizzone, F., & Guzzetti, F., (2011). *Seasonal landslides mapping and estimation of landslide mobilization rates using aerial and satellite images*. Geomorphology. doi:10.1016/j.geomorph.2011.01.013.

Forzieri, G., Guarnieri, L., Vivoni, E.R., Castelli, F., Preti, F., (2009). *Multiple attribute decision-making for individual tree detection using high-resolution laser scanning.* Forest Ecology and Management. 258, 2501–2510.

Forzieri, G., Moser, G., Vivoni, E.R., Castelli, F., Canovaro, F., (2010). *Riparian vegetation mapping for hydraulic roughness estimation using very high resolution remote sensing data fusion*. Journal of Hydraulic Engineering. ASCE 136, 855–867.

Forzieri, G., Catani, F. (2011). *Scale-dependent relations in land cover biophysical dynamics*. Ecological Modelling. 222, 3285–3290.

Forzieri, G., Castelli, F., Preti, F., (2012a). *Advances in remote sensing of hydraulic roughness*. International Journal of Remote Sensing. 33, 630–654.

Forzieri, G., Battistini, A., Catani, F., (2012b). *ES4LUCC: a GIS-tool for remotely monitoring landscape dynamics*. Computers & Geosciences. 49, 72–80.

Forzieri G., Tanteri L., Moser G., Catani F. (2013). *Mapping natural and urban environments using airborne multi-sensor ADS40–MIVIS–LiDAR synergies*. International Journal of Applied Earth Observation and Geoinformation, http://dx.doi.org/10.1016/j.jag.2012.10.004

Freeze, R.A., Cherry. J.A. (1979). *Groundwater*. Prentice-Hall, Inc. Englewood Cliffs, NJ. 604 p.

French, J.R., (2003). *Airborne LiDAR in support of geomorphological and hydraulic modelling*. Earth Surface Processes and Landforms. 28, 321-335.

Fruneau, B., Achache, J., Delacourt, C., (1995). *Observation and modeling of the Saint-Etienne-de-Tine´e Landslide using SAR interferometry*. Tectonophysics, 265.

Galloway, D.L. & Burbey, T.J. (2011). *Review: regional land subsidence accompanying groundwater extraction*. Hydrogeology Journal. 19, 1459–1486.

Gens, R. and Van Genderen J. L., (1996). *Review article sar interferometryissues, tech- niques, applications*. International Journal of Remote Sensing. 17, 1803-1835.

Gianinetto, M., Lechi, G., (2004). *The development of superspectral approaches for the improvement of land cover classification*. IEEE Transactions on Geoscience and Remote Sensing. 42, 2670–2679.

Glade, T. and Crozier, M.J., (2005). *The nature of landslide hazard impact*. In T. Glade, M. Anderson, and M. J. Crozier, editors, Landslide hazard and risk, pages 43-74. Wiley, U.S., 2005. 108

Glenn, N.F., Streutker, D.R., Chadwick, D.J., Thackray, G.D., Dorsch, S.J., (2006). *Analysis of LiDAR-derived topographic information for characterizing and differentiating landslide morphology and activity*. Geomorphology. 73, 131–148.

Goodenough, D.G., Dyk, A., Niemann, O., Pearlman, J.S., Chen, H., Han, T., Murdoch, M., West, C., (2003). *Processing Hyperion and ALI for forest classification*. IEEE Transactions on Geoscience and Remote Sensing. 41, 1321–1331.

Guzzetti, F., Carrara, A., Cardinali, M., Reichenbach, P., (1999). *Landslide hazard evaluation: a review of current techniques and their application in a multi-scale study, Central Italy*. Geomorphology. 32, 181-216.

Guzzetti, F., Malamud, B.D., Turcotte, D.L., Reichembach, P., (2002). *Power-law correlations of landslide areas in central Italy*. Earth and Planetary Science Letters. 195, 169-183.

Herold, M., Liu, X., Clarke, K.C., (2003). *Spatial metrics and image texture for mapping urban land use*. Photogrammetric Engineering and Remote Sensing. 69, 991–1001.

Hervás, J., Barredo, J. I., Rosin, P. L., Pasuto, A., Mantovani, F., & Silvano, S. (2003). *Monitoring landslides from optical remotely sensed imagery: The case history of Tessina landslide, Italy*. Geomorphology. 54, 63–75.

Hirano, A., Madden, M., Welch, R., (2003). *Hyperspectral image data for mapping wetland vegetation*. Wetlands. 23, 436–448.

Hungr, O., Evans, S.G., Bovis, M.J. and Hutchinson, J.N., (2001). *A review of the classification of landslides of the flow type*. Environmental & Engineering Geoscience. 7, 221-238.

IGOS GEOHAZARDS (2004). *Geohazards theme report: for the monitoring of our environment from space and from earth*. European Space Agency Publication, p. 55.

Jaboyedoff, M., Pedrazzini, A., Loye, A., Oppikofer, T., Guell, I., Pons, M., (2009). *Earth flow in a complex geological environment: the example of Pont Bourquin, Les Diablerets (Western Switzerland)*. In: Malet JP, Remaıtre A, Bogaard T (eds) Landslides processes—from geomorphologic mapping to dynamic modeling, proceedings of the landslide processes conference, 6–7 February 2009, Strasbourg, France.

Kasai, M., Ikeda, M., Asahina, T., Fujisawa, K., (2009). *LiDAR-derived DEM evaluation of deep-seated landslides in a steep and rocky region of Japan*. Geomorphology. 113, 57–69.

Kottek, M., Grieser, J., Beck, C., Rudolf, B. and Rubel, F., (2006). *World Map of the Köppen-Geiger climate classification updated*. Meteorologische Zeitschrift, Vol. 15, No. 3, 259-263

Kruse, F.A., Lefkoff, A.B., Boardman, J.B., Heidebrecht, K.B., Shapiro, A.T., Barloon, P.J., Goetz, A.F.H., (1993). *The spectral image processing system (SIPS)—interactive visualization and analysis of imaging spectrometer data*. Remote Sensing of Environment. 44 (2–3), 145–163.

Lagomarsino, D., Battistini, A., Tanteri, L., (2013). *High resolution multi-spectral and LiDAR data integration for landslides detection purposes*. Rendiconti Online della Società Geologica Italiana. 24, 187-189

Lee, K.M., Kerry Rowe, R., Lo, K.Y., (1992). *Subsidence owing to tunneling. I. Estimating the gap parameter*. Canadian Geotechnical Journal. 29(6), 929-940

Lee, S., & Lee, M.-J., (2006). *Detecting landslide location using KOMPSAT 1 and its application to landslide-susceptibility mapping at the Gangneung area, Korea*. Advances in Space Research. 38, 2261–2271.

Lee, I.-M., Nam S.-W., (2004). *Effect of tunnel advance rate on seepage forces acting on the underwater tunnel face*. Tunneling and Underground Space Technology. 19, 273-281.

Lee, S., Talib J.A., (2005). *Probabilistic landslide susceptibility and factor effect analysis*. Environmental Geology. 47, 982–990.

Lee, S., Tudan, N., (2005). *Probabilistic landslide susceptibility mapping in the Lai Chau province of Vietnam: focus on the relationship between tectonic fractures and landslides*. Environmental Geology. 48, 778–787.

Lillesand, T. M. and Kiefer, R. W., (1987). *Remote Sensing and Image Interpretation*. Wiley, New York, NY., 1987. 10

Lillesand, T.M., Kiefer, R.W., Chipman, J.W., (2008). *Remote Sensing and Image Interpretation*, 6th ed. John Wiley & Sons, Hoboken, NJ, USA.

Lin, P.-S., Lin, J.-Y., Hung, H.-C., and Yang, M.-D., (2002). *Assessing debris flow hazard in a watershed in Taiwan*. Engineering Geology. 66, 295–313.

Lu, P., Casagli, N., Catani, F., Tofani, V. (2012). *Persistent Scatterers Interferometry Hotspot and Cluster Analysis (PSI-HCA) for detection of extremely slow-moving landslides*. International Journal of Remote Sensing. 33 (2), 466-489.

Lu, S., Oki, K., Shimizu, Y., Omasa, K., (2007). *Comparison between several feature extraction/classification methods for mapping complicated agricultural land use patches using airborne hyperspectral data*. International Journal of Remote Sensing. 28, 963–984.

Malamud, B.D., Turcotte, D.L., Guzzetti, F., Reichembach, P., (2004). *Landslide inventories and their statistical properties*. Earth Surface Processes and Landforms. 29, 687-711.

Malet, J.P. & Maquaire, O. (2009) – *Risk Assessment Methods of Landslides*. RAMSOIL Project Report 2.2, Deliverable 2.3.2.4., 29 pp (http://goo.gl/0agt9).

Mantovani, F., Soeters, R. and Van Westen, C. J. (1996). *Remote sensing techniques for landslide studies and hazard zonation in europe*. Geomorphology. 15, 213-225.

Marcelino, E.V., Formaggio, A.R., & Maeda, E.E., (2009). *Landslide inventory using image fusion techniques in Brazil*. International Journal of Applied Earth Observation and Geoinformation. 11, 181–191.

Martha, T. R., Kerle,N. V. Jetten, VanWesten, C. J., & Vinod Kumar, K. (2010). *Characterising spectral, spatial and morphometric properties of landslides for semi-automatic detection using object-oriented methods*. Geomorphology. 116, 24–36.

Massonet, D. and Rabaute, T., (1993). *Radar interferometry: limits and potential*. IEEE Transaction on Geoscience and Remote Sensing. 31, 455-464.

Massonnet, D., Feigl, K.L., Rossi, M., Adragna, F., (1994). *Radar interferometric mapping of deformation in the year after the Landers earthquake*. Nature, 369.

Massonet, D., Briole, P., Arnaud, A., (1995). *New insights on Mount Etna from 18 months of radar interferometric monitoring*. Nature. 375, 567-570.

Massonnet, D., Thatcher, W., Vadon, H., (1996). *Detection of post-seismic fault zone collapse following the Landers earthquake*. Nature, 382.

Massonnet, D. and Feigl, K. L. (1998). *Radar interferometry and its application to changes in the earth's surface*. Reviews of Geophysics. 36, 441-500.

McKean, J., Roering, J. (2004). *Objective landslide detection and surface morphology mapping using high-resolution airborne laser altimetry*. Geomorphology. 57, 331–351.

Melesse, A.M., Weng, Q., Thenkabail, P.S., Senay, G.B. (2007). *Remote sensing sensors and applications in environmental resources mapping and modelling*. Sensors 7, 3209–3241.

Melgani, F., Bruzzone, L., (2004). *Classification of hyperspectral remote sensing images with support vector machines*. IEEE Transactions on Geoscience and Remote Sensing. 42, 1778–1790.

Metternicht G., Hurni, L. and Gogu, R. (2005). *Remote sensing of landslides: An analysis of the potential contribution to geo-spatial systems for hazard assessment in mountainous environments*. Remote Sensing of Environment. 98, 284-303.

Meusburger, K. and Alewell, C., (2008). *Impacts of anthropogenic and environmental factors on the occurrence of shallow landslides in an alpine catchment (Urseren Valley, Switzerland)*. Natural Hazards and Earth System Science. 8, 509–520

Mondini, A.C., Guzzetti, F., Reichenbach, P., Rossi, M., Cardinali, M., Ardizzone, F. (2011). *Semiautomatic recognition and mapping of rainfall induced shallow landslides using satellite optical images*. Remote Sensing of Environment. 115, 1743–1757.

Moser, G., Serpico, S.B., (2013). *Combining support vector machines and Markov random fields in an integrated framework for contextual image classification*. IEEE Transactions on Geoscience and Remote Sensing. 51 (5), 2734 - 2752

Moser, G., Serpico, S.B., Benediktsson, J.A., (2013). *Land cover mapping by Markov modeling of spatial contextual information in very high resolution remote sensing images*. Proceedings of the IEEE. 101 (3), 631 - 651

Mueller, R., Loew, S. (2009) *Predisposition and Cause of the Catastrophic Landslides of August 2005 in Brienz (Switzerland)*. Swiss Journal of Geosciences. 102(2), 331–344.

Mundt, J.T., Streutker, D.R., Glenn, N.F., (2006). *Mapping sagebrush distribution using fusion of hyperspectral and lidar classifications*. Photogrammetric Engineering and Remote Sensing. 72, 47–54.

Myneni, R.B., Hall, F.G., Sellers, P.J., Marshak, A.L., (1995). *The Interpretation of Spectral Vegetation Indexes*. IEEE transactions on geoscience and remote sensing. 33(2), 418, 486.

Nadim, F., Kjekstad, O., Peduzzi, P., Herold, C. and Jaedicke, C. (2006). *Global landslide and avalanche hotspots*. Landslides. 3, 159-173.

Navulur, K., (2007). *Multi-spectral Image Analysis Using the Object-oriented Paradigm*. CRC Press, Boca Raton, FL, USA.

Nichol, J., & Wong, M. S., (2005). *Satellite remote sensing for detailed landslide inventories using change detection and image fusion*. International Journal of Remote Sensing. 26, 1913–1926.

Oppikofer, T., Jaboyedoff, M., Keusen, H.R., (2008). *Collapse at the eastern Eiger flank in the Swiss Alps*. Nature and Geosciences. 1, 531–535.

Pignatti, S., Cavalli, R.M., Cuomo, V., Fusilli, L., Pascucci, S., Poscolieri, M., Santini, F.,(2009). *Evaluating Hyperion capability for land cover mapping in a fragmented eco system: Pollino National Park, Italy*. Remote Sensing of Environment. 113, 622–634.

Pignatti, S., Cavalli, R.M., Cuomo, V., Fusilli, L., Pascucci, S., Poscolieri, M. and Santini, F. (2009). *Evaluating Hyperion capability for land cover mapping in a fragmented eco system: Pollino National Park, Italy*. Remote Sensing of Environment. 113, 622-634.

Priestnall, G., Jaafar, J., Duncan, A., (2000). *Extracting urban features from LiDAR digital surface models*. Computers Environment and Urban Systems. 24, 65–78.

Raucoules, D., Le Mouélic, S., Carnec, C., King C., (2003). *Urban subsidence in the city of Prato (Italy) monitored by satellite radar interferometry*. International Journal of Remote Sensing. 24 (4), 891-897.

Rengers, N., Soeters, R., van Westen, C.J. (1992). *Remote sensing and GIS applied to mountain hazard mapping*. Episodes. 15, 36-45.

Richards, J.A., Jia, X., (2006). *Remote Sensing Digital Image Analysis*. sixth ed. Springer- Verlag, Berlin, Germany.

Roering, J.J., Kirchner, J.W., Dietrich, W.E., (2005). *Characterizing structural and lithologic controls on deep-seated landsliding: Implications for topographic relief and landscape evolution in the Oregon Coast Range, USA*. GSA Note Cards. 117 (5-6), 654-668.

Roering, J.J., Stimely, L., Mackey, B.H., Schmidt, D.A., (2009). *Using DInSAR, airborne LiDAR, and archival air photos to quantify landsliding and sediment transport*. Geophysical Research Letters. 36.

Rosen, P. A., Hensley, S., Joughin, I. R., Li, K., Madsen, S. N., Rodriguez, E. and Goldstein, R. M. (2000). *Synthetic aperture radar interferometry*. Proceedings of the IEEE. 88, 333-382.

Rosgen, D.L., (1994). *A classification of natural rivers*. Catena. 22 (3), 169-199

Rosin, P. L., & Hervás, J., (2005). *Remote sensing image thresholding methods for determining landslide activity*. International Journal of Remote Sensing. 26, 1075–1092.

Rott, H. and Nagle, T., (2006). *The contribution of radar interferometry to the assessment of landslide hazards*. Advances in Space Research. 37, 710-719.

Soeters, R. & Van Westen, C.J. (1996). *Slope instability recognition, analysis, and zonation.* In: Turner, K.A., Schuster, R.L. (Eds.), Landslides: investigation and mitigation, Transport Research Board Special Report, **247**, 129– 177.

Spinetti, C., Mazzarini, F., Casacchia, R., Colini, L., Neri, M., Behncke, B., Salvatori, R., Buongiorno, M.F., Pareschi, M.T., (2009). *Spectral properties of volcanic materials from hyperspectral field and satellite data compared with LiDAR data at Mt. Etna.* The International Journal of Applied Earth Observation. 11, 142–155.

Squarzoni, C., Delacourt, C. and Allemand, P. (2003). *Nine years of spatial and temporal evolution of the la valette landslide observed by SAR interferometry*. Engineering Geology. 68, 53-66.

Strozzi, T., Farina, P., Corsini, A., Ambrosi, C., Thuring, M., Zilger, J., Wiesmann, A., Wegmuller, U. and Werner, C., (2005). *Survey and monitoring of landslide displacements by means of l-band satellite sar interferometry*. Landslides. 2, 193-201.

Tansey, K., Chambers, I., Anstee, A., Denniss, A., Lamb, A., (2009). *Object-oriented classification of very high resolution airborne imagery for the extraction cover in agricultural areas*. Applied Geography. 29, 1145–1157.

Teza, G., Galgaro, A., Zaltron, N. and Genevois. R., (2007). *Terrestrial laser scanner to detect landslide displacement fields: a new approach*. International Journal of Remote Sensing, 28, 3425-3446.

Tomas, R., Herrera, G., Lopez-Sanchez, J.M., Vicente, F., Cuenca., A. and Mallorquì, J.J., (2010). *Study of the land subsidence in Orihuela City (SE Spain) using PSI data: Distribution, evolution and correlation with conditioning and triggering factors*. Engineering Geology. 115, 105-121.

Travelletti, J., Oppikofer, T., Delacourt, C., Malet, J., Jaboyedoff, M., (2008). *Monitoring landslide displacements during a controlled rain experiment using a long-range terrestrial laser scanning (TLS)*. Int Archi Photogramm Remote Sens. 37, 485–490.

Tsai, F., Hwang, J.-H., Chen, L.-C., & Lin, T.-H., (2010). *Post-disaster assessment of landslides in southern Taiwan after 2009 Typhoon Morakot using remote sensing and spatial analysis*. Natural Hazards Earth System Sciences. 10, 2179–2190.

Tso, B., Mather, P.M., (2000). *Classification Methods for Remotely Sensed Data*. CRC Press, Boca Raton, FL, USA.

Tucker, C. J. (1979). *Red and photographic infrared linear combinations for monitoring vegetation*. Remote Sensing of Environments 8, 127-150.

UN/ISDR. *Living with risk. a global review of disaster reduction initiatives. Technical report*, UN Publications, Geneva, 2004.

Vai, G.B., Martini, I.P, (2001). *Anatomy of an Orogen: The Apennines and Adjacent Mediterranean Basins*. ISBN 0-412-75040-6

Van Den Eeckhaut, M., Poesen, J., Govers, G., Verstraeten, G., Demoulin, A. (2007). *Characteristics of the size distribution of recent and historical landslides in a populated hilly region.* Earth and Planetary Science Letters. 256, 588-603.

Van Der Meer, F.D., van Der Werff, H.M.A., van Ruitenbeek, F.J.A., Hecker, C.A., Bakker, W.H., Noomen, M.F., van Der Meijde, M., Carranza, E.J.M., Smeth, J.B.D., Woldai, T., (2012). *Multi- and hyperspectral geologic remote sensing: a review*. The International Journal of Applied Earth Observation. 14, 112–128.

Varnes, D.J & International Association of Engineering Geology Commission on Landslides and Other Mass Movements (1984). *Landslide hazard zonation: A review of principles and practice*. Natural Hazards, 3, Paris, France. UNESCO, 63 pp.

Vilardo, G., Ventura, G., Terranova, F., Matano, F. and Nardò, S., (2009). *Ground deformation due to tectonic, hydrothermal, gravity, hydrogeological, and anthropic processes in the Campania Region (Southern Italy) from Permanent Scatterers Synthetic Aperture Radar Interferometry*. Remote Sensing of Environment. 113, 197-212

Weirich, F., & Blesius, L. (2007). *Comparison of satellite and air photo based landslide susceptibility maps*. Geomorphology. 87, 352–364.

Werner, C., Wegmuller, U., Strozzi, T., Wiesmann, A., (2003). *Interferometric Point Target Analysis for deformation mapping*. Proceedings of IGARSS 2003, Toulouse (France).

World Meteorological Organization "Weather Information for Barcelona".

WP/WLI (International Geotechnical Societies=UNESCO Working Party on World Landslide Inventory), 1993. *Multilingual Landslide Glossary*. BiTech Publishers Ltd.

Wright, A., Marcus, A., Aspinall, R., (2000). *Evaluation of multi-spectral, fine scale digital imagery as a tool for mapping stream morphology*. Geomorphology. 33, 107-120

Ye, X., Kaufmann, H. and Guo, X. F. *Landslide monitoring in the three gorges area using d-insar and corner reflectors*. Photogrammetric Engineering and Remote Sensing. 70, 1167-1172.

Ylmaz, I., (2008). *Landslide susceptibility mapping using frequency ratio, logistic Regression, artificial neural networks and their comparison: A case study from kat landslides(Tokat—Turkey)*., Computer & Geosciences. 35, 1125-1138.

Zhao, C. Y., Zhang, Q., Ding, X. L., Lu, Z., Yang, C. S., Qi, X. M. (2009). *Monitoring of land subsidence and ground fissures in Xian, China 2005–2006: mapped by SAR interferometry*. Environmental Geology. 58, 1533–1540.

7. Appendices

7.1.   Appendix 1: Attributes of the Tuscany Landslide Database

FIELD NAME	DESCRIPTION	TYPE	CODE
Sigla	Code for the state of activity	Text	a1 = indeterminate a1a = active a1q = dormant a1s = stabilized a1r = relict
Mov	Landslide type (Cruden & Varnes, 1996)	Text	a = indeterminate b = slide c = flow d = fall e= topple f = spread
Dir_UNIFI	Mean direction of movement	Short Integer	Degrees From 0°(excluded) to 360° (north)
Satellite	Satellite *dataset* utilized to perform the modification	Text	1a = ERS ascending orbit 1d = ERS descending orbit 2a = ENVISAT ascending orbit 2d = ENVISAT descending orbit
Modified	Polygon modified or not	Text	"s" = modified polygon "n" = original polygon
New	Landslide detected during the update and not contained in the original inventory.	Text	"s" = new landslide "n" = landlside contained in the original inventory
Mod_Perim	Modification to perimeter	Text	"s" = perimeter modified "n" = perimeter not modified
Mod_Activ	Modification to the state of activity	Text	"s" = state of activity modified "n" = state of activity not modified
Mod_Direct	Modification to the displacement direction	Text	"s" = direction modified "n" = direction not modified
Pro-Parte	Indicate if the polygon is a part of an original splitted polygon. Every part is classified as modified *pro-parte*	Text	"s" = part of a pre-existing polygon "n" = original polygon
LengUNIFI	Perimeter lenght of the polygon	Double	Value in meters
AreaUNIFI	Area of the polygon	Double	Value in square meters
COMUNE	Municipality in which the landlside is placed	Text	Municipality name
PROVINCE	Province in which the landlside is placed	Text	Province name
Conferma	Indicate if the original polygon attributes have been confirmed using the PS data.	Text	"s" = attributes confirmed by the PSs "n" = no PS data

7.2. Appendix 2: Parameters of the tree-decision classifier used in the change-detection process

Derived Features	Geophysical significance	Formulation	Measurement Unit	Sensor
Normalized Difference Vegetation Index	Surface spectral properties at the t time	$$NDVI_t = \frac{\rho_{NIR,t} - \rho_{RED,t}}{\rho_{NIR,t} + \rho_{RED,t}}$$	[-]	ADS40
Absolute value of the difference of Normalized Difference Vegetation Indices	Change of surface spectral properties	$$DNDVI = \left| NDVI_2 - NDVI_1 \right|$$	[-]	
Normalized Digital Surface Model	Object height	$$nDSM_t = DSM_t - DTM_t$$	[m]	LiDAR
Maximum of Normalized Digital Surface Models	Maximum object height	$$NDSM = \max_{i=1,2}\left(nDSM_i \right)$$	[m]	
Absolute value of the difference of Normalized Digital Surface Models	Changes of object height	$$DnDSM = \left| nDSM_2 - nDSM_1 \right|$$	[m]	
Average of Normalized Digital Surface Models	Average object height	$$nDSM_{avg} = \left(nDSM_2 + nDSM_1 \right)/2$$	[m]	
Average of the slope of Digital Terrain Models	Terrain slopes	$$dDTM_{avg} = \left(dDTM_2 + dDTM_1 \right)/2$$	[degrees]	
Average of the slope of Normalized Digital Surface Models	Surface roughness	$$dnDSM_{avg} = \left(DSM_2 + DSM_1 \right)/2$$	[degrees]	
Average of Digital Terrain Models	Ground level	$$DTM_{avg} = \left(DTM_2 + DTM_1 \right)/2$$	[m]	

7.3. Appendix 3: Other subsidences in Barcelona

Metro L5 between Horta and Vall d'Hebron.

Figure 92. Position of the area affected by subsidence between the stations of Horta and Vall d'Hebron.

In the northern part of the city a new section of the metro line L5 was under construction during the satellite acquisition time. It is a new segment that connect the stations of Horta and Vall d'Hebron which excavation works, and the consequent modification of the sub-superficial hydrogeological setting, have originated a general ground settlement of the area.

The study area is placed in correspondance of two tiles of the full frame.

Since the density of point processed reordering with a gamma value of 0,8 was already satisfying a further densification has been performed only in correspondence of the station Vall d'Hebron, lowering the gamma value from 0,85 to 0,83. The resulting of PS have been therefore geo-codified and analysed.

The results allow to perform a detailed delimitation and characterization of the area in terms of extent and deformation patterns during the satellite acquisition time (Figure 92).
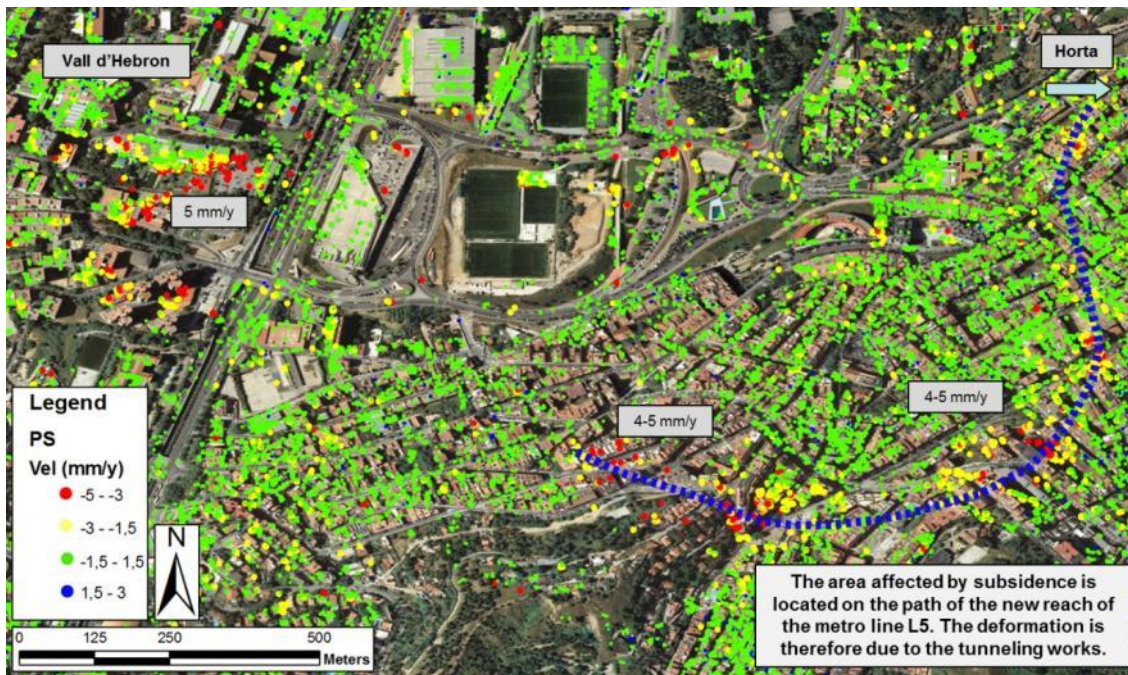
Figure 93. Geocoded velocity map obtained by the available TerraSAR-x data in the area of Horta and Vall d'Hebron.

The PS data resulted very useful to delimit the ground motion area that corresponds to the path of the new metro line 5 (Figure 93). The processed dataset has given a satisfyng points density that has highlighted the extent of the area.

The complexive deformation pattern measured during the entire time of acquisition shows a large area where the subsidence phenomenon reach velocity values that range between 3,5 and 7 mm/y, in proximity of Vall d'Hebron metro station.

A further significant subsidence area is visible on the velocity map. A belt-shaped area in correspondence of the path of line 5, in which the deformation velocities range around an average of 3 mm/y with maximum values up to 4,4 mm/y.

Parc Logìstic

The area neighbouring the new L9 metro station of Parc Logìstic is placed in the southern part of the city, between the hill of Montjuic and the Llobregat river.

This area is basically characterized by industrial units and recently builded superficial infrastructures that make it an important junction point in the street and railway network of the city (Figure 94).
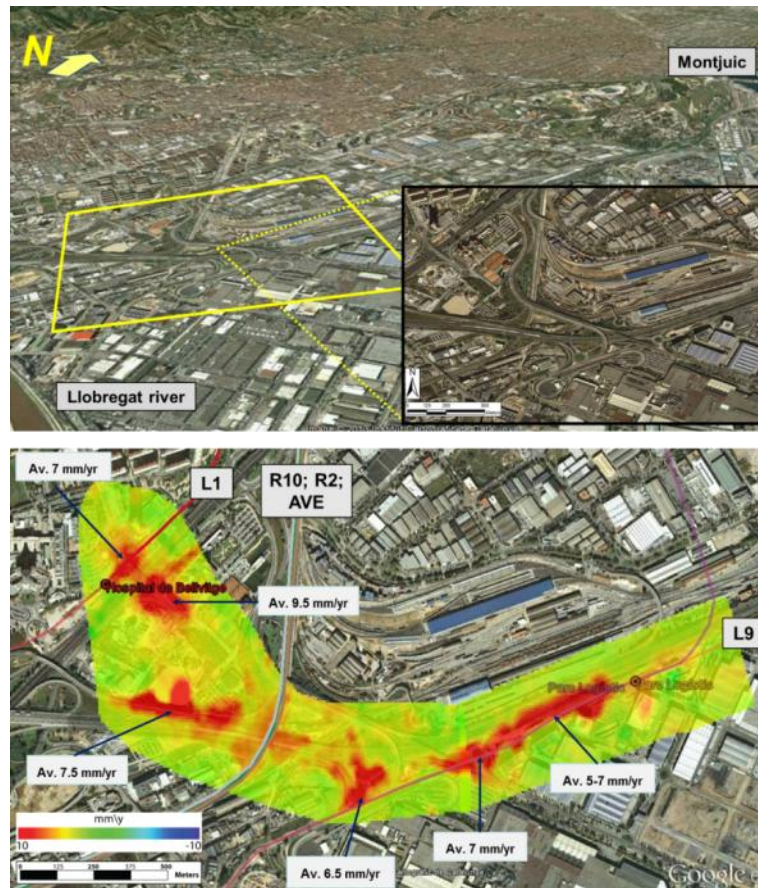
Figure 94. Position of the new industrial area of Parc Logìstic (top) with raster velocity map obtained interpolating the values measured by the PSs using the Inverse Distance Weighted algorithm.

As shown in Figure 95 the PS data show a complex pattern of surface deformation during the 2 years of observations.

In order to characterize the ground motion, the area has been divided in three parts, corresponding to the three zoom boxes.

Luca Tanteri − *"Integration of Remote-Sensing techniques and geomorphological analysis for the characterization and mapping of ground instability at regional scale"*
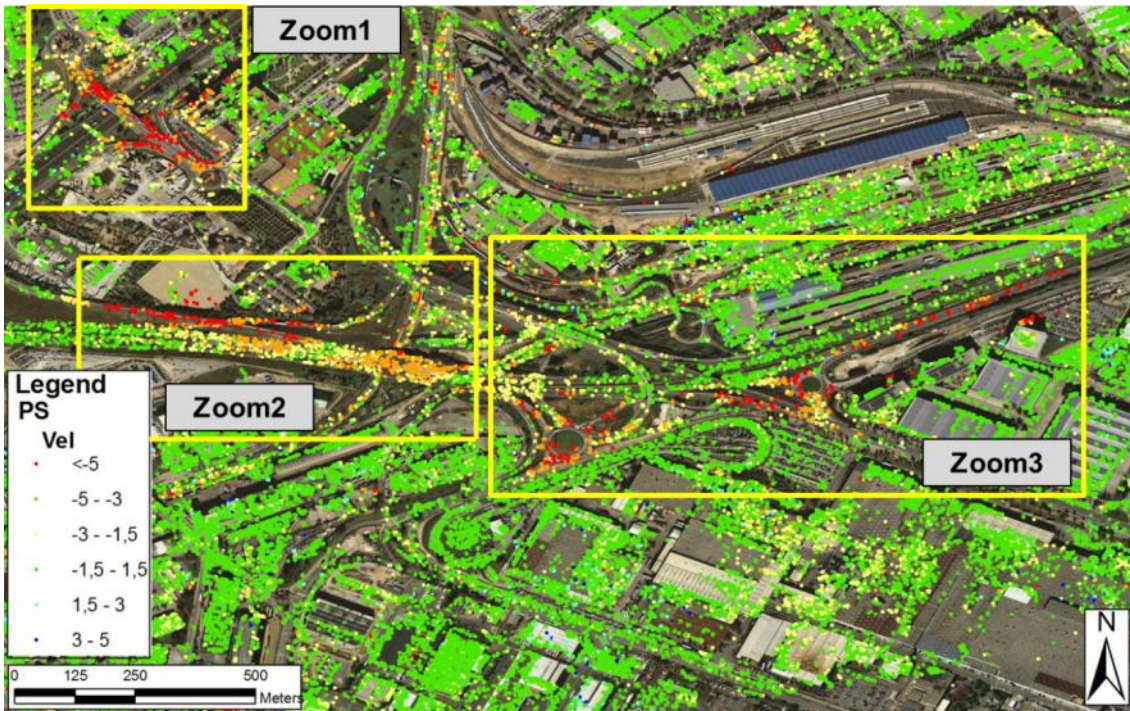
Figure 95. Parc Logìstic

In the zoom 1 (Figure 96) a new road (Camì Pau Redò) on a bridge that crosses the «Avinguda de la Gran Via de l'Hospitalet», built around 2005, show deformation with velocities of up to 8 mm/yr. The ground motion has been interpreted as a consequence of the normal compaction of soil due to the weight of the structure on the abutments that caused a general settlement of the area.

Figure 96. Zoom 1

In the zoom 2 (Figure 97) the deformation pattern is related to the bridge of Ronda Litoral that crosses the railway and to a small area of the road that connects Ronda Litoral and Gran Via de l'Hospitalet.

The PSs register an average velocity of about 4 mm/yr on the bridge, whereas on the road next to the Ronda Litoral the velocity values increase up to 8 mm/yr. The deformation measured on the bridge is related to a general settlement of the structure but could be also caused by a thermal expansi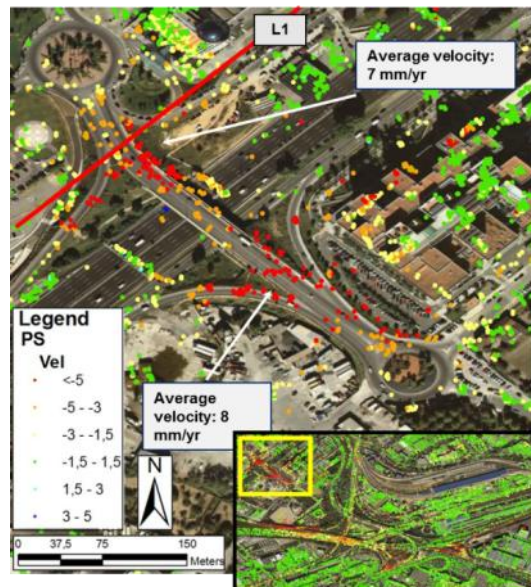on. The settlement of the road is probably due to a compaction of the soil in response to some works done between 2004 and 2006.
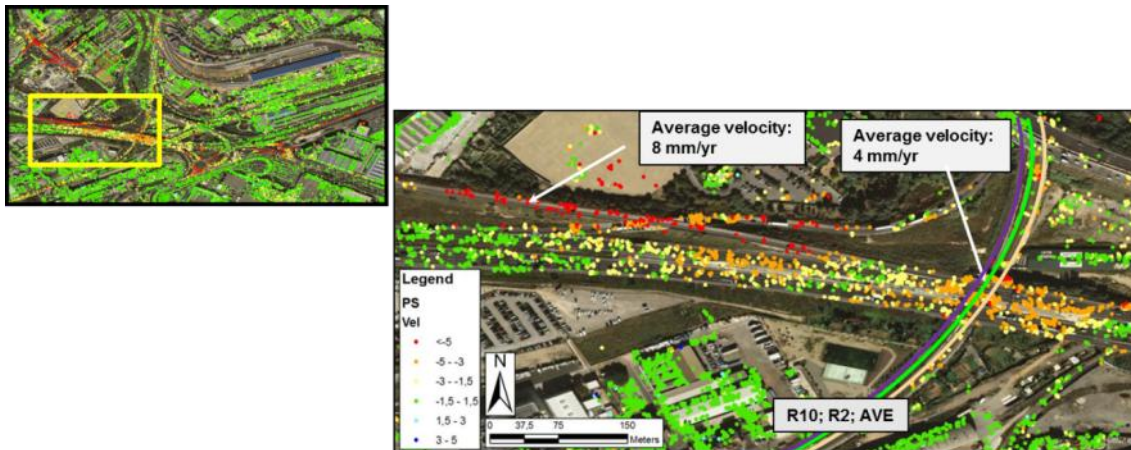
Figure 97. zoom 2

In the zoom 3 (Figure 98), the deformation pattern is related to the underground works carried out to build a new underground line (L9). The path of the line is shown in the orthophoto and there is a strong spatial connection between the line path and the subsidence area. The deformation velocity measured along the LOS of the satellite generally range between 5.5 mm/yr and 6.5 mm/yr.
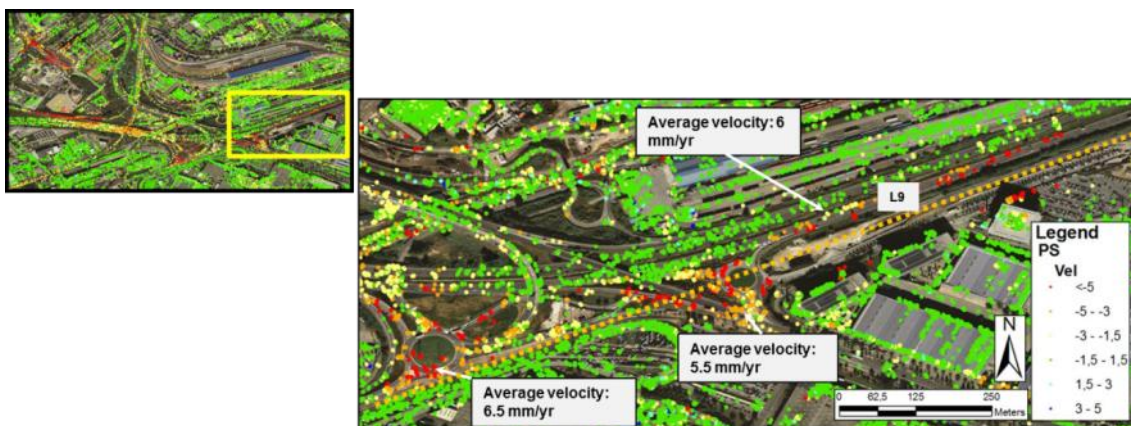
Figure 98. zoom 3

Several interferograms generated from TerraSAR-X images have been examined in order to better characterize the temporal evolution of the deformation. For this purpose only the interferometric pairs with very short (< 40 m) perpendicular baselines have been taken into account.

Unfortunately, due to the extremely high noise in the interferograms, fringes were not visible.

Luca Tanteri — *"Integration of Remote-Sensing techniques and geomorphological analysis for the characterization and mapping of ground instability at regional scale"*

8. Annexes

8. Annexes

Annex 1 – pag. 149

Lagomarsino, D., Battistini A., Tanteri, L. (2013)

"High resolution multispectral and LiDAR data integration for landslide detection purposes"

Rendiconti Online della Società Geologica Italiana, Vol.24, pp. 187-189

Annex 2 – pag. 152

Forzieri, G., Tanteri, L., Moser, G., Catani, F. (2013)

"Mapping natural and urban environments using airborne multi-sensor ADS40-MIVIS-LiDAR synergies"

International Journal of Applied Earth Observation and Geoinformation, Vol. 23, pp 313-323.

High resolution multispectral and LiDAR data integration for landslides detection purposes

Daniela Lagomarsino (*), Alessandro Battistini (*) & Luca Tanteri (*)

RIASSUNTO

Integrazione di dati multispettrali ad alta risoluzione e LiDAR per la mappatura di fenomeni franosi.

In questo studio è testata una procedura per individuare automaticamente i fenomeni franosi mediante l'applicazione di tecniche di *target detection* e *change detection* su dati acquisiti da sensori aviotrasportati. I dati utilizzati in questo studio sono stati acquisiti, con un sensore Multispettrale ADS40 e con un dispositivo LiDAR (*Light Detection And Ranging*), in due differenti sorvoli: rispettivamente nell'Ottobre 2009 e nel Novembre 2010. È stato sviluppato un sistema per classificare la copertura del suolo e definirne le variazioni eventualmente verificatesi tra le due campagne di acquisizione attraverso un algoritmo *pixel-oriented*, basato su un albero di classificazione multitemporale. Al fine di identificare al meglio i fenomeni franosi sono stati analizzati alcuni fattori morfometrici derivati dal DEM LiDAR, le cui variazioni, possono essere correlate alla verificarsi di frane nel periodo intercorso tra i due sorvoli. È stato costruito un *database* delle frane avvenute nel periodo di riferimento tramite fotointerpretazione per analizzare le caratteristiche morfometriche delle aree interessate da fenomeni franosi. Tali analisi statistiche hanno permesso di sviluppare un software che fornisce una mappa delle aree in cui si sono verificati dissesti di versante tra le due acquisizioni.

Key words: *Airborne sensors, change detection, high-resolution multispectral data, landslide detection, LiDAR.*

INTRODUCTION

The automatic detection of landslides is an important task to improve landslide hazard and risk management.

Many developments have taken place in the last decade related to method for the automatic detection of landslides based on their spectral or altitude characteristics (Van Westen *et alii*, 2008). Metternicht *et alii* (2005) analyzed the use of remote sensing techniques to detect and identify landslides. Several researcher employ DEMs to diagnostic landslide feature: Dragut & Blaschke (2006) use elevation, profile curvature, plan curvature and slope gradient derived from DTM, to automatically classify landform elements. Furthermore the identification of landslides can include analysis on vegetation, slope angle, slope morphology, drainage, tension cracks, presence of man-made features such as retaining walls, or artificial surface drainage (Martha *et alii*, 2010).

The purpose of this work is to test a method to automatically detect landslides by combining change detection techniques of airborne sensor data and morphological analysis of Digital Elevation Models (DTMs).

STUDY AREA

The proposed procedure is tested on a 80 km transect of the Marecchia Valley (Emilia Romagna, Italy – Fig. 1). The landscape morphology is highly affected by the geological setting. Even though climate is typically Mediterranean with summer drought and winter rains, the climatic regime is significantly modulated by orographic features and mitigating sea effects.

Frequent atmospheric disturbances from North-East may cause intense downpours even coming from the coastal plains along with intense snowfalls during the winter months.

REMOTELY SENSED DATASETS

Multispectral ADS40 and Light Detection and Ranging (LiDAR) data, acquired in October 2009 and November 2010, were used in this study to detect possible land cover changes between the two acquisitions. This process has been proved to be suitable to describe the spatiotemporal dynamics of geo-morphological features (fluvial changing landforms and slope instability).

High spatial resolution color-infrared aerial digital image data from the ADS40 sensor (Leica L-H System) has 4 spectral bands: blue (430–490nm), green (535–585 nm), red (610–660
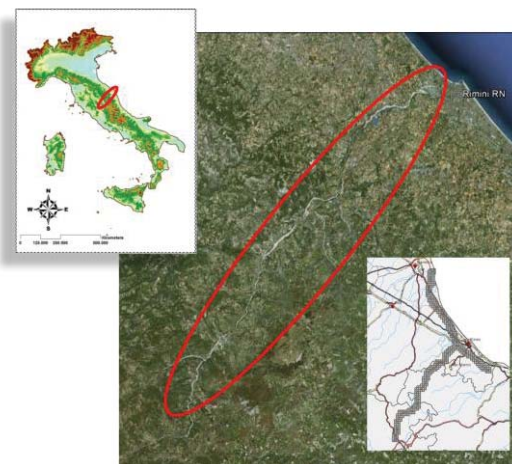

Fig. 1 – Study area.

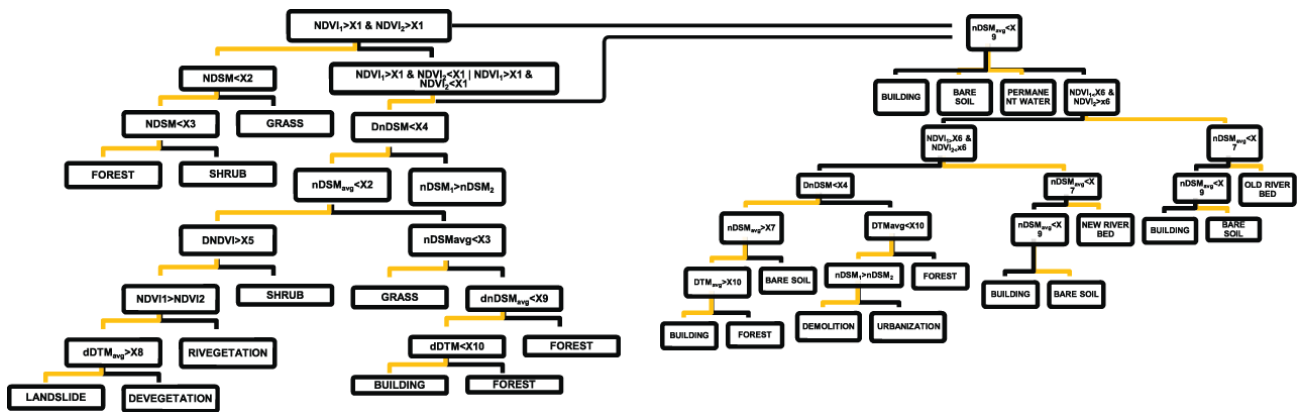(*) Dipartimento di Scienze della Terra, Università di Firenze.

Fig. 2 – Tree decision algorithm used in change-detection analysis.

nm), and near-infrared (NIR) bands (835–885 nm). The imagery data has a 12-bit radiometric depth, with 0.2 meter pixel size.

Airborne laser scanning data collected by a LiDAR sensor (Optech Gemini) were provided in terms of Digital Terrain Model (DTM) and Digital Surface Model (DSM) with 1-meter spatial resolution and 0.2 meters vertical accuracy.

CHANGE DETECTION

In order to consider the changes in the landcover between the two acquisitions, a pixel-oriented approach based on a tree-decision classifier has been adopted. This approach takes into account the changes of spectral and geomorphological parameters, such as NDVI (TUCKER, 1979) and height differences.

The tree-decision classifier (Fig. 2) is based on a set of rules in order to detect the target variables generating a binary branch structure. The process is shown in the above flow diagram. The threshold values have been a priori defined on the basis of a try-and-error procedure.

The output classified raster has been sieved class by class applying a 3×3 sized kernel, in order to establish if an isolated pixel belongs to the same class of the 8 surrounding cells. The outcome is a map containing the information about the main natural/human-induced surface processes, such as urban planning (urbanization/demolition), agricultural and forest management (crop rotation/rivegetation/devegetation), fluvial dynamics (river bed transitions) and slope instability (landslides/changing landforms).

GEOMORPHOLOGICAL ANALYSES

By comparing the optical images of 2009 and 2010 a landslide inventory map has been developed.

The inventory is at the base of all the statistical analyses proposed in this work.

The automatic characterization of landslide areas could be implemented in the change detection process by considering a potentially wide range of factors. (SOETERS & VAN WESTEN, 1996; VAN WESTEN *et alii*, 2008).

In this study we consider the change occurred between the two LiDAR acquisitions of the factors listed in this table. All these surface parameters were derived from DTM (Table 1).

The changes that resulted most correlated to the landslides occurrence were the height values of DTM, the slope and the

TABLE 1
Surface parameters derived from DTM

Data source	Variable	Description
Lidar (DTM)	Altitude	
	Slope angle	Slope angle value in degrees.
	Planar curvature	Second derivative of the surface perpendicular to the slope direction.
	Profile curvature	Second derivative of the surface in the direction of slope
	Roughness	Divergence of vectors normal to pixel surface
	Specific catchment area	Upslope area per unit width of contour
Secondary indices	Topographic Wetness Index	Depends on specific catchment area and slope angle
	Steam Power Index	Depends on specific catchment area and slope angle
	Sediment transport capacity index	Depends on specific catchment area and slope angle

roughness. The other parameters didn't show any different variation between the landslides and their surrounding area.

The parameters in this table were calculated in the landslides zone and around it, identifying a circular buffer of 100 m radius. Then the difference between the first and the second acquisition was calculated. To investigate if the parameters variation trend was different between the two analyzed areas, statistical analyses were performed.

The trend of the difference was analyzed in specific areas, defined observing the RGB data: bare soil, erosion, herbaceous areas and others showing a vegetation reduction between the two acquisitions.

In order to establish if the distribution of each parameter was different inside the landslides area with respect to the

others, the four statistical moments were calculated and a t-test was implemented. The results show that the DTM, the slope and the standard deviation of the DTM difference had a characteristic behavior inside the landslides zone.

The differences map was divided into several classes and, in order to verify the presence of prevailing classes, for such parameters the frequency ratio model was calculated (LEE & TUDAN, 2005; YILMAZ, 2008):

$$FR_i = \frac{NpixX_i / (\sum NpixX)}{NpixN_i / (\sum NpixN)} \quad (1)$$

where $NpixX_i$ is the number of pixels of the i class falling within polygons representing landslides, $NpixN_i$ is the total number of pixels within the class i. A landslide classification scheme was developed taking into account the increasing degree of membership probability. The probability P that a pixel contains a landslide occurred between the two acquisitions is then calculated (LEE & TALIB, 2005):

$$P = \sum_{j=1}^{N} FR_j \quad (2)$$

where j is the considered morphometric parameter, N is the total number of considered parameters (DTM, slope and the DTM standard deviation) and FR is the corresponding value of Frequency Ratio.

RESULTS

The result was then subdivided into 5 classes of probability: null, low, medium, high and very high.

Consequently, post-processing refinements have been used to reduce misclassification errors and mapping inconsistencies, which conducted to a lower number of membership classes and a decrease in uncertainty accounting for the range in probability values of neighboring pixels. Such techniques are based on morphological operations applied to the previously classified image by sequentially applying sieve and clump image processing techniques. Furthermore it was decided to aggregate the probability classes and classify as landslides only the pixels having a mean value, over a 3×3 m window, of at least 2.1, considering that it was assigned to the previously mentioned classes a numerical value from 1 to 5. In such way, a probability map of occurred landslides, with only 2 classes was built (Fig. 3). This map enables to better identify the perimeter of the detected landslides; furthermore the false alarms were strongly reduced.
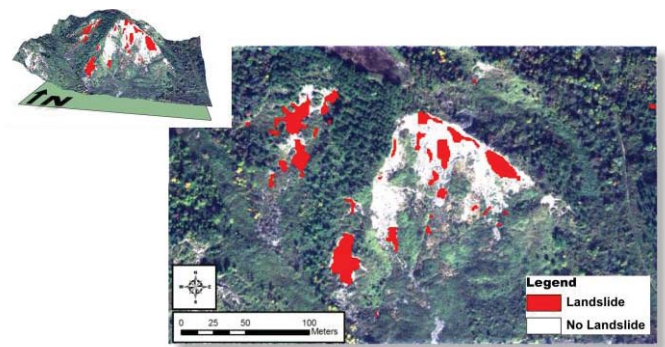

Fig. 3 – Resulting landslide probability map.

REFERENCES

DRAGUT L. & BLASCHKE T. (2006) - *Automated classification of landform elements using object-based image analysis.* Geomorphology, **81**, 330-344.

LEE S. & TALIB J.A. (2005). *Probabilistic landslide susceptibility and factor effect analysis.* Environmental Geology, **47**, 982–990.

LEE S. & TUDAN N. (2005). *Probabilistic landslide susceptibility mapping in the Lai Chau province of Vietnam: focus on the relationship between tectonic fractures and landslides.* Env. Geol., **48**, 778–787.

MARTHA T.R., KERLE N., JETTEN V.G., VAN WESTEN C.J. & KUMAR K.V. (2010) - *Characterising spectral, spatial and morphometric properties of landslides for semi - automatic detection using object-oriented methods.* Geomorphology, **116**, 24-36.

METTERNICHT G., HURNI L. & GOGU R. (2005) - *Remote sensing of landslides: An analysis of the potential contribution togeo-spatial systems for hazard assessment in mountainous environments.* Remote Sensing of Environment, **98**, 284-303.

SOETERS R. & VAN WESTEN C.J. (1996) - *Slope instability recognition, analysis, and zonation.* In: Turner K.A. & Schuster R.L. (Eds.) - Landslides: investigation and mitigation, Transport Research Board Special Report, **247**, 129–177.

TUCKER C.J. (1979) - *Red and photographic infrared linear combinations for monitoring vegetation.* Remote Sensing of Environment, **8**, 127-150.

VAN WESTEN C.J., CASTELLANOS E. & KURIAKOSE S. L. (2008) - *Spatial data for landslide susceptibility, hazard, and vulnerability assessment: An overview.* Engineering Geology, **102**,112-131.

YLMAZ I. (2008) – *Landslide susceptibility mapping using frequencyratio, logistic Regression, artificial neural networks and their comparison: A case study from kat landslides (Tokat—Turkey).* Computer & Geosciences, **35**, 1125-1138.
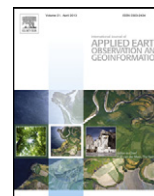
Mapping natural and urban environments using airborne multi-sensor ADS40–MIVIS–LiDAR synergies

Giovanni Forzieri [a,b,*], Luca Tanteri [b], Gabriele Moser [c], Filippo Catani [b]

[a] Climate Risk Management Unit, Institute for Environment and Sustainability, Joint Research Centre, European Commission, Ispra, Italy
[b] Department of Earth Sciences, University of Florence, Italy
[c] Department of Telecommunications, Electronic, and Electrical Engineering, and Naval Architecture, University of Genoa, Italy

A B S T R A C T

The recent and forthcoming availability of high spatial resolution imagery from satellite and airborne sensors offers the possibility to generate an increasing number of remote sensing products and opens new promising opportunities for multi-sensor classification. Data fusion strategies, applied to modern airborne Earth observation systems, including hyperspectral MIVIS, color-infrared ADS40, and LiDAR sensors, are explored in this paper for fine-scale mapping of heterogeneous urban/rural landscapes. An over 1000-element array of supervised classification results is generated by varying the underlying classification algorithm (Maximum Likelihood/Spectral Angle Mapper/Spectral Information Divergence), the remote sensing data stack (different multi-sensor data combination), and the set of hyperspectral channels used for classification (feature selection). The analysis focuses on the identification of the best performing data fusion configuration and investigates sensor-derived marginal improvements. Numerical experiments, performed on a 20-km stretch of the Marecchia River (Italy), allow for a quantification of the synergies of multi-sensor airborne data. The use of Maximum Likelihood and of the feature space including ADS40, LiDAR derived normalized digital surface, texture layers, and 24 MIVIS bands represents the scheme that maximizes the classification accuracy on the test set. The best classification provides high accuracy (92.57% overall accuracy) and demonstrates the potential of the proposed approach to define the optimized data fusion and to capture the high spatial variability of natural and human-dominated environments. Significant inter-class differences in the identification schemes are also found by indicating possible sub-optimal solutions for landscape-driven mapping, such as mixed forest, floodplain, urban, and agricultural zones.

© 2012 Elsevier B.V. All rights reserved.

1. Introduction

Land cover is a crucial variable, which plays an important role in most soil–atmosphere interactions (Feddema et al., 2005). The significance of providing accurate fine-scale land cover maps is emphasized by the evidence of marked impacts of land cover changes on local surface dynamics (Claessens et al., 2009). Remote sensing data classification represents an essential tool for environmental monitoring and sustainable land use management (Melesse et al., 2007), especially in heterogeneous landscapes characterized by many interconnected natural- and human-induced processes (Forzieri and Catani, 2011). Given the large number of diverse land cover types and their possible interclass spectral overlapping, automatic mapping of complex urban/rural patterns represents a

difficult task, particularly when very high spatial resolutions are concerned.

Modern space-borne hyperspectral (e.g., HYPERION, CHRIS/PROBA) and laser scanner (ICESat/GLAS) sensors recently offered an interesting potential in land surface characterization (e.g., Duca and Del Frate, 2008; Goodenough et al., 2003), but may still exhibit possible inaccuracies in monitoring environments that are highly variable in space (e.g., Cavalli et al., 2008; Pignatti et al., 2009). In this context, high-resolution airborne sensors represent enhanced mapping tools (e.g., Gianinetto and Lechi, 2004; Lu et al., 2007; Melgani and Bruzzone, 2004) and also preliminary tests to drive planned satellite-based systems (e.g., PRISMA, EnMAP, HyspIRI, Sentinel). High spatial resolution airborne color-infrared sensors (e.g., Intergraph DMC, ADS40, RC30) provided encouraging classification performances especially in antrophic areas, such as agricultural and urban zones (Belluco et al., 2006; Tansey et al., 2009). Airborne hyperspectral data, such as Multispectral Infrared Visible Imaging Spectrometer (MIVIS), Airborne Visible InfraRed Imaging Spectrometer (AVIRIS), and HyMap, thanks to their high

spectral resolutions, have demonstrated to be powerful tools to discriminate land cover classes with partially overlapping of spectral signatures in the feature space, such as forest and wetland ecosystems (Colombo et al., 2008; Forzieri et al., in press; Hirano et al., 2003) and geologic features (van Der Meer et al., 2012). Light Detection and Ranging (LiDAR) data have been extensively used for mapping tasks due to their ability to capture the 3D structure of the monitored surfaces, especially in vegetated and built-up areas (e.g., Forzieri et al., 2009; Priestnall et al., 2000).

Several data fusion methods have been successfully tested for classification of different landscape scenarios. Here, we point out that the terms "data fusion" and "multi-source (multi-sensor)" classification are used in this work as synonymous with the meaning of labeling pixels by drawing inferences from several input data sources, according to the definition given by Richards and Jia (2006). A common technique of data fusion for multi-source classification is the stacked vector approach that consists in generating extended pixel vectors stacking together the individual vectors that correspond to each input data source (Richards and Jia, 2006; Tso and Mather, 2000). The fusion of LiDAR and hyperspectral/multispectral data exhibited an interesting potential in several application fields including the retrieval of biophysical and geological properties of land surfaces (Anderson et al., 2008; Forzieri et al., 2012a; Spinetti et al., 2009). The combined use of laser scanner and spectral data was particularly effective in classification tasks to distinguish vegetation types (e.g., Dalponte et al., 2008; Elaksher, 2008; Mundt et al., 2006), anthropogenic surfaces (e.g., Chen et al., 2009), and land cover changes (Forzieri et al., 2012b). Additional derived features, such as texture or DTM-based layers, have been used to improve class discrimination over cropfields and riparian corridors (e.g., Forzieri et al., 2010; Herold et al., 2003).

Mapping approaches based on multisource data can be either contextual or noncontextual depending on the possible use of spatial information. Region- and object-based methods represent a primary subcategory of contextual classification methods. Noncontextual classifiers label the (multi-source) signature of each pixel regardless of all other pixels (e.g., Richards and Jia, 2006), thus discarding the spatial information associated with the image. Contextual approaches use both spectral and spatial information (Moser and Serpico, in press; Moser et al., in press). The former approach bears the obvious advantage of simplicity, but the latter generally includes more powerful classification techniques. Region-based and object-based methods currently play a primary role in the literature of contextual classification, especially when high-resolution data are concerned. A basic region-based approach may be two-step process involving: (1) segmentation of the image into homogeneous regions, possibly representing objects or parts of objects, and (2) classification of those regions (e.g., de Jong and van der Meer, 2004; Navulur, 2007). However, more sophisticated region-based architectures can be devised, depending on the nature of data being analyzed, their spatial resolutions, the computational resource available, and the intended application of the classified data (Lillesand et al., 2008; Moser et al., in press).

Even though the costs of airborne image acquisition are high compared to satellite remote sensing image procurement and may represent an operational constraint in several environmental applications, their exploitation can be viewed both as a preliminary step toward the development of spaceborne advanced monitoring systems and in the perspective of the application to specific monitored areas of particular environmental interest. In light of the recent advances in sensor technology, additional fusion experiments on modern airborne remote sensing data serve for a better understanding of the potential and limitations of current Earth observation systems. In particular, there is a great need for assessing optimized exploitation strategies of multi-sensor remote sensing data to maximize the inter-class separability in

heterogeneous landscape scenarios. In this context, hyperspectral MIVIS, color-infrared ADS40 and LiDAR data represent useful datasets to quantify multi-source synergies for image classification tasks. Given their very high spatial and spectral resolutions, such sensors have separately demonstrated to be effective for detailed land cover mapping (e.g., Belluco et al., 2006; Forzieri et al., in press), but their implementation into data fusion processes is still scarcely explored. For this purpose, in this paper we analyze different fusion strategies involving MIVIS, ADS40, and LiDAR data for classification tasks associated with complex landscapes. We generate an array of standard supervised pixel-based classification scenarios by varying a set of key choices (classifier and remote sensing data combination) and we identify the configuration with the highest accuracy on the test set. Sensor-derived marginal improvements and land cover-based performances are also investigated. The main novel contribution of this paper consists in the experimental investigation of possible synergies among high-dimensional multi-sensor airborne data (MIVIS, ADS40, LiDAR) for the classification of heterogeneous landscapes.

2. Methods

2.1. Study area

The study was conducted over a 20-km stretch of the Marecchia river ($\sim$40 km^2), that sources in Eastern Tuscany and runs at the border of the Emilia-Romagna and Marche regions, in North-Eastern Italy (43°N, 12°E) (Fig. 1). Such study area has been chosen for its complexity in land cover spatial variability and represents an excellent test to quantify multi-sensor remote sensing capability to classify heterogeneous landscapes. The hill slopes are characterized by a significant biodiversity of arboreal species, which include conifer and broad-leaved types, such as oak, pine, cypressus, and spruce (Fig. 1A, mixed forest). Riparian ecosystems exhibit complex patterns with flexible and stiff vegetation in different succession stages, such as willow, arundo donax, heatland, and poplar. Streamside caves for fluvial sediment extraction with related decantation basins are also present in the floodplain (Fig. 1B, floodplain). The valley floor is prevalently made up of fabrics/industrial units (Fig. 1C, urban zones), agricultural fields, such as croplands and olive groves, and semi-natural vegetation, such as meadows (Fig. 1D, agricultural areas).

We defined 17 main target land cover classes to be discriminated: water river (WR), water lagoon (WL), bare soil (BS), asphalt (AS), plowed field (PF), urban fabric (UF), industrial unit (IU), herbaceous (HE), heatland (HL), arundo donax (AD), poplar (PL), oak (OK), pine (PN), cypressus (CY), spruce (SP), willow (WI), and olive (OV).

2.2. Remote sensing and field data

For this study we used multi-sensor data, including optical ADS40, hyperspectral MIVIS, and LiDAR. Color-infrared aerial digital image data acquired by ADS40 have 4 spectral bands: blue (0.430–0.490 μm), green (0.535–0.585 μm), red (0.610–0.660 μm), and near-infrared (NIR; 0.835–0.885 μm). The data have 12-bit radiometric depth and 0.2-m pixel size. MIVIS is a whiskbroom hyperspectral sensor with high spatial (3-m pixel size) and radiometric (12 bit) resolution, and with variable spectral resolution (sr) depending on the spectrometer. This sensor records 102 bands spanning across the visible (20 bands within the 0.43–0.83 μm range with $sr = 0.02$ μm), near-infrared (8 bands within the 1.15–1.55 μm range with $sr = 0.05$ μm), middle-infrared (64 bands within the 1.983–2.478 μm range with $sr = 0.009$ μm) and thermal-infrared (10 bands within the 8.18–12.7 μm range
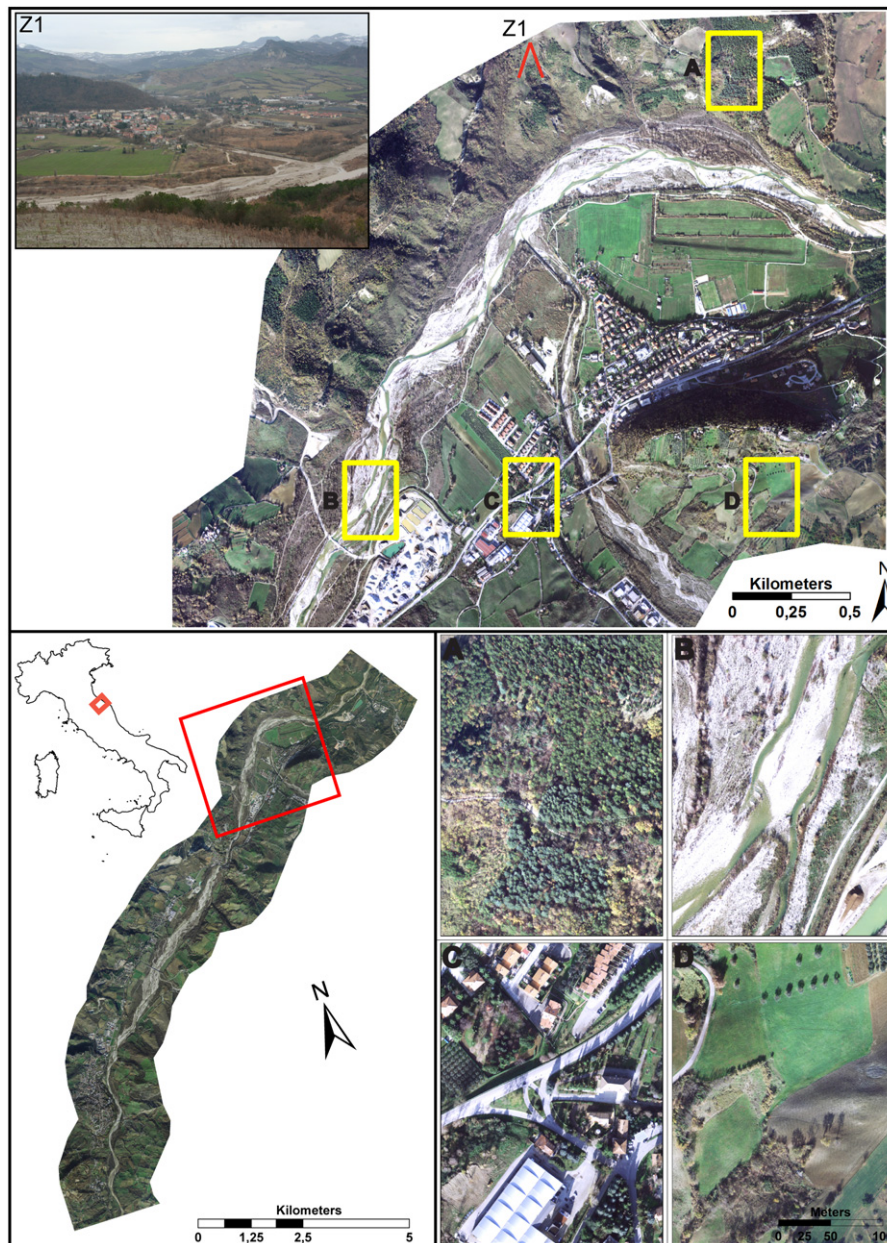
Fig. 1. Study area: key map and entire monitored 20-km stretch of the Marecchia river (Emilia Romagna, Italy) (bottom left map), reference 3-km × 3-km inset box and panoramic view (Z1) (upper map), typical investigated landscapes including mixed forest (A), floodplain (B), urban zone (C) and agricultural area (D).

with sr from 0.34 to 0.54 μm). LiDAR data were provided in terms of Digital Terrain Model (DTM) and Digital Surface Model (DSM) with 1-m spatial resolution and 0.2-m vertical accuracy. The airborne platform (Casa 212/C I-MAFE) was prepared for two camera hatches. Multi-sensor data were acquired in December 6 and 11, 2009, within a time-frame spanning from 10.00 to 14.00 UTC: ADS40 and MIVIS data were simultaneously acquired in the former acquisition date, while LiDAR data were taken in the latter date.

Training and test pixels have been collected during the same season of the remote sensing acquisitions through field surveys and through the visual interpretation of the ADS40 image. While delineating training and test polygons, pixels located along the edges between land cover types were avoided to reduce the impact of potential small registration errors and to prevent the inclusion of mixed pixels in the training and test sets. The resulting sample sizes are listed in Table 1 in terms of number of 1-m pixels.

2.3. Methodology

The proposed procedure explores different strategies of exploitation of multi-sensor remote sensing data for fine-scale mapping of 17 land cover classes. The method generates a large array of classification scenarios obtained with different sensor/setting combinations and, similar to a model identification problem, identifies the combination which maximizes the classification accuracy. The configuration to identify include: (1) classification algorithm (al); (2) multi-source data combination (FS); and (3) number n of hyperspectral channels. The array of the classification maps can be described by the following mathematical notation:

$$H = \mathrm{K}(al, FS, n) \qquad (1)$$

where H is the classification accuracy associated with the triplet (al, FS, n) used as input in the classification routine (K).

Table 1
The seventeen spectral classes used for training and testing, their codes, and the corresponding number of 1-m pixels.

Land cover class	Code	Training set [# 1-m pixels]	Testing set [# 1-m pixels]
Water river	WR	23,855	26,368
Water lagoon	WL	4448	3310
Bare soil	BS	52,414	55,022
Asphalt	AS	14,253	10,855
Plowed field	PF	90,262	81,411
Urban fabric	UF	16,557	14,587
Industrial unit	IU	13,748	12,515
Herbaceous	HE	300,477	265,074
Heatland	HL	56,977	50,986
Arundo donax	AD	10,258	9828
Poplar	PL	13,114	13,358
Oak	OK	96,804	97,532
Pine	PN	15,793	15,718
Cypressus	CY	11,241	11,996
Spruce	SP	26,774	29,576
Willow	WI	6446	6490
Olive	OV	5976	5116

2.3.1. Explored classification solutions

Fig. 2 displays the flowchart of the generation of the explored array of classification results. This generation is organized in five sequential steps.

2.3.1.1. Pre-processing.
The remote sensing data were orthorectified and co-registered in the UTM-WGS84 projection by ground control points. MIVIS radiance data were used for classification, i.e., no preliminary atmospheric correction was applied to map radiance to reflectance data. On one hand, this correction would allow atmospheric effects affecting spectra absorption features (e.g., effects associated with the bidirectional reflectance distribution function, adjacency effects) to be addressed. On the other hand, atmospheric correction in itself may introduce biases or distortions, which might negatively affect the classification performances. Therefore, similar to many previous applications of supervised classification to the problem of land-cover mapping from hyperspectral sensors (e.g., Landgrebe, 2003; Serpico and Moser, 2007), data were used in radiance format for the classification study discussed here.

Fig. 2. Flowchart of the developed classification scheme. Data, pre-processing, feature extraction, feature reduction, stacked vector and mapping procedures are differently displayed according to the reference shaded color.

2.3.1.2. Feature extraction.
To better discriminate the spectral signatures of the shadow and shadow-free areas we calculated the hillshade modeling (HM) by using the Digital Terrain Model and the solar position parameters related to the spectral data acquisition time (Burrough and McDonell, 1998). We also calculated the normalized Digital Surface Model (nDSM) by the simple subtraction of DTM and DSM to increase the inter-class separability for the 3D-derived information. Finally we computed three popular texture features (range, mean, variance, collectively labeled in the following as TX) estimated by means of a first-order statistical analysis (Haralick et al., 1973) with a 3 m × 3 m window size on a simulated panchromatic channel. This channel is defined as the average of the ADS40 channels weighed on the spectral acquisition range of each band (Wang et al., 2010). A preliminary analysis supported the suitability of the selected window size to capture spatial correlation patterns (e.g., croplands, olive fields, and road networks). Hillshade modeling (HM), normalized digital surface model (nDSM) and texture layers (TX) have been used in this study as additional features in the mapping procedure.

2.3.1.3. Feature reduction.
Within the available MIVIS dataset, we have only used the first 24 bands (spanning within the 0.43–1.319 μm spectral range), as the remaining channels were corrupted (Forzieri et al., in press). The main problematic issue in the analysis of hyperspectral data is related to the high dimensionality of the spectral space: when increasing the number of features, the Hughes' phenomenon (Hughes, 1968) may occur, that consists in a loss of classification accuracy caused by the mismatch between the number of available training samples and the number of samples that should be needed to reliably estimate the classifier parameters (Landgrebe, 2003). In order to reduce possible hyperspectral-derived dimensionality effects, we applied the Sequential Forward Selection (SFS) to the MIVIS bands (Serpico et al., 2002). This selection algorithm is based on a sub-optimal iterative search strategy, it is initialized with an empty set of selected features, and iteratively identifies the best feature subset (see Fig. 2) that can be obtained by adding to the current feature subset one feature at a time (whose size ranges in our case from 1 to 24) until the desired number n of features is achieved. The Jeffries–Matusita measure was used as an inter-class distance measure to guide this selection process (Richards and Jia, 2006). We used feature selection strategies instead of feature space transformations to preserve the physical meanings of the discriminant components of the MIVIS subsets. Within the selection methods, we chose SFS thanks to its limited computational burden and because it has been demonstrated to be a powerful and efficient tool in hyperdimensional feature space reduction (Serpico et al., 2002).

2.3.1.4. Stacked vector approach.
A straightforward approach to classify mixed data is to form extended pixel vectors stacking together the individual vectors that correspond to each input data source (stacked vector method; Richards and Jia, 2006; Tso and Mather, 2000). Here, 16 options for stacking the original (ADS40, MIVIS) and derived information (nDSM, HM, TX) were explored. The data from the resulting 16 multi-source feature spaces (FS, in Fig. 2) – which differently combine the available remote sensing information (Table 2) – were resampled at the common 1-m spatial resolution. The resampling cell size was chosen to finely capture the spatial variability of land covers without asking for massive computing power or excessive computing time.

2.3.1.5. Mapping procedure.
The generated multi-stacks were classified by means of three popular classifiers (al in Fig. 2) that have been chosen in this study for their simple implementations and computational efficiencies: the well known Maximum Likelihood (ML, Richards and Jia, 2006), Spectral Angle Mapper (SAM, Kruse
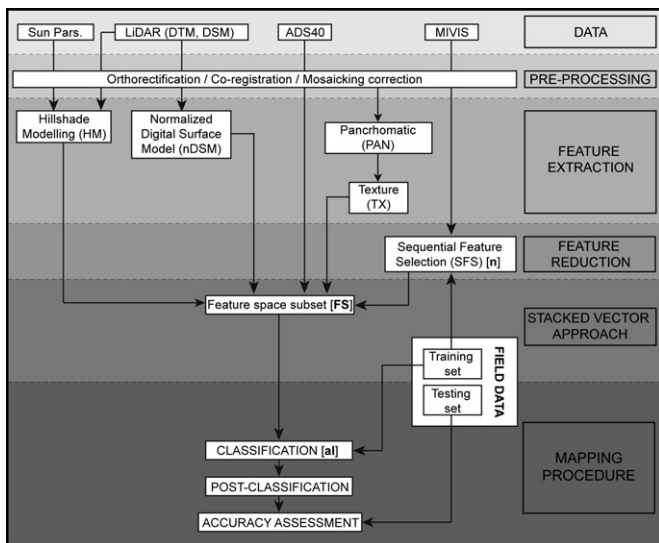
Table 2

The sixteen feature spaces used in the classification procedure (FS1, ..., FS16) including: normalized Digital Surface Model (nDSM), hillshade modeling (HM), multispectral data (ADS40), texture layers (TX) and hyperspectral data (MIVIS). Admissible numbers of input features are shown in brackets.

Feature space	nDSM [1]	HM [1]	ADS40 [4]	TX [3]	MIVIS [1:24]
FS1			X		
FS2					X
FS3	X		X		
FS4	X				X
FS5	X		X		X
FS6		X	X		
FS7		X			X
FS8	X	X	X		
FS9	X	X			X
FS10	X	X	X		X
FS11			X	X	
FS12				X	X
FS13	X		X	X	
FS14	X			X	X
FS15	X		X	X	X
FS16	X	X	X	X	X

et al., 1993), and Spectral Information Divergence (SID, Chang, 2000) classifiers. Since SAM needs as input, at least, a two-band set, all classification scenarios were accordingly developed with a minimum of two input bands to better compare the performances of different algorithms. In order to reduce possible salt-and-pepper effects, we also applied a post-classification majority filter to the resulting maps with a 3 m × 3 m kernel size (Yuan et al., 2005).

This strategy produced 1104 land cover maps with different configurations of the afore-mentioned variables (3 classifiers × 16 feature spaces × 23 hyperspectral subsets).

2.3.2. Classification accuracy assessment

Training/testing samples were used to calibrate/validate each generated configuration. The classification performances were quantified in terms of confusion matrix (M), overall accuracy (OA), commission (COM)/omission (OMI) errors and kappa conditional statistics (K_s).

Marginal improvements derived from each individual data source were also investigated by extracting, from the full array, the subsets that include/exclude the source under investigation. For each data source, we selected two different subsets (X, Y) defined as follows:

$$X = K(al, FS = fs_x, n),$$
$$Y = K(al, FS = fs_y, n), \quad al = ML, SAM, SID; \quad n = 2, \ldots, 24 \quad (3)$$

where fs_x (fs_y) denote the feature spaces that include (exclude) the considered source. These spaces are listed in Table 3 with regard to each source (ADS40, MIVIS, nDSM, HM, and TX). Then, the Behrens–Fisher statistics with 0.95 confidence level was computed for testing the difference between the means (μ) of the two overall accuracies calculated separately with the X and Y subsets. We analyzed two different tests:

$$t_1 : \begin{cases} H_0 : \mu_x = \mu_y \\ H_1 : \mu_x > \mu_y \end{cases} ; \quad t_2 : \begin{cases} H_0 : \mu_x = \mu_y \\ H_1 : \mu_x < \mu_y \end{cases} \quad (4)$$

The rejection of the null hypothesis H_0, in favor of the target hypothesis H_1, in the t_1 (t_2) case indicates a prevalent positive (negative) impact of the investigated data source on the classification performances. The large size of the classification array (1104 land cover maps) allowed for a robust quantification of the statistical significance of the possible benefits associated with each source (Kottegoda and Rosso, 1997).

2.3.3. Classification scheme identification

As mentioned previously, the behavior of the classification performances within the array of generated classification results can be assimilated to a three-parameter function ($H = K(al,FS,n)$), whose global maximum value identifies the optimal classification scheme, with respect to the criterion of maximizing the overall classification accuracy on the test set. In order to highlight specific parameter-dependent improvements and to define possible sub-optimal alternatives we described the classification scheme identification through 3 sequential steps, by progressively fixing one optimal configuration variable at a time and by accordingly reducing the size of the search space:

1st-step array subset, classifier choice;

$$H_{al}(FS, n) = \max_{al}[K(al, FS, n)] \quad (5)$$

2nd-step array subset, choice of the stacked vector configuration;

$$H_{al,FS}(n) = \max_{(FS)}[H_{al}(FS, n)], \quad (6)$$

3rd-step array subset, choice of the number of hyperspectral channels.

$$H_{al,FS,n} = \max_{(n)}[H_{al,FS}(n)], \quad (7)$$

We also explored the variability of the three key parameters (al, FS, n) across the investigated land covers to assess possible sub-optimal classification solutions more suited to specific environments, such as mixed forest, floodplain, urban, and agricultural zones.

3. Results and discussions

3.1. Classification algorithm performances (al identification)

In this section we focus on the impact of the tested classifiers (ML, SAM, SID) on the overall accuracy to identify the best performing classification algorithm (first step of the identification scheme). Fig. 3 is organized in 16 plots, each related to an individual investigated feature space (FS variable). The selected subsets composed of increasing numbers of MIVIS bands (n variable) and overall accuracies (OA) are displayed on the x-axis and y-axis, respectively (see Section 3.3 for details on the optimization of n). The three different color lines refer to the three classifiers.

Classification accuracies are obviously n-independent in the feature spaces not including MIVIS bands (Fig. 3A, C, F, H, M and O). It is evident that ML provides higher performances with all the 16 feature space configurations, especially in the highest-dimensional cases (Fig. 3B–E, G, I, L, N and P–R), than SAM and SID. These two classifiers generally exhibit comparable accuracies, with slightly better performances of SAM than of SID in low-dimensional feature spaces (Fig. 3A, C, F, H and M) and vice versa in high-dimensional ones (Fig. 3E, L, N and P). The improved accuracy of ML over SAM and SID is an expected result due to the capability of ML to take into account first- and second-order statistics of the data associated with each class. On the contrary, SAM and SID essentially characterize each class with a unique prototype and consequently do not allow appreciating the shapes of the class-conditional distributions in the feature space (Richards and Jia, 2006).

ML is based on a Gaussian unimodal model for each class-conditional statistics. In order to verify the possible unimodal spectral distribution of the data associated with each land cover, we applied the Hartigan test (Hartigan and Hartigan, 1985) and

Table 3

Array subsets for each input source (ADS40, MIVIS, nDSM, HM, TX) used in the source marginal improvement assessment: fs_x and fs_y include and exclude the reference data source, respectively. Statistical test results (t_1 and t_2) of the array subsets for each input source are listed: 1 (0) values of the Behrens–Fisher test indicate rejection (no rejection) of the H_0 null hypothesis with 0.95 confidence level.

Tested features	Array subset		Behrens–Fisher test	
	fs_x	fs_y	t_1 $H_0: \mu_x = \mu_y H_1: \mu_x > \mu_y$	t_2 $H_0: \mu_x = \mu_y H_1: \mu_x < \mu_y$
ADS40	1,3,5,6,8,10,11,13,15,16	2,4,7,9,12,14	0	1
MIVIS	2,4,5,7,9,10,12,14,15,16	1,3,6,8,11,13	1	0
nDSM	3,4,5,8,9,13,14,15,16	1,2,6,7,11,12	1	0
HM	6,7,8,9,10,16	1,2,3,4,5,11,12,13,14,15	0	0
TX	11,12,13,14,15,16	1,2,3,4,5,6,7,8,9,10	1	0

estimated the corresponding probability through a 500-sample bootstrap permutation scheme. High probability values of the unimodal distribution hypothesis are obtained for normalized digital surface and texture features and for most MIVIS bands, especially when conditioned to forest classes (average probability > 0.75), thus supporting the use of ML for classification purposes in the considered case study. More sophisticated approaches, based for example on classifier Ensembles, Markov random fields or support vector machines, could represent valuable alternatives to further improve the classification accuracy (e.g., Melgani and Bruzzone, 2004; Moser and Serpico, in press; Pal and Mather, 2005; Zhang et al., 2011).

3.2. Feature space combination (FS identification)

To optimally combine the available multi-source remote sensing data, the feature space configuration (FS) corresponding to the highest accuracy was determined (second step of the identification scheme). To this purpose, a preliminary testing analysis was performed to assess the marginal improvements derivable from each data source. Fig. 4 shows 5 plots related to the marginal improvements of ADS40, MIVIS, nDSM, HM, and TX. Each plot displays the distributions of overall accuracies (OA, on the y-axis) of the two reference array subsets (X and Y, on x-axis), defined in Eq. (3) and listed in Table 4. The classification performances are displayed through box plots where the central mark is the median (Me), the edges of the box are the 25th and 75th percentiles, and the whiskers extend to the most extreme data points. X median values greater (lower) than Y median values suggest possible source-dependent positive (negative) impacts.

Results suggest that the use of ADS40 in the classification process mainly negatively affects classification performances (Me(X) < Me(Y) in Fig. 4A and $t_1 = 0$ and $t_2 = 1$ in Table 3). This negative effect is likely imputable to the possible redundancy due to the overlapping of spectral signatures between ADS40 and MIVIS in the visible range. Furthermore lower probability values in the Hartigan test for unimodal distribution were also found for the ADS40 channels. This last issue could highlight possible limitations of the
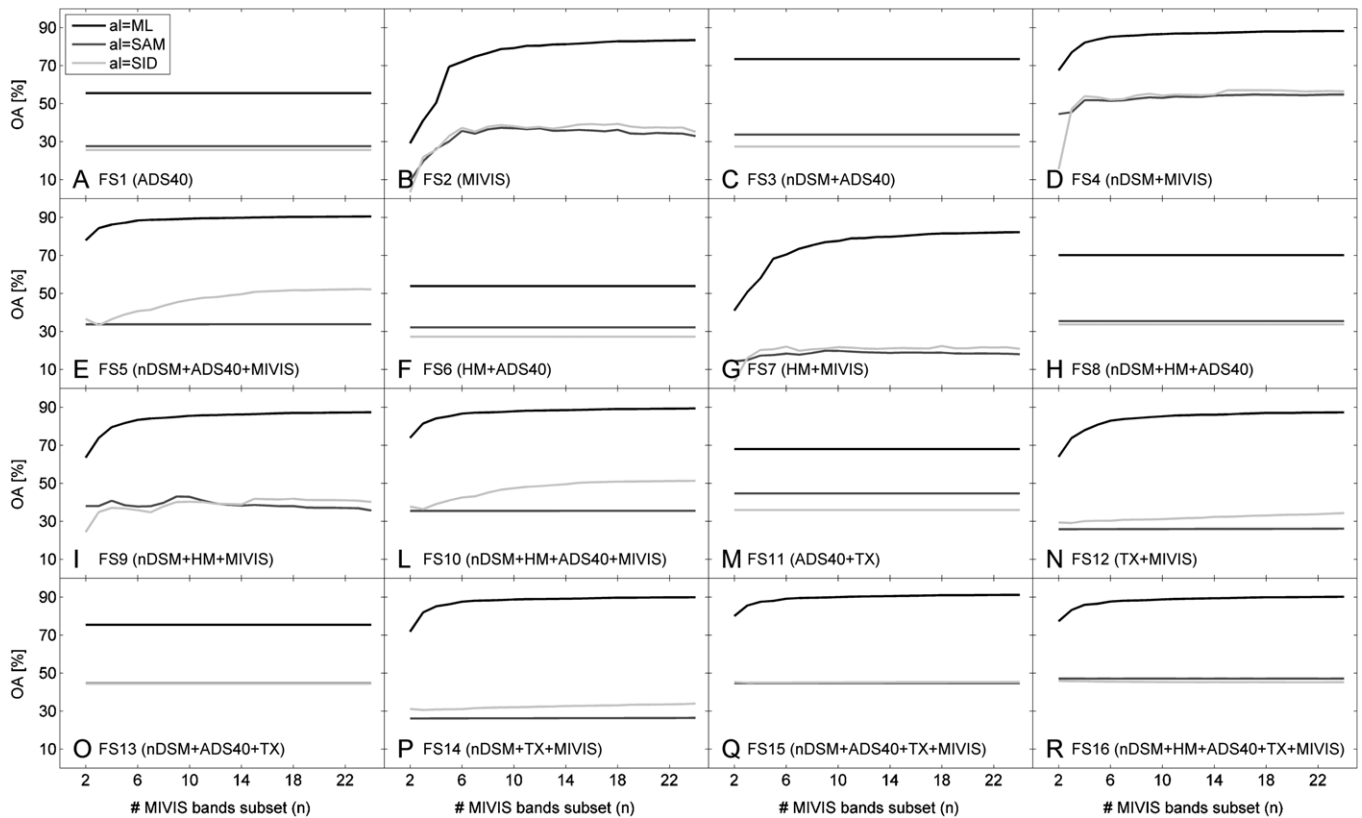

Fig. 3. Classification accuracies for the sixteen tested feature spaces displayed separately on different plots. Selected subsets of increasing input MIVIS bands and overall accuracies (OA) are displayed on the x-axis and y-axis, respectively. The three different color lines refer to the three classification algorithm performances (ML, SAM, SID), as indicated in the legend.
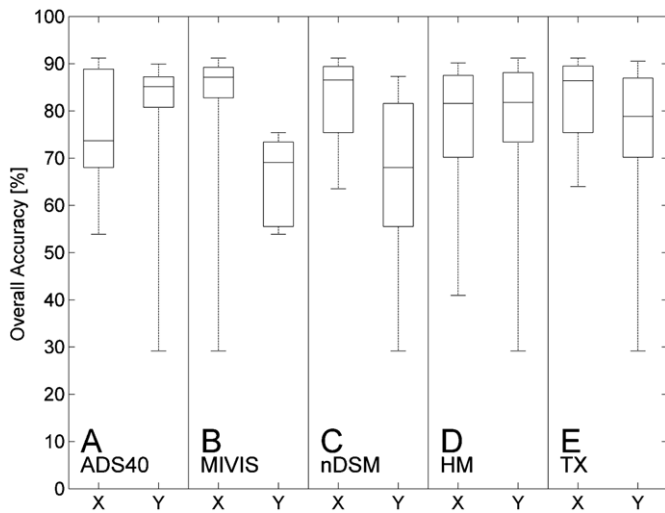
Fig. 4. Marginal improvements of specific data source: ADS40 (A), MIVIS (B), nDSM (C), HM(D) and TX(E). Each plot displays the distributions of overall accuracies (OA, y-axis) of the two reference array subsets (X and Y, x-axis, see Table 3 for the definition). The classification performances are displayed in box plots where the central mark is the median and the edges of the box are the 25th and 75th percentiles, the whiskers extend to the most extreme data points.
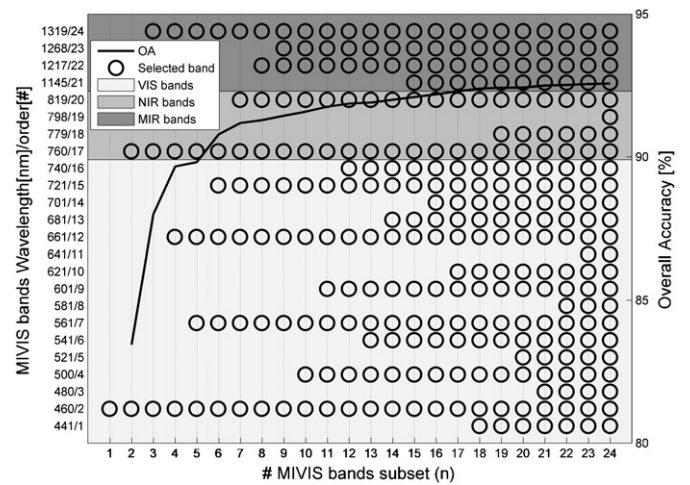

Fig. 5. The iterative selection of MIVIS subsets (on x-axis) with the progressive increasing of the number of hyperspectral bands (on left y-axis). Selected bands are displayed in black circles, while gray shaded colors define the reference spectral regions: visible (VIS), near infrared (NIR) and middle infrared (MIR). The overlaid overall accuracy is visualized as a solid black line and refers to the right y-axis.

selected classifiers, which essentially assume a monomodal behavior for each class-conditional statistics, in correctly capturing the spectral signature of this sensor.

Hillshade modeling (HM) does not improve the mapping accuracy ($Me(X) \sim Me(Y)$ in Fig. 4D and $t_1 = 0$ and $t_2 = 0$ in Table 3). Although HM well discriminates shaded/free-shaded areas in urban zones, this marginal classification benefit is negatively counterbalanced by the HM-derived noise in forest patterns (not shown here for brevity).

In contrast, MIVIS, nDSM, and TX features represent the most important discriminant contributions in the classification process ($Me(X) > Me(Y)$ in Fig. 4B, C and E and $t_1 = 1$ and $t_2 = 0$ in Table 3). Despite the evident cutoff of the original MIVIS bands (from 102 to 24 bands) results confirm the high capability of the remaining hyperspectral channels of classifying complex landscapes. Furthermore, LiDAR-derived 3D information (nDSM) and spatial textural features (TX) introduce additional discriminant information and positively contribute to maximize the inter-class separability.

Table 4 lists, for each explored feature space combination, the maximum classification accuracy, the ranking (r_k), and the

Table 4
Maximum overall accuracy (MOA), corresponding ranking order (r_k) and relative improvement with respect to FS1 (I_{FS1}) and FS2 (I_{FS2}), for each feature space (FS1, ..., FS16). Relative improvements are calculated as $I_{FSi}(FSj) = 100 \cdot [MOA(FSj) - MOA(FSi)]/MOA(FSj)$ where $i = 1, 2$ and $j = 1, ..., 16$.

Feature space	MOA (%)	Rank r_k	I_{FS1} (%)	I_{FS2} (%)
FS1	55.51	15	0.00	−50.24
FS2	83.4	9	33.44	0.00
FS3	73.42	12	24.39	−13.59
FS4	88.21	6	37.07	5.45
FS5	90.54	2	38.69	7.89
FS6	53.9	16	−2.99	−54.73
FS7	82.25	10	32.51	−1.40
FS8	70.2	13	20.93	−18.80
FS9	87.39	7	36.48	4.57
FS10	89.38	5	37.89	6.69
FS11	68	14	18.37	−22.65
FS12	87.32	8	36.43	4.49
FS13	75.41	11	26.39	−10.60
FS14	89.91	4	38.26	7.24
FS15	91.19	1	39.13	8.54
FS16	90.17	3	38.44	7.51

relative improvements as compared to the original sets of ADS40 (FS1) and MIVIS (FS2) channels. The use of multi-source data leads to classification improvements ranging up to ~40% and ~8% as compared to ADS40 and MIVIS alone. Interestingly, FS15 (ADS40 + MIVIS + TX + nDSM) represents the optimal multi-source configuration (OA = 91.19%, Table 4). This identified best combination represents an extreme point of the box plot in Fig. 4A (percentile > 75th). Comparable performances are obtained on configurations without ADS40 (e.g., FS14, OA = 89.91%, Table 4). Although, as discussed above, ADS40 generally yields a negative impact on the classification performances, as demonstrated through t-tests, its use can lead to improved accuracy if included within specific classification schemes. This might be interpreted as due to the 0.835–0.885 μm spectral range covered by ADS40 but not by MIVIS.

In the following sections FS15 (ADS40 + MIVIS + TX + nDSM) is retained as the best configuration of multi-source data for classification of heterogeneous landscapes on the considered data set.

3.3. Hyper-spectral contribution (n identification)

The number n of MIVIS channels remains the last issue (third step of the identification scheme) to determine in the proposed multi-source data fusion scheme. Fig. 5 shows the iteratively selected MIVIS subsets based on the SFS (x-axis) and the available hyperspectral bands (left y-axis) included in FS15. The selected bands are displayed in circles, while gray shaded colors define the reference spectral regions: visible (VIS), near infrared (NIR), and middle infrared (MIR). The overlaid overall accuracy (OA) is visualized as a solid black line and refers to the right y-axis.

The MIVIS bands are iteratively selected from the VIS, NIR, and MIR ranges, thus suggesting that the whole spectral span of the sensor is relevant for class discrimination, at least, for the considered data set. This result can be related to the high number and spatial variability of complex landscapes that likely benefit from spectral contributions from all the investigated spectral regions. The OA curve shows a sharp increment up to the #6 MIVIS bands subset and a subsequent monotonically increasing trend. This behavior suggests that the data variability may be prevalently captured by the 6-feature subset (#2, 7, 12, 15, 17, 24 MIVIS bands), at least, with respect to the task of discriminating the considered land cover classes. The highest accuracy (OA = 91.19%) is obtained with all
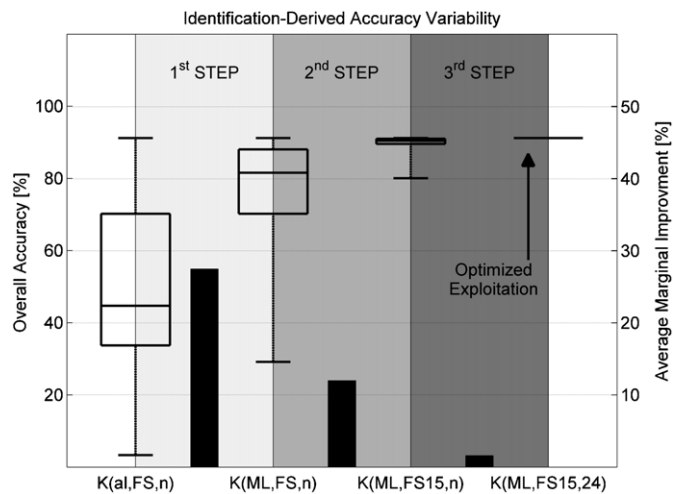
Fig. 6. Synoptic view of the accuracy improvements resulting through the three steps of the procedure adopted to identify the optimal classification scheme K(ML,FS15,24). Each box plot displays the variability of the overall accuracies of the mentioned array subsets: the central mark is the median, the edges of the box are the 25th and 75th percentiles, the whiskers extend to the most extreme data points. Black bars indicate the average marginal improvement (AMI) obtained by the identification process (in shaded colors) by referring to the right y-axis.

MIVIS channels and is used as a reference hyperspectral configuration for the final optimized exploitation.

3.4. Marginal accuracy improvements

Fig. 6 shows a synoptic view of the accuracy improvements resulting from the adopted classification scheme as compared to the original full array, K(al,FS,n) up to the final solution, K(ML,FS15,24), identified through the aforementioned 3-steps (in different gray scales). Each box plot displays the variability of the overall accuracies of the reference array subset labeled on the x-axis: the central mark is the median, the edges of the box are the 25th and 75th percentiles, the whiskers extend to the most extreme data points, whose range is indicated as DR (data range) in the following lines. Black bars indicate the average marginal improvement (AMI) associated with each step and obtained as the difference between the average values of the classification accuracies in two subsequent array subsets.

The first two identification steps (i.e., those related to the al and FS variables) prove most effective in reducing classification errors. The classifier selection (K(al,FS,n) → K(ML,FS,n)) significantly lowered the variability in classification accuracy (DR from ~90% to ~60% with AMI ~28%). The subsequent selection of the feature-space configuration provides for a further reduction in the range of accuracies (DR from ~60% to ~10%) and for an enhancement in classification performance (AMI ~12%), (K(ML,FS,n) → K(ML,FS15,n)). Although the third step – the optimization of n (K(ML,FS15,n) → K(ML,FS15,24)) – has a smaller impact on the final classification accuracy than the previous steps (DR decreased from ~10% to 1%, AMI = ~2%), it allows for an important accuracy improvement for certain classes, i.e., water bodies (WR, WL, reduction of commission/omission errors of ~50–70%), forest plant species (OK, PN, CY, SP, reduction of commission/omission errors of ~50%) and agriculture zones (PF, HE, reduction of commission/omission errors of ~70–80%).

3.5. Optimized multi-sensor data fusion

The resulting scheme, characterized by the ML classifier and by the feature space including ADS40, TX, nDSM, and the full set of MIVIS bands, is retained as the best performing multisource classification configuration with respect to the discrimination of the 17 classes in the considered data set. The final majority filter allows reaching a 92.57% OA. Fig. 7 shows the obtained high resolution land cover map: the entire monitored transect (bottom left map); the 3-km × 3-km reference window (upper map); and four zoomed classification views on typical landscapes (inset boxes A, B, C, and D). It is evident by a visual comparison of Figs. 1 and 7 that the obtained classification map captures well the spatial variability of the monitored area, especially considering that, at the data acquisition times, most of the vegetation types were in the senescence phase and consequently exhibited low reflectance values.

The coverage data, which exhibit the lowest error rate, are – as expected – the classes with well defined spectral signatures such as water river (COM(WR) = 1.38%, OMI(WR) = 3.66%), bare surfaces (COM(BS) = 3.58%, OMI(BS) = 5.92%), plowed fields (COM(PF) = 1.84%, OMI(PF) = 2.48%), herbaceous patterns (COM(HE) = 0.97%, OMI(HE) = 2.32%), and oak forests (COM(OK) = 3.08%, OMI(OK) = 14.71%). However, by referring to the confusion matrix M (M(u,v)) expressed in terms of percentage values (where the (u, v)-th entry M(u, v) refers to pixels classified in land cover u and belonging to the test set of land cover v), persistent errors are found due to possible inter-class spectral overlapping: bare surfaces classified as asphalt (M(AS, BS) = 11.78%); some industrial units labeled as urban fabric (M(UF,IU) = 21.33%); heatlands, herbaceous, oak, poplar and arundo donax partially incorrectly detected (e.g., M(HL,HE) = 5.33%, M(HL,OK) = 5.97%, M(AD,HL) = 9.96%, M(AD,OK) = 14.36%, M(PP,OK) = 37.01%); misclassifications in mixed conifer forests (M(CY,SP) = 26.47%, M(PN,SP) = 5.39%); possible errors between willows and poplar (M(WI,PP) = 10.13%), and misclassification errors on olive groves and herbaceous fields (M(OV,HE) = 24.12%).

3.6. Possible land cover-based optimized solutions

The optimized classification scheme represents the configuration that best performs on the considered 17-class set of land covers. Exploring the possible dependences of the aforementioned identification process on land cover can suggest possible alternative strategies to extend the proposed approach to landscapes with only certain land covers or with a marked predominance.

Fig. 8 shows the key variables for each land cover and for the top 10 classification schemes: the al, FS, and n choices that maximized the kappa conditional statistics are displayed in plots A–C. Rank order and land covers are shown on the x-axis and y-axis, respectively. For the sake of clarity, we grouped the land cover classes as: mixed forest (OK, PN, CY, SP); floodplain (WR, WL, RS, HL, AD, PL, WI); urban zone (AS, UF, IU); and agricultural area (PF, HE, OV).

3.6.1. Mixed forest

ML represents the best candidate classifier for all the monitored vegetation species (Fig. 8A) and is supported by significant probabilities of unimodal distributions in the Hartigan tests. Oak (OK), pine (PN), and cypressus (C) are better identified through FS7, FS5, FS4, respectively, as the preferential multi-source combinations maximizing the kappa conditional statistics (Fig. 8B), thus confirming the central role of hyperspectral data for classification of complex forest landscapes. The selected MIVIS subset is generally large (about > 16 channels, Fig. 8C). Interestingly, spruce patterns (SP) show multiple sub-optimal solutions in terms of FS and n.

3.6.2. Floodplain

ML represents the best classifier within the considered ones, for all the land covers with the exception of water lagoon (WL) where SID performs better in terms of kappa conditional statistics (Fig. 8A). Feature space combinations very different from the
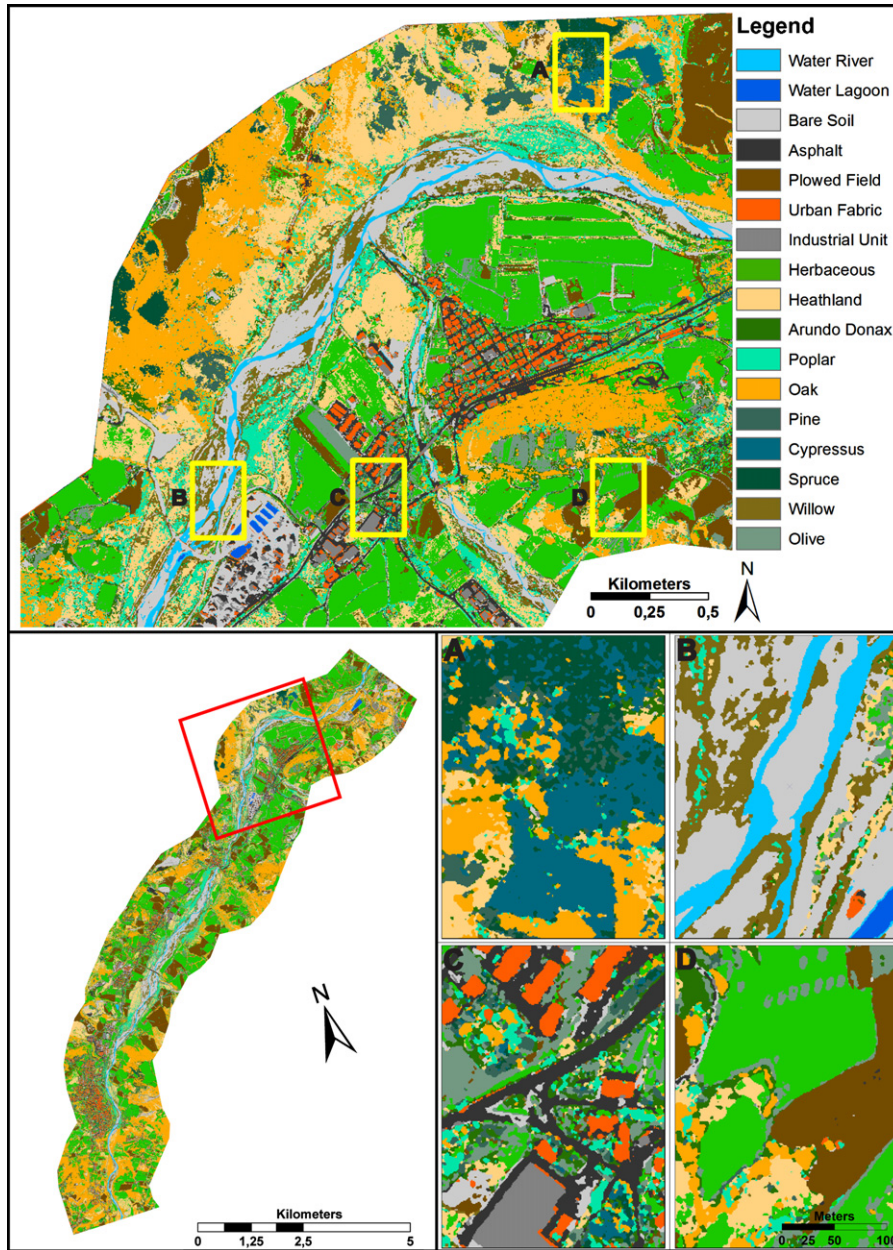
Fig. 7. Classification map resulting from the proposed optimized exploitation of multi-source remote sensing data, K(ML,FS15,24). Entire monitored 20-km stretch (bottom left map), reference 3-km × 3-km inset box (upper map), typical investigated landscapes including mixed forest (A), floodplain (B), urban zone (C) and agricultural area (D).
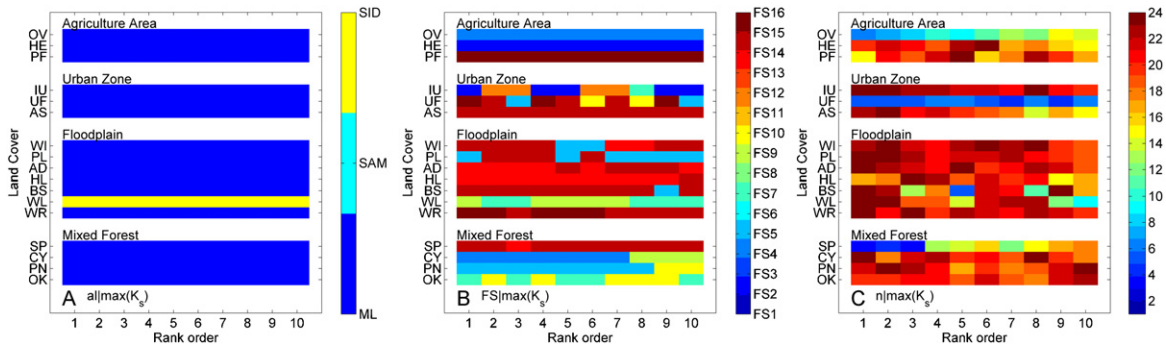

Fig. 8. Main classification variables for 4 grouped typical landscapes: mixed forest, floodplain, urban zone and agricultural area. Algorithm (*al*), feature space (*FS*) and MIVIS subset (*n*) maximizing kappa conditional statistics (K_s) are shown on plots A/B/C for each land cover and for the top 10 classification schemes. Rank order and land cover are shown on the *x*-axis and *y*-axis, respectively.

reference optimized solution K(ML,FS15,24) are identified for WL (FS7–9). Possible multi-modal spectral distributions of the surface response (low probability of unimodal distribution), possibly impacting on the performances of ML, are found through the Hartigan test (p(WL) = 0.05) and could be imputable to a high spatial variability of suspended sediments into the monitored lagoons. Analogously to forest landscapes, the best multi-source combinations for the riparian vegetation prevalently include MIVIS-based schemes (such as FS14, FS15 and FS16 for AD, WR, HE, HL, AD, PL, Fig. 8B). A certain agreement is reached, with the identification of a MIVIS subset, between land covers of typical floodplain areas and the optimized solution (n > 20) (Fig. 8C).

3.6.3. Urban zone

Within the considered classifiers, ML represents the best candidate for the monitored land cover classes in urban scenarios, such as asphalt (AS), urban fabric (UF) and industrial unit (IU). MIVIS, normalized Digital Surface Model, texture, and hillshade modeling play the most important contribution and are then selected into the multisource combination FS2, FS15, FS16 (Fig. 8B). Lower dimensionality MIVIS subsets are preferred (n < 7) for urban fabric over industrial unit and asphalt (n > 16) (Fig. 8C).

3.6.4. Agricultural area

Herbaceous (HE) and plowed fields (PF) are well discriminated by ML according to the reference optimized solution (Fig. 8A). For HE and OV, preferential feature space combinations are represented by FS2 and FS4. FS16, by exhibiting a positive contribution of texture layers, is selected as the best feature space for plowed field. Mainly lower dimensional MIVIS subsets (n < 20) than in K(ML,FS15,24) and multiple valuable alternatives with different hyperspectral bands are found appropriate for agricultural land covers.

4. Conclusions

In this paper we investigated an optimized scheme to jointly exploit hyperspectral MIVIS, color-infrared ADS40, and LiDAR data for land cover mapping of heterogeneous landscapes. The methodology focuses on the generation of an array of possible classification scenarios obtained by varying classifiers, multi-source stacks, and subsets of hyperspectral channels, and on the subsequent identification of the best performing configuration.

The proposed procedure resulted a valuable tool for identifying the optimal multi-source remote sensing data combination (with respect to the criterion of classification performances over test samples) by providing a final accurate map (OA = 92.57%). Among the three tested classifiers (ML, SAM, SID), the Maximum Likelihood is confirmed to be a suitable algorithm for mapping purposes (classifier selection has a 28% impact on the final optimized exploitation OA). The feature space including ADS40 (only in certain data combinations), nDSM, TX, and MIVIS data was the optimal multisource dataset to maximize class discrimination (additional 10% on the final OA). In particular, the optimal hyperspectral subset turned out to be the full available set of MIVIS channels (2% further marginal improvement). Significant inter-class differences are also found in the identification schemes, by indicating possible landscape-driven land cover mapping solutions to maximize classification performances.

Additional analysis on independent test areas and multi-scene acquisitions would contribute to fully define optimization strategies in the use of high dimensional remote sensing data and to strengthen the transferability of the proposed approach. However, the exploited remote sensing dataset and spatial domain are considered a good case study (in terms of multi-source imagery, size of the classification array, areal extension, and land cover variability) to quantify the multi-sensor capability for high resolution mapping of heterogeneous landscapes. In particular, the conducted analysis provided an experimental framework of the potential and limitations of the combined use of MIVIS, ADS40, and LiDAR sensors for classification tasks by focusing on certain natural- and human-dominated environments of interest for different application fields, such as urban planning, river restoration, agricultural, and forestry resource management. Future developments should focus on a better understanding of the contribution of ADS40 – that showed highly variable benefits across the tested feature space configurations – when used in combination with hyperspectral MIVIS and LiDAR data.

An advantage of airborne remote sensing, compared to satellite remote sensing, is the capability of offering very high spatial resolution images and detailed thematic maps. The main disadvantages are low coverage area and high cost per unit area of ground coverage. In light of the recent progresses in spaceborne sensor technology (e.g., ENMAP, Sentinel, ICESat/GLAS), the proposed approach can be viewed also as a preliminary investigation of the synergic use of spectral and laser data originating from different sources for fine-scale classification purposes, whose translation to forthcoming satellite systems would allow for higher cost-effectiveness of land use/land cover mapping, especially for continuous monitoring.

References

Anderson, J.E., Plourde, L.C., Martin, M.E., Braswell, B.H., Smith, M.L., Dubayah, R.O., Hofton, M.A., Blair, J.B., 2008. Integrating waveform lidar with hyperspectral imagery for inventory of a northern temperate forest. Remote Sensing of Environment 112, 1856–1870.

Belluco, E., Camuffo, M., Ferrari, S., Modenese, L., Silvestri, S., Marani, A., Marani, M., 2006. Mapping salt-marsh vegetation by multispectral and hyperspectral remote sensing. Remote Sensing of Environment 105 (1), 54–67.

Burrough, P.A., McDonell, R.A., 1998. Principles of Geographical Information Systems. Oxford University Press, NY, USA.

Cavalli, R.M., Fusilli, L., Pascucci, S., Pignatti, S., Santini, F., 2008. Hyperspectral sensor data capability for retrieving complex urban land cover in comparison with multispectral data: Venice city case study (Italy). Sensors 8, 3299–3320.

Chang, C.I., 2000. An information-theoretic approach to spectral variability, similarity, and discrimination for hyperspectral image analysis. IEEE Transactions on Information Theory 46, 1927–1932.

Chen, Y., Su, W., Li, J., Sun, Z., 2009. Hierarchical object oriented classification using very high resolution imagery and LIDAR data over urban areas. Advances in Space Research 43 (7), 1101–1110.

Claessens, L., Schoorl, J.M., Verburg, P.H., Geraedts, L., Veldkamp, A., 2009. Modelling interactions and feedback mechanisms between land use change and landscape processes. Agriculture Ecosystems & Environment 129 (1–3), 157–170.

Colombo, R., Meroni, M., Marchesi, A., Busetto, L., Rossini, M., Giardino, C., Panigada, C., 2008. Estimation of leaf and canopy water content in poplar plantations by means of hyperspectral indices and inverse modeling. Remote Sensing of Environment 112 (4), 1820–1834.

Dalponte, M., Bruzzone, L., Gianelle, D., 2008. Fusion of hyperspectral and lidar remote sensing data for classification of complex forest areas. IEEE Transactions on Geoscience and Remote Sensing 48 (5), 1416–1427.

de Jong, Y.M., van der Meer, F.D., 2004. Remote Sensing Image Analysis Including the Spatial Domain. Kluwer Academic Publishers, Dordrecht, Netherlands.

Duca, R., Del Frate, F., 2008. Hyperspectral and multiangle CHRIS–PROBA Images for the generation of land cover maps. IEEE Transactions on Geoscience and Remote Sensing 46 (10), 2857–2866.

Elaksher, A.F., 2008. Fusion of hyperspectral images and LiDAR-based dems for coastal mapping. Optical Laser Engineering 46 (7), 493–498.

Feddema, J.J., Oleson, K.W., Bonan, G.B., Mearns, L.O., Buja, L., Meehl, G., Washington, W.M., 2005. The importance of land cover change in simulating future climates. Science 310 (5754), 1674–1678.

Forzieri, G., Guarnieri, L., Vivoni, E.R., Castelli, F., Preti, F., 2009. Multiple attribute decision-making for individual tree detection using high-resolution laser scanning. Forest Ecology and Management 258 (11), 2501–2510.

Forzieri, G., Moser, G., Vivoni, E.R., Castelli, F., Canovaro, F., 2010. Riparian vegetation mapping for hydraulic roughness estimation using very high resolution remote sensing data fusion. Journal of Hydraulic Engineering. ASCE 136 (11), 855–867.

Forzieri, G., Catani, F., 2011. Scale-dependent relations in land cover biophysical dynamics. Ecological Modelling 222 (17), 3285–3290.

Forzieri, G., Moser, G., Catani, F. Assessment of hyperspectral MIVIS sensor capability for heterogeneous landscape classification. ISPRS Journal. Photogrammetry, http://dx.doi.org/10.1016/j.isprsjprs.2012.09.011, in press.

Forzieri, G., Castelli, F., Preti, F., 2012a. Advances in remote sensing of hydraulic roughness. International Journal of Remote Sensing 33 (2), 630–654.

Forzieri, G., Battistini, A., Catani, F., 2012b. ES4LUCC: a GIS-tool for remotely monitoring landscape dynamics. Computers & Geosciences 49, 72–80.

Gianinetto, M., Lechi, G., 2004. The development of superspectral approaches for the improvement of land cover classification. IEEE Transactions on Geoscience and Remote Sensing 42 (11), 2670–2679.

Goodenough, D.G., Dyk, A., Niemann, O., Pearlman, J.S., Chen, H., Han, T., Murdoch, M., West, C., 2003. Processing Hyperion and ALI for forest classification. IEEE Transactions on Geoscience and Remote Sensing 41 (6), 1321–1331.

Haralick, R.M., Shanmugan, K., Dinstein, I., 1973. Textural features for image classification. IEEE Transactions on Systems, Man and Cybernetics 3 (6), 610–621.

Hartigan, J.A., Hartigan, P.M., 1985. The dip test of unimodality. Annals of Statistics 13 (1), 70–84.

Herold, M., Liu, X., Clarke, K.C., 2003. Spatial metrics and image texture for mapping urban land use. Photogrammetric Engineering and Remote Sensing 69 (9), 991–1001.

Hirano, A., Madden, M., Welch, R., 2003. Hyperspectral image data for mapping wetland vegetation. Wetlands 23 (2), 436–448.

Hughes, G.F., 1968. On the mean accuracy of statistical pattern recognizers. IEEE Transactions on Information Theory 14 (1), 55–63.

Kottegoda, N.T., Rosso, R., 1997. Statistics, Probability, and Reliability for Civil and Environmental Engineers. McGraw-Hill, NY, USA.

Kruse, F.A., Lefkoff, A.B., Boardman, J.B., Heidebrecht, K.B., Shapiro, A.T., Barloon, P.J., Goetz, A.F.H., 1993. The spectral image processing system (SIPS)—interactive visualization and analysis of imaging spectrometer data. Remote Sensing of Environment 44 (2–3), 145–163.

Landgrebe, D., 2003. Signal Theory Methods in Multispectral Remote Sensing. John Wiley & Sons, Hoboken, NJ, USA.

Lillesand, T.M., Kiefer, R.W., Chipman, J.W., 2008. Remote Sensing and Image Interpretation, 6th ed. John Wiley & Sons, Hoboken, NJ, USA.

Lu, S., Oki, K., Shimizu, Y., Omasa, K., 2007. Comparison between several feature extraction/classification methods for mapping complicated agricultural land use patches using airborne hyperspectral data. International Journal of Remote Sensing 28 (5), 963–984.

Melesse, A.M., Weng, Q., Thenkabail, P.S., Senay, G.B., 2007. Remote sensing sensors and applications in environmental resources mapping and modelling. Sensors 7 (12), 3209–3241.

Melgani, F., Bruzzone, L., 2004. Classification of hyperspectral remote sensing images with support vector machines. IEEE Transactions on Geoscience and Remote Sensing 42 (8), 1778–1790.

Moser, G., Serpico, S.B. Combining support vector machines and Markov random fields in an integrated framework for contextual image classification. IEEE Transactions on Geoscience and Remote Sensing, http://dx.doi.org/10.1109/TGRS.2012.2211882, in press.

Moser, G., Serpico, S.B., Benediktsson, J.A. Land cover mapping by Markov modeling of spatial contextual information in very high resolution remote sensing images. Proceedings of the IEEE, http://dx.doi.org/10.1109/JPROC.2012.2211551, in press.

Mundt, J.T., Streutker, D.R., Glenn, N.F., 2006. Mapping sagebrush distribution using fusion of hyperspectral and lidar classifications. Photogrammetric Engineering and Remote Sensing 72, 47–54.

Navulur, K., 2007. Multispectral Image Analysis Using the Object-oriented Paradigm. CRC Press, Boca Raton, FL, USA.

Pignatti, S., Cavalli, R.M., Cuomo, V., Fusilli, L., Pascucci, S., Poscolieri, M., Santini, F., 2009. Evaluating Hyperion capability for land cover mapping in a fragmented eco system: Pollino National Park, Italy. Remote Sensing of Environment 113 (3), 622–634.

Pal, M., Mather, P.M., 2005. Support vector machines for classification in remote sensing. International Journal of Remote Sensing 26 (5), 1007–1011.

Priestnall, G., Jaafar, J., Duncan, A., 2000. Extracting urban features from LiDAR digital surface models. Computers Environment and Urban Systems 24 (2), 65–78.

Richards, J.A., Jia, X., 2006. Remote Sensing Digital Image Analysis, sixth ed. Springer-Verlag, Berlin, Germany.

Serpico, S.B., D'Incà, M., Melgani, F., Moser, G., 2002. A comparison of feature reduction techniques for classification of hyperspectral remote-sensing data. In: Proceedings of the SPIE—Conference on Image and Signal Processing for Remote Sensing VIII, Crete, Greece, September 22–27, 2002, pp. 347–358.

Serpico, S.B., Moser, G., 2007. Extraction of spectral channels from hyperspectral images for classification purposes. IEEE Transactions on Geoscience and Remote Sensing 45 (2), 484–495.

Spinetti, C., Mazzarini, F., Casacchia, R., Colini, L., Neri, M., Behncke, B., Salvatori, R., Buongiorno, M.F., Pareschi, M.T., 2009. Spectral properties of volcanic materials from hyperspectral field and satellite data compared with LiDAR data at Mt. Etna. The International Journal of Applied Earth Observation 11, 142–155.

Tansey, K., Chambers, I., Anstee, A., Denniss, A., Lamb, A., 2009. Object-oriented classification of very high resolution airborne imagery for the extraction cover in agricultural areas. Applied Geography 29 (2), 1145–1157.

Tso, B., Mather, P.M., 2000. Classification Methods for Remotely Sensed Data. CRC Press, Boca Raton, FL, USA.

van Der Meer, F.D., van Der Werff, H.M.A., van Ruitenbeek, F.J.A., Hecker, C.A., Bakker, W.H., Noomen, M.F., van Der Meijde, M., Carranza, E.J.M., Smeth, J.B.D., Woldai, T., 2012. Multi- and hyperspectral geologic remote sensing: a review. The International Journal of Applied Earth Observation 14, 112–128.

Wang, Z., Liu, S., Huang, X., 2010. Simulation of low-resolution panchromatic images by multivariate linear regression for pan-sharpening IKONOS imageries. IEEE Transactions on Geoscience and Remote Sensing 7 (3), 515–519.

Yuan, F., Sawaya, K.E., Loeffelholz, B.C., Bauer, M.E., 2005. Land cover classification and change analysis of the Twin Cities (Minnesota) Metropolitan Area by multitemporal Landsat remote sensing. Remote Sensing of Environment 98 (2–3), 317–328.

Zhang, B., Li, S., Jia, X., Gao, L., Peng, M., 2011. Adaptive Markov random field approach for classification of hyperspectral imagery. IEEE Transactions on Geoscience and Remote Sensing 8 (5), 972–977.